FINAL TECHNICAL REPORT

Award No. DE-FG36-06GO16054

Project Period: September 1, 2006 to September 30, 2010

Nanocoatings for High-Efficiency Industrial Hydraulic and Tooling Systems

Clifton B. Higdon III
Eaton Corporation
26201 Northwestern Highway
Southfield, MI 48076
(248) 226-6432
cliftonhigdon@eaton.com

Prepared jointly with:

Greenleaf Corporation
Ames Laboratory
Oak Ridge National Laboratory

December 31, 2010

Acknowledgement, Disclaimer, and Proprietary Data Notice

Acknowledgement

This report is based upon work supported by the U.S. Department of Energy, Energy Efficiency and Renewable Energy, Industrial Technologies Program, Materials for Energy Efficient Industrial Processing under Award No. DE-FG36-06GO16054.

Research at the Oak Ridge National Laboratory was sponsored by the U.S. Department of Energy, Office of Energy Efficiency and Renewable Energy, Industrial Technologies Program, under contract DE-AC05-00OR22725 with UT-Battelle, LLC.

Research at the Ames Laboratory was sponsored by the U.S. Department of Energy, Office of Energy Efficiency and Renewable Energy, Industrial Technologies Program, under contract DE-AC02-07CH11358 with Ames Laboratory, Iowa State University.

The authors wish to thank Dr. Mahesh Jha for reviewing this document and Ms. Kodie Arnold for her efforts in preparing the document for publication. The authors also wish to express their sincere thanks to Bohdan Lisowski, Ms. Lyudmila Solovyeva, Dr. Alaa Elmoursi, Dr. Dong Zhu, Robert Milner, Ms. Lucinda Shane, James Anderegg, Choll Jun, and Ron Malone for their specific contributions to the development of the $AlMgB_{14}$-TiB_2 nanocoatings technology.

Table of Contents

List of Figures

List of Tables

Abbreviations and Acronyms

AFM	Atomic Force Microscopy
ASTM	American Society for Testing Materials
at.	Atomic
BAM	$AlMgB_{14}$-based material
BAMC	$AlMgB_{14}$-TiB_2+C coating
BTU	British thermal unit(s)
CVD	Chemical Vapor Deposition
deg	Degree(s)
DOC	Depth of Cut
DOE	Department of Energy
EDS	Electron dispersion spectroscopy
GPM	Gallon(s) per Minute
h	Hour(s)
HT	High Temperature
Hz	Hertz
IC	Innovation Center (Eaton Research)
IPR	Inch(es) per Revolution
in	Inch(es)
K-WATT	Kilowatts
kW	Kilowatts
LOC	Length of Cut
L	Liters
lbF	Pounds-Force
LT	Low Temperature
MTBF	Mean Time between Failures
min	Minute(s)
N	Newton(s)
NDA	Non-Disclosure Agreement
ORNL	Oak Ridge National Laboratory
PLD	Pulsed Laser Deposition
Psi	Pounds per Square Inch
PVD	Physical Vapor Deposition
REV	Revolution(s)
RPM	Revolution(s) per Minute
sec	Second(s)
SEM	Scanning electron microscopy
SFM	Surface Foot per Minute
TEM	Transmission electron microscopy
VIS	Valve-in-Star (motor configuration)
wt.	Weight
XPS	X-ray photo spectroscopy
XRD	X-ray diffraction

1.0 Executive Summary

This report summarizes the work performed by an Eaton-led project team under a 4-year DOE-ITP sponsored project titled, “Nanocoatings for High-Efficiency Industrial Hydraulic and Tooling Systems.” The Report serves as the project deliverable for the Grant # DE-FG36-06GO16054.

1.1 Purpose

The primary objective of this project was the development of a variety of thin film nanocoatings, derived from the $AlMgB_{14}$ system, with a focus on reducing wear and friction in both industrial hydraulics and cutting tool applications. Prior work had shown $AlMgB_{14}$ composites to exhibit super-hard behavior, and so the selection of the two applications was based largely on the concept of improved mechanical interface efficiencies for energy conservation. For mobile hydraulic systems, efficiency gains through low friction would translate into improved fuel economy and fewer greenhouse gas emissions. Industrial hydraulic systems, accordingly, would consume less electrical power. Reduced tooling wear in machining operations would translate to greater operating yields, while lowering the energy consumed during processing.

1.2 Purpose

To accomplish the above objective, the project was divided into 3 phases with the following specific objective and work scope:

Phase I – Proof of Concept : The focus of this phase was to conduct “proof-of-concept” evaluation of the applicability of the $AlMgB_{14}$- based coatings to hydraulic and tool inset applications by:

- Determining mechanical and tribological properties of single-phase and composite boride thin films made by PLD at Ames and then comparing with baseline thin film coatings provided by Eaton and Greenleaf.

- Developing unbalanced magnetron PVD technology at Eaton for the deposition of $AlMgB_{14}$-TiB_2 nanocomposites on coupons and hydraulic system components.

- Evaluating tool wear at Greenleaf on Ti and Ti-6Al-4V workpiece materials in lathe turning tests with $AlMgB_{14}$-coated and $AlMgB_{14}$-TiB_2-coated WC-6%Co inserts to be prepared at Ames and Eaton.

Phase II – Coating Process Scale-up: The focus of this phase was to conduct process scale-up to generate coated prototypes by:

- Establishing scaled-up process to the proven PLD technology practices at Ames.

- Conducting process scale-up studies at Eaton and then utilizing its production capable unbalanced magnetron PVD equipment. Some coupon testing completed to verify coating performance.

- Conducting limited scale-up study at Greenleaf using a theoretical PVD system. Some coupon testing was done to verify coating performance.

- Having Ames and ORNL provide technical support for the above scale-up studies through selected characterization and performance testing of coatings made using the scaled-up equipment.

Phase III – Functional Testing and Commercialization: The focus of this phase was to validate performance and durability improvements by functional testing of product-intent prototypes. The second step was to estimate energy savings potential based on these results and available market information and then establish a commercialization strategy by:

- Validating energy savings for both hydraulic and tooling systems through the functional testing of production-intent prototypes.

- Validating performance and durability improvements on both hydraulic and tooling systems thorough functional testing with production-intent prototypes.

- Conducting limited prototype tests of commercially available alternatives to establish a value proposition for $AlMgB_{14}$-based coatings.

- Finalizing a strategy for commercialization of AlMgB14-based nanocoatings for both industrial hydraulics and cutting tool applications

1.3 Results

The key results from the work are discussed below.

1.3.1 Characterization

Characterization of the films revealed their semi-crystalline nature; as a single phase, $AlMgB_{14}$ appears amorphous. Pairing this particular material with TIB_2 (known to be crystalline) through comminution of very fine scale powders (50 -100 nm), however, produces a bulk solid that exceeds the hardness of its respective constituent phases. Through physical vapor deposition processing, the nanocomposite coating that results combines the wear resistance characteristic of hard materials (e.g. the $AlMgB_{14}$) with a regenerating lubricant.

Within the top layers (10-20 nm) of the nanocomposite coating, the same TiB_2 phase used to enhance the strength and provide ductility to the otherwise brittle $AlMgB_{14}$ material reacts with available hydrogen and oxygen ions to form boron oxide. As the atoms of TiB_2 continue to react, layers of boric acid begin to form at the surface. Boric acid's relatively weak bonds are analogous to a deck of playing cards, whereby the individual atomic layers can easily slide with respect to one another.

1.3.2 Tribological Modeling

Tribology testing performed on both representative coupons and end-use components has shown that there is a sound correlation between experimental results and the data. Simulative tribology testing has been used effectively to represent "real world" application of the $AlMgB_{14}$-based nanocoating. In one application, for example, the resultant friction and velocity data plots

closely mimicked the theoretical Stribeck curve used to map out the three lubricant regimes: boundary, mixed, and elastohydrodynamic. Theory predicts the greatest degree of wear occurring in the boundary condition, as there is far greater metal-on-metal contact.

1.3.3 Establishment of robust coating process parameters

Physical vapor processing parameters were evaluated and optimized throughout the project to minimize the difficulties common to transitioning a laboratory-scale process or technology to a salable product. Coating process times and temperatures, process gas flows and ramp rates, and a host of other adjustable parameters have been finely tuned based on the results of both testing and coating characterization. The overriding goal of all of these efforts, as expected, was a repeatable coating process that yields the benefits observed in the laboratory, independent of the intended product or market.

1.3.4 Hydraulic Performance Testing

From the perspective of industrial hydraulics, the $AlMgB_{14}$ nanocoatings technology has progressed beyond baseline laboratory efficiency tests into measurable energy savings and enhancements to product durability. Eaton Corporation has identified three key markets that stand to benefit from implementation: industrial vane pumps, orbiting valve-in-star hydraulic motors, and variable displacement piston pumps. In the vane pump application, the overall product efficiency was improved by as much as 11%. Similar results were observed with the hydraulic motors tested, whereby efficiency gains of over 10% were noted. For the variable displacement piston pump line, the overall efficiency was improved by 5%.

1.3.5 Tooling Performance Testing

The most significant gains in productivity (and, accordingly, the efficiency of the machining process as a whole) were associated with the roughing and finishing of titanium components for aerospace systems. Use of the $AlMgB_{14}$ nanocoating in customer field tests has shown that the coated tools were able to withstand machining rates as high as 500sfm (limited only by the substrate material), with relatively low flank wear when compared to other industrial offerings. As an example of the material's superb wear resistance, $AlMgB_{14}$ coated tools exhibited a 60% improvement over similarly applied TiAlN thin films. $AlMgB_{14}$-based coatings in these particular tests lasted twice as long than their TiAlN counterparts at the 500sfm feed rates.

1.4 Conclusions

This project demonstrated that application of the $AlMgB_{14}$-based coatings technology will result in efficiency savings in both industrial hydraulics and tooling systems. It is expected that the use of this technology in other, energy–sensitive markets will also yield savings.

Highlights of the coating research throughout the project include the following:

- A 97% reduction in the coefficient of friction between the $AlMgB_{14}$-based nanocoating and the steel counterface material, all while running in a water glycol lubricant (known to exhibit higher pressure-viscosity values than standard mineral oil-based fluids).

- A 40% lower coefficient of sliding friction than the industry's lowest friction offerings in the noted mineral oil lubricant.

- Extensive performance testing of industrial hydraulic systems showed measurable efficiency gains when the $AlMgB_{14}$-based coatings were applied to the sub-components - some exceeding 12 percent above baseline.

- A 38 percent improvement in tool life was shown for tungsten carbide-based cutting tools when using the group's novel nanocoatings.

- Coefficients of sliding friction ranging between 0.02-0.04 at 32,400 meters in a lubricant-starved, pin-on-disk tribotest using mineral oil as the lubricant

- Coefficients of sliding friction between 0.02-0.04 observed for a lubricant-starved pin-on-disk tribotest using water-glycol (to 5400 meters).

Full implementation of the technology into the industrial hydraulic and cutting tool markets equates to a worldwide energy savings of 46 trillion BTU/year by 2030. U.S.-based GHG emissions associated with the markets identified would fall accordingly, dropping by as much as 50,000 tonnes annually.

1.5 Recommendations

There are some unanswered questions regarding the coating and how much further its performance could be enhanced. Current knowledge of the material's electronic structure is somewhat established, though future changes in composition could yield nanocoatings with even greater wear or frictional performance. Further R&D work would help define how far this particular material system can be advanced in terms of friction, wear, and durability.

1.6 Commercialization

The nanocoating's superb wear and frictional performance test results led way to the following commercialization opportunities over the course of the project. In each of the systems discussed, the $AlMgB_{14}$ coatings were applied onto existing substrates or less expensive substrate materials to offset any added processing costs:

Hydraulic vane pumps – Application of the $AlMgB_{14}$-based coating improves the overall efficiency and enhanced the durability of the product over a wide range of operating conditions. These products are currently used in a variety of heavy energy-intensive applications, such as injection molders and steelmaking equipment.

Hydraulic motors – The $AlMgB_{14}$-based coating improves the mechanical efficiency of the system at startup. Motors typically exhibit lower than peak efficiencies at low speed and are often oversized to accommodate the torque needed. Hydraulic motors are used predominantly in mobile markets, including skid loaders and tracked agricultural vehicles.

Hydraulic piston pumps – The $AlMgB_{14}$-based coatings have been shown to improve the efficiency of these pumps over their entire operating space. Product durability has been enhanced as well. Piston pumps are used throughout a variety of industries including mobile hydraulics, industrial systems, and aerospace actuation.

Industrial tooling – Tools coated with $AlMgB_{14}$-based coatings have enhanced durability and can be used at higher feed rates. The most significant gains associated with the nanocoatings technology has been shown in the machining of titanium components for aerospace markets.

The reader is referred to Section 6.0 (Commercialization) for specific details regarding the commercialization pathways for these coatings.

Eaton Corporation and Greenleaf are presently moving forward with plans to commercialize the nanocoatings technology. Recent economic conditions in the industrial hydraulics markets are such that efficiency gains through technology are not being pursued by the customer base. It is expected, however, that if diesel fuel prices return to the $3.80 per gallon levels of 2008, the end-customer base (namely, the large fleet operators and mobile-market/agricultural leasing services) will demand similar efficiency improvements as those realized during this project. Recent tests of the $AlMgB_{14}$-TiB_2 nanocoating in an aerospace hydraulics pump have resulted in a significant enhancement to product life and overall performance. Pending the outcome of scheduled durability testing on production-intent prototype components, the coatings technology may be introduced in a high-visibility commercial aircraft application.

The wear performance and reduced processing costs (through higher feed rates) associated with the titanium machining pilot trials have generated interest by Greenleaf's customer base. Greenleaf sees its next step towards commercialization as deciding between in-house processing of the material and using a production-intent supplier with the commercially available $AlMgB_{14}$-TiB_2 coating. Prior to choosing their commercialization path, though, Greenleaf plans to execute performance comparisons between the Eaton $AlMgB_{14}$-TiB_2 derivative and the commercially available coating. The terms of this evaluation are being reviewed as part of the non-disclosure agreement (NDA) between Greenleaf and their supplier. Upon completion of the aforementioned testing and establishment of the processing path, Greenleaf will begin customer validation and introduce the coating as a commercial product for purchase.

2.0 Introduction

Industrial manufacturing in the U.S. accounts for roughly one third of the 98 quadrillion Btu total energy consumption. Motor system losses amount to 1.3 quadrillion Btu, which represents the largest proportional loss of any end-use category, while pumps alone represent over 574 trillion BTU (TBTU) of energy loss each year [1].

The efficiency of machines with moving components is a function of the amount of energy lost to heat as a result of friction between contacting surfaces. The friction between these interfaces also contributes to downtime and the loss of productivity through component wear and subsequent repair. The production of new replacement parts requires additional energy. Among efforts to reduce energy losses, wear-resistant, low-friction coatings on rotating and sliding components offer a promising approach that is fully compatible with existing equipment and processes. In addition to lubrication, one of the most desirable solutions is to apply a protective coating or surface treatment to rotating or sliding components to reduce their friction coefficients, thereby leading to reduced wear. Historically, a number of materials such as diamond-like carbon (DLC), titanium nitride(TiN), titanium aluminum nitride (TiAlN), and tungsten carbide(WC) have been examined as tribological coatings (e.g., [2, 3]. While certain coatings and surface treatments offer attractive advantages in specific environments, the search continues for a cost-effective, wear-resistant, low-friction coating suitable across a wide range of applications.

With an obvious need for development and commercial deployment of a robust, wear-resistant, low-friction coating to improve energy efficiency across many industries, the Industrial Technologies Program (ITP) of Energy Efficiency and Renewable Energy (EERE) division of the U. S. Department of Energy (DOE) selected this project for financial support in 2006 under a competitive solicitation. It was a cost-shared research and development project with, Eaton Corporation as the lead organization and Greenleaf Corporation as a sub recipient. Eaton's business interests lie in the industrial hydraulic applications whereas Greenleaf was interested in cutting tool applications. The project team included two DOE national laboratories, The Ames Laboratory and Oak Ridge National Laboratory.

The primary focus of the project was on the development and commercialization of a family of nanoscale composites in which the hardness is derived from microstructural engineering of the constituent phases, referred to as extrinsic hardness [4]. Proof-of-concept studies leading up to this project had shown that the constituent phases, $AlMgB_{14}$ and TiB_2, were capable of producing low-friction coatings by pulsed laser deposition. These coatings combine high hardness with a low friction coefficient, and were shown to substantially reduce wear in laboratory tribology tests [5]. Since the coatings are produced from nanoscale composite targets and exhibit a similar scale of phase mixing in coating form, they are referred to as '*Nanocoatings,*' hence the title of this project.

Although many potential applications exist for ultra-hard, self-lubricating coatings, two major application spaces were selected for development in this project:

(1) Hydraulic system components to yield mechanical and volumetric efficiency improvements in vane pumps, hydraulic motors, and piston pumps. These coatings were also designed to facilitate elimination or reduction of the “de-rating” of vane pumps in environmentally friendly water-glycol hydraulic fluids. In addition, application of the coatings was intended to improve start-up torque efficiency in valve-in-star (gerolers) hydraulic motors.

(2) Coatings on a range of cutting tool inserts (primarily carbides, with the potential to pursue cermet and ceramic inserts as well) to improve the cutting efficiency and increase tool life.

At the beginning of the project, the goal was set to develop coatings that would improve pump performance by 5%. A 5% energy savings sounds modest, but when one considers that pumps are one of the largest energy users in the U.S. manufacturing sector, this represents approximately $8x10^6$ BTU of energy savings per pump annually for a medium displacement - medium duty pump with an assumed annual usage of 2000 hours. When factoring in diesel engine efficiencies and the percentage of engine output that powers the system, this translates to approximately $300 - $400 per pump in fuel savings annually, assuming $2.80/gallon diesel fuel. Extending this to a global perspective, if only 50% of hydraulic pumps worldwide were to adopt this coating, the diesel energy savings would exceed 5 TBTU and a potential for $200 million in fuel savings. The goal for cutting tool applications was set at a 50% or greater increase in tool life.

The scope of the project included development of two coating deposition methods – pulse laser deposition (PLD) and physical vapor deposition (PVD). Scale up and quality control were important considerations.

3.0 Background

3.1 Current State of Industrial Coatings

Given the potential number of applications that would stand to benefit from an industry-leading, low friction coating, it is important to first review a selection of the many compositions available. Even a cursory review of literature or market data would show that there are many variants of surface treatments that, in effect, strive to accomplish a similar outcome. Given this, the $AlMgB_{14}$-based nanocoatings that are the focus of this project would need to demonstrate an advantage in performance beyond that which is available today.

3.1.1 Cr or Ni-Cr electroplating

Electroplating Cr or Ni-Cr alloy onto components has long been used to harden components' surfaces and to improve efficiency and wear resistance. These coatings have an advantage over boride nanocoatings because they can be applied without the need for a vacuum chamber, which imposes size limitations on boride coatings and raises cost. Unfortunately, the Cr in these coatings must be applied using hexavalent (Cr^{+6}) salts in the electrolytic bath. Cr^{+6} is highly toxic and poses a threat to both workers and the environment. For these reasons, use of Cr electroplating has declined sharply in recent years, and many companies are striving to eliminate electroplated Cr from their products completely.

Even when Cr electroplating is used, the application procedure is complex and costly, requiring multiple baths to first clean the component (usually steel), then apply a strike coating of Cu and/or Ni to assure bonding to the substrate. It is worth noting that Cr is brittle and has a much lower coefficient of thermal expansion than steel, and so the Cr coating almost always contains a microscopic network of cracks. Pack coating and gas coating techniques exist to apply Cr coatings without the use of Cr^{+6}, but these processes require high temperatures (900˚C or higher) that ruin the impact of the prior heat treatment. The outcome is a rough, dull finish that has a much higher coefficient of sliding friction than Cr electroplate.

3.1.2 TiN

Titanium nitride (TiN) is widely used to make a hard, conductive coating on cutting tools, medical implants, and electronic assemblies. It is usually applied via physical vapor deposition or chemical vapor deposition and leaves coated parts a distinctive gold color. TiN coatings are electrically conductive, allowing them to be used for certain electronic and switchgear applications. TiN coatings are perhaps best known for extending the service life of drill bits and tools in mills and lathes.

TiN may be the coating material that most closely resembles the $AlMgB_{14}$ family of nanocomposite coatings. Notably, TiN requires a vacuum chamber for PVD or CVD coating and it has a coefficient of thermal expansion (9×10^{-6}/C˚) close to those of steel and titanium. TiN coatings perform well in the machining of steel and cast iron.

3.1.3 TiAlN

TiAlN is a family of materials similar to TiN, but it possesses greater hardness and oxidation resistance. TiAlN is available in a range of compositions through varying the Ti:Al ratios. Its hardness varies between 26 and 33 GPa, higher than that of TiN and is usually applied to steel cutting tools by physical vapor deposition methods to improve wear resistance. TiAlN is oxidation resistant up to about 800°C, approximately 300°C higher than TiN. Above 850˚C (approximate), TiAlN begins to segregate into two phases (AlN and TiN). The coefficient of friction (dry) is 0.4 against uncoated steel at room temperature and its coefficient of thermal expansion is approximately 7.5 (10^{-6}) $C^{\circ -1}$, extrapolated from TiN and AlN respectively.

3.1.4 Diamond-like Carbon (DLC)

Diamond-like carbon (DLC) coatings have gained wide acceptance in recent years as ultra-hard, protective coatings for components as diverse as razor blades, computer hard disk readers, and artificial hearts. DLC coatings are applied in cathodic arc or chemical vapor deposition vacuum chambers and have a wide range of compositions and crystal structures. The coatings containing little or no graphite or hydrogen provide the highest hardness but are the most difficult to produce. DLC coatings may contain cubic, hexagonal, or amorphous diamond, often in nanoscale nodules that nucleate independently from one another during the deposition process and grow until they encounter their neighboring nodules.

DLC coatings can exhibit hardness values as high as that of pure, crystalline diamond and have a coefficient of sliding friction of about 0.1, which is lower than that of most metals. They maintain their low coefficient of friction in vacuum, whereas graphite and boride coatings do not because they require small amounts of water vapor or liquid water to form their lubricious surfaces. As such, DLC coatings are preferred in spacecraft or vacuum system applications.

Diamond-like carbon thin films have two major disadvantages when compared to boride compositions. First, they are reactive with Fe and Ti, so they are ill suited to use on steel or titanium alloys in applications involving elevated temperatures. For example, DLC results in poor performance on cutting tools because the carbon dissolves into the Fe work piece at the temperatures normally encountered during machining [6,7]. This leads to rapid removal of the hard, wear-resistant surface. Second, the coefficient of thermal expansion of diamond is near zero and may result in a mismatch to steel (11.5 x 10^{-6}/C˚) or titanium (8.4 x 10^{-6}/C˚). Thus, DLC coatings tend to crack or spall on these metal substrates if elevated temperatures are encountered during service.

3.1.5 TiB_2

TiB_2 is a refractory ($T_{m.pt.}$ = 3200˚C), hard (25 to 30 GPa) material with an unusually high thermal conductivity (96 W/m·K) and low electrical resistivity (15 $\mu\Omega$·cm) for a non-metallic material. TiB_2 resists oxidation well up to approximately 1000˚C, and it is sometimes used as a coating on steel or other substrates to improve wear resistance. Bulk TiB_2 is a somewhat difficult material to process, since it requires sintering temperatures above 1750˚C to densify. At this elevated temperature, grain growth can progress rapidly, resulting in an undesirably coarse-grained material. The anisotropy of TiB_2's hexagonal lattice makes coarse-grained specimens vulnerable to cracking during temperature changes because the coefficient of thermal expansion varies from 6.4 to 9.2 (10^{-6}) $C^{\circ -1}$, depending on crystallographic orientation. To reduce this problem, Fe, Cr, or C are sometimes added to TiB_2 powders as sintering aids. The coefficient of friction of unlubricated TiB_2 is 0.7 to 0.9 at room temperature but drops to as low as 0.25 at 800˚C.

3.1.6 Anodizing

Anodizing treatments harden metal surfaces by deliberately thickening the metal's naturally occurring oxide surface layer. As most oxides are harder than their parent metal, surface hardness increases can be achieved, thus enhancing the wear resistance. An anodized surface treatment is achieved by making the part to be anodized the anode in an electrolytic cell of chromic acid (Cr^{+6}), sulfuric acid, or one of several other organic acids. While anodizing does not require a vacuum system and the coating is electrically insulating, the anodized surface is porous unless special steps are taken. In addition, the coefficients of friction of oxides are generally greater than 0.1, and their measured hardness is about one half that of boride compositions.

Perhaps the greatest drawback of anodizing is that it cannot be used to coat iron or steel components, because the oxide layer does not adhere to iron. (More than 90% of all metal products are steel, stainless steel, or cast iron). Conversely, anodizing does work well on Al, Ti, Mg, Zn, Nb, and Ta.

3.2 Specific Area Being Addressed

$AlMgB_{14}$ is a lightweight, low-friction, wear resistant material that can be used in both the large-scale bulk form and as a protective coating. This material is the only available product that combines high wear resistance with a regenerating lubricant that delivers an extremely low coefficient of friction. Initially developed by Ames Laboratory, the material is synthesized through conventional powder processing techniques. Department of Energy funding was used to support further development of the technology through materials research, tribological modeling and simulation, and end-application performance testing to facilitate the commercial implementation and thereby realize energy savings in the industry.

3.3 Statement of Project Objectives

In order to facilitate both the fundamental technology development and the effort towards commercialization, the project was divided into three distinct phases:

Phase I – Proof of Concept

The focus of this phase was to conduct "proof-of-concept" evaluation of the applicability of the $AlMgB_{14}$- based coatings to hydraulic and tool inset applications by:

- Determining mechanical and tribological properties of single-phase and composite boride thin films made by PLD at Ames and then compare with baseline thin film coatings provided by Eaton and Greenleaf.

- Developing unbalanced magnetron PVD technology at Eaton for the deposition of $AlMgB_{14}$-TiB_2 nanocomposites on coupons and hydraulic system components.

- Evaluating tool wear at Greenleaf on Ti and Ti-6Al-4V workpiece materials in lathe turning tests on WC-6%Co inserts coated with $AlMgB_{14}$ and $AlMgB_{14}$-TiB_2 nanocomposite films to be prepared at Ames and Eaton.

Phase II – Coating Process Scale-up

The focus of this phase was to conduct process scale-up to generate coated prototypes by:

- Establishing scaled-up process to the proven PLD technology practices at Ames.

- Conducting process scale-up studies at Eaton, utilizing its production capable unbalanced magnetron PVD equipment. Some coupon testing will be done to verify coating performance.

- Conducting limited scale-up study at Greenleaf using a theoretical PVD system. Some coupon testing will be done to verify coating performance.

- Having Ames and ORNL provide technical support for the above scale-up studies through selected characterization and performance testing of coatings made using the scaled-up equipment.

Phase III – Functional Testing and Commercialization

The focus of this phase was to validate performance and durability improvements by functional testing of product-intent prototypes, estimate energy savings potential based on these results and market information and establish a commercialization strategy by:

- Validating energy savings for both hydraulic and tooling systems through the functional testing of production-intent prototypes.

- Validating performance and durability improvements on both hydraulic and tooling systems thorough functional testing with production-intent prototypes.

- Conducting limited prototype tests of commercially available alternatives to establish a value proposition for $AlMgB_{14}$.

- Finalizing a strategy for commercialization of $AlMgB_{14}$ coating for both hydraulic and tooling systems.

3.4 Technical Approach and Hypothesis

The proposed research, development, and commercialization plan was largely focused on improving materials' resistance to degradation in two distinct industrial applications: a) Industrial hydraulic systems, and b) tooling systems. These applications were well suited for fundamental technology development and eventual technology transfer because they are inherently ubiquitous in their scope, application space, and function. Furthermore, the two applications identified offer tremendous potential for broad industrial adoption and related energy savings.

Industrial process efficiency is directly linked to the wear and degradation of materials used in these applications. The preferred route to minimizing wear and enhancing product performance lies in the application of sufficiently hard coatings such that the coated surfaces experience lower friction and resist wear (thus prolonging component life). With reduced friction between contacting surfaces, less energy is required to combat frictional losses during start-up and/or operation of the larger system(s), thereby yielding improved energy efficiency. While the increase in efficiency per component (e.g., hydraulic pump, seal, shaft, bearings) may be modest, the large number of pumps in operation results in a substantial cumulative energy savings. Clearly, hard materials are needed, and interest is especially high for materials exhibiting so-called "superhardness," or hardness exceeding 40 GPa. Diamond, diamond-like carbon (DLC), and cubic BN all fall within this category. While each such material possesses high hardness, each also falls short in critical performance areas. For example, diamond and DLC coatings are prone to oxidation at temperatures exceeding ~ 600°C, and they can undergo undesirable chemical reactions upon contact with ferrous metals. CBN, which is relatively inert with respect to ferrous metals, is difficult to deposit by PVD at thicknesses exceeding 300 nm because of residual stresses that build up in the films.

The family of $AlMgB_{14}$-based nanocomposites emerged prior to the onset of this project and offered some potentially substantial advantages. In this particular subset of boride composites, the hardness is derived from microstructural engineering of the constituent phases, referred to as extrinsic hardness. Studies performed on the primary constituent phase, $AlMgB_{14}$, demonstrated the feasibility of producing thin film coatings of the compound by pulsed laser deposition (PLD), one of the several distinct types of physical vapor deposition (PVD) processes. As was discovered during the project, these coatings combine high hardness with a low friction coefficient, and have been shown to reduce tool wear substantially in lathe turning tests.

3.5 Initial Energy Savings Calculations

Initial benefit estimates for industrial hydraulic applications were based on applying the $AlMgB_{14}$-based coatings to seals, seats, and shafts in 15-30 hp industrial process pumps including piston pumps, G/G motors, gear pumps, and vane pumps/motors. The pumps require shaft seals, which permit the rotation of the impeller while blocking both leakage of the process fluid into the environment and environmental gases or liquids from entering the product. Approximately 10% of pumps use double seals for improved reliability at the expense of increased energy losses associated with seal friction. For a 15 hp ANSI pump, average single and double seals consume

0.5 and 1.0 hp in frictional losses, respectively. NAMB-coated seals can result in a six-fold reduction in the frictional torque of the pump shaft, which translates into an 80% reduction in frictional energy losses.

Based on the GPRA analysis for hydraulic systems, an energy savings of 29.6 trillion Btu/year and related energy cost saving of $173million per year by 2030 was calculated. These GPRA analyses closely follow earlier analyses for the Argonne program on ultra nano-crystalline diamond coatings[8], and the Ames program on ultra-hard borides [9].

Metal cutting, as the second identified industrial application, is a complex operation, with a number of forces simultaneously acting on a workpiece and chip. The central issue relating to energy efficiency during machining is tool wear. As a tool begins to wear, the amount of force needed to maintain the desired depth-of-cut increases dramatically. For example, during high-speed cutting of high nickel low alloy steel with a depth-of-cut of 0.1 inch (2.5 mm), the required tangential cutting force nearly doubles from 275 lb (1223 N) to 560 lb (2500 N) after 6 minutes. To a first approximation, doubling the tangential cutting force requires a doubling of the input power. Taking 90 m/min as a typical machining speed and scaling the tangential tooling forces accordingly, one arrives at an average tangential force of ~ 2400 N during normal-mode machining, and ~ 5000 N during the heavy wear-mode, near the end of the tool's usable life. From the cutting force relationship during machining, the average power requirement during normal machining is 6545W (372 BTU/min), which increases to 13,636W (775 BTU/min) during the end-of-life wear mode.

Assuming that normal-mode operation accounts for 75% of the typical tool life, and heavy wear mode accounts for the remaining 25%, a total of 4983 watt-hr of energy would be expended in normal-mode machining, while 3409 watt-hr of energy would be consumed during heavy wear-mode. Added together, this accounts for a yearly total energy expenditure of 8392 watt-hr. By adopting tools with improved wear resistance, life is extended and entry into the heavy wear-mode phase is delayed. If the same number of machining hours can be performed without entry into the heavy wear-mode, the total energy consumption would be 6645watt-hr. These values were used as unit input for energy savings calculations.

According to statistics supplied by the U. S. Department of Commerce 2002 Manufacturing Sector Economic Census for NAICS subsector 333 (manufacturing), the total number of machining hours for all manufactured products was 2.63×10^8. The U.S. machining industry spends ~$900M/year on cutting tool inserts, which corresponds to more than 230 million inserts. Based on the number of tool inserts used and the total annual machining hours, each insert has an average life of approximately 1hr and costs an average of $4. The above information was used to run a second GPRA set of analyses for tool inserts. The calculations suggested an energy savings of 1.08 trillion BTU and related energy cost saving of $6M/year by 2030.

3.5.1 Industrial Hydraulics

Substantial economic benefits were expected through increased reliability of pumps with $AlMgB_{14}$-based nanocoatings. The mean-time-between-failure (MTBF) for pumps was estimated to increase (positively) from 0.5 years to 1.4 years. Similarly, the MTBF due to seal failures was estimated to increase (again, positively) from 0.7 years to 10 years. At an average cost of $2,000 per failure, the reduced MTBF would result in substantial savings. Based on this input into GPRA, an economic saving of $3,246million per year was projected by year 2030. For industrial tooling, it was assumed that $AlMgB_{14}$-based coatings will increase tool life by 50% and

that the coating would cost $0.50 for each tool insert. Although the tool insert life would double, we assumed that there would be a reduction of 20% in tool inserts needed per year. This information was used to calculate the cost savings. Such an improvement in tool life would produce a saving of $90M year in the cost of tool inserts, which is a 10% savings, as compared to the annual spending of $900M for tool inserts in the United States. The GPRA calculations showed an economic saving of $31M/year by year 2030.

3.5.2 Cutting Tool Applications

In addition to the substantial environmental benefits associated with reduced energy consumption, $AlMgB_{14}$-based coatings for pumps were also projected to reduce volatile hazardous air pollutants by 10% or more compared to best available control technology. For tool inserts, the environmental benefits are primarily associated with reduced energy consumption. Additional environmental benefits are expected from a 20% reduction in tool insert production.

The U.S. machining industry spends ~ $900M per year on cutting tools inserts (not including other machining tools), which corresponds to more than 230 million inserts for industrial machining over a wide variety of applications. These consumable cutting inserts affect the energy efficiency, productivity, and quality of products manufactured by machining. While machining industries are motivated to increase energy and cost efficiency by cutting faster with less downtime, current cutting tools can frustrate such efficiency efforts due to the accelerated wear associated with high feed rates and machining speeds, especially when working very hard to machine materials like titanium alloys.

Currently available coatings constitute the baseline against which the newly developed $AlMgB_{14}$ films were to be measured against. The first goal was to improve on these by 10-50% in both increased speed and tool life. A secondary goal was to find applications for the new coating technology in high-speed machining of other high-strength and metal alloys. Studies included coating/substrate architecture as well as coating on tooling substrate materials.

3.6 Key project participants

Eaton Corporation:
Clifton Higdon and Alaa Elmoursi: Provided project management for the Nanocoatings effort. Also provided vanes and the physical vapor deposition (PVD) system for depositing coatings on test articles and for testing coated pump components in their in-house instrumented systems. Higdon developed a number of analytical models to predict efficiency gain and energy savings resulting from implementation of Nanocoatings in various hydraulic pumps and motors. Higdon also actively investigated additional applications for Nanocoatings within Eaton's diverse product portfolio.

Ames Laboratory:
Bruce Cook, Alan Russell, and Joel Harringa: Conducted research that led to original discovery and corresponding patents; assisted in finding partners interested in licensing the technology; Cook and Harringa collaborated on pulsed laser deposition (PLD) coatings process development, and Russell determined PLD parameters for later coatings trials. All three developed the proper composition of the materials to increase wear-resistance. Ames Laboratory provided some of the material used as targets for physical vapor deposition, along with analysis of coatings before and after dynamometer testing, and ongoing technical support.

Oak Ridge National Laboratory:
Peter Blau and Jun Qu: Designed and conducted tribological tests of coated coupons and provided mechanistic understanding of the superior friction and wear performance via lubrication and wear modeling. The laboratory testing of friction and wear of coated coupons required the design of instrumentation specific to the applications of interest to the industrial partners in order to simulate the wear environments of various pumps and cutting tools accurately.

Greenleaf Corporation:
Jason Goldsmith: Provided standard cutting tool inserts for deposition substrates and in-house and external cutting tests utilizing coated tools. Goldsmith developed appropriate testing protocols for various machining scenarios and provided interpretation of results. He also developed energy-saving models to predict the impact of Nanocoatings in high-speed machining applications and investigated additional applications for the technology.

4.0 Results/Discussion

Over the course of the project, the project participants focused on a deeper understanding of the fundamental material properties of this particular nanocomposite that lead to improved product efficiencies and general performance. Part of the project deliverables included the development and characterization of $AlMgB_{14}$ films, establishing reproducible processing parameters, and performance testing of various end applications to establish a measurable energy savings.

4.1 Development and Characterization of $AlMgB_{14}$-TiB_2 PLD Films

This task was concerned with the identification of technical issues related to the deposition of ultra-hard, wear resistant $AlMgB_{14}$ coatings on steel and tungsten carbide substrates. Prior exploratory work consisted of pulsed laser deposition of thin (e.g., 100 to 300 nm) films on oxidized silicon, glass, or WC. The films typically exhibit high hardness (30 – 40 GPa) based on nanoindentation measurements, a low surface roughness, and a low coefficient of friction (~0.04) in laboratory tests. Unknown at the start of this project were the requirements for producing a highly adherent, protective coating on industrial materials such as the M2 steel vanes employed in Eaton's hydraulic pumps and production-grade WC as manufactured by Greenleaf for advanced cutting tool inserts.

4.1.1 Microstructural and Mechanical Characterization

Initial depositions were conducted using a Lambda-Physik Compex 201 Kr-F excimer laser with a characteristic wavelength of 248 nm, operated at a pulse frequency of 10 Hz. Based on prior work, the power settings of 80 to 100 mJ were estimated to yield an effective deposition rate of ~0.013 nm per second. The initial depositions were performed continuously over an 8-hour period on M2 and polished WC substrates. These initial depositions revealed important processing issues related to the surface treatment of the substrates. For example, it was discovered that the boride coatings on WC substrates were affected by the presence of a tenacious surface residue that was not removable by a standard solvent rinse treatment. The residue was not discovered until the coatings on two samples were found to exhibit localized delamination. Analysis revealed that the delamination was associated with the residue, and various surface cleaning procedures were examined in order to remove the residue completely prior to deposition. An example of the local delamination on coated, as-received WC is shown in **Figure 4.1.1-1**.

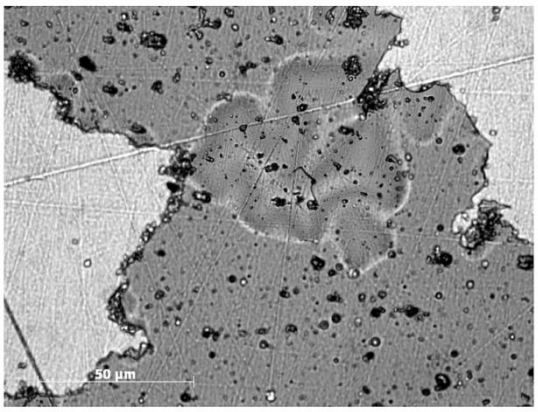

Figure 4.1.1-1: Example of a first-generation PLD coating on as-received WC, showing large-scale delamination due to the presence of substrate surface residue.

The residue was found to be associated with the polishing procedure, as seen in a photomicrograph of the as-received surface in **Figure 4.1.1-2**. The scale bar in this figure corresponds to 200 microns.

Figure 4.1.1-2: As-received and polished surface of WC, showing regions of residue from the metallographic polishing process. The presence of surface residue was found to affect coating adhesion dramatically.

A series of cleaning steps was evaluated and implemented in order to remove the residue completely prior to deposition. It was found that simple rinsing with organic solvents was ineffective at removing the residue, as shown in **Figure 4.1.1-3**. Only aggressive scrubbing, combined with an acid rinse with dilute HCl was found to clean the surface to an acceptable degree.

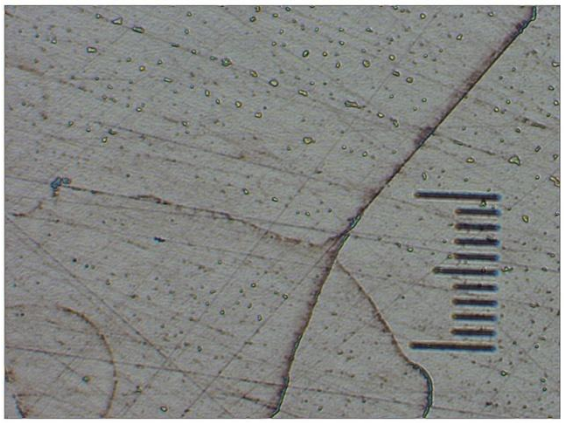

Figure 4.1.1-3: Surface of polished WC following multiple rinsing steps with acetone and ethanol. Note the presence of persistent residue on the surface. (scale bar = 200 microns)

Once the more aggressive surface cleaning procedure was implemented, all subsequent boride coatings exhibited excellent adherence and possessed the expected hardness of 30 to 40 GPa. This exercise constituted an important learning step for the advancement of the Nanocoatings technology, since surface preparation and finishing strongly affect coating performance.
In addition to the role of substrate surface preparation, the morphology of coatings produced by PLD was another focal point of the initial investigations. As it came to be understood later in this project, coating morphology plays a dominant role in determining the overall friction and wear behavior, and as such constitutes one of the primary quality assurance metrics. The presence or absence of surface asperities can contribute to three-body wear and lead to premature failure. SEM evaluation of the initial PLD coatings revealed the presence of numerous particulates attached to the surface. Particulates typically result from a transition from conventional sputtering to exfoliation sputtering. An example of the typical surface morphology is shown in **Figure 4.1.1-4**, which was obtained by PLD at a laser setting of 100 mJ. Also shown in the figure is an example of particulate detachment resulting from mild abrasion.

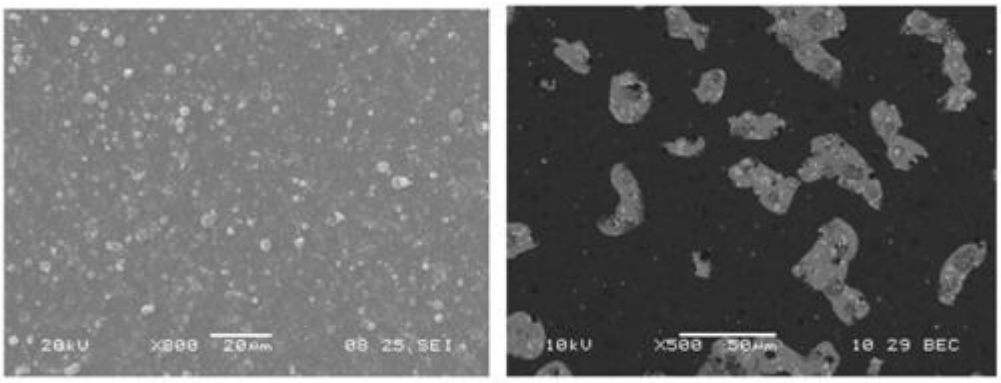

Figure 4.1.1-4: Surface particulates resulting from nanosecond PLD of $AlMgB_{14}$ on an M2 steel vane (left), and consequence of detachment or spallation of particles exposing the M2 substrate (right).

When these surface particles detach from the coating surface during tribological testing, they can act as micro-abrasives and accelerate wear. The observed wear rates can then become artificially high, when compared to a smooth, particulate-free coating. The particulates result from a number of factors, especially what is referred to as exfoliation sputtering. Exfoliation sputtering results from detachment of particles from the target as a consequence of repeated thermal shock, and is more pronounced in materials possessing a high thermal expansion coefficient, a high Young's modulus, or a high melting temperature (Tm), for which the pulse-induced thermal excursion are less than Tm. In order to correlate the density of particulates with ablation rate (e.g., laser power), a series of depositions were performed on M2 steel vane substrates and the resulting coatings were subsequently examined in an SEM. In general, higher laser energy results in an increased ablation rate, which directly translates to a higher deposition rate. Laser power settings varied from 80 mJ to 140 mJ while deposition time was held constant at 9 hours. These depositions were all performed at a constant substrate temperature of 22°C. After deposition, the particle density was determined from SEM analysis of the coating surface. **Table 4.1.1-1** lists the calculated particulate density as a function of laser energy.

Table 4.1.1-1: Density of Surface Particulates vs. Laser Energy

Laser Energy (mJ)	Particulate Density (particles/cm^2/h) x 10^5
80	4.58
100	8.62
120	9.93
140	11.25

Despite the presence of surface particulates and the resulting three-body abrasive wear during pin-on-disk tests, the single-phase $AlMgB_{14}$ PLD coatings exhibited reduced wear and friction under certain test conditions as reported by ORNL (see separate section).
In order to reduce the size of the surface particles in the coatings, the nanosecond laser was replaced by a state-of-the-art femtosecond laser. The femtosecond laser is characterized by ultra-short pulse widths of less than a picosecond (10^{-12} s). The "Solstice" laser, manufactured by Spectra-Physics, is capable of sustaining 2.5W of output at a 1 kHz repetition rate, which was 100x higher than possible with the nanosecond laser. The laser was adapted for use in the existing PLD system using a 750 mm focal length lens. A photograph of the PLD chamber with the femtosecond laser is shown in **Figure 4.1.1-5**.

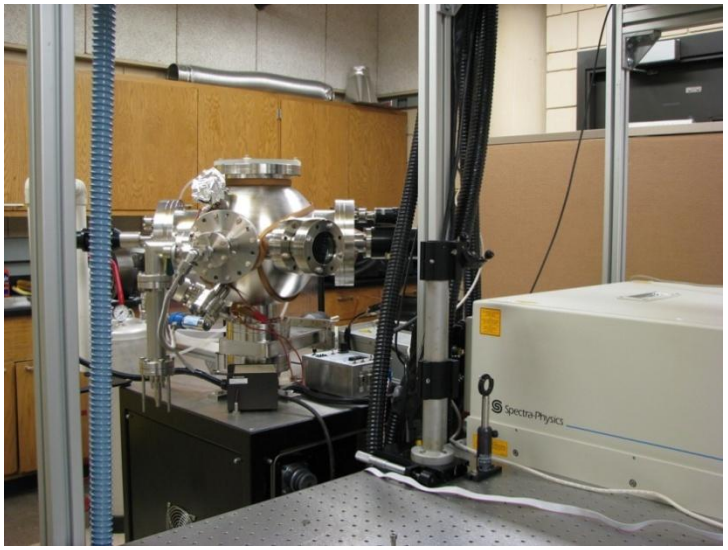

Figure 4.1.1-5: PLD chamber with Spectra-Physics "Solstice" femtosecond laser (right). Initially, all of the films obtained with this laser were prepared from baseline composition targets. As seen in Figure 4.1.1.6, coatings produced by the femtosecond laser contained no large (e.g., micron-sized) particles.

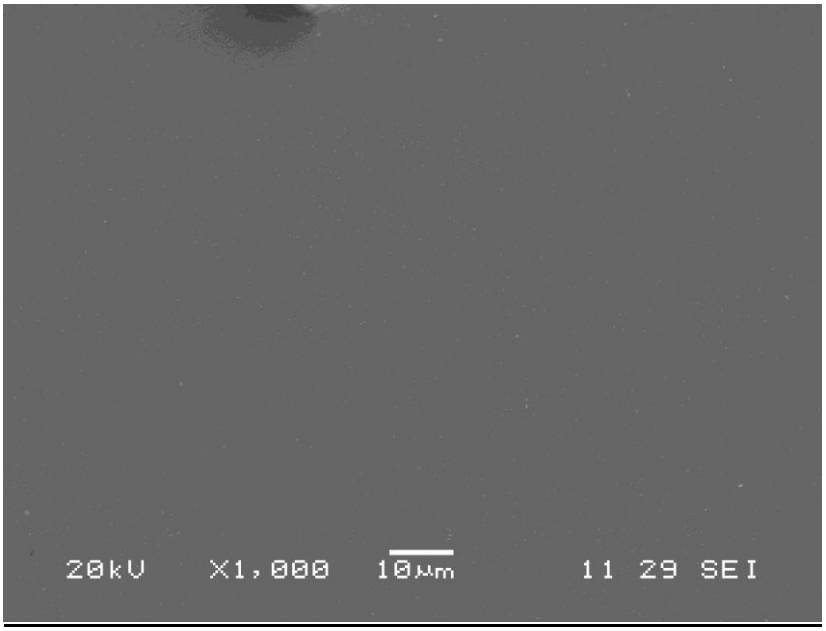

Figure 4.1.1-6: Surface of $AlMgB_{14}$ film produced with a femtosecond laser. (Note the absence of discrete particles at this magnification)

The figure shows that compared with the nanosecond laser, films produced with the femtosecond laser are exceedingly smooth at low magnification. At higher magnifications, the films are seen to contain numerous small particles in the range of 100 nm and below. These nanoscale particles appear stacked on top of one another, resulting in a surface that is somewhat rough at the nanometer length scale. **Figure 4.1.1-7** shows a comparison of the films produced using the nanosecond laser and the films produced using the femtosecond laser at high magnification.

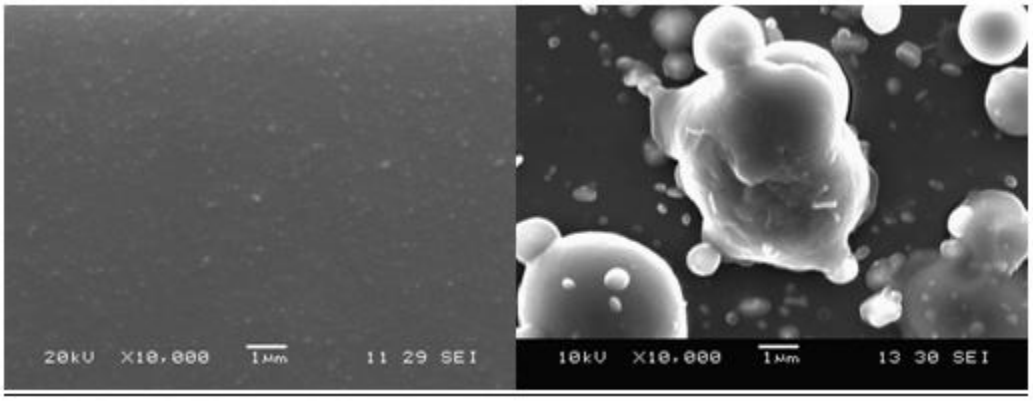

Figure 4.1.1-7: Comparison of films produced by a femtosecond laser (left) and films produced by a nanosecond laser (right) (Same magnification). Note the dramatic difference in surface morphology between the two films.

The formation of the nanoscale particles is believe to be associated with the high repetition rate of the femtosecond laser, allowing less time for heat dissipation from the surface layer of the target. Because the average size of particles resulting from the femtosecond laser is much smaller than the radius of the abrading surface during wear testing, the presence of these particles was found to be less detrimental to the wear behavior as the larger particles generated by the nanosecond laser. This was a significant improvement in the quality of coatings via PLD. The deposition rate using the femtosecond laser was compared with that of the nanosecond laser by depositing coatings of $AlMgB_{14}$ from each device onto polished M2 steel inserts as used in Eaton's vane pumps. A portion of each substrate was masked during deposition to form a step between the coated and uncoated regions of the film. Film thickness was measured with a stylus profilometer. The deposition parameters and resulting thickness for these coatings are summarized in **Table 4.1.1-2.**

Table 4.1.1-2: Deposition parameters used to investigate PLD coating thickness

Sample ID	Laser Type	Pulse Energy (mJ)	Repetition Rate (Hz)	Deposition Time (s)	Film Thickness (μm)	Deposition Rate (μm/min)
S100907	Nano	80	10	32,400	0.55	0.00102
S101107	Nano	100	10	32,400	0.56	0.00104
B062408	Femto	2	1000	240	0.42-0.46	0.110
B062408-2	Femto	2	1000	360	0.79-0.83	0.135

The calculated deposition rate resulting from the femtosecond laser was approximately one hundred times greater than that of the nanosecond laser. Was the higher deposition rate primarily a consequence of a shorter pulse width or a higher repetition rate? To answer that question, we compared the thickness of film deposited per pulse, for which it is seen that both the nano- and femtosecond lasers deposit roughly the same amount of film per pulse. The observation of similar deposition rates when evaluated on a deposition thickness per pulse basis indicates that the two lasers were about equally effective at depositing the thin film. However, because the femtosecond laser can be operated at a significantly higher repetition rate than the nanosecond laser, the resulting deposition rate proportionally higher.
The deposition rate of the femtosecond laser as a function of time was determined by depositing a series of films using the procedure above onto glass slides for lengths of times ranging from 15 to 900 seconds. The measured film thickness and corresponding deposition rates are summarized graphically in **Figures 4.1.1-8 and 4.1.1-9**.

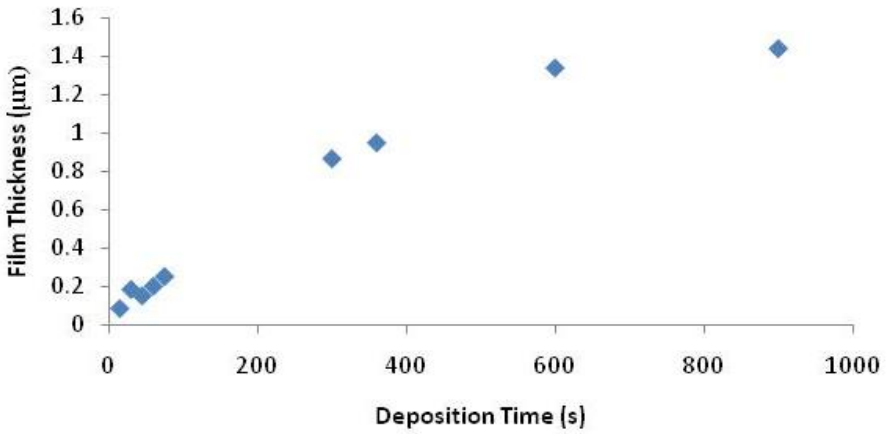

Figure 4.1.1-8: Measured film thickness vs. deposition time for films deposited using a pulsed femtosecond laser.

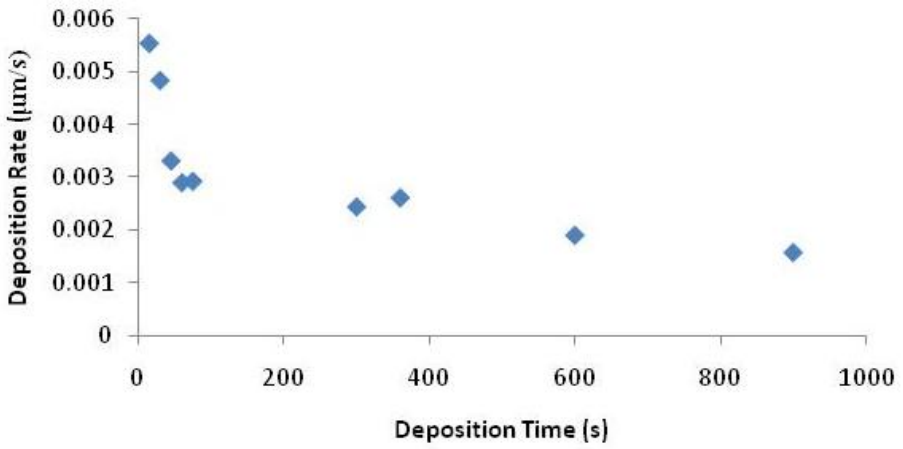

Figure 4.1.1-9: Calculated average deposition rate vs. deposition time for films deposited using a pulsed femtosecond laser.

After an initial run-in period, the deposition rate was found to decrease slowly with ablation time. The run-in period corresponds to surface alterations by the laser during the ablation process. After ablation, the target was found to be rougher than the original surface, and this rough surface was found to ablate less efficiently. As a result, we determined that scanning or rastering the beam across the surface of the sample was necessary to produce good quality coatings of at least 1 micron in thickness. In addition to the presence of particulates in the coatings, another variable affecting morphology is surface roughness of the substrate. In order to correlate coating morphology with the underlying substrate topography, profilometry was performed on an as-received M2 surface and the results are summarized in **Figure 4.1.1-10**.

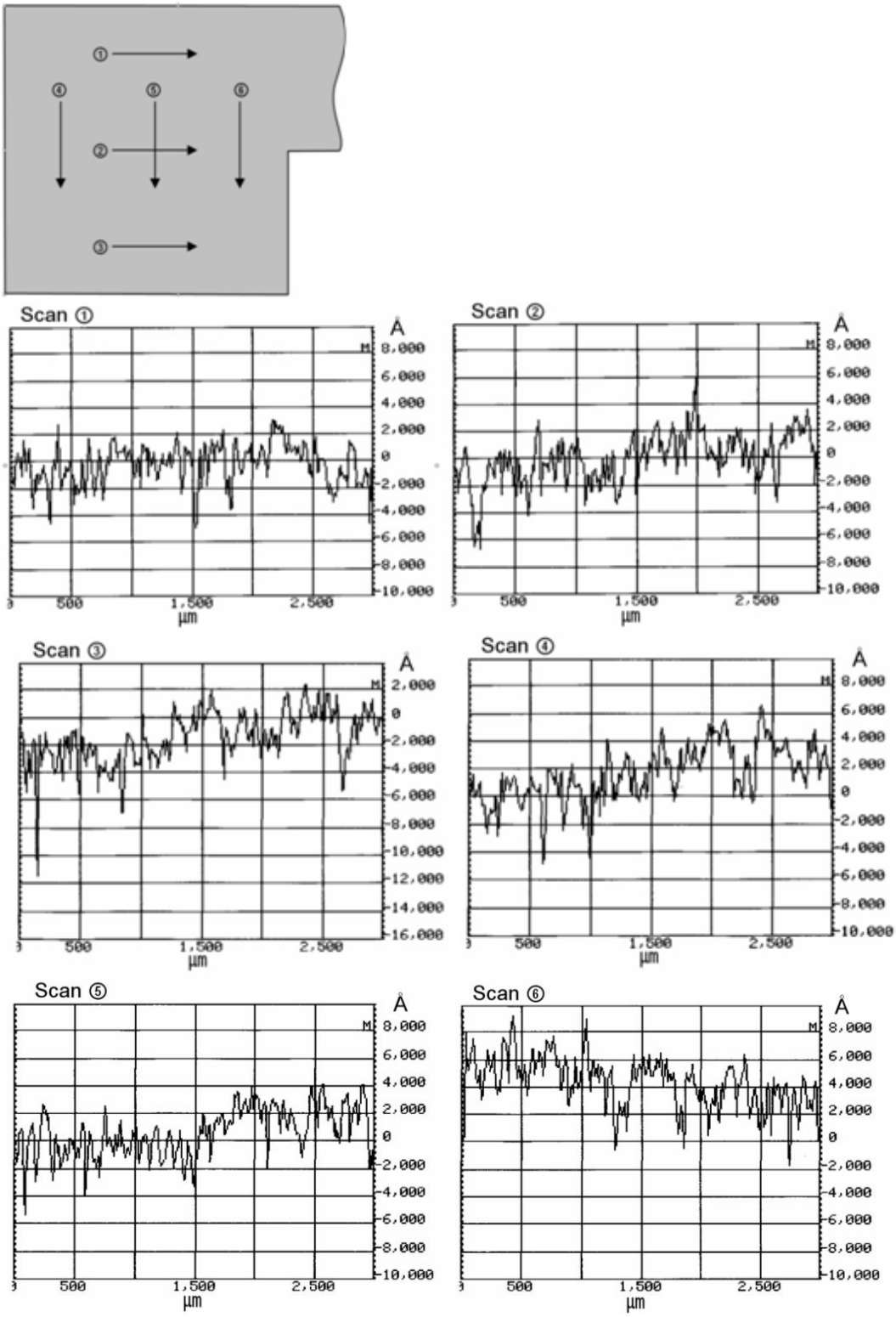

Figure 4.1.1-10: Results of profilometry on the surface of an as-received M2 vane flat.

The individual traces in the figure show that, depending on location on the vane flat, the surface roughness can vary from a few hundred nanometers to nearly 2 microns. The average film thickness produced by an 8-hour PLD deposition is 600 to 800 nm, so regions of maximum peak height may not become fully coated. Solutions were found to include an increase in deposition time, laser pulse energy, or a decrease in the surface roughness. Since exfoliation sputtering is associated with increased laser energy, surface conditioning of the M2 vanes was adopted for all depositions in the later stages of the project, in which the substrates were polished metallographically to 100 nm.

In an early application of X-ray photoelectron spectroscopy (PHI™ Physical Electronics 5500 Multitechnique ESCA system), compositional information was obtained on the baseline $AlMgB_{14}$ thin films. The Au $4f_{7/2}$ and Cu $2p_{3/2}$ excitations at 84.0 eV and 932.6 eV were used for energy calibration, and the atomic concentration was calculated by using the sensitivity factors provided with the PHI™ acquisition software. The films were subjected to an Ar^+ ion bombardment using 4 kV Ar^+ ions at 3 μA total target current to remove the surface oxide layer before the XPS analysis. **Figure 4.1.1-11** shows that boron concentration stabilizes at ~ 80 at. % with increased sputtering time (i.e., depth into the coating). Other elements remain constant in concentration regardless of sputtering time. Oxygen concentration drops from 55 at.% at the surface to below 10 at.% in the bulk with increased sputtering time, which is critical to the performance of the film because high oxygen content has been found to aggravate the mechanical properties of $AlMgB_{14}$ thin films. The Fe in the films arises from steel mill vial and media wear debris introduced into the target material during the high-energy ball mill process used to produce the targets. The atomic ratio of Al, Mg, and B for the film is close to 1:1:14 stoichiometry. These results established early on that PLD is capable of reproducing the chemical stoichiometry of the target materials in the resultant coatings.

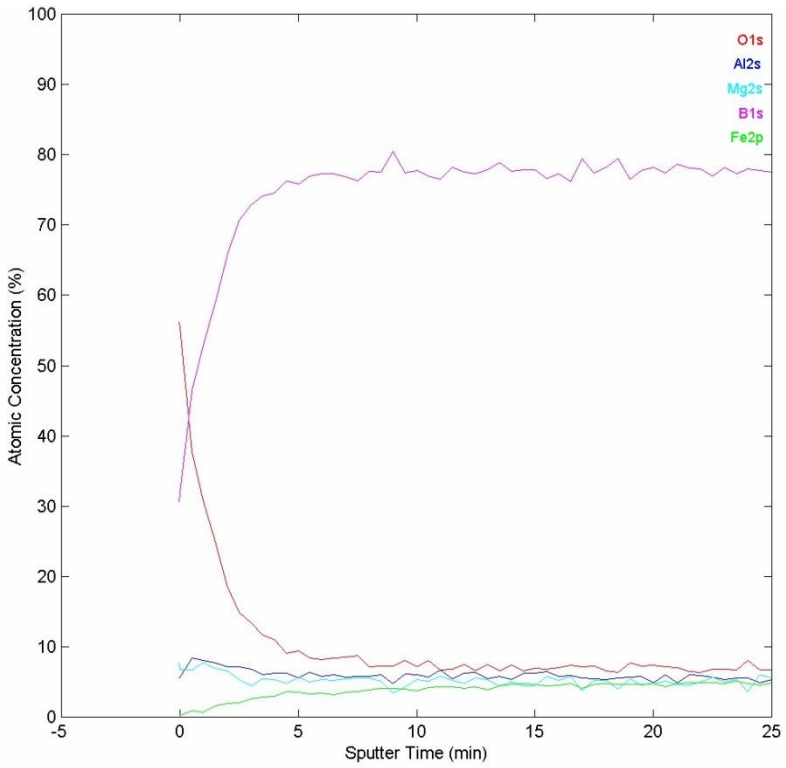

Figure 4.1.1-11: XPS depth profile of a baseline $AlMgB_{14}$ thin film obtained by PLD.

4.1.2 PLD Deposition Trials

At the start of this project, it was not known whether the mixed-phase coatings would crystallize upon deposition or assume an amorphous character. This was addressed in a preliminary experiment, in which a 150 nm coating of baseline boride was deposited on an oxidized silicon substrate. The substrate temperature was maintained at 22°C during deposition. After deposition, the substrate was sectioned using a low-speed diamond wafering saw and the individual sections were heat treated in argon at 300°C and 600°C. X-ray diffraction indicated that the as-deposited and 300°C annealed films were amorphous, while the 600°C film was partially crystallized. Surface roughness was determined by a Digital Instruments Dimension 3100 atomic force microscope (AFM) operated in tapping mode with a silicon pyramidal probe. AFM images of a section of the 300°C and 600°C annealed coatings are shown in **Figure 4.1.2-1** indicating a surface roughness of 6.3 nm in the former and 2.5 nm in the latter.
Given that the as-deposited coating was amorphous, a Hysitron nanoindentor was employed to measure the local hardness and elastic modulus of a similar coating deposited on an M2 vane segment obtained from Eaton. An AFM attachment was first employed to locate regions of suitable smoothness for the indentation. Results are shown in **Figure 4.1.2-2**.

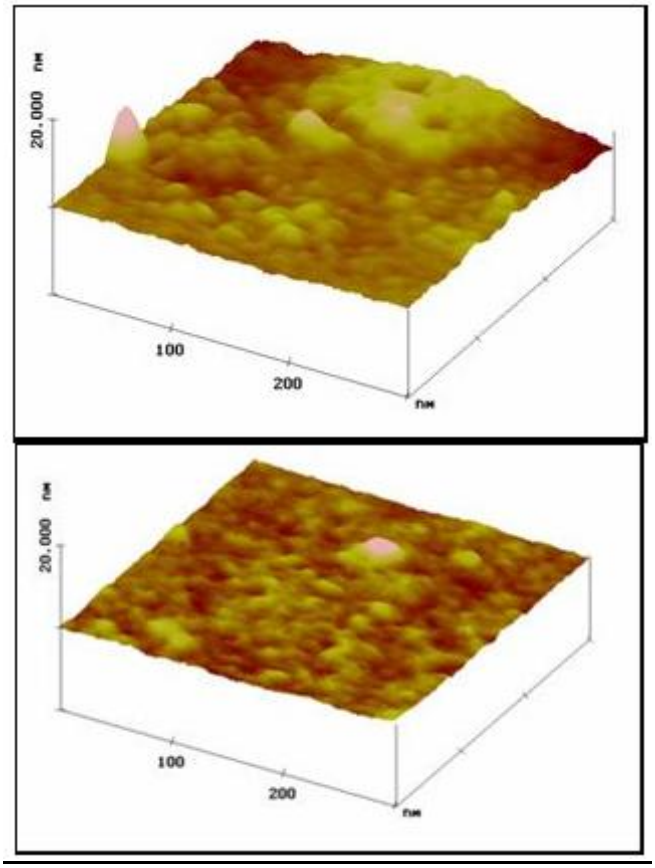

Figure 4.1.2-1: AFM image of baseline boride coating applied to an oxidized silicon substrate at 300K. (Top: annealed at 300°C; Bottom: annealed at 600°C)

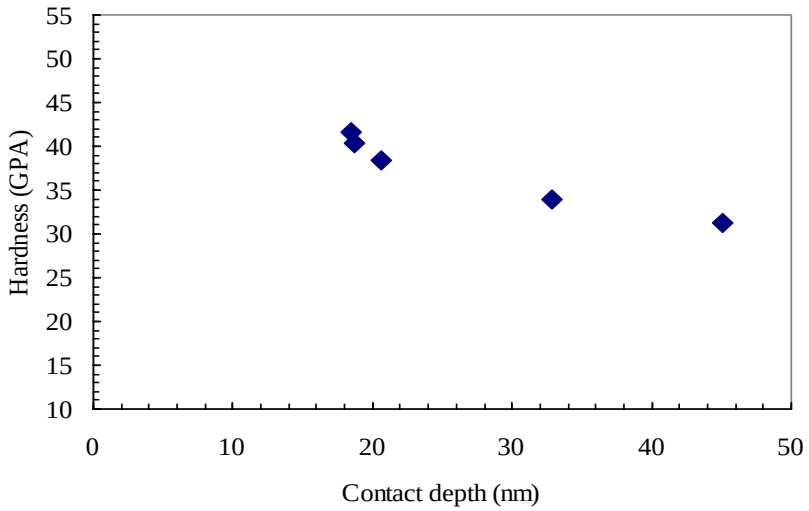

Figure 4.1.2-2: Results of nanoindentation tests on first-generation $AlMgB_{14}$ coatings deposited on M2 vanes by PLD.

Taking into consideration the substrate effect, and that the penetration of the indentor should not exceed 10% of the thickness of the film, the apparent hardness of the coating falls within the 30 to 40 GPa range, consistent with earlier results on oxidized silicon and glass substrates.

Initial determination of deposition temperatures leading to optimal coating adhesion with the substrate were conducted using the femtosecond laser, described in section 4.1.1. A set of coatings from the same mixed-phase hot pressed boride target were deposited for 7.5 minutes on glass and M2 steel substrates. Film B061908-2 was deposited with a substrate temperature of 80°C while B062008 was deposited at 300°C. After deposition, three Rockwell C indents were introduced on each film. Adhesion was assessed by observing the amount of damage around each indent under an optical microscope. This test showed that increasing the temperature of the substrate during deposition appears to improve adhesion. While the sample deposited with a substrate temperature of 80°C exhibited both radial cracks and film delamination in the area surrounding the indents, the film deposited on the sample held at 300°C showed no damage around the HRC indents. Improvement in resistance to damage from indentation with increasing deposition temperature is thought to come from one of two sources. The first is that the increased temperature results in higher mobility for the species as they strike the substrate, allowing for more stress relief in the film as it is deposited. The decrease in internal stresses in the film is then observed as an increase in the force required to remove the film from the substrate. Alternatively, heating the substrate before and during deposition may improve adhesion by driving off volatile molecules adsorbed on the surface of the substrate such as water and hydrocarbons. This allows the film to bond directly to the steel, which may improve the adhesive strength of the film and improve its ability to resist damage from indents. The improved adhesion with temperature is consistent with the results obtained on coatings produced by Eaton's PVD system.

4.1.3 Friction and Wear Testing of PLD Films

The results of POD friction and wear tests on five coupons tested are summarized in the following **Table 4.1.3-1**. These coatings were tested for a total distance of 32,400 m, or slightly greater than 20 miles, under lubrication-starved conditions with two drops of DTE-24 oil introduced at the start of each test.

Table 4.1.3-1: Results of Pin-on-Disk wear test results of PLD Nanocoatings

Coating	Coating Thickness (μm)	Wear rate of vane ($mm^3/N*m$)	Wear Rate of ball ($mm^3/N*m$)	Steady state COF
$AlMgB_{14}$	0.32	n/m ($<0.1*10^{-8}$)	$0.01x10^{-8}$	0.09
$AlMgB_{14}$-TiB_2 (coating fractured)	0.63	$3.3x10^{-8}$	$0.3x10^{-8}$	0.06
$AlMgB_{14}$ with Ti interlayer	0.42 (0.31)	$2.4x10^{-8}$	$2.3x10^{-8}$	0.06
$AlMgB_{14}$-TiB_2 with Ti interlayer	0.99	$2.0x10^{-8}$	$0.08x10^{-8}$	0.07
$AlMgB_{14}$-TiB_2 (20 min deposition)	0.72	$0.4x10^{-8}$	$0.05x10^{-8}$	0.06

The COF vs. distance curves for these samples are shown in **Figure 4.1.3-1**.

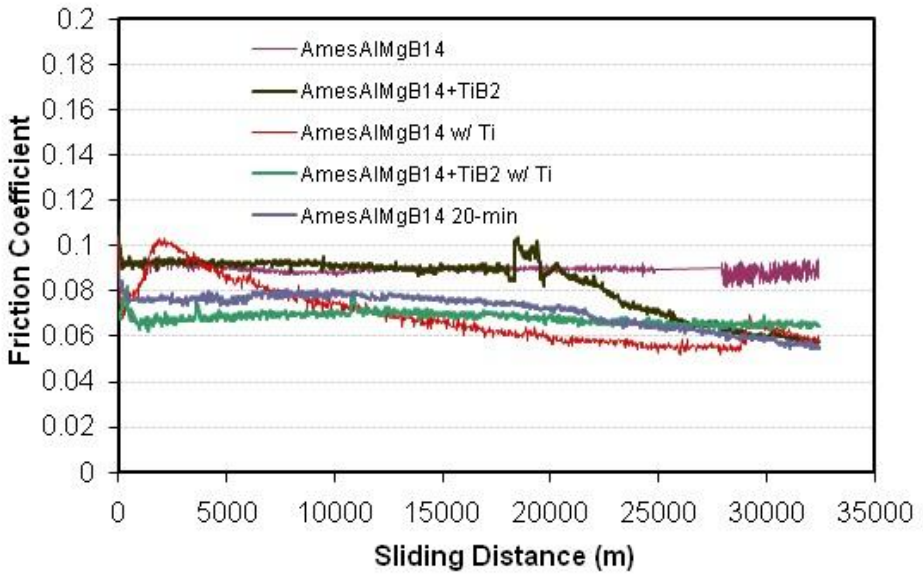

Figure 4.1.3-1: COF vs. distance of $AlMgB_{14}$-based PLD coatings as measured by ORNL. All tests were performed under lubrication-starved conditions with 2 drops of DTE-24 oil added at the beginning of the test.

In these studies, the single-phase $AlMgB_{14}$ exhibited the best overall wear performance among the PLD coatings, but also the highest friction coefficient. The addition of the titanium interlayer was found to decrease the coefficient of friction while increasing the wear on both the coating and the counterface. Increased ball wear often corresponds to lower friction because a larger contact area leads to lower contact stress and a thicker boundary lubricant film, thus a higher lambda ratio (assuming no variation in surface roughness). The $AlMgB_{14}$-TiB_2 thin films adhesion and wear resistance were improved with the addition of the titanium interlayer, although the friction coefficient was not significantly affected. The $AlMgB_{14}$-TiB_2 film with a longer deposition timed showed better wear resistance and friction. The longer deposition film only had small, localized failures unlike the shorter deposition counterpart, which failed at a sliding distance of ~18000 meters. It should be noted that the substrates were polished to ~100nm prior to deposition, which is different from the surface treatment applied to production-grade M2 vanes for PVD coating at Eaton. As discussed in the next section, PLD coating morphology is characterized by sub-micron particulates whereas the PVD coatings consist primarily of micron-sized growth columns.

4.1.4 Characterization of PLD Films

Effect of target grain size

The effect of grain size in the target material on the properties of the associated nanocoating was unknown at the start of this project. It has been established for bulk materials that a finer grain size leads to improved wear resistance (erosive and abrasive); however, such a correlation had not been established in the case of thin film coatings. As the Nanocoatings project advanced into Phase III of commercialization, this became a relevant issue because of the higher costs associated with processing of high-purity, nanoscale targets. The net cost of implementing nanocoatings includes preparing bulk targets for PVD and, if large-grained targets yield coatings of comparable quality to those obtained from nanoscale materials, there would be a distinct cost advantage.

In order to address this issue, two coatings were prepared by PLD from different targets. The targets were both hot pressed from $AlMgB_{14}$ + 50 vol. % TiB_2 powder; one batch was high-energy ball milled for an additional 30 minutes to reduce particle size. The resulting microstructures of the two targets are shown in **Figure 4.1.4-1.**

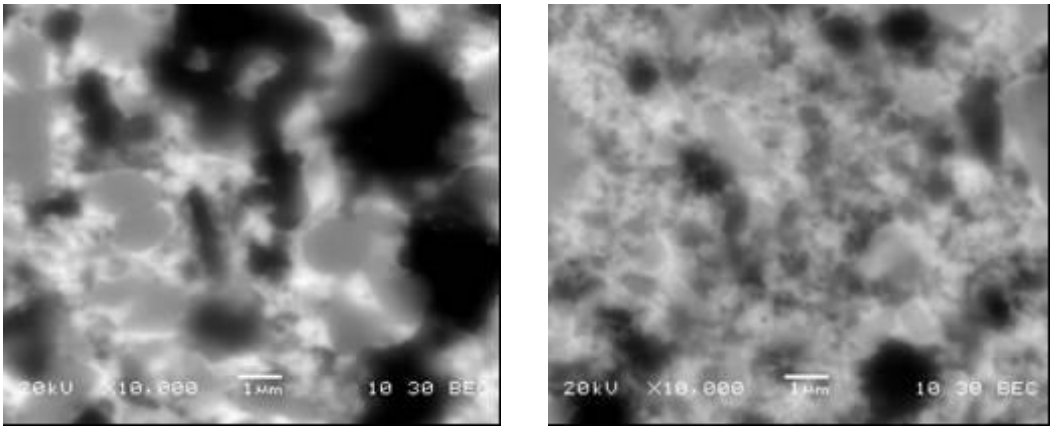

Figure 4.1.4-1: Backscattered electron micrographs of $AlMgB_{14}$-TiB_2 PLD target samples hot pressed at 1400ºC. The microstructure on the right was obtained by additional high-energy ball milling of the starting powder used for the processing of the sample on the left. Note the finer grain size in the target processed by additional milling.

Both coatings were deposited under identical conditions for 6 minutes on polished M2 tool steel substrates. The resulting films had a thickness estimated at between 0.5 and 1.0 micron. The films were examined by SEM to determine if there was any obvious morphological difference between them and the results are shown in **Figure 4.1.4-2**. It can be seen that there is no noticeable difference between the two films that can be attributed to the microstructure of the target. Backscattered imaging (not shown) revealed no differences in composition or phase distribution of the coatings.

Theory predicts that, in the case of a femtosecond laser, ablated material is completely vaporized and condenses during transit into nano-sized particles that comprise the resulting film. As long as there are no inhomogeneities in the target, and the grain size is smaller than the laser spot size, grain size would not be expected to have an effect on the deposition plume. In practice, the ablation track is significantly larger than the laser spot; about 0.5 mm wide, which is much larger than either of the microstructures investigated.

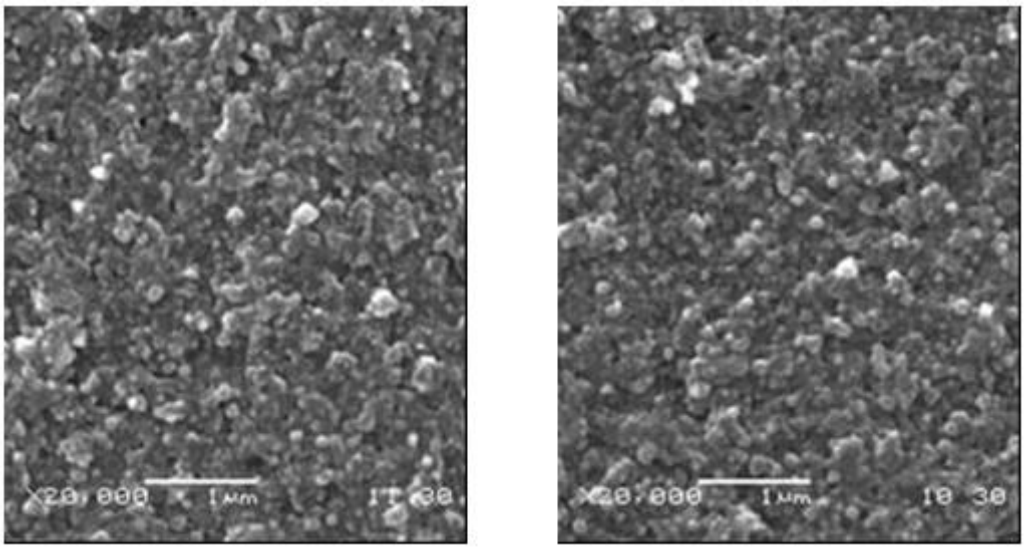

Figure 4.1.4-2: Micrographs of the surface of PLD coatings prepared from course-grained (left) and fine-grained (right) $AlMgB_{14}$-TiB_2 targets.

Other differences in the films, such as thickness, adhesion, etc. have been shown to be heavily dependent on other factors including statistical variation. It is then likely that any differences in such measured properties could not be solely attributed to the grain size of the targets. Thus, composites with grain size up to 5 µm appear to be equally suitable for targets as those with finer microstructures. It should be emphasized that target density plays a significant role in film quality, and that coarser powders tend to be more difficult to densify.

TEM analysis of PLD coatings

During the course of this project, there was anecdotal evidence that the $AlMgB_{14}$ phase assumes an amorphous nature when deposited by either PLD or PVD, whereas the TiB_2 tends to assume a crystalline structure. X-ray diffraction patterns taken of mixed-phase coatings on glass exhibit peaks associated with the TiB_2, but because of the much stronger scattering power of Ti atoms, any signal from the $AlMgB_{14}$ phase is generally lost in the background noise. In order to resolve this long-standing question, depositions of single- and mixed-phase boride targets by PLD were performed on carbon grids for examination in a TEM. An additional objective of this effort was to determine the size of the particles generated by laser ablation of these boride targets during PLD. It was believed that switching from a nanosecond laser to a femtosecond laser would result in a decrease in particle size, but a quantitative measurement had not been obtained. A typical particle distribution resulting from ablation of a single-phase $AlMgB_{14}$ target is shown in **Figure 4.1.4-3 (a)**, along with a selected area diffraction pattern (SADP) from one of the particles, shown in **Figure 4.1.4-3 (b)**. Many of the particles fall within the 5 to 50 nm size range and the presence of diffuse halos in the SAD pattern indicated that these particles were amorphous, as suspected. These particles are roughly spherical and are believed to result from “in-flight” condensation of the vapor product of ablation. Given their spherical shape, it is hypothesized that most solidify in-flight prior to impingement on the substrate. In contrast, particles ablated from a single-phase TiB_2 target are largely crystalline, as evidenced by the bright diffraction spots in the SAD pattern shown in **Figure 4.1.4-4 (b)**. **Figure 4.1.4-4 (a)** show the typical range of particles produced during ablation of TiB_2.

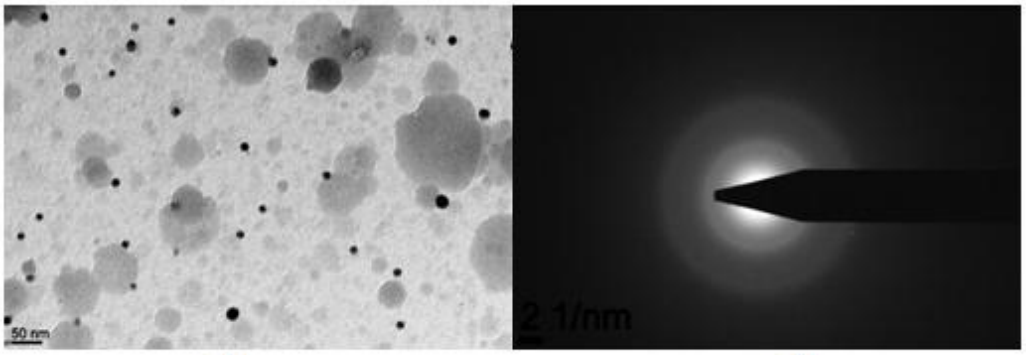

Figure 4.1.4-3 (a): Bright-field image of particles deposited by PLD onto a carbon grid from a single-phase $AlMgB_{14}$ target. (b) SADP from one of the particles.

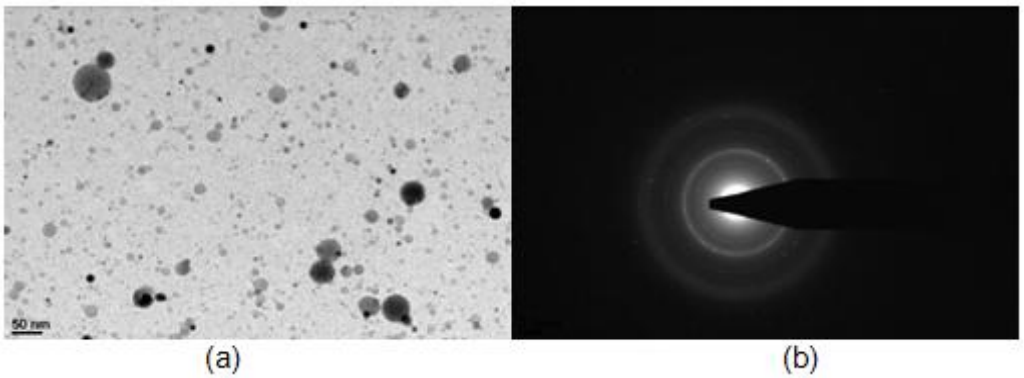

Figure 4.1.4-4: (a) Bright-field image of particles deposited by PLD onto a carbon grid from a single-phase TiB_2 target. (b) SADP from one of the particles.

Information about the particle size and crystallinity of coatings prepared by PLD is important for two reasons: 1) comparison of tribology test results between coatings produced by PLD and those produced by PVD requires an understanding of the physical-chemical nature of the material, and 2) analysis of the PLD coatings provides insights into how these films nucleate and grow in general, which ultimately places limits on expected performance in hydraulic and machine tooling systems.

4.1.5 Optimization of PLD Processing Parameters

Bond coat development

It is common practice for DLC coatings to employ a compliant interlayer in order to reduce the effect s of high residual stress in the coating and the accompanying poor adhesion to steel substrates. In general, an interlayer possesses a coefficient of thermal expansion intermediate between that of the substrate and coating, thereby reducing stresses resulting from CTE mismatch. Indeed, DLC would not have achieved the current level of interest had it not been for the development of such duplex coatings. Since the boride coatings share some common characteristics with DLC, such as high hardness and a tendency to exhibit brittle behavior, their performance in hydraulic components and in machining tools may be improved by adopting a duplex configuration, employing a semi-compliant interlayer. In order to determine the effect of such an interlayer, a series of 12 single-phase $AlMgB_{14}$ and mixed-phase $AlMgB_{14}$-TiB_2 coatings were deposited on polished M2 substrates by PLD, using a femtosecond laser. Half of these coatings were deposited directly onto the steel substrate, while the remaining half included a 200 to 400 nm Ti interlayer. The Ti interlayer was obtained by ablation of a Ti target for 3 minutes, after which the target was substituted for the boride material. Deposition of the boride phase was performed for a total of 10 minutes, producing a 600 nm to 1 micron thick coating, as determined by optical profilometry. As a qualitative measure of the relative adhesive strength of the coatings, a Rockwell “C” indentation test was performed, in which the coatings were subjected to a diamond indenter under a 150 kg load. The indents result in plastic flow within the substrate, which then causes cracking and/or delamination of the coating. This test was developed by the Union of German Engineers, (Verein Deutscher Ingenieure, VDI) and is also referred to as the *Daimler-Benz* test. The extent of cracking and delamination is rated according to a scale ranging from 1 to 6, with the lower value indicating minimal cracking and the higher value corresponding to large-scale failure of the coating, as depicted in **Figure 4.1.5-1.**

The adhesion of all coatings was found to be good-to-excellent, although some of the mixed-phase coatings deposited directly onto M2 exhibited minor delamination, as shown in **Figure 4.1.5-2(b)** in the case of the mixed-phase boride. Based on the known deposition rates of the single-phase and mixed-phase targets, the thickness of both sets of coatings is expected to be roughly the same. No delamination or cracking was observed in any of the coatings prepared with an interlayer. Four of these coatings were sent to ORNL for pin-on-disk testing, consisting of one each with single-phase and mixed-phase compositions directly on M2 and on M2 with a Ti interlayer. Results are discussed in a separate section of this report.

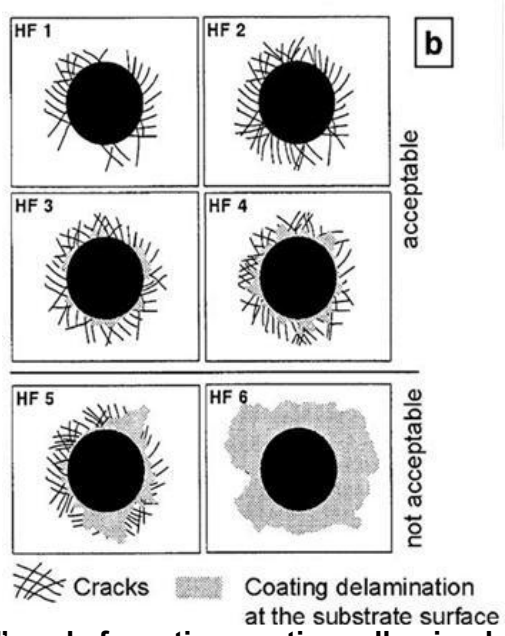

Figure 4.1.5-1: The "HF" scale for rating coating adhesion based on a Rockwell "C" indentation test.

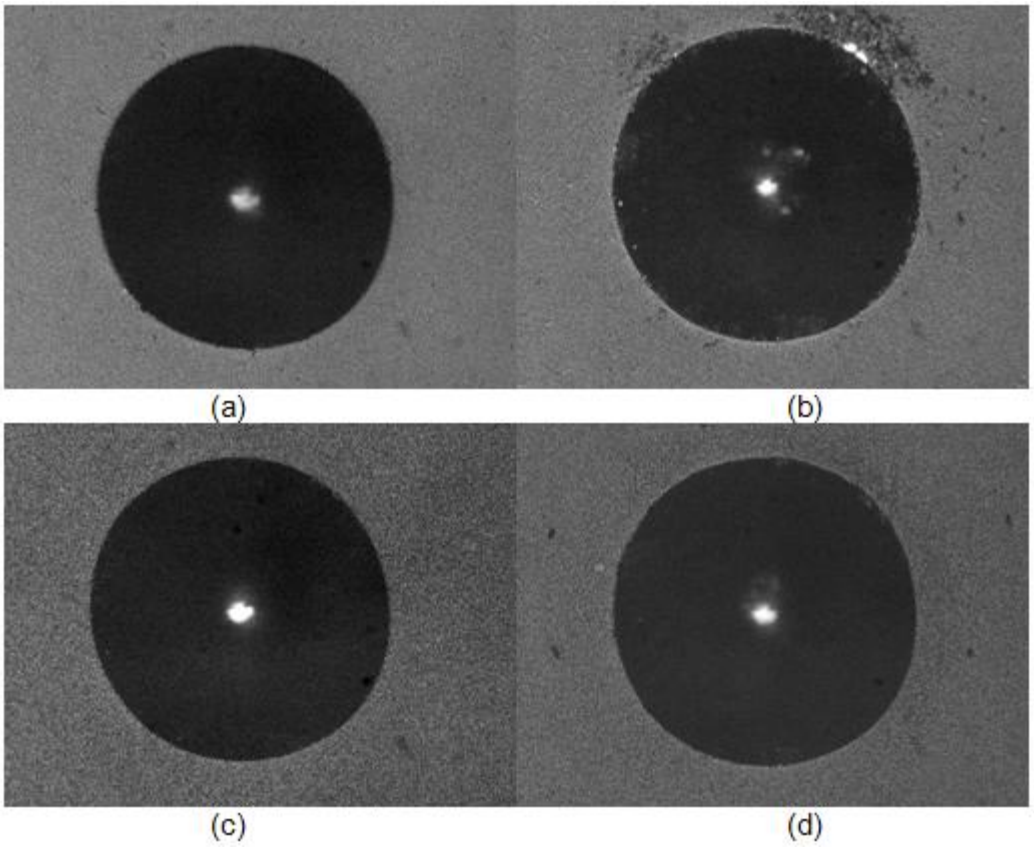

Figure 4.1.5-2: Results of a Rockwell "C" adhesion test as applied to PLD-coated M2 substrates. (a) single-phase $AlMgB_{14}$ (no interlayer); (b) mixed-phase (no interlayer); (c) single-phase $AlMgB_{14}$ with Ti interlayer; (d) mixed-phase with Ti interlayer.

4.1.6 Identification of Factors that Contribute to Low Friction Performance

In order to understand the mechanisms responsible for ultra-low friction in $AlMgB_{14}$-TiB_2 nanocoatings, x-ray photoelectron spectroscopy (XPS) was employed for a detailed analysis of surface chemistry in PLD and PVD coatings. Using this technique, we established that boron oxidizes to form boron oxide, B_2O_3, which then reacts with moisture to form boric acid, $B(OH)_3$. It is the presence of boric acid that is believed to be responsible for the observed low friction coefficients observed on boride Nanocoatings. While $B(OH)_3$ was conclusively identified by XPS, it was not known whether the boric acid originated from the $AlMgB_{14}$ phase, from the TiB_2 phase, or whether each phase contributes equally to its formation. The reason why it was important to understand the source of the boric acid is that in designing coatings for particular applications, some applications may require a higher degree of wear resistance while others may require low friction to be the primary driver. By understanding which component contributes to the formation of boric acid, the ratio of that component can be increased or decreased in the target composition to achieve the desired combination of wear resistance and friction behavior in the coating. A set of bulk boride samples were metallographically polished to 1 micron with diamond paste, rinsed with hexane (which leaves no residue upon drying), and then placed in steam generated from de-ionized water for 30 minutes. The surface chemistry of the samples was then analyzed by XPS. The samples analyzed included single-phase $AlMgB_{14}$, single-phase TiB_2, and a mixed-phase $AlMgB_{14}$-70 wt. % TiB_2. The relevant XPS boron 1s emission spectra are shown in **Figure 4.1.6-1**, in which it is seen that the single-phase $AlMgB_{14}$ sample (top plot) exhibited comparatively little oxide formation on the surface, whereas the single phase TiB_2 (middle plot) shows a very pronounced oxide peak, in addition to a shoulder corresponding to $B(OH)_3$. It was originally thought that the highly stable TiB_2 phase might be more resistant to oxide formation than the $AlMgB_{14}$, but our results clearly indicated the opposite behavior. This experiment was repeated, once for a one-hour steam treatment, a second time for a 72-hour soak in water, and a third time after repolishing and long-term exposure to ambient moisture. In each case, the results were the same. These results suggested that a composition with reduced TiB_2 concentration may offer better long-term tolerance to a water-based environment than aTiB_2-rich composition.

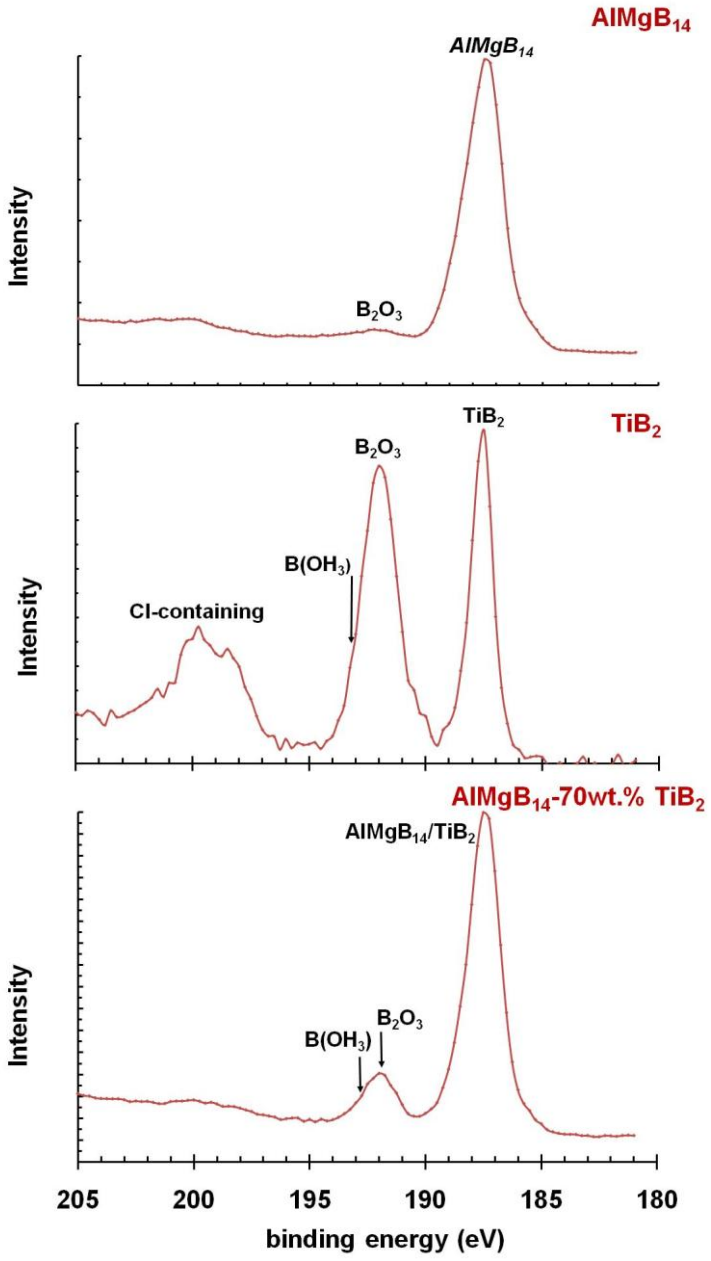

Figure 4.1.6-1: XPS binding energy plots of $AlMgB_{14}$ (top), TiB_2 (middle), and mixed-phase $AlMgB_{14}$-70 wt. % TiB_2 (bottom) after exposure to moisture.

4.2 Development and Characterization of $AlMgB_{14}$-TIB_2 PVD Films

One of the key areas of concern throughout the project was in transitioning the laboratory level PLD work performed at the onset of $AlMgB_{14}$-TiB_2 film development to a robust and repeatable process that would yield real performance increases in both of the industrial applications identified. These new coatings would have to be tested and the retested again in a variety of industrial applications to retire the risks associated with introducing a new technology into established markets. The production-intent coatings would be subject to long-term durability testing so as to ensure that any performance gains would be realized over the life of the product and that use of ultra-hard films would not be detrimental to long term use. Lastly, a major goal of the assembled team was to develop or modify testing methods that could be used to assess the performance of the coating prior to any field trials so that any optimization needed would be complete.

4.2.1 Development of PVD Coating Process

The CemeCon CC800/8 PVD coating system utilized throughout this program employs a patented high ion density magnetron sputtering technology. Moreover, as alternative coatings to the $AlMgB_{14}$-based films proposed would be processed by the system as well, the system had to be flexible in terms of both setup and in processing. Fortunately, this particular system can be used to deposit most PVD coatings that are commercially available in the market today.

To get the system ready for the project required replacement and/or maintenance of key components including the chiller system, some of the RF matching networks, and one of the cathode's DC power supplies. **Figure 4.2.1-1** shows a picture of this unit and an illustration of a PVD coating on a large gear, in addition to an SEM cross section of the coating from some earlier work at Eaton.

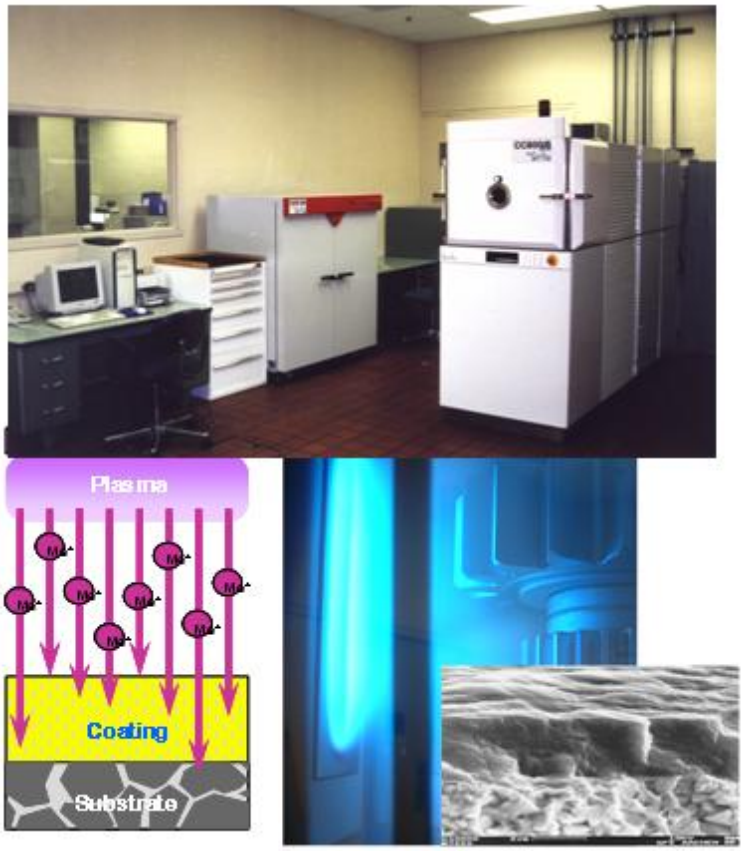

Figure 4.2.1-1: CemeCon PVD System with advanced high ion sputtering technology.

Coating trials were conducted early on in the project for a variety of different materials and different process temperatures. These included low temperature TiN, low and high temperature TiAlN, TiAlN plus carbon, high temperature TiN and TiB_2 (a proposed component for an $AlMgB_{14}$-based nano composite), and low temperature WC+C and B_4C+C, etc. The purpose of conducting all these coating trials was to: 1) test the system capability and ensuring its readiness to receive the $AlMgB_{14}$-based targets; 2) provide coated coupons for characterization and process optimization; 3) provide coated Falex rings for wear and friction evaluation to compare to $AlMgB_{14}$ coatings. **Figure 4.2.1-1** shows a low temperature TiN coating processed in this quarter. It demonstrates good adhesion and uniformity although the process temperature was below 160º C.

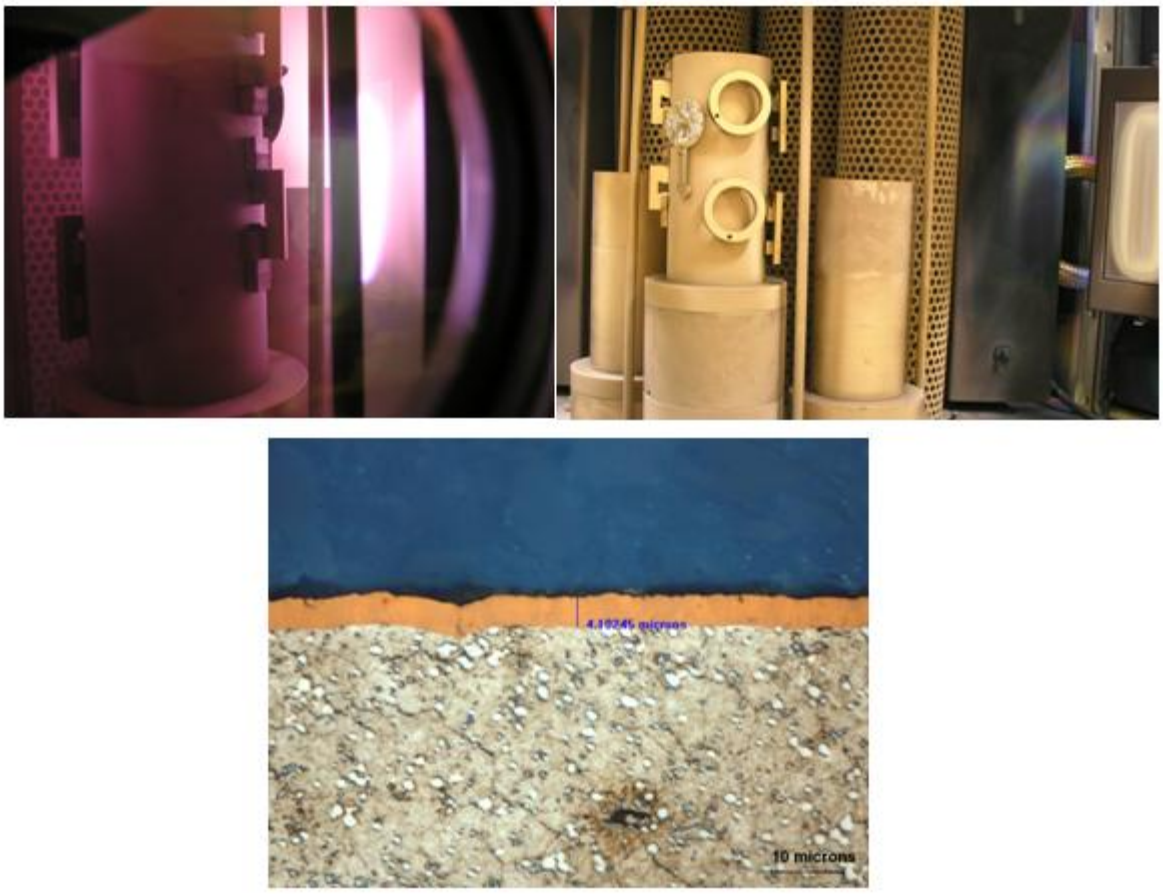

Figure 4.2.1-2: Processing of $AlMgB_{14}$-based coatings via PVD.

As the processing of $AlMgB_{14}$-based coatings via PVD was one of the key deliverables for this project, many of the efforts early on were focused on the production of several 4" diameter discs of $AlMgB_{14}$. These samples would later be machined into rectangular pieces and then subsequently brazed on to a copper plate for final assembly into a fully capable PVD target.

First attempts at producing an $AlMgB_{14}$ coating were met with several technical challenges. The targets received early on in the project comprised of a single brazed 'tile' and were much more prone to cracking than those offered today. During the first run, as an example, the first $AlMgB_{14}$-based target used cracked into multiple pieces and needed repair before any additional coating runs could be processed. High thermal stresses associated with use of such a large cross sectional area was identified as a key factor and so the target sent out for repair would be completely disassembled and sectioned into four distinct quadrants (the 80x200mm effective target space would be composed of 4 distinct 50x200mm tiles, rather than one, large, single tile). As sections of the target appeared to suffer from weak bonding, the brazing parameters used in the target assembly were also investigated in detail. Furthermore, the initial power used in the sputtering process was deemed as far too high at 3kW, and so this was lowered such that stresses on the material would be further minimized during sputtering.

A final area of development over the early stages of the project was the establishment of optimal target densities and optimal target compositions.

A number of issues related to the processing of large-scale PVD targets needed to be addressed early on in this project. In order to realize the maximum benefit from these coatings, the amount of spinel and porosity in the targets needed to be minimized, and it needed to be shown that the processing was reproducible. Spinel, $MgAl_2O_4$, is moderately hard (15 GPa) yet highly brittle, like many other oxide ceramics, with a K_{1c} value of 1.7 – 2 MPa$\sqrt{m}$ at room temperature. Its presence in the bulk targets and subsequent coatings decreases fracture toughness and the tendency for cracking. Excessive porosity can lead to non-uniform deposition and the presence of low-density pockets in the coatings, which can lead to premature spallation and coating failure. In addition, the presence of contaminant phases based on iron or tungsten carbide from the milling process also needed to be understood and controlled. The constituent materials are typically comminuted by high-energy milling techniques using metallic media, which introduces wear debris of low hardness into the target material and subsequent coatings. Processing studies at AMES developed methods of producing fully dense targets possessing minimal amounts of spinel and metallic impurities. Results of these studies were documented and communicated to NewTech Ceramics.

Refer to **Figure 4.2.1-3** for representative photographs of the first iteration of $AlMgB_{14}$ PVD tiles.

a) Cracked target due to thermal stress and/or poor brazing

b) repaired target

Figure 4.2.1-3: First $AlMgB_{14}$-based PVD targets used for physical vapor deposition.

In spite of the many challenges and the various issues with the repair and remanufacture of cracked targets, the first $AlMgB_{14}$-TiB_2-based PVD film was successfully deposited onto a tool steel substrate with Eaton's batch number 1037, processed in August of 2007, shown below in **Figure 4.2.1-4**.

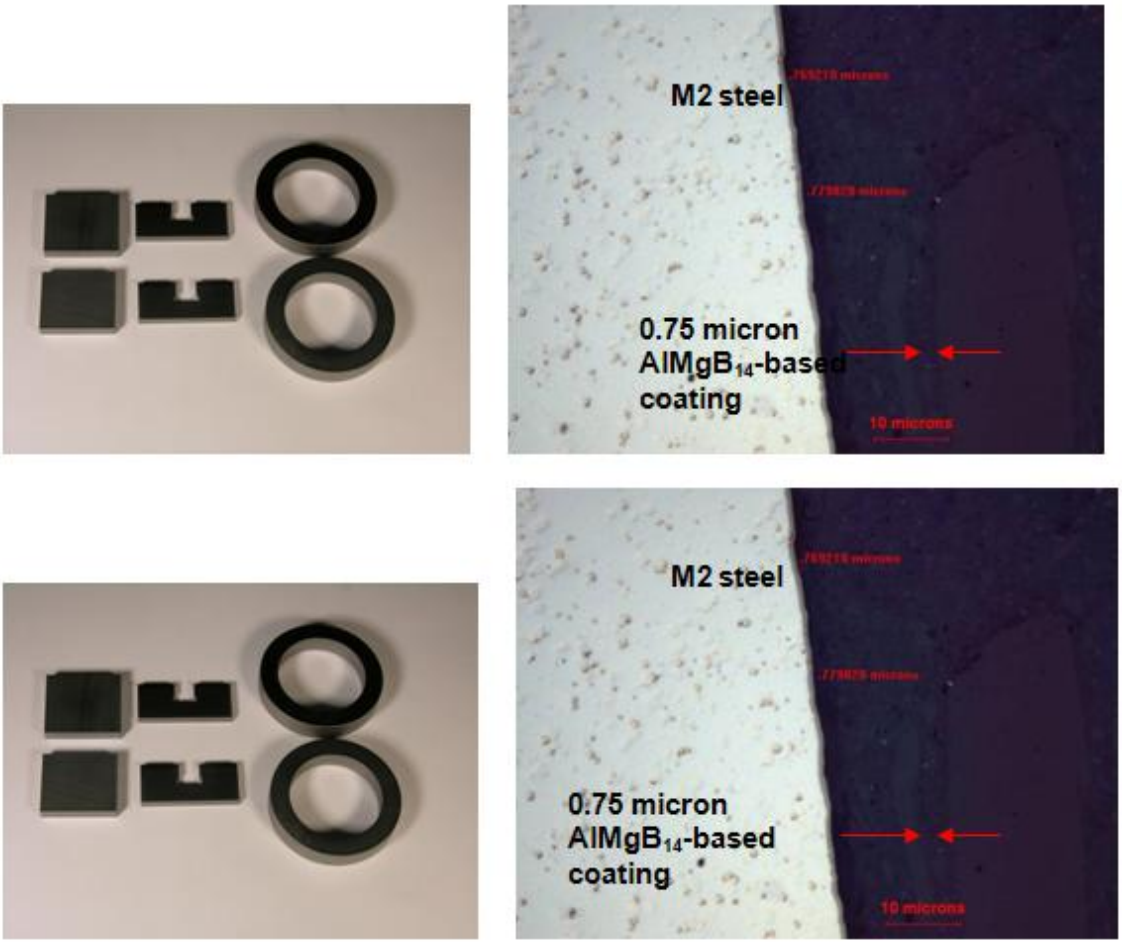

Figure 4.2.1-4: High temperature PVD deposited $AlMgB_{14}$-based coating. The coating thickness on the vane is about 0.75 microns (vane Material: M2 Steel).

With a successful $AlMgB_{14}$-TiB_2 physical vapor coating deposited onto an application-based substrate, the focus was then turned on the testing of coated components for improvements in mechanical efficiency. Eaton coating batch #1065 was used in the first of many vane pump efficiency measurements. See Figure X below for a representative collection of the components selected for coating. Of interest are the Falex tribology rings, the tool steel vane blades, and the tooling.

Figure 4.2.1-5: Falex tribology rings, the tool steel vane blades, and the tooling.

Test results from the performance evaluation of the vane kit processed in Eaton batch #1065 revealed some opportunities for optimization in the coating process. While the TiB_2 phase incorporation yields very high hardness (these coatings have been measured to values over 30 GPa) and wear resistance, they did not display the expected reduction in coefficient of sliding friction in the end application. Accordingly, a new effort to incorporate a carbon gradient coating within the standard $AlMgB_{14}$-based PVD coatings was started. The purpose of this work was to reduce the friction coefficient further by providing a less abrasive surface to the counter-face material. The concept of this gradient carbon layer was to be deposited by one of two methods: a) introducing an acetylene gas (C_2H_2) that forms a reactive layer with the $AlMgB_{14}$-based coating or, b) sputtering from a solid carbon target simultaneously while sputtering the $AlMgB_{14}$ target.

In the last quarter of 2007, about 20 coating batches were completed at Eaton Innovation Center on various test-coupons, Eaton hydraulic components, and cutting tool inserts from Greenleaf. Coating efforts were predominantly focused on $AlMgB_{14}$-TiB_2 (mixed phase $AlMgB_{14}$), but for comparison and evaluation purposes, a few other coatings were also processed. The strategy of this effort was to develop and improve processes for $AlMgB_{14}$-based coatings while the group continued to explore other commercial offerings such as DLC. The final benefit identified was that the processing would be useful in assessing the inclusion of graded carbon layers in the $AlMgB_{14}$ coatings as a means to improve upon their friction performance. The list of PVD coating materials processed during this period include:

1) $AlMgB_{14}$-TiB_2 mixed phase, an Innovative Material's target was provided by Ames.
2) $AlMgB_{14}$ (single phase from Super Conducting Materials) + TiB_2 using separate targets for each boride alloy.
3) $AlMgB_{14}$ (mixed phase) + Carbon top layer using an additional carbon sputtering target
4) $AlMgB_{14}$ (mixed phase) + graded carbon top layer using acetylene gas
5) TiAlN
6) TiAlN + Carbon top layer using an additional carbon target
7) WC + graded carbon top layer using acetylene gas
8) TiN

Refer to **Figures 4.2.1-6 through 4.2.1-9** for representative photomicrographs of various Eaton $AlMgB_{14}$-TiB_2+C PVD films.

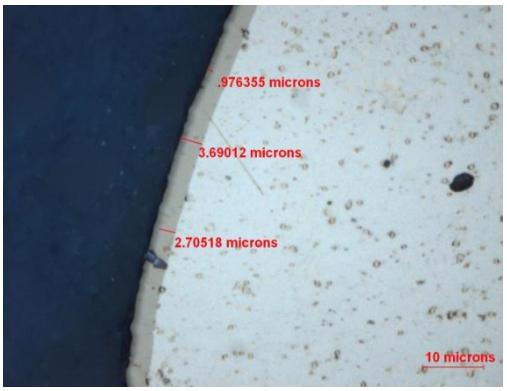

Figure 4.2.1-6: Early PVD processing of $AlMgB_{14}$-TiB_2+C film on tool steel substrate.

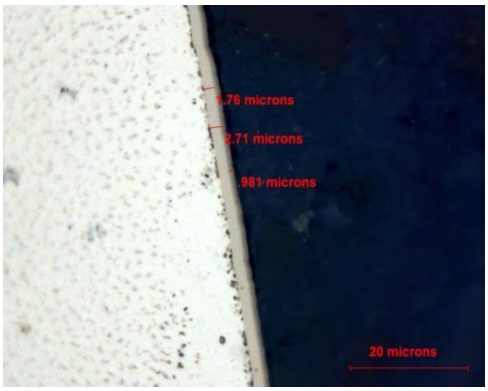

Figure 4.2.1-7: PVD processing of $AlMgB_{14}$-TiB_2+C film on tool steel substrate with adjusted acetylene flow rates.

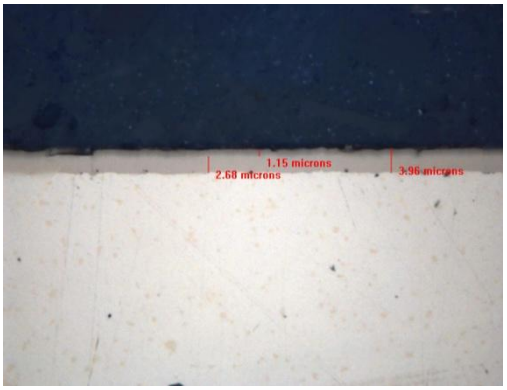

Figure 4.2.1-8: Application of $AlMgB_{14}$-TiB_2+C film on tool steel to Illustrate uniformity of film thickness.

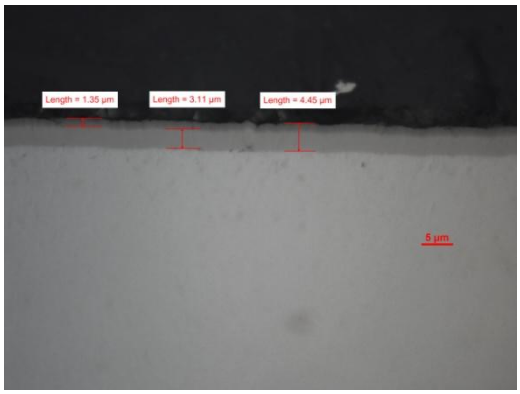

Figure 4.2.1-9: $AlMgB_{14}$-TiB_2+C film on tool steel substrate to show the columnar nature of film growth.

Note that most processes were conducted at high substrate temperatures (about 300 -350 ºC) in order to enhance the adhesion and cohesion of the coating. However, low temperature batches (~ 150 ºC) were also tried with $AlMgB_{14}$, TiAlN and WC/C coatings, specifically for components made of low tempering temperature carbon steel such as carburized 8620. The thicknesses of these coatings were in the range of 1.5 – 3.5 μm, to avert delamination due to internal stresses. In evaluating the coating adhesion, a micro–blast tester was used. For many of the applied films, it takes up to 10 minutes to remove/penetrate the coating on M2 vanes and Falex rings, even for the coatings applied at low temperatures. Many commercial coating entities identify a target of up to 3 minutes in micro-blast abrasion as an acceptable adhesion quality control. Noting this detail provides an indication of the improvements in wear resistance associated with the $AlMgB_{14}$-based films.

As processing of the coatings (including the carbon gradient films) became a routine task over the course of the project, a greater emphasis was placed on increasing the number of components used in a particular batch and in the addition of additional processing targets to drive down the processing times. Mid-way through 2009, however, several of the tested vane pump and VIS motor kits delivered to the division for efficiency and durability testing began to experience premature wear. This wear, in turn, was found to influence the performance of the respective applications negatively and so efforts were made to “duplicate” the performance of

some of Eaton's early PVD coatings. Recall that, after 250 hours of endurance testing in Mobil DTE-24$_{TM}$ hydraulic fluid, vane pump blades run in an early batch (#1067) still had $AlMgB_{14}$-TiB_2 coating was intact. For this particular kit of parts tested, the coating was measured to be approximately 70% of its original thickness.

Given that high wear rate coatings manifest themselves with lower than baseline efficiency results, it was imperative that any notable differences between these coatings and high performing coatings be established. Backscattered electron detection was used throughout the project to illustrate the degree of coating wear with respect to time. The best performing coatings (from an efficiency perspective) exhibited some wear after endurance testing. This was measured to be approximately 27% of the overall coating thickness after 250 hours **(Figure 4.2.1-10).**

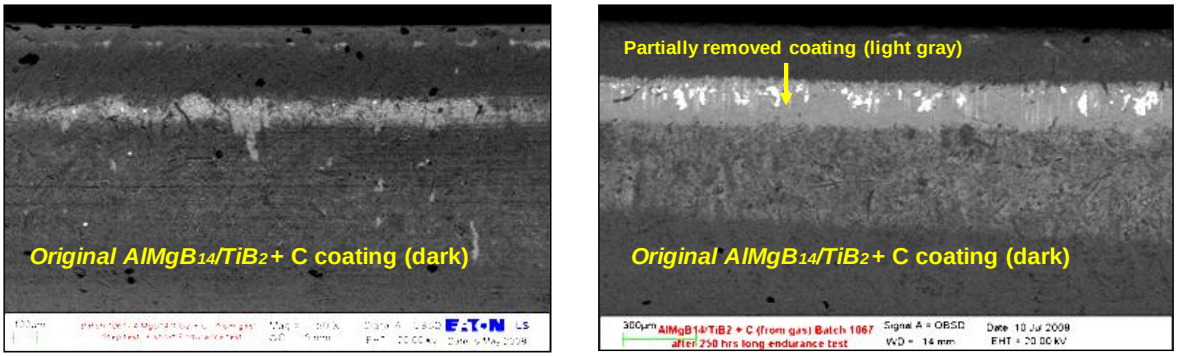

After Step test and short endurance test

After 250 hrs long endurance test

Figure 4.2.1-10: Backscattered electron imaging from Eaton Batch 1067 after "stepped load" testing and 24-hour endurance testing (left) as well as 250-hour endurance testing (right).

In contrast, similar backscattered electron photographs taken for low-performing coatings **(Figure 4.2.1-11)** illustrate a more severe wear rate, as he coating appears to have been completely removed. Furthermore, little if any evidence of the carbon gradient layer wearing while leaving the base $AlMgB_{14}$-TiB_2 layer intact is present. It should be noted that this photograph was taken after the vane pump kit had completed "stepped" testing and 24-hour endurance testing. No durability testing was performed on this particular film. This significant difference in wear performance demonstrates the importance of the associated processing parameters – most notably with $AlMgB_{14}$-TiB_2 films.

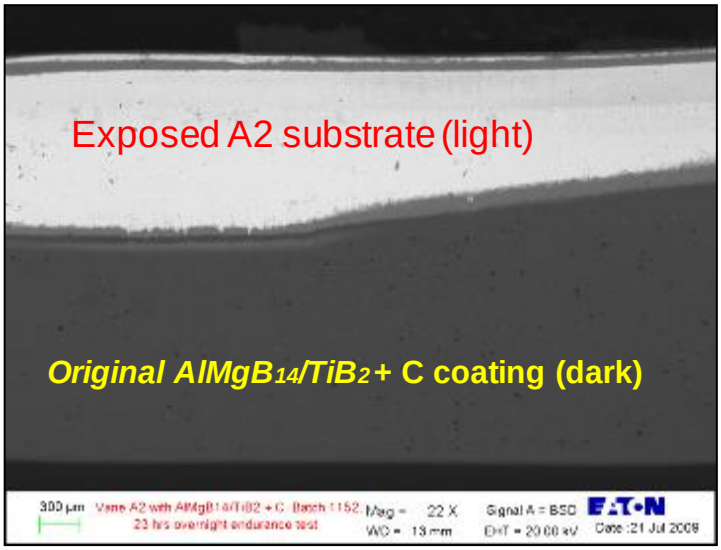

Figure 4.2.1-11: Backscattered electron imaging from Eaton Batch 1152 after "stepped load" testing and 24-hour endurance testing (left). Note that, in the area of primary contact, the coating appears to have been completely removed.

Input factors were reviewed by the team and those agreed to be the most likely in terms of affecting coating wear behavior were target wattage, level of carbon present during coating, number of targets selected for coating, substrate material selected for deposition, and coating temperature. Through the process of elimination and via use of DFSS (design for Six Sigma) methodologies, the target wattage and carbon present during coating emerged as the most significant variables. Late in October of 2009, the Eaton PVD system was comprehensively cleaned for suspected contamination, a maintenance batch was run, and a high temperature, 2500W batch including some M2 vane blades, was run for durability and performance testing at Eaton's Hydraulic facility in Eden Prairie. Results from this testing led to the conclusion that the Eaton PVD system began to develop carbon contamination as a result of oil vapor buildup under static vacuum. Efforts were also made to reduce target power further during PVD processing. Resolution of these two primary issues led to a coating that was, in effect, similar in wear behavior to the earlier films. (Refer to section 4.2.4. titled, "Characterization of PVD Coatings" for additional details on resolution of processing issues during development of this technology.)

Prior to any subsequent dynamometer tests of additional $AlMgB_{14}$-TiB_2 coatings, polished vane blade surfaces were used as "coupons" and were compared with those vane blades that yielded efficiency gains in performance testing. Eaton batches #1067, 1174, and 1176, for example, all yielded measurable and significant mechanical (and volumetric) efficiency gains over the baseline condition. Vanes from these particular batches would be identified as "master reference" samples. One of many characteristics evaluated on the newly processed coating would be the general surface appearance at high magnification. Differential interface contrast imaging techniques were employed to assess the general texture of the newly deposited films. Those coatings that exhibited a tightly knit appearance were expected to perform well in efficiency and durability testing – akin to the Thornton growth model displayed in Section 4.2.4.

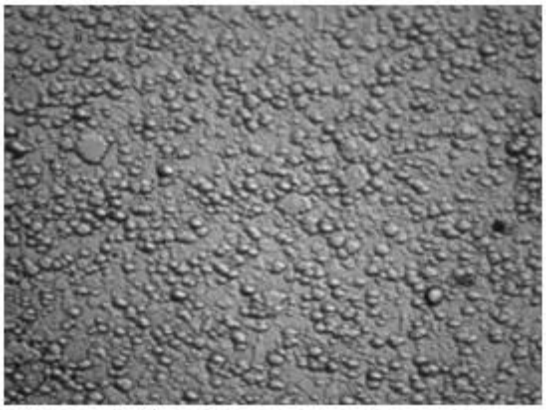

Differential interface contrast photomicrograph of vane blade from Eaton Batch #1176.

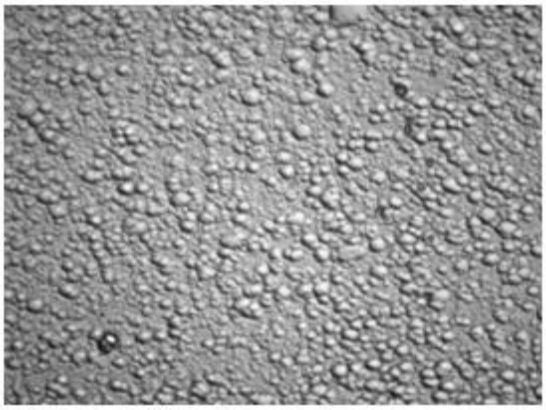

Differential interface contrast photomicrograph of vane blade from Eaton Batch #1174.

Figure 4.2.1-12: Surface photomicrographs of polished vane blades from Eaton $AlMgB_{14}$-TiB_2+C PVD processing runs 1176 and 1174.

The purpose behind this evaluation was to determine if subsequent PVD processing runs after Batch #1174 could result in similar coating morphologies. This testing was completed prior to dynamometer testing was initiated for the vane kits from Batch #1176 in an effort to predict coating performance.

For comparison, a representative differential interface contrast photomicrograph of a vane blade from Eaton Batch #1169 (determined to be a low performance coating for both wear and efficiency) is included below.

Figure 4.2.1-13: Surface photomicrographs of vane blades (note that these are not polished to 100nm, as in the case of the vanes from batches 1174 and 1176) from Eaton $AlMgB_{14}$-TiB_2+C PVD processing run number 1169.

From all of these findings, then, the selection input variables that lead to “good” coatings from both the perspective of test performance and achieving minimal wear became increasingly important. An Ishikawa diagram, often referred to as a “fishbone” diagram, has been instrumental in capturing all of these input variables into one central structure for evaluation **(Figure 4.2.1-14)**.

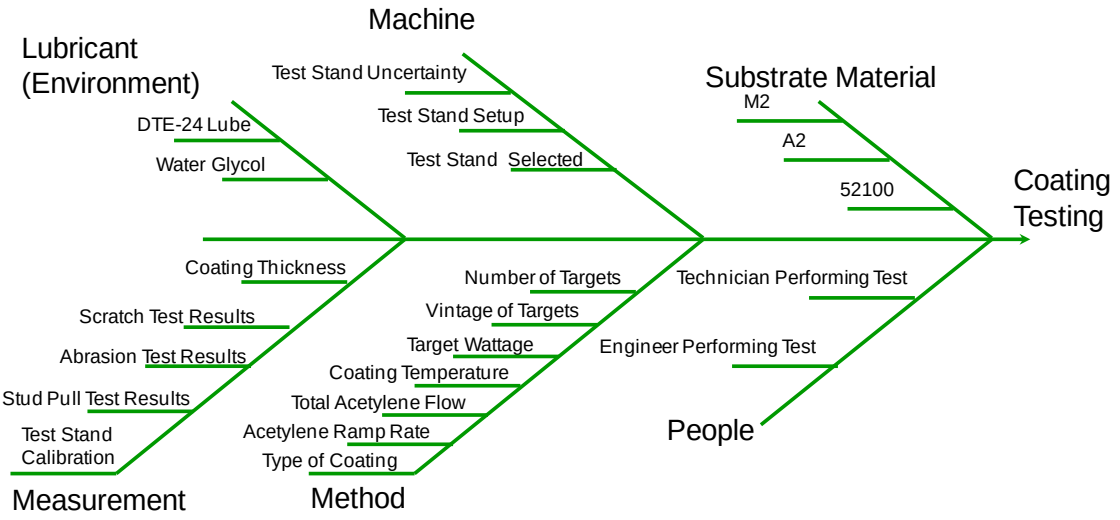

Figure 4.2.1-14: A simplified breakdown of the various coating input variables that are considered to affect dynamometer test performance with respect to pump kit mechanical efficiency.

In terms of determining which input factors can be characterized as a “root cause” to driving coating wear rate in mechanical testing, it would be nearly impossible to test all of the possible permutations. The assembled team benefited from several key factors in process improvement and optimization:

1. An operator skilled in system operation, careful selection of processing parameters, and in post-test characterization.
2. On-site wear testing to evaluate films for frictional performance and wear.
3. Availability of end-component testing facilities and personnel.
4. Off-site tribology simulation, friction, and wear testing staffed by industry experts.
5. A thorough knowledge of the material’s bulk mechanical characteristics and availability of research-grade instrumentation and equipment.

4.2.2 Establishment of End Application Performance Needs

Over the program's period of performance, Eaton identified three distinct hydraulic applications where the benefits of nanocoatings would be most impactful. These include, but in an industrial sense, are certainly not limited to, vane pumps, geroler (valve-in-star type) motors, and variable displacement piston pumps. Existing product performance (meaning prior to implementation of surface enhancement technology such as nanocoatings) is inherently limited by the degree to which friction reduces mechanical efficiency and the degree to which non-uniform wear affects volumetric efficiency. A pump's mechanical efficiency, then, can be expressed by the following equation (note that simplification of the many variables influencing a pump's efficiency, namely conveyance, torque ripples, and so forth have been assumed as negligible):

$$mechanical\ efficiency = \frac{outlet\ pressure - inlet\ pressure}{speed\ *\ input\ torque}$$

To arrive at this equation requires proper instrumentation of the system, with test gaging and acquisition of the inlet pressure, outlet pressure, inlet fluid temperatures, tank fluid temperatures, input torque, outlet flow, and drive speed across a wide range of operating conditions. Additional calculations used in determining pump work, to quantify energy savings, are included below.

U.S Units	Metric Units
1) Flow: $\frac{\frac{in^3}{rev} \times rpm}{231}$ (gpm)	1) Flow: $\frac{\frac{mL}{rev} \times rpm}{1000}$ (L/min)
2) Torque: $\frac{\frac{in^3}{rev} \times psid}{2\pi}$ (lb-in)	2) Torque: $\frac{\frac{mL}{rev} \times bar^*}{20\pi}$ (N*m)
3) Power (Shaft): $\frac{Torque \times rpm}{63,025}$ (hp)	3) Power (Shaft): $\frac{\pi \times Torque \times rpm}{30}$ (watt)
3a) Power (Hyd): $\frac{gpm \times psid}{1,714}$ (hp)	3a) Power (Hyd): $\frac{5}{3} \times \frac{L}{min} \times bar^*$ (watt)
	** KPa/100 or 10 MN/m2 may be used in place of bar*

Note: The above equations give theoretical values: that is, 100% efficiency is assumed. Actual pump outlet flow is less by the amount of pump internal leakage, and input torque to the pump is greater by the amount of torque loss.

In order to establish each application's performance "need," it is best to first examine the current operating spectrums and then determine how much further each application could be pushed such that there is a) a measurable energy savings associated, b) a market differentiation that justifies commercialization, c) a cost viable path to provide maximum value to the end user.

In the case of hydraulic vane pumps, the internal mechanics are conceptually simple; vanes are mounted to a motor-driven rotor that rotates inside of an asymmetric cavity. In some cases, these vanes can be of variable length and/or are tensioned to maintain contact with the walls as the pump rotates. One of the key advantages of a vane pump's design is that it readily lends itself to being a variable displacement pump. In this particular design, the eccentric ring pivots or translates relative to the rotating group and displacement (commonly expressed by the centerline distance from the rotor to the eccentric ring) can be varied. In some cases, it is even possible for vane pumps to pump in reverse if the eccentric ring moves far enough, although performance is generally not optimized for two-way flow. Refer to **Figure 4.2.2-1** for a schematic of a Vickers vane pump and the components within.

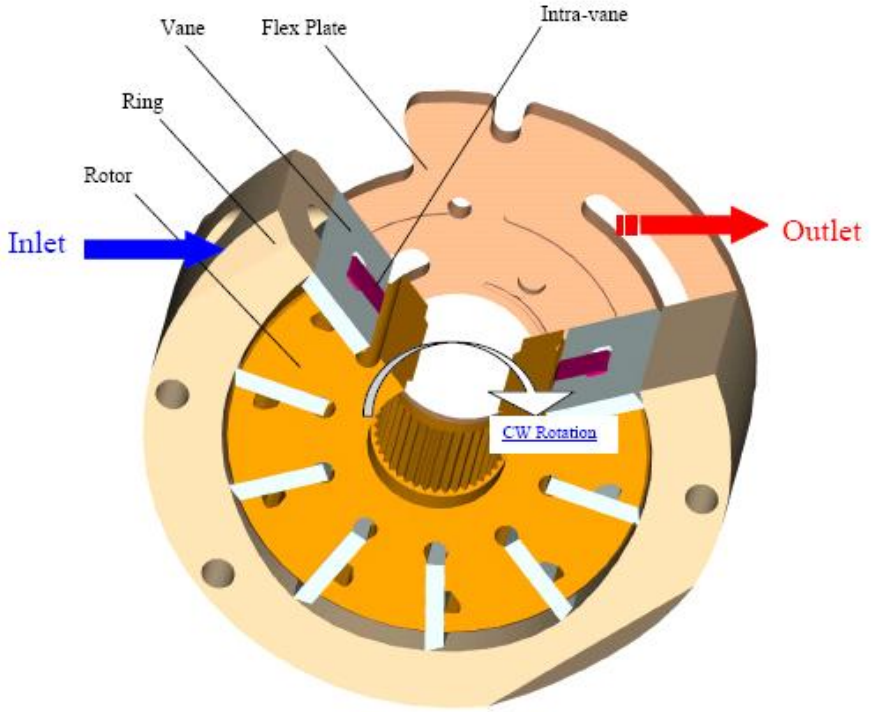

Figure 4.2.2-1: Schematic of a Vickers vane pump and the components within.

Eaton's Vickers series of vane pump products were one of the key products selected within the scope of this project, namely because of component volume, name recognition, and the opportunity for energy savings, assuming that efficiency improvements were realized. A cross section of an Eaton Vickers vane pump and the key modeling parameters are shown in **Figure 4.2.2-2.** Four angular positions, 0º, 45 º, 90 º, and 135 º, were selected for analysis. Contact and lubrication analyses were conducted under a smooth surface assumption at these four angular positions, by using a newly developed 3-D line contact mixed elastohydrodynamic lubrication model and a relevant computer program. Note that the variable P_H is the maximum Hertzian

contact pressure, the variable ‘a’ represents the half-width of the Hertzian contact zone, the variable H_C is the lubricant film thickness at the contact center, and ‘f’ represents the coefficient of friction. Since no roughness is involved, all of the analyzed cases show no direct contact between the two surfaces, and the film thickness is in the range from 75 to 260 nm. Typical simulation results for pressure along the vane tip and lubricant film thickness are displayed in **Figures 4.2.2-3 through 4.2.2-7.** A table summarizing some of the input variables used to develop the model is included below in **Table 4.2.2-1.**

Table 4.2.2-1: Input variables used to develop the model

1800 RPM and 2500 psi	Position	Applied Load on the vane	Vane Tip Radius at Contact	Ring Inner Radius at Contact	Sliding Speed	Contact Length
	[deg]	[lbf]	[in]	[in]	[in/sec]	[in]
1	0	78.2	0.120	1.640	309	1.5809
2	45	106.9	0.120	2.000	343	1.0189
3	90	34.1	0.120	1.863	350	1.5809
4	135	5	0.040	2.000	343	1.5809
1	0	78.2	0.120	1.640	309	1.5809
2	45	106.9	0.120	1.900	336	1.0189
3	90	34.1	0.120	1.822	342	1.5809
4	135	5	0.040	1.900	336	1.5809

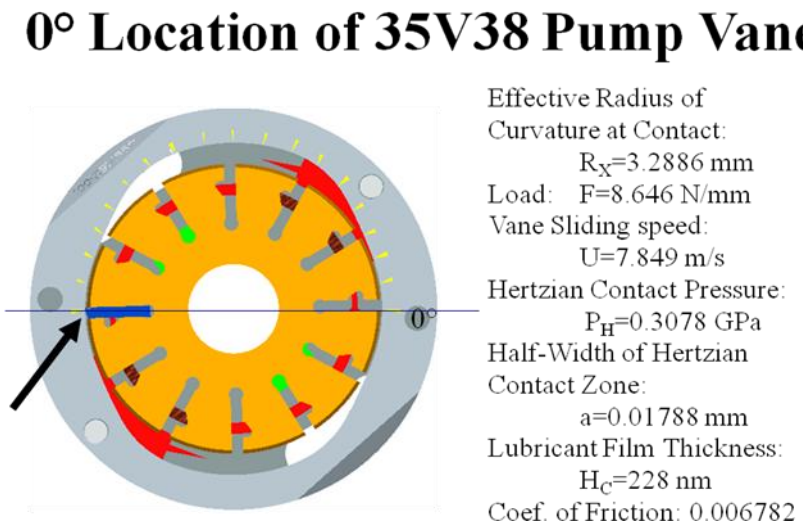

Figure 4.2.2-2: Eaton Vickers vane pump and the key modeling parameters.

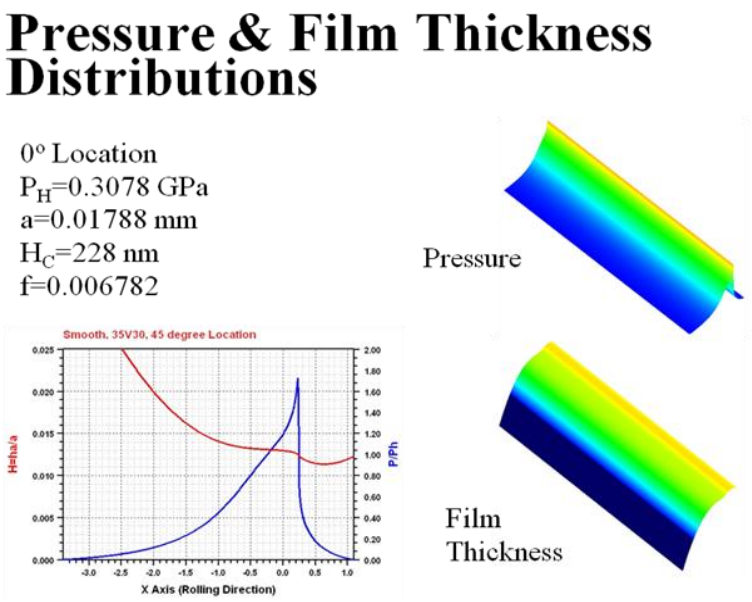

Figure 4.2.2-3: Simulation results for vane- pump at 0-degree angular location.

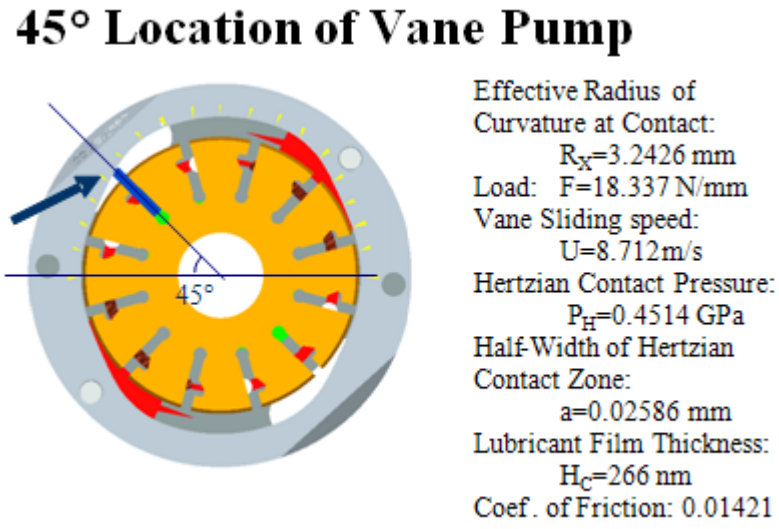

Figure 4.2.2-4: 45 Degree Location of Vane Pump.

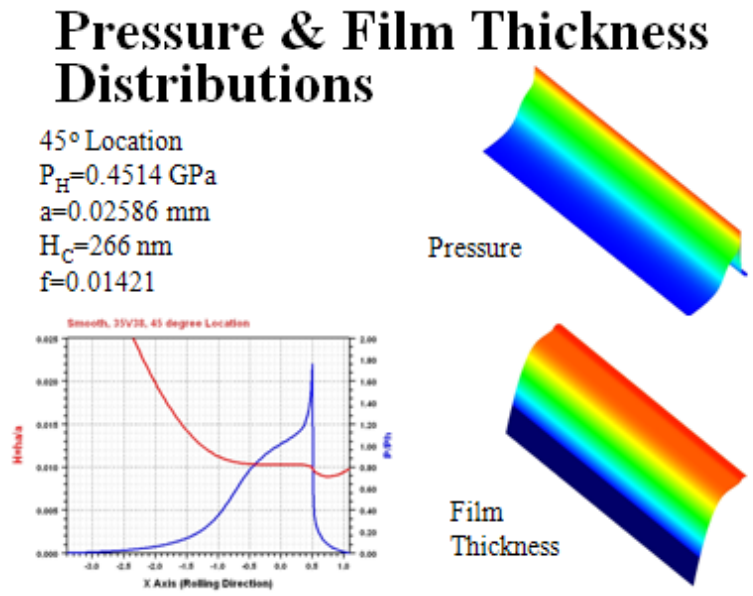

Figure 4.2.2-5: Simulation results for vane- pump at 45-degree angular location.

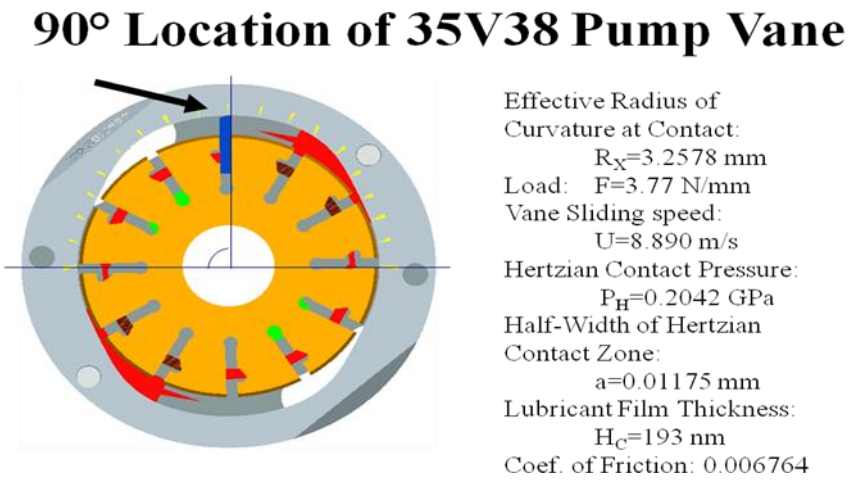

Figure 4.2.2-6: Simulation results for vane- pump at 90-degree angular location.

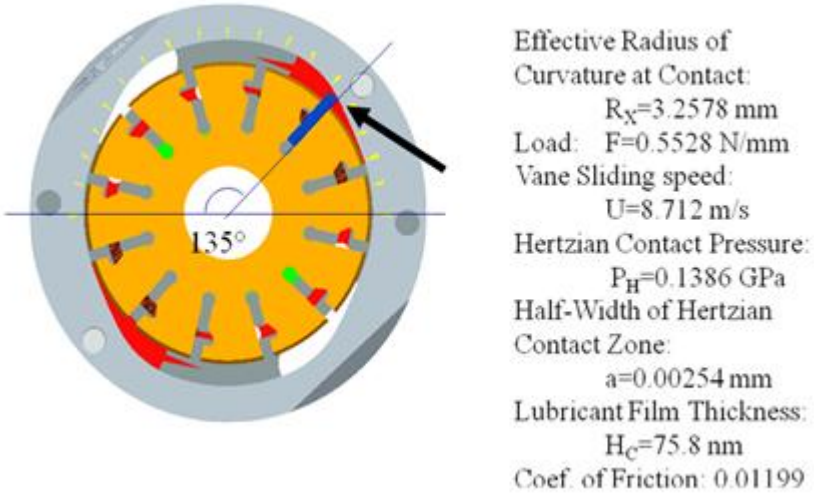

Figure 4.2.2-7: Simulation results for vane- pump at 135-degree angular location.

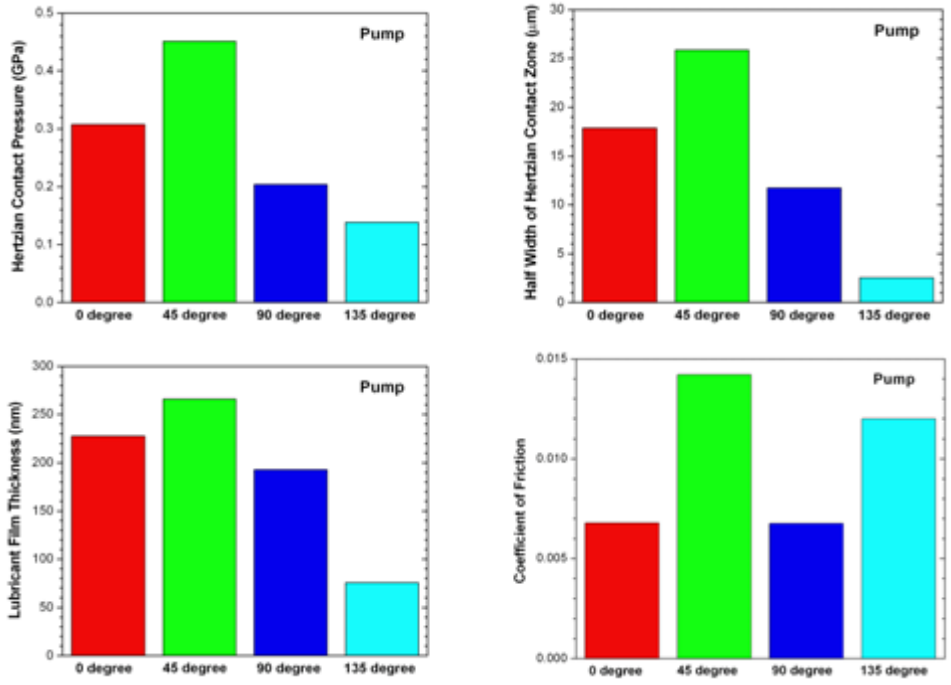

Figure 4.2.2-8: Summary of results for vane-pump.

Computational results for the aforementioned vane-pump are displayed in **Figure 4.2.2-8** and. It is worth noting that, based on the idealized smooth surface assumption and the full film hydrodynamic lubrication that results from modeling, the friction coefficient is found to be small, within a range from 0.006 to 0.014. Furthermore, the measured surface roughness of pump vane is around Ra=200 nm and that of the actual pump ring around 300 nm. In reality, there are asperity contacts at the interface, meaning that the coefficient of friction (as a result in a shift towards boundary lubrication) is likely much higher than the 0.006 to 0.014 range. It is important to note in the results that the Hertzian contact between the vane and ring surfaces is very narrow. With a half-width in the range from 2.54 to 25.4 microns, the discretization accuracy of

rough surface topography does not match that of contact / lubrication analysis. When surface finish parameters from actual components used in production pumps were input into the model **(Table 4.2.2-2)**, coefficient friction results increased by nearly an order of magnitude. This data is included in **Figure 4.2.2-9** and is more likely to be representative of the actual system than previous computations.

Table 4.2.2-2: Surface Finish Parameters

Surface Finish Parameters

Part	Ra Before	Ra After	Rsk Before	Rsk After	Wa Before	Wa After
Ring Major Dia	8.87	7.41	-0.37	-0.59	21.07	18.56
Ring Minor Dia	6.01	5.90	-0.67	-1.66	13.57	14.06
RING Ave	**7.44**	**6.66**	**-0.52**	**-1.13**	**17.32**	**16.31**
Vane #1	4.66	4.11	-0.84	-2.09	60.30	51.04
Vane #2	5.65	4.10	-1.00	-1.31	89.60	51.19
Vane #3	5.04	4.66	-1.21	-3.25	73.27	53.83
Vane #4	6.36	4.56	-1.69	-1.81	72.28	57.46
Vane #5	5.81	3.49	-1.37	-0.97	181.18	117.49
Vane #6	5.51	4.19	-1.30	-1.00	79.69	47.82
VANE Ave	**5.51**	**4.19**	**-1.24**	**-1.74**	**92.72**	**63.14**
	0.60	0.42	0.30	0.86	44.39	26.82

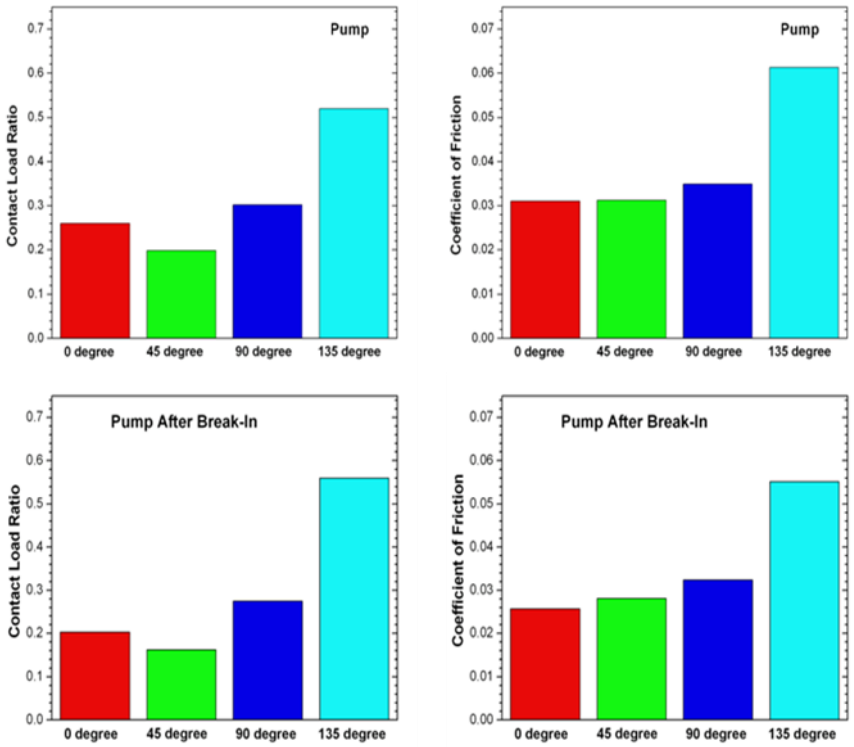

Figure 4.2.2-9: Summary of results for vane-pump.

With vane surfaces modeled, the next step in determining potential benefits associated with the nanocoatings technology involves examination of current baseline performance. The group's first baseline vs. coated samples testing focused on a set of vanes coated with diamond like carbon. These vanes were subject to mechanical efficiency test under different loads (250 – 2500 psi) at constant speed (1800 rpm). The results for the uncoated and DLC coated vanes are shown in **Figure 4.2.2-10**. There was at least a 2% (absolute) increase in mechanical efficiency across the entire pressure range. From this information, then, the basis for pursuing the $AlMgB_{14}$-TiB_2 films was established. If the proposed compositions could supersede the performance of DLC, then there would be a marked advantage for commercialization. Furthermore, elimination of the vane blade wear (**Figure 4.2.2-10** below) associated with step load testing would yield sustained improvements in volumetric efficiency, as this decreases over time as wear accelerates on the vane interface.

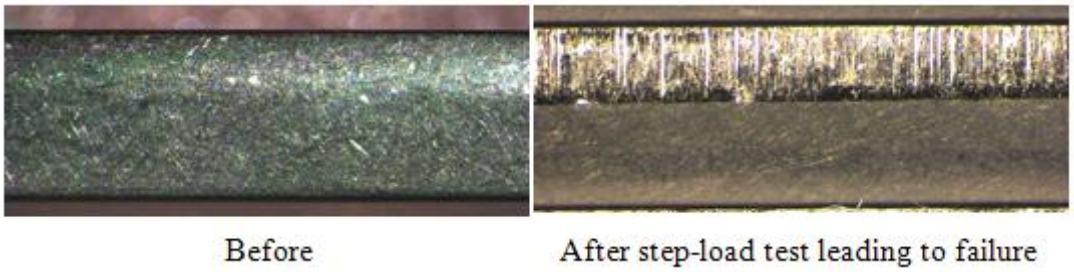

Figure 4.2.2-10: Uncoated and DLC coated vanes results

While the aforementioned DLC testing was encouraging from the standpoint that coated vanes would inherently yield higher efficiency pumps, the products would still undergo durability schedules to ensure long term benefits and to eliminate any risks with the coatings negatively affecting service life. This testing is discussed further in Section 4.2.5.

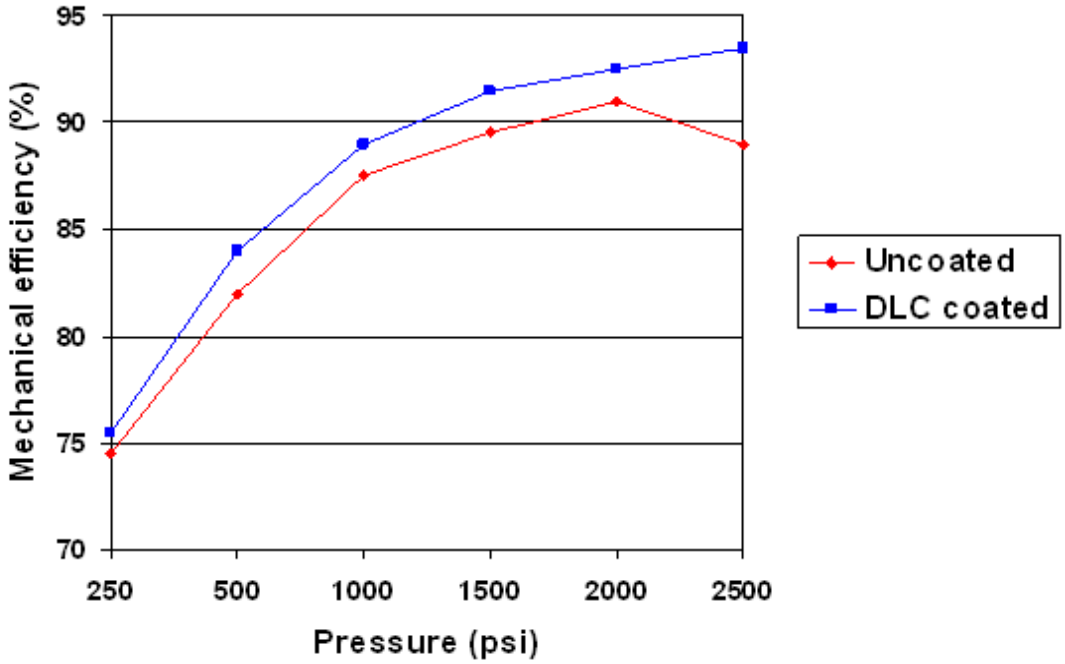

Figure 4.2.2-11: Mechanical efficiency performance of DLC-coated versus uncoated vanes in a vane-pump assembly.

For the proposed hydraulic geroler motors, often referred to as valve-in-star (VIS) motors because of the orbiting star valve, there are three key components that affect the performance of the system; the first being the orbiting star that is mounted via a spline interface to a drive shaft. The star is aligned in the same plane orientation as the second component, the ring housing. The ring serves to contain the internal hydraulic pressure and to hold the final components, the rollers. Via the inlet porting, hydraulic pressure builds in the cavity between the ring, roller, and star components. This forces the star to orbit to the next roller and the localized hydraulic pressure to be released. The process repeats itself as the star rotates. This motor design is known for producing very high drive torque at relative low rotational speeds (typically below 800 RPM) - all in a compact geometry. As with the previously discussed vane pump, a key driver in the performance of these motors is mechanical efficiency, most notably at lowered speeds. Refer to **Figure 4.2.2-12** that illustrates the components discussed in the hydraulic VIS motor.

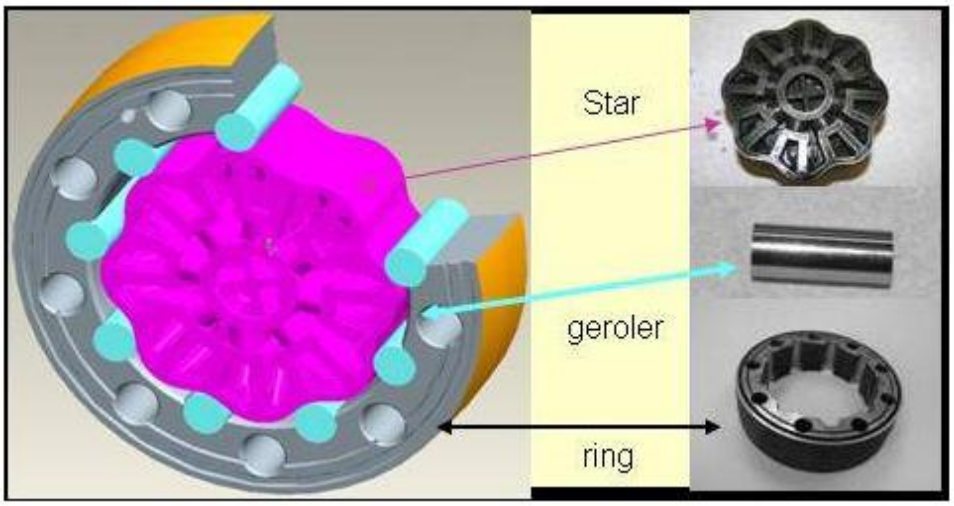

Figure 4.2.2-12: Graphical representation of components used in the hydraulic valve-in-star (VIS motor).

Data from dynamometer testing indicates that the VIS motor mechanical efficiency has strong relationship to the motor rotational speed and drops linearly when the speed is below 4 rpm, as at start-up (see **Figure 4.2.2-13**).

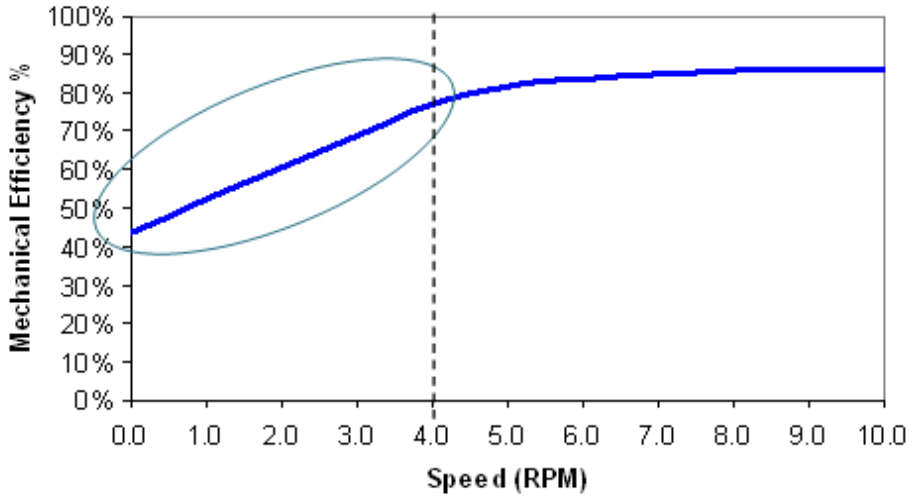

Figure 4.2.2-13: VIS motor mechanical efficiency as a function of the motor speed.

The VIS motor mechanical efficiency is mainly affected by the friction forces at the star-roller interface and at the roller-ring pocket interface. The friction coefficient at each interface is determined by the lubrication regime, motion mode (rolling or sliding), surface textures, and the materials. The lubrication regime is usually determined by the λ ratio (defined in Equation 1) between the lubricant film thickness (h) and the composite roughness (σ) a contact interface.

$$\lambda = \frac{h}{\sigma}$$
$$\sigma = \sqrt{\sigma_1^2 + \sigma_2^2} \quad (1)$$

Where, σ_1 and σ_2 are the RMS surface roughness of the two contact surfaces. **Table 4.2.2-3** shows the lubrication regimes for various ranges of the λ ratio, and the individual and composite roughness values for the star-roller and roller-ring contacts are shown in **Table 4.2.2-4.**

Table 4.2.2-3: Lubrication regimes

λ ratio	Lubrication regime	Note
λ >= 4	Elastohydrodynamic (EHL)	Interface fully separated by a lubricant film No asperity contact
1<= λ < 4	Mixed (ML)	Interface partially separated by a lubricant film
λ < 1	Boundary (BL)	Two solid counterfaces in contact

Table 4.2.2-4: Roughness of the star, rollers, and ring pockets.

	Star	Roller	Ring
Roughness R_q (μm)	0.406	0.058	0.316
	Star-Roller		Roller-Ring
Composite roughness σ (μm)	0.41		0.32

Given the VIS motor operation parameters, the lubricant film thickness t at the star-roller and roller-ring interfaces (both in line contacts) were calculated using Dowson's line-contact EHL lubricant film thickness equation [10] and are summarized in **Table 4.2.2-5** for three VIS motor operating conditions. The nominal operation is 440 rpm at 180^o F and the other two represent slower, start-up conditions.

Table 4.2.2-5: Calculated film thicknesses and λ ratios.

Motor operating condition	Star-Roller		Roller-Ring	
	t (μm)	λ	t (μm)	λ
0.1 rpm @ RT	~0.002	<1 (BL)	~0.02	<1 (BL)
4.0 rpm @ RT	~0.02	<1 (BL)	~0.38	~1 (ML)
440 rpm @ 180 °F	~0.15	<1 (BL)	~2.15	>4 (EHL)

Based on the aforementioned calculations, several interpretations can be drawn regarding the relationship between speed and motor efficiency:

1) At the start-up, when the star rotation speed is lower than 4 rpm, both the star-roller and roller-ring interfaces are under boundary lubrication (BL) and experience relatively high friction. The high friction at the roller-ring contacts causes a high slip ratio at the star-roller contacts. Therefore, more torque is required to overcome the BL sliding friction forces (typical coefficient of friction (COF) in the range of 0.05-0.15). This results in lower mechanical efficiency. Reducing the BL COF for the star-roller and/or roller-ring contacts is the key to improving the start-up mechanical efficiency.

2) When the star rotation speed >= 4 rpm, the star-roller contacts are still under BL (high friction) but the roller-ring contacts transition to ML (mixed lubrication) or elastohydrodynamic (EHL) (lowest friction). The nearly free spinning of the rollers in the ring pockets enables a low slip ratio at the star-roller contacts. As a result, a much lower torque is needed to overcome the rolling friction forces (typical COF<0.05) that occurs at the star-roller contacts and the ML/EHL sliding friction forces at the roller-ring contacts (typical COF<0.05). This explains why the VIS motor reaches its highest mechanical efficiency only when the motor rotates at 4 rpm or above.

To determine if there would be any associated performance gains with application of the proposed nanocoatings, several commercially available films were deposited onto the various components. It is worth noting that all PVD coatings were processed at the Eaton Innovation Center. Commercial coatings that were evaluated included diamond-like-carbon (DLC) processed by CVD.

Table 4.2.2-6: Nanocoatings processed on star valve component

Coating	Min Starting Torque Eff.		
	Aport	Bport	Average
	.1 RPM	.1 RPM	.1 RPM
Standard VIS	48.72	43.89	46.31
DLC lateral surface	52.10	48.21	50.16
DLC lateral surface+top+bottom	49.23	49.06	49.15
WC+C with Cr	51.44	45.04	48.24

Table 4.2.2-7: Nanocoatings processed on ring component

Coating	Min Starting Torque Eff.		
	Aport	Bport	Average
	.1 RPM	.1 RPM	.1 RPM
Standard VIS	48.72	43.89	46.31
WC+C with Cr bond layer	53.01	50.24	51.63
Cr+Teflon	52.03	46.57	49.30

As outlined in **Tables 4.2.2-6 and 4.2.2-7** performance was determined on a start-up simulation test to determine mechanical efficiency at 0.1 rpm and 5000 psi.

From the initial verification tests, the standard VIS motor without any coatings has a starting torque efficiency of about 46%. Application of commercially available coatings yielded improvements as large as 4% assuming a coated star and 6% with a coated ring. In addition to these improvements, additional performance tests (commonly referred to as ATS tests) that measure mechanical and volumetric efficiencies at typical operating conditions showed that application of these coatings yielded overall efficiency gains (overall efficiency being the product of the volumetric efficiency component and the mechanical efficiency component) of 7% over the baseline efficiency .

The key metric selected for the variable displacement hydraulic piston pump performance was mechanical efficiency. This assembly, as shown in **Figure 4.2.2-14** is comprised of a series of sliding pistons that develop pressure within a cylinder barrel assembly. Actuation of the pistons is the result of mating shoes sliding against a stationary inclined plane (the swash plate). As the pistons (and the barrel) rotate with respect to the swash plate, hydraulic fluid is pulled into the individual cylinder barrel bores, pressurized through the sliding piston actuation, and then outlet via the valve plate that mates to the cylinder barrel. Variable displacement piston pumps are actuated via a control piston that changes the angular plane of the swash plate. The idle condition for a piston pump assembly, which assumes minimal outlet flow, is represented when the working interface of the swash plate is normal (90 degrees) to the axis of the pumping pistons and the cylinder barrel. Full flow, conversely, is represented when the swash plate is at its maximum angle and full piston stroke is achieved. Because there are several working interfaces within a piston pump, the team partners specifically explored those that would yield the highest theoretical mechanical efficiency improvement, namely the piston shoe-swash plate coupling, the pistons to cylinder barrel, and the valve plate to cylinder barrel.

The key surfaces that contribute to dynamic friction and lessen the pump's mechanical efficiency over the operating range are (material currently used is included for reference):

a. Control Piston (8620 carburized low alloy steel)
b. Pump Housing (Gray cast iron)
c. Pump pistons (8620 carburized low alloy steel)
d. Cylinder Barrel (4140 steel)
e. Swash Plate (8620 carburized)
f. Piston Shoes (Mueller brass)
g. Valve Plate (hardened steel, 80-10-10 bronze sintering)

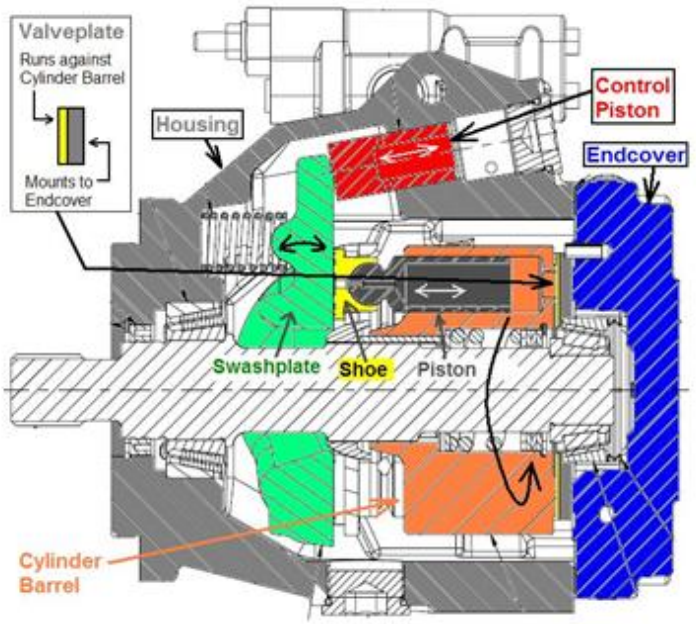

Figure 4.2.2-14: Eaton variable displacement, medium duty, axial piston pump with components identified

A graphical representation of each interface is included for reference in **Figures 4.2.2-15** through **Figure 4.2.2-17.**

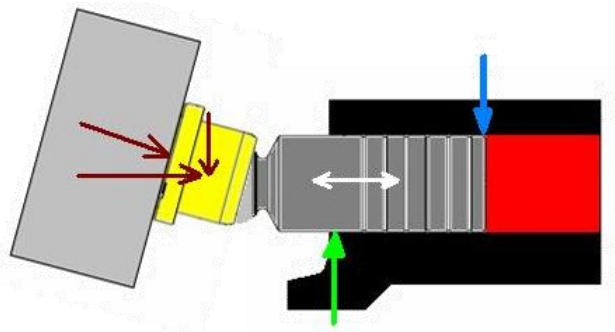

Figure 4.2.2-15: Graphical representation of the loading conditions at the piston-cylinder barrel interface.

In the case of the pumping pistons to cylinder barrel interface, the side load that develops as the swash angle hits its peak reaches 390 lbf. This is equivalent to a pressure of 5000+ psi. As the piston begins to accelerate to its maximum velocity, the side loading decreases slightly to 190 lbf, though the velocity rapidly rises to 520+ ft/min, resulting a pressure*velocity (P*V) product of 1.6 million psi*ft/min. The slide loads experienced by the piston reach their minimum at the bottom dead center condition, whereby outlet pumping is complete.

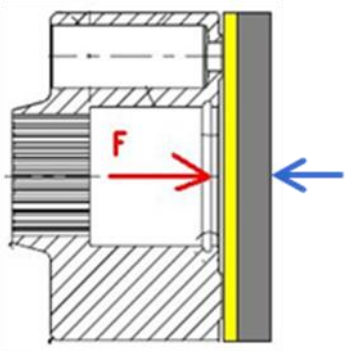

Figure 4.2.2-16: Graphical representation of the loading conditions at the cylinder barrel-valve plate interface.

At the valve plate to cylinder barrel interface, there is a maintained contact force of 220 lbf to ensure that fluid losses are kept to a minimum. The key factor in this interface, though, is that there is a relative velocity between the two components of 2450 ft/min, resulting in a P*V product of 420,000 psi*ft/min. Frictional improvement gains at this interface would be considered significant, as the application of bronze to the valve plate is costly.

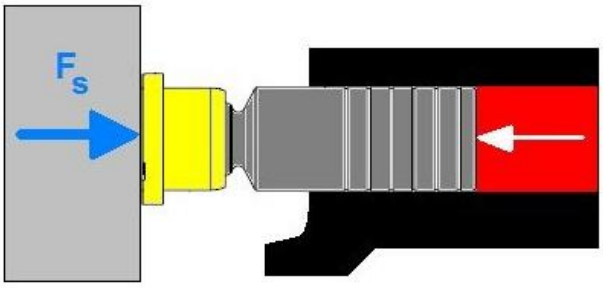

Figure 4.2.2-17: Graphical representation of the loading conditions at the piston shoe-swash plate interface.

The shoe to swash plate interface in this particular application is unique, as there is an inherent pressure balance that develops between the two components at higher velocities. Before the system is primed with hydraulic fluid, the forces exerted exceed 2700 lbf, though at steady state, because of this pressure balance, the forces are reduced to 20lbf. In spite of the relatively low loading between the piston shoe and the swash plate, the relative velocity is high at 2450 ft/min, resulting in a P*V product of 110,000 psi*ft/min.

.As shown in **Figure 4.2.2-18** the majority of the oscillation cycle for a piston sliding in a cylinder bore experiences elastohydrodynamic lubrication (EHL), with the effect of producing very low friction and wear. The critical locations are near the direction reversal points when the sliding speed is low, causing boundary lubrication (BL) with high friction and wear. For this reason, the bench test condition was designed to simulate the loading and motion near the stroke-ends. Based on Hertzian stress and Dowson lubricant film modeling, the normal load and sliding speed are determined to be 245 N (Hertzian contact stress: 3094 psi) and 0 – 52 ft/min (8.4 Hz w/ 10 mm stroke), respectively. Test temperatures ranged from room temperature to 240 ^{o}F, covering the full range of the operation temperatures for an actual pump. The lubrication modeling predicted mixed lubrication regime at room temperature and boundary lubrication at 240 ^{o}F.

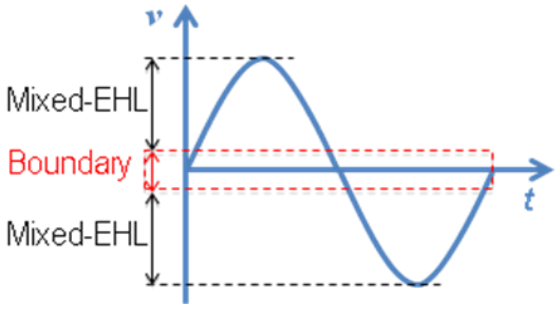

Figure 4.2.2-18: Lubrication regimes in an oscillation cycle for a piston sliding in a bore.

To assess the current performance criteria and to identify any opportunities for potential gains, Eaton's Aerospace hydraulics division provided the Innovation Center with various pump assemblies for coating trials. The baseline system, without any coatings applied to the various working interfaces yielded the following efficiency map **(Figure 4.2.2-19)**.

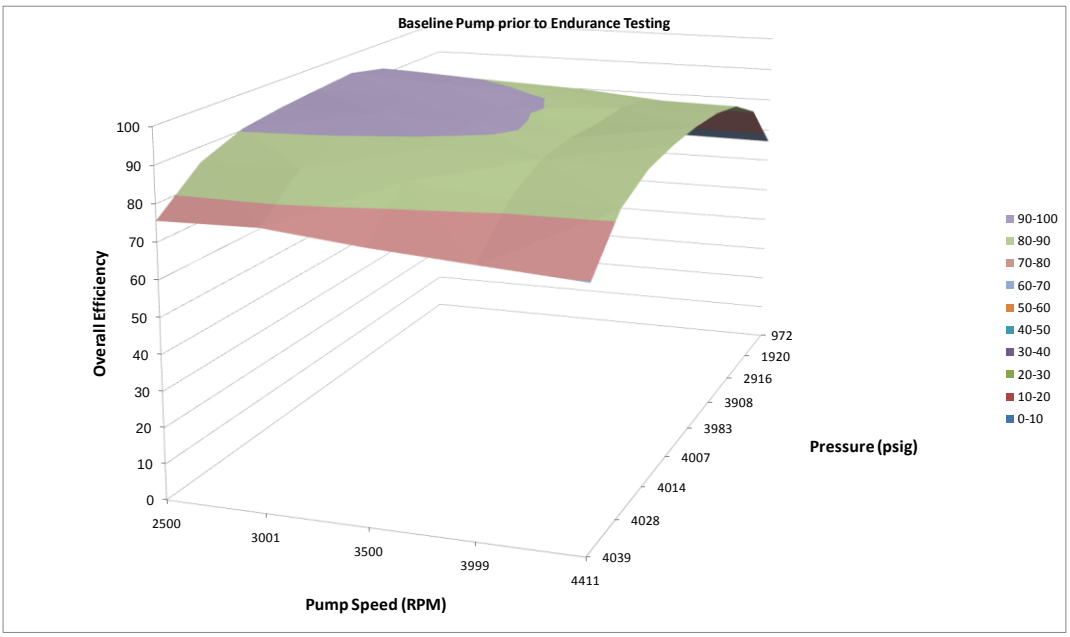

Figure 4.2.2-19: Performance of the baseline pump (no coatings) before full-scale endurance testing. This pump was cycled at 2500, 3000, 3500, 4000, and 4411 rpm with a variety of outlet pressures as part of the calibration.

It is worth noting that, over most of the pump's operating space, the overall efficiency ranges between 85-95%. It is only at the extreme ends of the pressure and speed where efficiency drops below 80%, notably at outlet pressures exceeding 4030 psi and at outlet pressures below 1900 psi. Only one region of the efficiency map showed values below 70%. This corresponded to low outlet pressures of 1000 psi and under at pump speeds over 4000 RPM.

When the system was put through a full durability schedule (in excess of 250 hours), the overall performance dropped by an average of 3% throughout the operating space. **Figure 4.2.2-20** illustrates that this particular pump delivered a peak overall efficiency between 2900 and 4000 psi outlet pressure and between 2500 and 2800 RPM. Lower overall efficiency was noted at outlet pressures exceeding 4000 psi and, as with the previously discussed results, outlet pressures below 1900 psi. The aim in applying coatings to the various working surfaces in this variable displacement piston pump was to broaden the operating space where the overall efficiency of the system is at its maximum and lessen the impact to performance at the two pressure extremes.

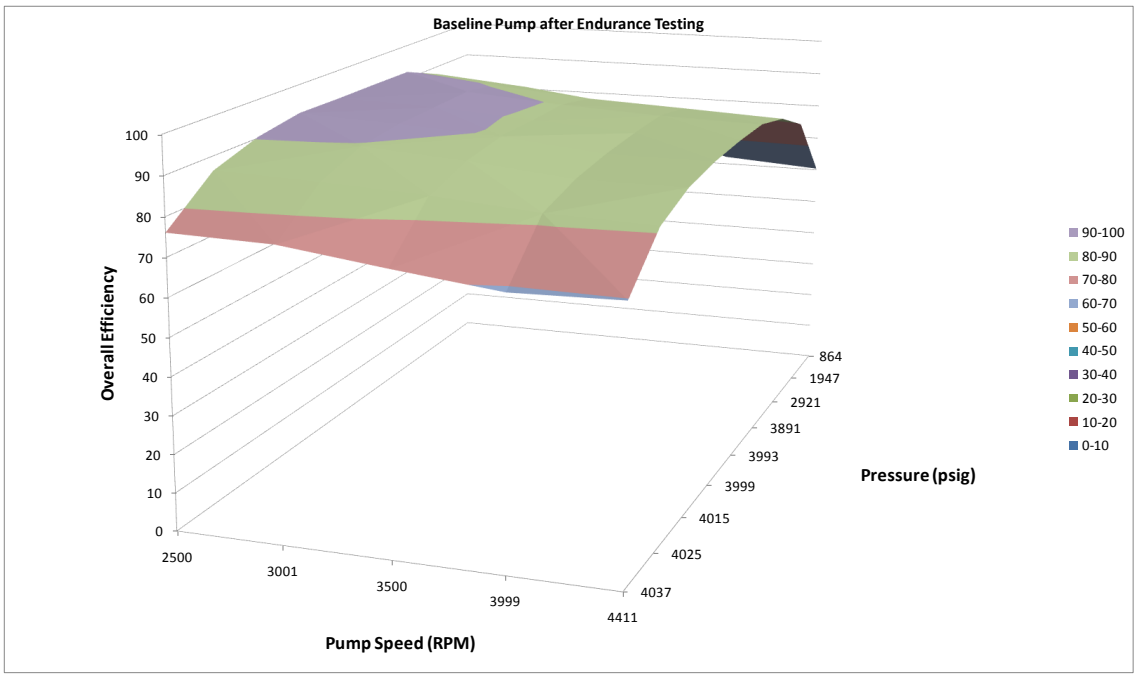

Figure 4.2.2-20: Performance of the baseline pump after calibration testing and a full-scale (280+-hour) durability schedule. Note that peak efficiency of the pump has dropped and that, in some pressures and speeds, the overall efficiency has dropped as low as 40 percent.

4.2.3 Friction and Wear Testing of PVD Films

The coating compositions covered under the scope of this project were evaluated using a advanced friction and wear tests in an effort to assess the durability of the films, the repeatability of processing parameters, and quantify the low-friction performance.

4.2.3.1 Tribosystem Analysis

Tribosystem analysis (TSA) is an organized means by which to characterize the environments under which materials come into contact under friction or wear-critical conditions. It comprises a problem definition that includes the geometry of contact, dimensions of parts, contact loads, sliding speeds for various operating conditions, lubricant identification and properties, operating temperatures, surface finishes, and analysis of the modes of wear and surface damage that are typically observed on the contacting parts in that tribosystem. Once a TSA is developed, it can also be used to select test methods to simulate operating conditions and screening candidate materials. **Figure 4.2.3-1a-c** shows the structure of the TSA form used in this project.

Using a format developed by P. Blau of ORNL, and with information provided by engineers at Eaton Corporation, TSAs were prepared for the following hydraulic pumps:

- Vane pump (vanes sliding on the internal diameter of the pump)
- Valve In Star (VIS) Motor/Pump – several interfaces within the pump section
- Piston pump – several interfaces including pistons, swash plate, and wear plate

Since the TSA contains information specific to certain of Eaton's commercial products, the above documents were shared with project team members, but are not included in this report. To support development of the VIS motor TSA, ORNL was also provided with a worn VIS motor for examination. An analysis of the surface damage, largely from rolling contact fatigue and abrasion by trapped wear debris, was prepared and circulated to the project team members in a six page supplemental (team members only) report dated June 18, 2008.

Tribosystem Analysis (TSA) Entry Form

Project Title		Component / Application	
Manufacturer(s)		Date of TSA	
Contact person (phone / e-mail)		Problem type:	[ ] product design [ ] field problem [ ] warranty issue [ ] other:

1.0 Hardware Configurations and Materials

(Diagram or schematic)
(A) Interface location 1
(Diagram or schematic)
(B) Interface location 2
(Diagram or schematic)
(C) Interface location 3

NOTES (optional):

(A) Interface location 1 – Component descriptions

Interface (A)	Triboelement A1	Triboelement A2
1.1 General contact geometry		
1.2 Triboelement shape and general dimensions		
1.3 Current material or surface treatment		
1.4 Surface finish on the contacting area (as-finished)		
1.5 Final finishing step (on the contact area)		

(insert tables for addityional locations 2 etc.)

Figure 4.2.3.1-1 (a): Tribosystem analysis form, Part 1.0 (generic).

2.0 Operating Environment

(The 'A', 'B', 'C' designations refer, respectively, to the Hardware Configurations in Part 1.0)

2.1 Type of relative motion (e.g., rolling, reversed sliding, unidirectional sliding, erosion, fretting, etc.)	A) B) C)
2.2 Speed of relative motion or duty cycle	A) B) C)
2.3 Contact load, contact pressure, or pressure x velocity (PV) product on the contacting surface	A) B) C)
2.4 Temperature(s) of operation, peak /average)	A) Peak pump temperature of 260F – average temperature of oil inside pump B) Peak pump temperature of 260F – average temperature of oil inside pump C) Peak pump temperature of 260F – average temperature of oil inside pump
2.5 Lubricants of interest	A,B,C)
2.6 Lubrication supply system (drip, full flooded, vapor, if any)	A) B) C)
2.7 Characterization of third bodies (e.g., debris, grit, abrasives contaminants, if any) that appear on worn parts	
2.8 Other operating conditions relevant to the problem (corrosion, vibration, etc.)	

Figure 4.2.3.1-1 (b): Tribosystem analysis form, Part 2.0 (generic).

3.0 Problem Description

3.1 Main concern(s)	[ ] friction reduction [ ] seizure avoidance [ ] wear reduction [ ] surface damage avoidance [ ] other: _____
3.2 Which triboelement(s) is/are experiencing the problem?	A) B) C)
3.3 Dominant surface altering process(es) or wear modes for each tribo-element*	A) B) C)
3.4 Metric(s) for wear used in the application, if any (e.g., lifetime, product contamination, clearance, visual criteria, mass loss, etc)	
3.5 Problem's impact on component performance	
3.6 Cost issues or constraints on material selection	

Attach images or supporting data:

Figure 4.2.3.1-1 (c): Tribosystem analysis form, Part 3.0 (generic).

4.2.3.2 Materials and Characterization Methods

A variety of materials, ranging from steel pump vane materials to $AlMgB_{14}$ coated surfaces were characterized and tested during the course of this project. The following methods were used:

a) Optical microscopy of surfaces and cross-sections of surfaces
b) Microindentation hardness testing
c) Micro-abrasion ball cratering for coating thickness
d) Friction and wear testing using a simple coupons
e) Friction and wear testing using parts cut from hydraulic parts
f) Full-scale hydraulic pump tests
g) Coated insert testing in machining trials of titanium and other metals
h) Scanning electron microscopy
i) X-ray Photoelectron Spectroscopy
j) Auger Electron Spectroscopy

Results of several of these are reported elsewhere in the final report for the entire ITP project. Specifically, method (f) was conducted at Eaton Corporation facilities, method (g) was used by Greenleaf Corporation, and methods (h)), (i), and (j) were used at Ames Laboratory. Sections 4.2.3.3, 4.2.3.4, and 4.2.3.5 describe the test methods performed at ORNL in support of this effort.

4.2.3.3 Microindentation hardness of coated surfaces

Traditionally, microindentation hardness tests of surfaces are obtained by slowly applying a normal load to an indenter, typically diamond that has been ground to a specific shape. After the indenter is allowed to rest on the surface under load for 5 to 25 seconds, typically, and then removed, a microscope is used to measure the diagonal length of the remaining impression. That dimension is used to calculate the microindentation hardness number. Two common scales are the Vickers and Knoop. The differences are that the Vickers is a four-sided pyramid that is slightly sharper than the Knoop indenter (which is an elongated pyramid). The latter was invented in 1938 to enable hardness testing of brittle materials in which the sharp Vickers indenter would produce undesirable cracking. The geometry of these indenters is described in ASTM E384.

Vickers hardness numbers (HV) are calculated based on load per unit facet area, but the Knoop hardness numbers (HK) are calculated from the load per unit-projected area of the impression. Equations used to calculate HV and HK implicitly assume that the indenter's ideal shape is exactly replicated on the surface being tested. Because most materials exhibit varying degrees of elastic shape recovery, depending on their elastic/plastic behavior, the HV and HK equations are not precise. However, they are commonly used without corrections for elastic recovery effects, effects that can become significant especially under low indentation loads and when the properties of materials vary with depth below the test surface. Note that so-called nanohardness is generally calculated using depth sensing rather than residual impression measurements by microscopy. These 'under-load' hardness numbers therefore should not be directly compared to microindentation hardness numbers without compensating for that difference in the measurement methodology.

The basic attributes of the Knoop and Vickers microindentation hardness test are given in **Table 4.2.3-1**. In the table, *P* is the load (in grams-force), *D* is the length of the impression diagonal (in micrometers), and *z* is the depth (in micrometers) of the impression based on the ideal indenter shape, neglecting elastic recovery. In HV testing, the diagonal length (D) is the average length of the two diagonals of the square-shaped impression. Whereas, in HK testing, the diagonal length (D) is that of the longer of two diagonals of the elongated diamond-shaped impression.

The form of the hardness equations is $H = C\ (P/D^2)$, where *C* is a geometric constant depending on indenter shape, hardness scale, and units.

Table 4.2.3.3-1: Comparison of Knoop and Vickers Microindentation Hardness Test Methods

	Knoop	Vickers
Constant *C* for HV or HK in units of GPa	139.6	18.19
Constant *C* for HV or HK in units of kg/mm^2	14229.	1854.4
Depth of penetration, z, relative to D	D / 30.52	D / 7.000
Depth of penetration, z, relative to HV or HK in GPa	0.387 (P/HK)$^{1/2}$	0.371 (P/HV)$^{1/2}$
Ratio of facet contact area to projected area	1.105	1.079

When a coating is applied to a surface, measurement of its indentation hardness becomes more complex. Unless the coating is so thick that it behaves as if it were a bulk material (i.e., the deposit thickness is many times the depth of indentation), the microindentation hardness number reflects the properties of a *material system* consisting of a coating atop a substrate. Factors affecting the numerical valves and repeatability of the results include the relative sizes of the impression depth and coating thickness, whether the coating is polyphase or single phase, the strength of the coating-substrate interface, and whether the elastic modulus and strength of the coating are less than, equal to or greater than those of the substrate. The residual stress state in the coating can also affect the resulting hardness number.

As shown in **Figure 4.2.3.3-1** the response of the material system to indentation reflects a combination of substrate and coating properties. Therefore, there is no such thing as the 'microindentation hardness of a coating' if the indentation depth is greater than a substantial fraction of the coating thickness. The hardness number is that for a material 'A' coated with a material 'B' under the prescribed conditions. Note that elastic recovery (ER) is typically greater in the vertical direction than in the horizontal direction, further distorting the impression shape compared with the shape of the indenter that produced it. In light of the foregoing considerations, the microindentation hardness data presented in Section 4.2.3.7 should be viewed with caution.

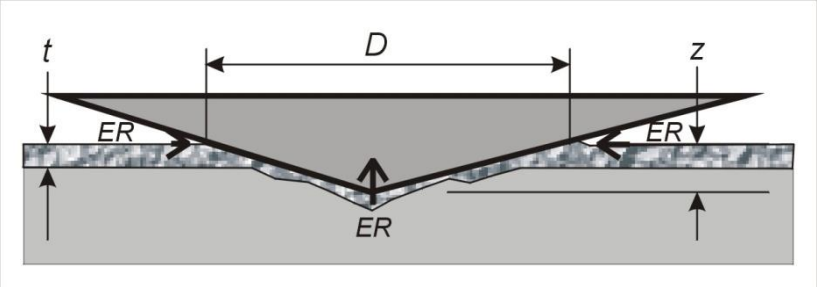

Figure 4.2.3.3-1: Indentation of a coating in which the depth of penetration (*z*) exceeds coating thickness (*t*). ER represents the elastic recovery of the impression once the indenter is removed.

4.2.3.4 Coating thickness measurement method

A bench-top, coating thickness measurement system based on micro-abrasion was received and set-up during this period. This equipment enables rapid and convenient measurements of coating thicknesses from approximately 0.2 to 10 micron. It is also suitable for thickness measurements on parts that have curved surfaces. A close-up view of the inclined ball resting on a test specimen is shown in **Figure 4.2.3.4-1** A few drops of special polishing slurry are placed on the ball and it is rotated for a fixed time or number of cycles. This produces a dimple containing an inner ring of exposed substrate. Three quantities are required to measure the thickness of the coating (*t*): the ball radius *R*, the outer diameter of the dimple d_o, and the inner diameter of the exposed substrate d_i. Thus:

$$t = \frac{1}{2}\left(\sqrt{4R^2 - d_i^2} - \sqrt{4R^2 - d_o^2}\right) \qquad (1)$$

Figure 4.2.3.4-2 shows a dimple in a specimen of $AlMgB_{14}$. A polished cross-section taken near the edge of the same specimen indicated a thickness of 2.2 microns, a very good agreement, considering that the coating could have been thinner nearer the edge of the specimen.

Figure 4.2.3.4-1: Motor drive unit with a 30 mm diameter ball used for micro-abrasion.

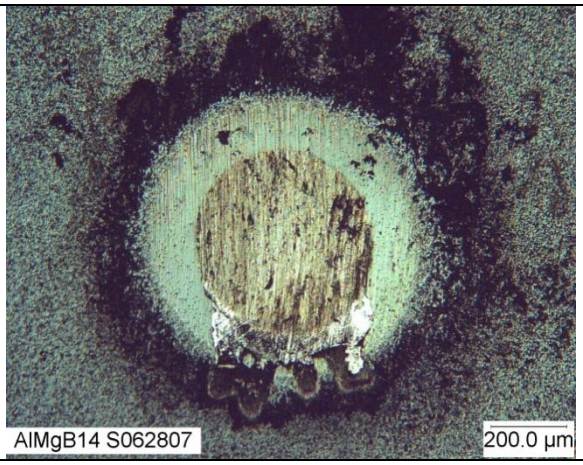

Figure 4.2.3.4-2: Dimple on a 2.51 micron-thick coating of $AlMgB_{14}$ prepared at Ames Lab.

4.2.3.5 Friction and wear test methods.

The following test methods were used in the course of this effort. The first two were rather basic laboratory-scale tests, and the second two were more simulative, using sections cut from actual hydraulic pump components:

(a) A fixed ball sliding against the surface of a rotating flat specimen, referred to as the pin-on-disk (POD)
(b) A fixed ball sliding against the surface of a linearly oscillating flat specimen, referred to as the reciprocating pin-on-flat (RPOF)
(c) A vane edge sliding against the outside diameter of a circular test ring (VEOR)
(d) An oscillating section of a piston sliding against a section of the barrel.
(e) An oscillating, rolling cylinder in a round socket against cross-oriented twin-cylinders.

Tests were run either dry or lubricated with a commercial hydraulic fluid, Mobil DTE-24, or a glycol-water mixture.

Pin on disk (POD) tests were generally run using a fixed AISI 52100 steel ball (9.525 mm diameter) as the slider. The typical applied load was 10 N and the sliding speed was 0.5 m/s. The duration of sliding, reported in meters of sliding distance, was varied depending on the frictional behavior and the need for longer test times to generate measurable wear. Wear volumes of balls and flats were measured using a Wyko (Veeco) model 9100 vertical scanning interferometer. The wear volume per unit applied load and per-unit sliding distance (mm^3/N-m) was reported as the wear rate.

Reciprocating pin on flat (RPOF) tests also used a fixed AISI 52100 steel ball (9.525 mm diameter) as the slider. The typical applied load was 1 or 5 N, and the sliding speed was 0.02 m/s (2.5 Hz, with a 4 mm stroke length). The duration of sliding was typically 10.2 m. Like the POD tests, RPOF tests used an interference method to map surfaces and obtain wear rates in units of (mm^3/N-m).

The vane-edge-on-ring geometry was developed in order to study the wear of the coatings against the interior surface of a vane pump. That geometry is shown in **Figure 4.2.3.5-1**. Steel test rings were heat treated by Eaton to attain the same hardened condition as the interior of the pump housing. A series of scoping tests in hydraulic fluid revealed that the conditions imposed were too severe to be used as a screening method for thin NAMB coatings. A drawback of the vane edge-on-ring was that lubricant could flow around the vane and therefore did not produce the kind of hydrodynamic conditions that forces vanes and bores apart in confined pump housing. A high rate of adhesive wear occurred on both the vanes and the rings, as well as a high level of noise and vibration. **Figure 4.2.3.5-2** shows metallic flakes, characteristic of severe adhesive wear, floating in the lubricant bath.

After a number of attempts to modify the test conditions for the project, the vane edge-on-ring test method was abandoned, and no data are reported for that configuration.

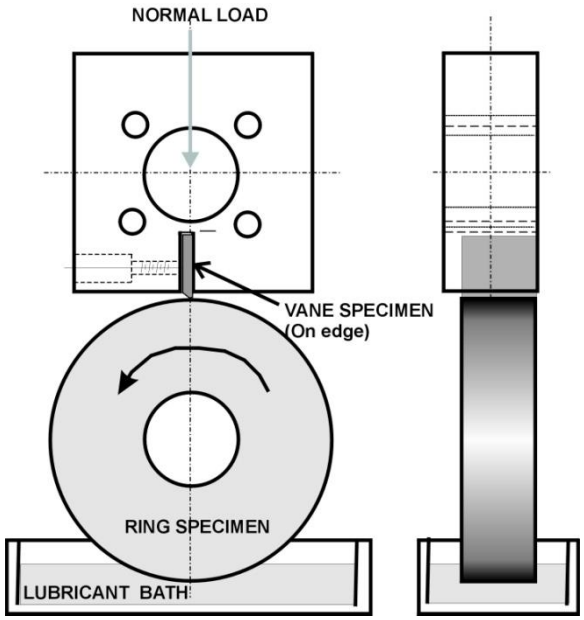

Figure 4.2.3.5-1: Vane edge of ring geometry.

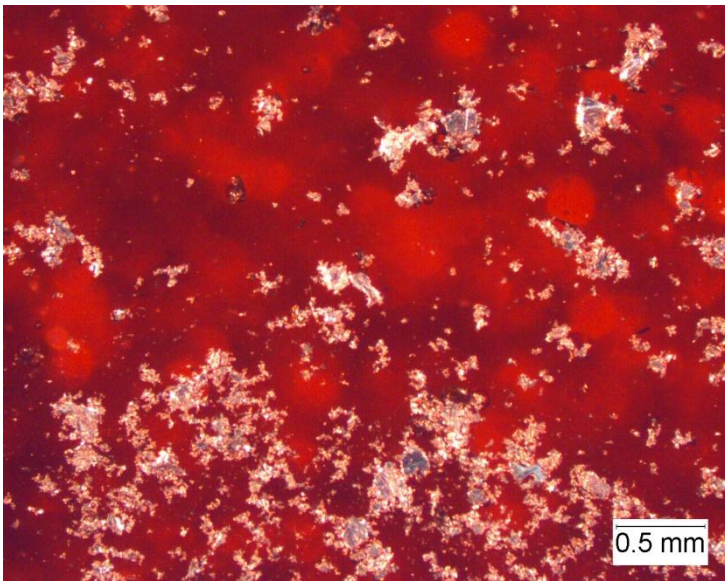

Figure 4.2.3.5-2: Metallic wear particles floating in the lubricant bath.

In addition to the POD and RPOF tests performed during Phase I, more simulative tests were developed and conducted in Phases II and III. These were based on the contact geometry and operating conditions that were listed in the TSAs for the components of interest. There were several objectives for these experiments: (a) to establish the friction and wear performance of the AMB coatings under two types of pumping fluids (Mobil DTE 24 and a water-glycol solution), (b) to determine the extent to which laboratory data would agree with pumping efficiency data from full-scale pumping tests, (c) to better understand the running-in and other transitional behavior of various nanocomposite coating combinations, and (d) to screen variants of the coating process to determine which held most promise for commercialization.

A bench test was designed and set up at ORNL to simulate the piston-bore interface in a piston pump, as shown in **Figure 4.2.3.5-3**. Load, speed, and temperature were selected to simulate the operating conditions in an actual piston pump. The resultant maximum PV value, 25000 psi*ft/min, in the reciprocating sliding test is in line with that for an actual piston pump, according to data from Eaton.

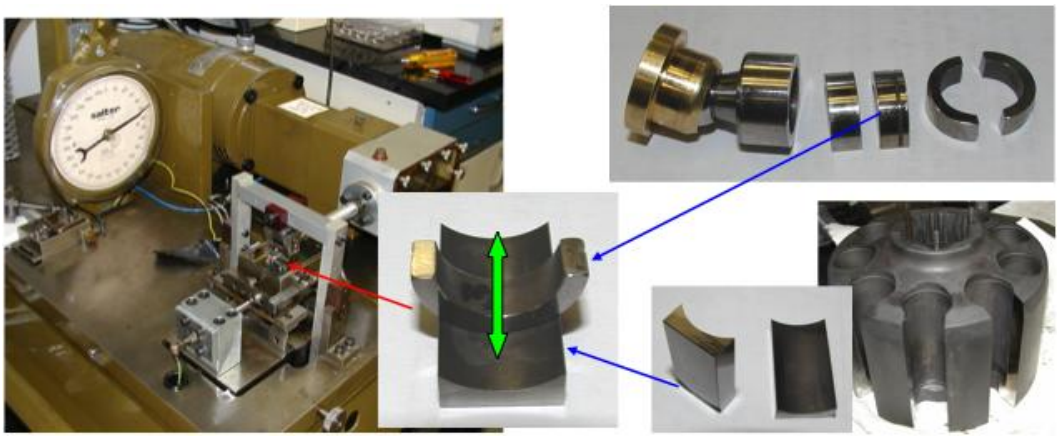

Figure 4.2.3.5-3: Setup of the bench test simulating the piston-bore interface in a piston pump.

Probably the most challenging of the simulative tests was one involving rolling combined with sliding as for the rollers the VIS motor, as shown in **Figure 4.2.3.5-4 (a).** Specimen holders on a Plint model TE-77 reciprocating wear machine were modified such that the top holder was cut from the roller groove of an actual VIS. An actual roller was inserted into this groove and allowed to roll or slide back and forth on two cross-oriented cylinders to simulate the 'star' component. This setup is shown in **Figure 4.2.3.5-4 (b).** This bench test is intended to simulate the startup (low-rpm) operation condition that is characterized by a reduced mechanical efficiency. Analysis of this situation is rather tricky because there are two tribocontacts of interest: (1) the rolling element in its groove, and (2) the rolling element against the 'star' (two cross-oriented cylindrical specimens in our experiments.) J. Qu of ORNL developed an analysis of the various cases in which rolling, sliding, or both occurred. For example, if the roller rolled on the bottom specimen, there would be slip between the roller and the groove. Alternatively, if the roller slides on the bottom specimen (no rolling), there might be no motion between the roller within its groove. Various combinations are possible. The challenge in controlling friction and wear is to minimize sliding unless the lubricating film thickness is great enough to avoid significant solid contact (hydrodynamic lubrication). If the component is operating under mixed, or worse, boundary lubrication, then protective coatings like AMB nanocomposites could mitigate the solid-on-solid situation, lowering wear and friction.

(a) Bearing interfaces in an actual VIS motor.

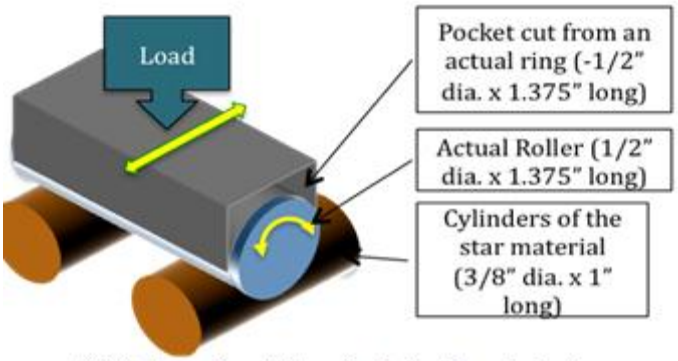

(b) Schematic of the simulated bench test.

Figure 4.2.3.5-4 (a) (b): Simulated bench test for VIS motor.

Observations of the experiments confirmed hypotheses about the simulation's validity and led to the development of slide-roll maps to reflect the interaction of the contact interfaces. In these maps (see, for example**, Figure 4.2.3.5-5**, the contact stress is plotted versus star rotation speed. Regions of acceptable and unacceptable performance, corresponding to different levels of friction coefficient, can be identified on such slide-roll maps. Low contact stress and high speed (lower left corner of the figure) combine to produce low friction and wear.

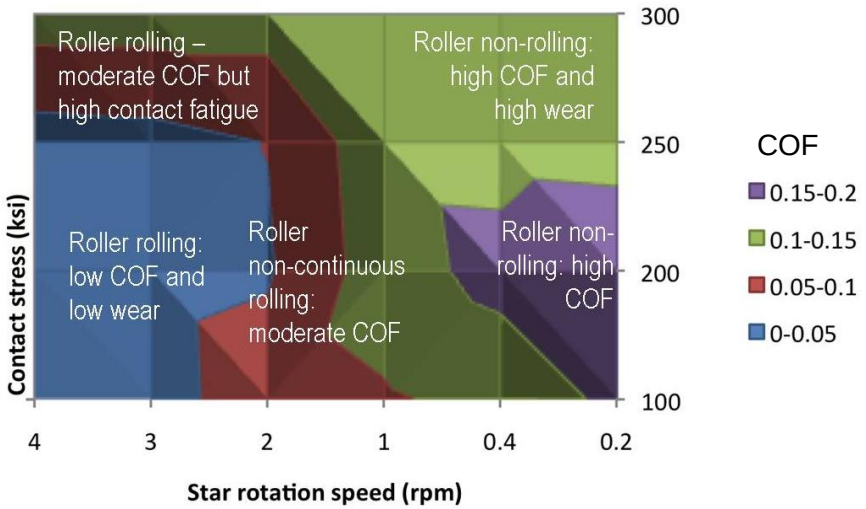

Figure 4.2.3.5-5: Slide-roll map developed at ORNL.

4.2.3.6 Tooling applications

A limited number of high-temperature pin-on-disk tests (400 ^{o}C and 800 ^{o}C) were performed on tungsten carbide and coated tungsten carbide (WC) to address a cutting tool application (cutting of aerospace Ti alloys). Test disks for these studies were provided by Greenleaf Corporation. Early tests of WC disks against pins of titanium alloy Ti-6Al-4V at 800 ^{o}C (load 60.33 N, speed 0.9 m/s, in air) produced severe degradation and macroscopic delamination of the surface of disk specimens, largely due to oxidation (see **Figure 4.2.3.6-1 (a)).** The nanocomposite coating protected the surface **(Figure 4.2.3.6-1 (b)).** It is concluded that the main benefit of coatings is to prevent oxidation of the WC under temperatures that are generated by the cutting process.

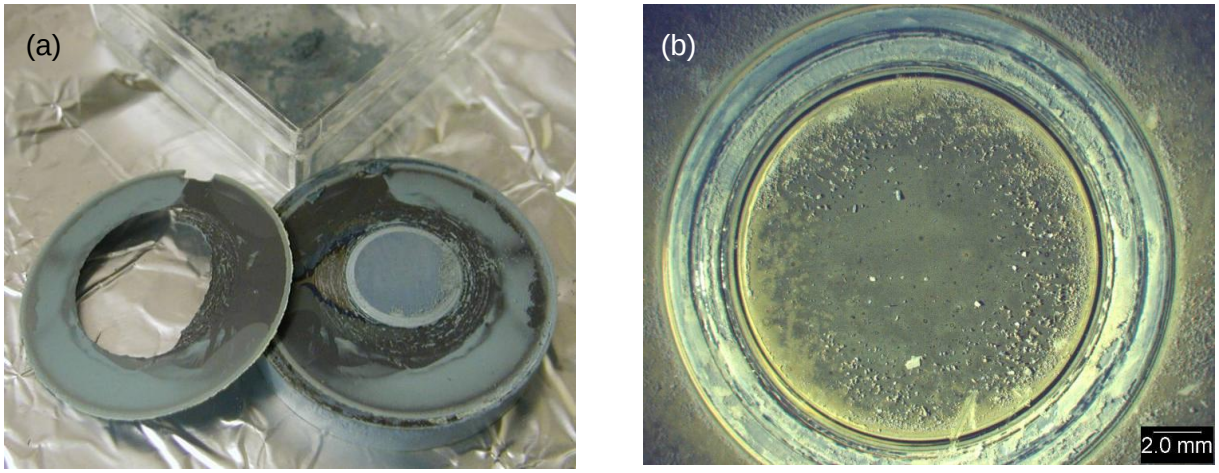

Figure 4.2.3.6-1((a) (b) The entire top surface of the uncoated WC-Co disk specimen delaminated during testing at 800^{o} C in air. (b) Although the Ti pin wore through the AMB, the non-worn areas protected the disk from atmospheric attack under the same conditions.

4.2.3.7 Coating Thickness and Hardness Measurements

The thickness of coatings was measured by Eaton Corporation by polished cross-sections and by ORNL using a ball-cratering method. Microindentation hardness numbers, subject to the limitations discussed in 4.2.3.3, were measured using the Knoop scale at 100 grams-force applied load. Surface roughness of the specimens, reported as an arithmetic average (Ra), was measured using a stylus profiling instrument. Results of these measurements are summarized in **Table 4.2.3.7-1**, along with ratios of parameters:

t / Ra = ratio of coating thickness to roughness
z / t = ratio of indentation penetration depth to coating thickness

The (*t/Ra*) ratio indicates how much thicker or thinner the coating was relative to the as-coated microgeometry of the surface. Low (*t/Ra*) ratios suggest that the coating follows the surface finish and might be prone to fail at the profile's peaks. The (*z/t*) ratio suggests the degree to which the properties of the substrate would influence the apparent hardness of the coating-substrate system (anvil effect). This latter quantity varied from about 0.19-0.75, with larger values indicating that the substrate properties had greater influence on the hardness number.

Table 4.2.3.7-1: Consolidated Thickness, Roughness, and Hardness Data for Nanocoatings.

Specimen	*t* (microns)	R_a (microns)	t/R_a	*HK* (GPa, 100 g-f)	*z* (microns)	*z/t*
M2 steel vane (no ctg)	n/a	0.18	n/a	9.4	1.26	
DLC + TiN interlayer	1.2	0.16	7.5	17.2	0.93	0.78
EB1065-HT $AlMgB_{14}$-TiB_2	3.8	0.16	23.8	29.1	0.72	0.19
DLC2	2.5	0.18	13.9	18.7	0.89	0.36
EB1071-LT $AlMgB_{14}$-TiB_2	3.0	0.17	17.6	19.8	0.87	0.29
EB1101 Ti-TiB_2	2.4	0.19	12.6	21.2	0.84	0.35
EB1106 $AlMgB_{14}$-TiB_2+high-C	3.1	0.21	14.8	11.0	1.17	0.38
EB1108 $AlMgB_{14}$-TiB_2+C, LT	3.8	0.20	19.0	11.1	1.16	0.31
EB1112 $AlMgB_{14}$-TiB_2+C-target	3.4	0.18	18.9	18.9	0.89	0.26
EB1114 $AlMgB_{14}$-TiB_2+C	2.5	0.15	16.7	10.3	1.21	0.48
EB1115 $AlMgB_{14}$-TiB_2+low-C	2.4	0.15	16.0	19.5	0.88	0.37
EB1107-HT $AlMgB_{14}$-TiB_2	2.6	0.18	14.4	25.2	0.77	0.30
EB1121-LT $AlMgB_{14}$-TiB_2	1.2	0.14	8.6	13.2	1.07	0.89
EB1124 $AlMgB_{14}$-TiB_2+C	3.2	0.16	20.0	12.8	1.08	0.34
EB1124 $AlMgB_{14}$-TiB_2+C on 52100 steel	2.7	0.13	20.8	16.4	0.96	0.35
EB1166 $AlMgB_{14}$-TiB_2+C on A2 steel	4.3	0.23	18.7	15.1	1.00	0.23
EB1166 $AlMgB_{14}$-TiB_2+C on M2 steel		0.17		15.1	1.00	
EB1174 $AlMgB_{14}$-TiB_2+C	4.5	0.14	32.1	13.3	1.06	0.24
EB1176 $AlMgB_{14}$-TiB_2+C	4.1	0.14	29.3	12.0	1.12	0.27

Pin-on-Disk Tribotest Results

Pin-on-disk friction and wear tests were conducted over a four-year period, and the results have been consolidated in **Table 4.2.3.7-2**, for Mobil DTE-24 test fluid, and **Table 4.2.3.7-3** for water-glycol test fluid. In this and subsequent tables, the 'vane' material was used for the rotating disk specimen and the pin was 52100 steel.

Table 4.2.3.7-2: Pin-on-Disk Tribotest Results for Specimens Tested in Mobil DTE-24.

Vane Material	Sliding Dist. (m)	Final COF	WR of Vane (mm^3/N-m)	Wear Rate of Ball (mm^3/N-m)
M2 steel vane	5,400	0.58	12.0x10-8	239x10-8
DLC on M2 (w/o TiN)	10,800	0.1	n/m*	0.6x10-8
DLC on M2 (w/ TiN)	10,800	0.14	n/m*	1.1x10-8
AlMgB14-TiB2 on M2 (EB1065)	10,800	0.14	n/m*	1.0x10-8
AlMgB14-TiB2 on M2 (EB1071)	10,800	0.08	n/m*	2.9x10-8
TiB2 on M2 (EB1101, vane #2)	11,100	0.07	n/m*	2.0x10-8
AlMgB14-TiB2+C on A2 (EB1166)	32,400	0.02	4.0x10-8	1.2x10-8
AlMgB14-TiB2+C on M2 (EB1166)	32,400	0.02	3.0x10-8	0.9x10-8
AlMgB14-TiB2+C (EB1174)	32,400	0.03	4.4x10-8	0.1x10-8
AlMgB14-TiB2+C (EB1176)	32,400	0.05	3.0x10-8	0.1x10-8
AlMgB14-TiB2+C (1186)	32,400*	0.04	7.6x10-8	0.80x10-8
AlMgB14-TiB2+C (1187)	32,400*	0.06	5.0x10-8	0.15x10-8
AlMgB14-TiB2+C (1188)	32,400	0.06	4.0x10-8	0.32x10-8
AlMgB14-TiB2+C (1189)	32,400	0.04	4.6x10-8	0.43x10-8
AlMgB14-TiB2+C (1190)	32,400	0.07	3.8x10-8	0.15x10-8
AlMgB14-TiB2+C (1191)	32,400	0.07	4.3x10-8	0.15x10-8
AlMgB14-TiB2+C (1192)	32,400	0.07	4.5x10-8	0.05x10-8

* n/m = not measurable (<1 x 10^{-7}), WR = wear rate, COF = coefficient of friction

Table 4.2.3.7-3: Pin-on-Disk Tribotest Results for Specimens Tested in Water/Glycol*

Vane Material	Sliding Dist. (m)	Final COF	WR of vane (mm^3/N-m)	WR of ball (mm^3/N-m)
M2 steel vane	1000	0.24	2.2x10-7	13.9x10-7
M2 steel vane	1000	0.61	3.6x10-7	19.5x10-7
DLC (w/ TiN)	1000	0.11	*n/m**	5.5x10-7
DLC (w/o TiN)	1000	0.1	(<0.5x10-7)	2.5x10-7
AlMgB14-TiB2 (EB1065)	1000	0.1		0.9x10-7
AlMgB14-TiB2 (EB1071A)	5400	0.02	0.8x10-7	0.6x10-7
AlMgB14-TiB2 (EB1071B)	5400	0.03	0.9x10-7	0.3x10-7
AlMgB14-TiB2 (EB1071B2)	5400	0.05	0.5x10-7	0.5x10-7
DLC (w/ TiN)	10800	0.04	*n/m**	0.3x10-7
AlMgB14-TiB2+lowC (EB1115)	5400	0.11	<0.5x10-7	0.5x10-7
AlMgB14-TiB2+C (EB1114)	5400	0.1	1.7x10-7	0.1x10-7
AlMgB14-TiB2+C-LT (EB1108)	5400	0.12	1.8x10-7	0.1x10-7
AlMgB14-TiB2+C-target (EB1112)	5400	0.1	<0.5x10-7	0.8x10-7
Ti-TiB2 (EB1101) (vane 1)	5400	0.24	0.7x10-7	0.5x10-7
Ti-TiB2 (EB1101) (vane 2)	5400	0.04	*n/m**	0.8x10-7

Final friction coefficients at the ends of the tests, as reported in **Tables 4.2.3.7-2** and **4.2.3.7-3** did not reflect the frictional variations observed during the tests. Sometimes, due to initial abrasion from the harder of the coated surfaces, the friction began higher and then settled to a lower value as the surfaces wore-in. Examples of friction coefficient versus sliding distance behavior are shown in **Figure 4.2.3.7-1.**

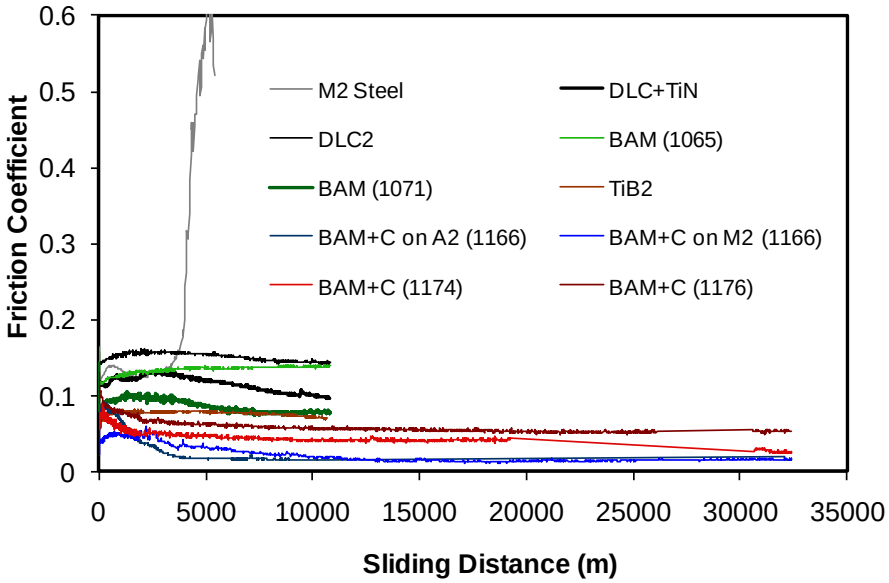

Figure 4.2.3.7-1: Friction coefficients exhibited running-in behavior. The lowest final friction coefficients were observed with long tests. Friction of the uncoated M2 steel rose quickly and the test was terminated.

4.2.3.8 Reciprocating Pin on Flat Tribotest Results

Table 4.2.3.8-1 shows a summary of reciprocating pin-on-flat tests. Since the reciprocating motion disturbs the lubricant regime and did not simulate the constant sliding direction in pumps, these tests did not prove to be as useful as the pin-on-disk results presented. Therefore, only a modest matrix was completed.

Table 4.2.3.8-1: Reciprocating Pin-on-Flat Tribotest Results for Dry Conditions and for Lubrication with Mobile DTE-24

	Lubrication conditions and test load			Vane WR	Pin WR
	(none)	(none)	DTE-24	(none)	(none)
	Load = 1 N	Load = 5 N	Load = 5 N	(mm^3/N-m)	(mm^3/N-m)
M2 steel vane	0.67	0.56	0.14	n/m*	3.57x10-5
Ames S062807	0.7		0.18	n/m*	11.0x10-5
Ames S072607	0.20 ~ 0.80		0.13	1.61x10-5	0.52x10-5
Ames S080907	0.21~ 0.72			0.55x10-5	3.96x10-5
Ames S091007	0.8			1.17x10-5	1.05x10-5
Ames S102307	0.81			1.03x10-5	0.54x10-5
Ames S111307	0.74			0.74x10-5	0.87x10-5
Eaton EB1038A	0.78			10.1x10-5	1.50x10-5
Eaton EB1039A	0.83			4.26x10-5	0.26x10-5
Eaton EB1065A	0.84			n/m*	1.66x10-5
Eaton DLC	0.21	0.18	0.12	n/m*	0.28x10-5
Ames SAM-L-TB-M1	0.16 ~ 0.98			1.39x10-5	0.21x10-5
Ames SAM-TB70-TC-M1	0.17~ 1.12			0.60x10-5	0.27x10-5

4.2.3.9 Results from Bench Tests to Simulate Components in Piston Pumps

Comparative friction tests for uncoated, DLC-coated, and $AlMgB_{14}$-TiB_2+C-coated pistons against the uncoated bores were carried out in the full temperature range and results are shown in **Figure 4.2.3.9-1.** Apparently, the $AlMgB_{14}$-TiB_2+C coating exhibited the best frictional behavior with friction reduction up to 60% compared to the uncoated production piston. The DLC coating, however, produced mixed results. Twenty-four hour wear tests were conducted to examine the long-term friction performance and coating durability. The friction coefficient for the $AlMgB_{14}$-TiB_2+C-coated piston produced consistently lower friction than the uncoated and DLC-coated ones along the test. The $AlMgB_{14}$-TiB_2+C coating had no measurable wear but mild polishing after the 24-hr wear test.

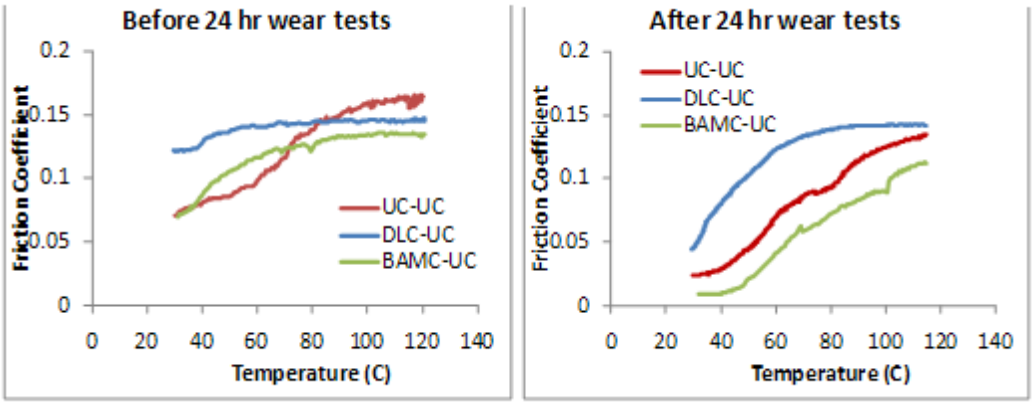

Figure 4.2.3.9-1: $AlMgB_{14}$-TiB_2+C-coated piston produced substantial lower friction compared with the uncoated and DLC-coated pistons over the full range of pump operation temperatures.

4.2.3.10 Results from Bench Tests to Simulate Components in VIS Motors

VIS-simulative rolling-sliding bench tests were carried out on three different material combinations as follows:

- Uncoated (UC)-Uncoated-Uncoated: uncoated steel ring, roller, and star,
- Uncoated-$AlMgB_{14}$-TiB_2+C-$AlMgB_{14}$-TiB_2+C: uncoated ring, $AlMgB_{14}$-TiB_2+C-coated roller, and $AlMgB_{14}$-TiB_2+C-coated star
- Uncoated-DLC-$AlMgB_{14}$-TiB_2+C: uncoated ring, DLC-coated roller, and $AlMgB_{14}$-TiB_2+C-coated star.

A series of contact pressure and sliding speed combinations were used to cover the full range of the startup operating condition for a VIS motor. Tests were conducted at room temperature and lubricated by Mobil DTE-24™ oil.

The combination of uncoated steel ring, DLC-coated roller, and $AlMgB_{14}$-TiB_2+C-coated pins (star material) showed significantly reduced traction (friction) compared to the conventional uncoated version, as shown in **Table 4.2.3.10-1** and **Figure 4.2.3.10-1**. Results suggest that the combination of DLC and $AlMgB_{14}$-TiB_2+C nano-coatings can substantially improve the startup efficiency for the VIS motor. The self-mated $AlMgB_{14}$-TiB_2+C contact, however, showed little benefit, and even underperformed the uncoated set under certain conditions (see **Figure 4.2.3.10-1**). This confirms our prediction that similar materials rubbing each other more likely causes friction and wear issues due to high adhesion at the interface.

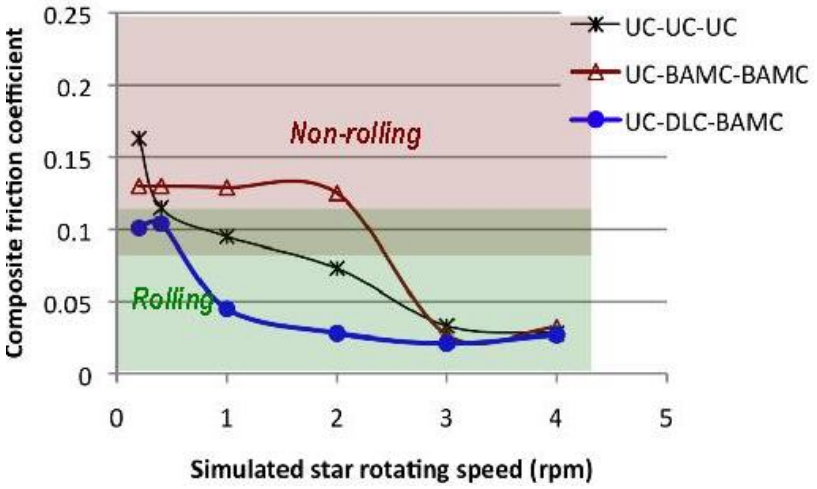

(a) Under a constant load of 10 N (109 psi)

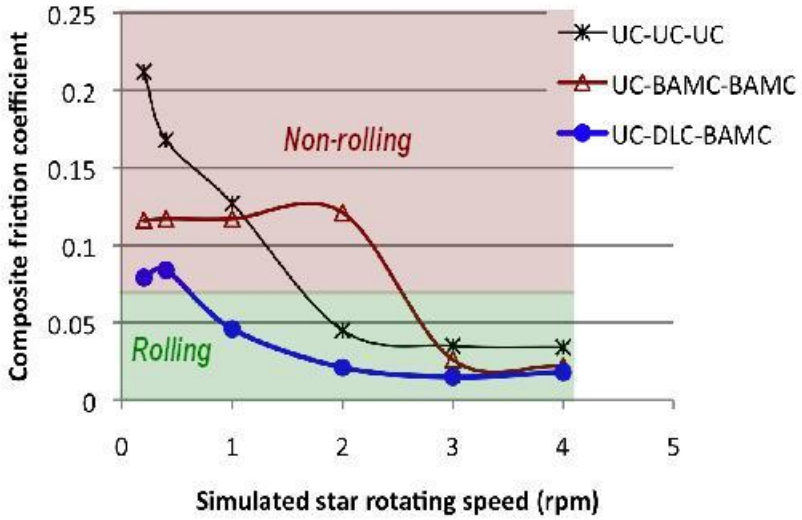

(b) Under a constant load of 60 N (198 psi)

Figure 4.2.3.10-1 Roller rolling status versus composite friction coefficient.

Table 4.2.3.10-1: Summary of results for the pin-on-twin bench test for VIS motors. Note that BAMC refers to the $AlMgB_{14}$-TiB_2+C coating.

Ring-Roller-Pin Materials		Uncoated-uncoated-uncoated		Uncoated-BAMC-BAMC		Uncoated-DLC-BAMC	
Load	Slid-Freq (Star w)	Roller rolling?	Comp. COF	Rolling?	COF	Rolling?	COF
10 N (109 ksi)	1 Hz (4 rpm)	Yes	0.028	Yes	0.032	Yes	0.027
	0.75 Hz (3 rpm)	Yes	0.033	Yes	0.027	Yes	0.021
	0.5 Hz (2 rpm)	Yes	0.073	No	0.125	Yes	0.028
	0.25 Hz (1 rpm)	Yes after re-aligned	0.095	No	0.129	Yes	0.045
	0.1 Hz (0.4 rpm)	Yes after re-aligned	0.115	No	0.130	No	0.104
	0.05 Hz (0.2 rpm)	Non-continuous	0.163	No	0.130	No	0.101
60 N (198 ksi)	1 Hz (4 rpm)	Yes	0.034	Yes	0.022	Yes	0.018
	0.75 Hz (3 rpm)	Yes	0.035	Yes	0.026	Yes	0.015
	0.5 Hz (2 rpm)	Yes	0.045	No	0.121	Yes	0.021
	0.25 Hz (1 rpm)	Non-continuous	0.127	No	0.117	Yes	0.046
	0.1 Hz (0.4 rpm)	No	0.168	No	0.117	No	0.084
	0.05 Hz (0.2 rpm)	No	0.212	No	0.116	No	0.079
120 N (249 ksi)	1 Hz (4 rpm)	Yes	0.027	Yes	0.042	Yes	0.023
	0.75 Hz (3 rpm)	Yes	0.033	Yes	0.052	Yes	0.022
	0.5 Hz (2 rpm)	Yes	0.051	No	0.116	Yes	0.033
	0.25 Hz (1 rpm)	No	0.133	No	0.113	Yes	0.056
	0.1 Hz (0.4 rpm)	*Not tested*		*Not tested*		No	0.082
	0.05 Hz (0.2 rpm)	No	0.124	No	0.112	No	0.081
200 N (295 ksi)	1 Hz (4 rpm)	Stopped rolling after 20s	0.069→0.123	No	0.115	Yes	0.024
	0.75 Hz (3 rpm)	*Not tested*		*Not tested*		Yes	0.031
	0.5 Hz (2 rpm)	*Not tested*		*Not tested*		Yes	0.046
	0.25 Hz (1 rpm)	*Not tested*		*Not tested*		No	0.084
	0.05 Hz (0.2 rpm)	*Not tested*		*Not tested*		No	0.083

4.2.3.11 Lubrication Modeling

Lubrication modeling was conducted at ORNL to gain mechanistic understanding of the friction and wear behavior for the bearing components in actual hydraulic systems to aid the coating development.

Background - lubrication regime analyses and lubricant film thickness calculation

There are three lubrication regimes, elastohydrodynamic (EHL), boundary (BL), and mixed (ML) lubrication, as illustrated by the Stribeck curve in **Figure 4.2.3.11-1**. Under EHL (low load and/or high velocity), the two solid surfaces are totally separated by a liquid lubricant film, resulting in a low friction and virtually no wear. The friction coefficient is entirely controlled by the lubricant viscosity and pressure-viscosity coefficient. Under boundary lubrication (high load and/or low velocity), the two solid surfaces are in contact and usually generate higher friction and more wear. The friction behavior is determined by the mechanical and thermal properties of both the solid and liquid in a synergistic effect. The ML falls in between EHL and BL and, because of the nature of a transition regime, the associated friction and wear are sensitive to the operation condition and material properties.

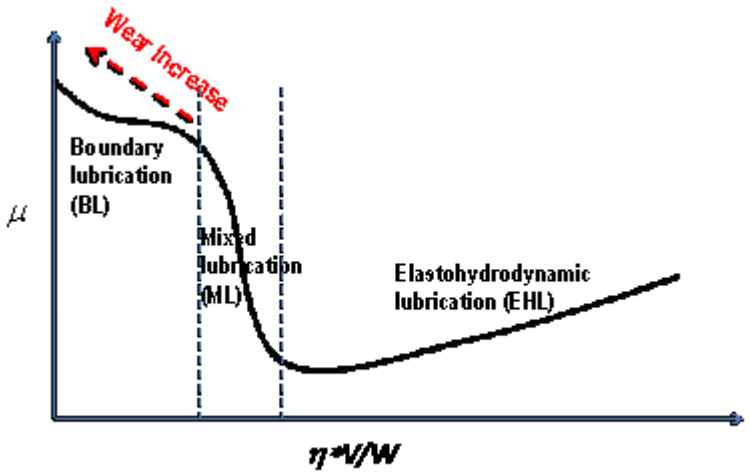

Figure 4.2.3.11-1: Stribeck curve illustrating the three lubrication regimes.

The ratio (λ) between the lubricant film thickness (h) and the composite roughness (σ) is usually used to determine the lubrication regime, as shown below:

$$\lambda = \frac{h}{\sigma} \qquad \begin{cases} \lambda \le 1, & BL \\ 1 < \lambda \le 4, & ML \\ \lambda > 4, & EHL \end{cases} \tag{1}$$

The composite roughness is defined as $\sigma = \sqrt{\sigma_1^2 + \sigma_2^2}$, where σ_1 and σ_2 are the RMS roughness of the two contact surfaces, $\sigma_1 = R_{q,1}$ and $\sigma_2 = R_{q,2}$.

The lubricant film thickness can be calculated using the Hamrock and Dowson formulas. For example, Equations (2) and (3) compute the minimum film thickness in the contact area for a Hertzian point contact and a Hertzian line contact, respectively.

$$h_{point} = \frac{3.63U^{0.68}G^{0.49}}{W^{0.073}}[1 - e^{-0.68\kappa}] \cdot R_x \tag{2}$$

$$h_{line} = \frac{2.65U^{0.7}G^{0.54}}{W^{0.13}} \cdot R_x \tag{3}$$

Where W, U, G,κ, R_x, R_y E' *are dimensionless parameters as expressed below.*

$$\text{Load: } W = \frac{w}{R_x^2 \cdot E'}$$

$$\text{Speed: } U = \frac{\eta_0 \cdot (u_1 + u_2)}{2R_x \cdot E'}$$

$$\text{Material: } G = \alpha \cdot E'$$

$$\text{Ellipticity: } \kappa = 1.0339 \left(\frac{R_y}{R_x}\right)^{0.636}$$

$$\text{Effective Radii: } R_x = \frac{R_{1x} \cdot R_{2x}}{R_{1x} + R_{2x}}, \; R_y = \frac{R_{1y} \cdot R_{2y}}{R_{1y} + R_{2y}}$$

$$\text{Composite modulus of elasticity: } E' = \frac{2}{\frac{1-\nu_1^2}{E_1} + \frac{1-\nu_2^2}{E_2}}$$

Where:
w – Normal load
η_0 – Atmospheric absolute viscosity
α – Viscosity-pressure coefficient
u_1, u_2 – Surface velocities of the two surfaces in x direction
R_{1x}, R_{2x} – Radii of the two surfaces in x direction
R_{1y}, R_{2y} – Radii of the two surfaces in y direction
E_1, E_2 – Modula of elasticity of the two surfaces
ν_1, ν_2 – Poisson ratios of the two surfaces

Case study – analysis of the low start-up efficiency for VIS motors

According to the field experience at Eaton Corp., the VIS motor mechanical efficiency has strong relation to the motor rotation speed and drops linearly when the speed is below 4 rpm (at start-up), as shown in **Figure 4.2.3.11-2** Lubrication modeling was conducted at ORNL to understand the mechanism and provide potential solutions.

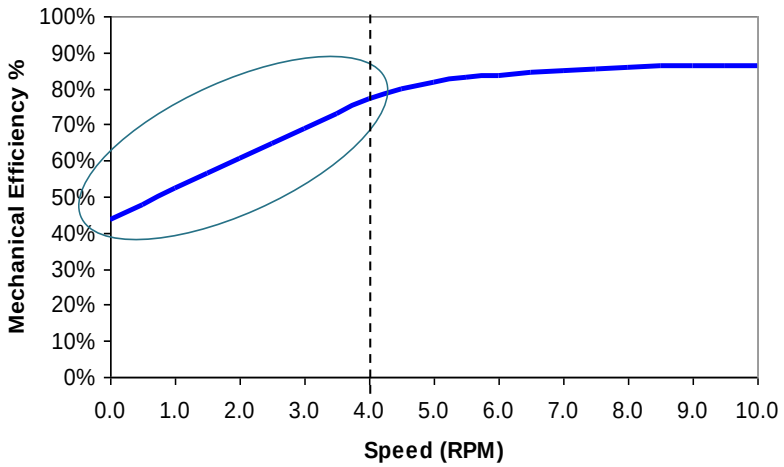

Figure 4.2.3.11-2: VIS motor suffers low mechanical efficiency at start-up.

The VIS motor mechanical efficiency is mainly affected by the friction forces at two sets of interfaces: (1) the star against rollers and (2) rollers against the ring pockets. The friction coefficient at each interface is determined by the lubrication regime, motion mode (rolling or sliding), surface textures, and the materials.

The individual and composite roughness values for the star-roller and roller-ring contacts are shown in **Table 4.2.3.11-1.** Given the VIS motor operation parameters, the lubricant film thickness and λ-ratio at the star-roller and roller-ring interfaces (both in line contacts) were calculated for three VIS motor operating conditions: 0.1 and 4 rpm at the start-up and 440 rpm at the nominal operation, as shown in **Table 4.2.3.11-2.**

Table 4.2.3.11-1: Roughness of the star, rollers, and ring pockets.

	Star	Roller	Ring
Roughness R_q (μm)	0.406	0.058	0.316
	Star-Roller	Roller-Ring	
Composite roughness σ (μm)	0.41	0.32	

Table 4.2.3.11-2: Lubricant film thickness and λ-ratio at the star-roller & roller-ring interfaces

Motor operation condition	Star-Roller		Roller-Ring	
	t (μm)	λ	t (μm)	λ
0.1 rpm @ RT	~0.002	<1 (BL)	~0.02	<1 (BL)
4.0 rpm @ RT	~0.02	<1 (BL)	~0.38	~1 (ML)
440 rpm @ 180 °F	~0.15	<1 (BL)	~2.15	>4 (EHL)

At the start-up, when the star rotation speed is lower than 4 rpm, both the star-roller and roller-ring interfaces are under BL and experience relatively high friction. The high friction at the roller-ring contacts causes a high slip ratio at the star-roller contacts. Therefore, a relatively high torque is required to overcome the BL sliding friction forces (typical coefficient of friction (COF) in the range of 0.05-0.15). This results in a low mechanical efficiency. Reducing the BL COF for the star-roller and/or roller-ring contacts is the key to increase the start-up mechanical efficiency.

When the star rotation speed more than 4 rpm, the star-roller contacts are still under BL (high friction) but the roller-ring contacts transition to ML or EHL (low friction). The nearly free spinning of the rollers in the ring pockets enables a low slip ratio at the star-roller contacts. As a result, a much lower torque is needed to overcome the rolling friction forces (typical COF<0.05) dominated at the star-roller contacts and the ML/EHL sliding friction forces at the roller-ring contacts (typical COF<0.05). This explains why the VIS motor reaches its high mechanical efficiency only after the motor runs at >4 rpm.

The lubrication analyses successfully explained the low-efficiency issue at startup for VIS motors. Furthermore, based on the observation of the $AlMgB_{14}$-TiB_2+C coatings' low friction behavior at in the POD tests (BL), we predicted the $AlMgB_{14}$-TiB_2+C coatings to improve the start-up mechanical efficiency for the VIS motor by allowing rollers rolling on the star at a lower speed and reducing the roller-star sliding friction, as illustrated in **Figure 4.2.3.11-3.** This was later validated in the simulated bench test, as shown in **Figure 4.2.3.10-1** and **Table 4.2.3.10-1**, and confirmed by dynamometer tests at Eaton Corp., as shown in **Figure 4.2.3.11-4.**

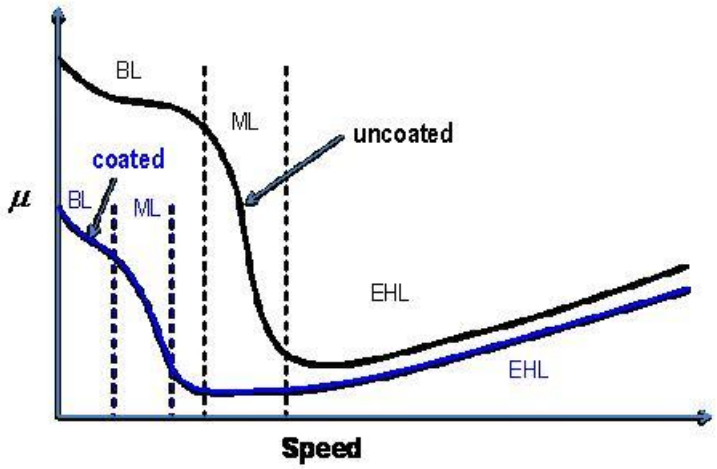

Figure 4.2.3.11-3: Modeling predicted friction reduction matching the experimental results. (In Figure 4.2.3.10-1).

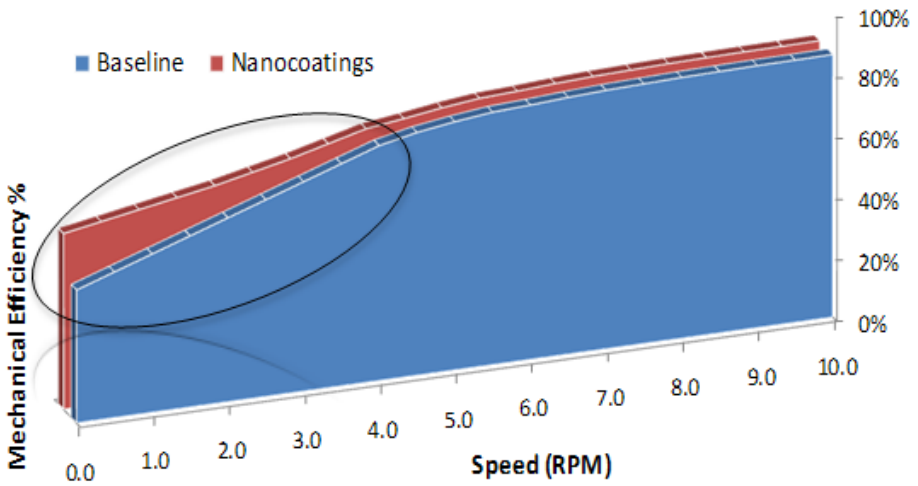

Figure 4.2.3.11-4: Results of dynamometer tests at Eaton confirmed the efficiency improvement by nanocoatings for VIS motors.

4.2.4 Characterization of PVD Films

During the course of this project, a critical task was the characterization of coatings and the establishment of a correlation between chemistry and coating morphology with friction and wear behavior. While development of a robust equivalent of the Thornton structure-zone model, adapted for the $AlMgB_{14}$-TiB_2 coatings, was beyond the scope of this project, a clear correlation was established between coating chemistry, morphology, and wear behavior. This correlation is expected to serve as the groundwork for future quality assurance standards for performance of production-grade components. Included among the array of characterization methods were x-ray diffraction (XRD), Auger electron spectroscopy (AES), X-ray photoelectron spectroscopy (XPS), and scanning electron microscopy (SEM).

4.2.4.1 Early characterization of $AlMgB_{14}$-TiB_2 physical vapor deposition batches

Detailed multi-level characterization of PVD coatings began with the selection of coated vanes representing three distinct process variations. These coatings, identified as batch 1065, 1067, and 1068 were produced from a hot pressed target of $AlMgB_{14}$-70 wt. % TiB_2. In the case of batch 1065, the deposition was performed using only the mixed phase boride target, while batch 1067 was produced by sputtering in an acetylene atmosphere and batch 1068 involved use of a second target of graphite. The latter two batches were designed to introduce carbon into the coatings for improved toughness. A series of SEM micrographs of the as-deposited coatings is shown in **Figure 4.2.4.1-1.**

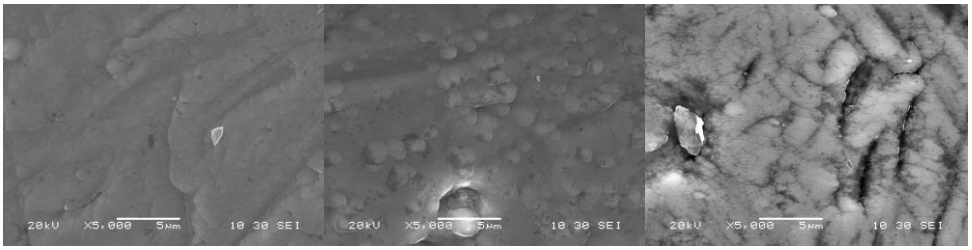

Figure 4.2.4.1-1: SEM micrographs of PVD-coated M2 vanes. From left to right: batch 1065 ($AlMgB_{14}$-70 wt. % TiB_2), 1067 ($AlMgB_{14}$-70 wt. % TiB_2 + C (gas)), and 1068 ($AlMgB_{14}$-70 wt. % TiB_2 + C (solid)).

The micrographs show a significant difference in morphology among the three coatings, the batch 1065 characterized by a relatively smooth, layered surface, whereas batch 1067 is comprised of discrete particles and batch 1068 contains particles and elongated ribbons. Coated vanes from the three batches were analyzed by x-ray diffraction to observe phases present in the coatings. **Figure 4.2.4.1-2** shows the x-ray pattern obtained from the as coated vanes, along with the pattern from a non-coated vane. Broad peaks are observed at ~ 27 degrees and 56 degrees. These peaks appear strongest in the 1065 vane in which no C was deposited. The peak positions of $AlMgB_{14}$, TiB_2, and $MgAl_2O_4$, the four phases typically seen in bulk $AlMgB_{14}$- TiB_2 composites, are presented for comparison.

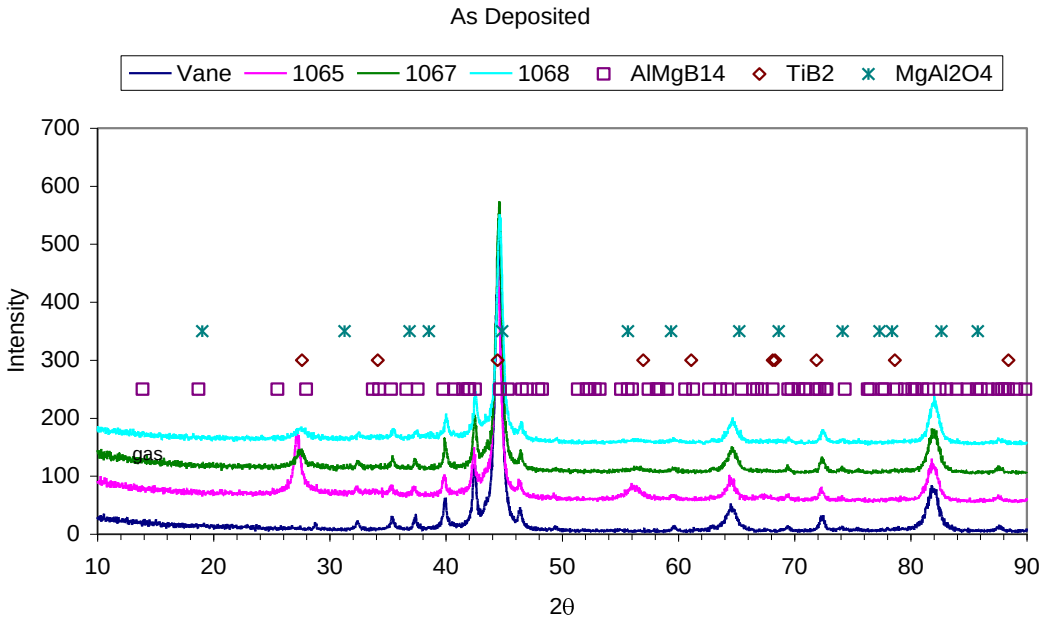

Figure 4.2.4.1-2: X-ray diffraction patterns of as-deposited PVD coatings from batch 1065, 1067, and 1068.

A vibrating probe was used to introduce damage on each of the films, and the results are shown in **Figure 4.2.4.1-3**

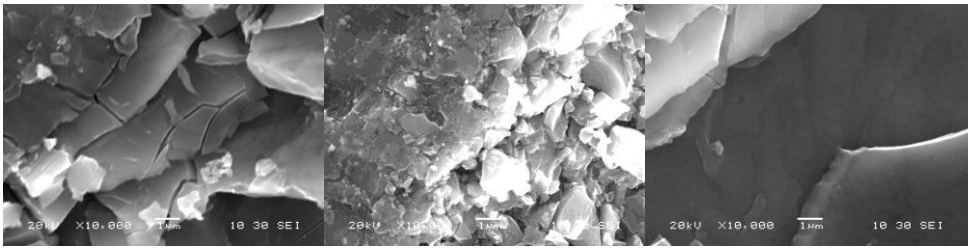

Figure 4.2.4.1-3: SEM micrographs of the films shown in Figure 4.2.4.1-1 after contact with a vibrating probe. (The order of the films is the same as shown in Figure 4.2.4.1-1)

While not a quantitative test, the probe introduces damage to a region of the film and provides an indication of the relative resistance to brittle fracture. As seen in the micrographs, the batch 1065 film appears to exhibit more widespread fracture, whereas damage in the batch 1067 film is more localized and on a finer scale. This roughly correlates with the results of step-loading tests in which the 1067 coating showed excellent performance, whereas the 1065 coating did not.

In order to assess the thermal stability of the coatings, each was sealed in quartz and heat treated for 2 hours at a temperature of 600°C. SEM micrographs of the heat-treated coatings are shown sequentially in **Figure 4.2.4.1-4**

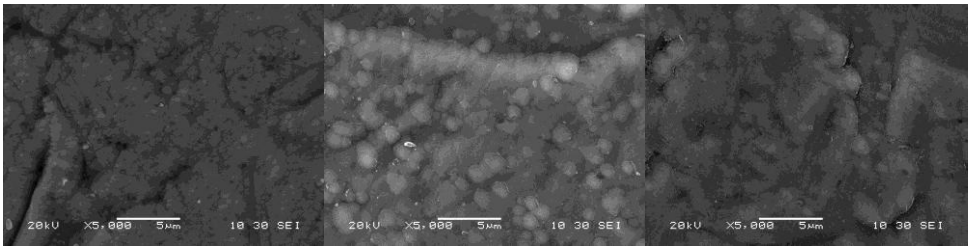

Figure 4.2.4.1-4: SEM micrographs of the films shown in Figure 4.2.4.1-1 after heat treatment at 600°C for 2 hours in argon.
(The order of the films is the same as shown in Figure 4.2.4.1-1)

As seen in the figure, the 600°C heat treatment had virtually no observable effect on the surface morphology, revealing a high degree of thermal stability in these coatings. A subsequent test with the vibrating probe also showed no observable difference with respect to the as-deposited coatings. The batch 1065 and 1067 coatings were again sealed under argon in quartz tubes and heat treated for an additional 2 hours at 1000°C. While 1000°C falls well outside of the anticipated operating conditions for hydraulic pumps, the purpose of this study was to induce crystallization of the amorphous coating and then determine if the same relative toughness is observed. After the 1000°C heat treatment, a significant difference in morphology was observed, as shown in **Figure 4.2.4.1-5.** These micrographs were particularly informative in that significant cracking was observed in the batch 1065 coating whereas almost no cracking was seen in the batch 1067 coating, confirming the improved fracture toughness of the latter.

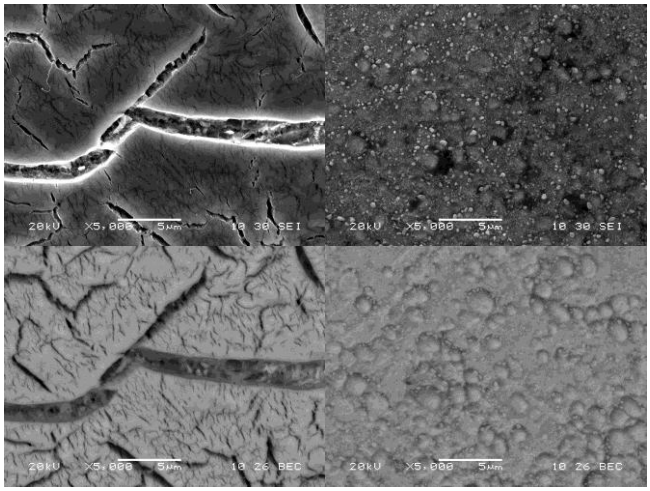

Figure 4.2.4.1-5: SEM micrographs of the films shown in Figure 4.2.4.1-1 after heat treatment at 1000°C for 2 hours in argon.
(left: batch 1065; right: batch 1067)
(top: secondary electron imaging; bottom: backscattered imaging)

As the Nanocoatings project advanced from proof-of-concept deposition studies to actual performance trials in hydraulic pumps and advanced machine tooling, an understanding of the chemistry of the coatings and its relationship to that of the target materials became essential to process optimization. For example, some coatings showing relatively poor wear resistance were found to contain elevated levels of oxygen or other contaminant phase. In support of this effort, a significant number of PVD coatings were characterized by x-ray photoelectron spectroscopy, a surface analysis technique highly sensitive to light elements, including boron. Initially, four PVD coatings were examined along with a baseline $AlMgB_{14}$ coating prepared by PLD. **Table 4.2.4.1-1** lists the measured concentration in atomic percent of several early PVD coated vanes, in addition to a baseline AlMgB14-coated vane (no TiB2) prepared by PLD. Since the coatings were first sputtered with argon ions under high vacuum before acquisition, the x-ray signals were generated from an estimated depth of 50 to 100 nm into the coating.

Table 4.2.4.1-1: Results of XPS characterization of PVD and PLD films (in atomic %)

Element	Eaton 1065 PVD	Eaton 1071 LT	Eaton 1081 HT	Eaton 1101	Ames B081908
Boron	61.48	58.13	28.49	39.23	75.87
Carbon	6.23	5.69	12.7	13.24	3.08
Oxygen	10	15.24	33.99	21.68	13.3
Magnesium	1.1	0.97	4.75	0	3.98
Aluminum	3.03	2.37	4.92	0	3.52
Titanium	17.68	17.21	13.22	25.01	0
Iron	0.27	0.38	1.95	0.84	0.25
	AlMgB14+TiB2 (HT)	AlMgB14 + TiB2 (LT)	AlMgB14+TiB2+C (HT)	Ti/TiB2 (HT)	baseline AlMgB14

Batch 1081 was prepared with carbon from acetylene gas and reflects a higher concentration than the other coatings. Oxygen concentration is also seen to be relatively high in some of the PVD coatings. The PLD film is seen to replicate the composition of the $AlMgB_{14}$ target closely. Since XPS proved early on to be an invaluable tool for determining the surface chemistry of the coatings, its use was expanded for a more detailed analysis of PVD coatings in an effort to understand the mechanisms responsible for the extremely low friction coefficients measured by Oak Ridge. For example, the wear tracks of coatings following pin-on-disk testing at Oak Ridge were examined for evidence of tribo-chemical reactions with the lubricants. Coatings studied

included two mixed-phase boride coatings ($AlMgB_{14}$ – 50 wt. % TiB_2) from batch 1071, one DLC coating with a TiN interlayer, and one TiB_2 coating with a Ti interlayer (EB1101), all deposited at Eaton by PVD on M2 steel substrates. A summary of the pin-on-disk tribo tests on these coatings at Oak Ridge is shown in the following table.

Table 4.2.4.1-2: Pin-on-disk results for PVD nanocoatings tested at ORNL and subsequently examined by XPS and AES.

ID	Lubricant	Distance (m)	COF	Wear on disk	Wear on pin
24 DLC w/ TiN interlayer	DTE-24	10800	0.10	n/m	1.1E-08
26 $AlMgB_{14}$-TiB_2 (EB1071A)	DTE-24	10800	0.08	n/m	
25 $AlMgB_{14}$-TiB_2 (EB1071A)	Water glycol	5400	0.02	7.5E-08	5.6E-08
32 TiB_2 + Ti (EB1101)	Water glycol	5400	0.24	7.2E-08	4.9E-08

Detailed characterization of each coating is described in the following sub-sections.

4.2.4.2 DLC in DTE-24

Little observable change in topology was observed within the wear scar, although localized regions of Fe contamination from the pin were detected, as seen in the backscattered image in **Figure 4.2.4.2-1**. The scratches and valleys seen within the wear tracks are also observed on the as-deposited surfaces and correspond to surface roughness of the M2 substrate. XPS depth profiles reveal only carbon and oxygen at the surface, with the oxygen signal quickly diminishing as the coating was etched to a depth of tens of nm. A typical XPS signal from just below the surface is shown in **Figure 4.2.4.2-2.**

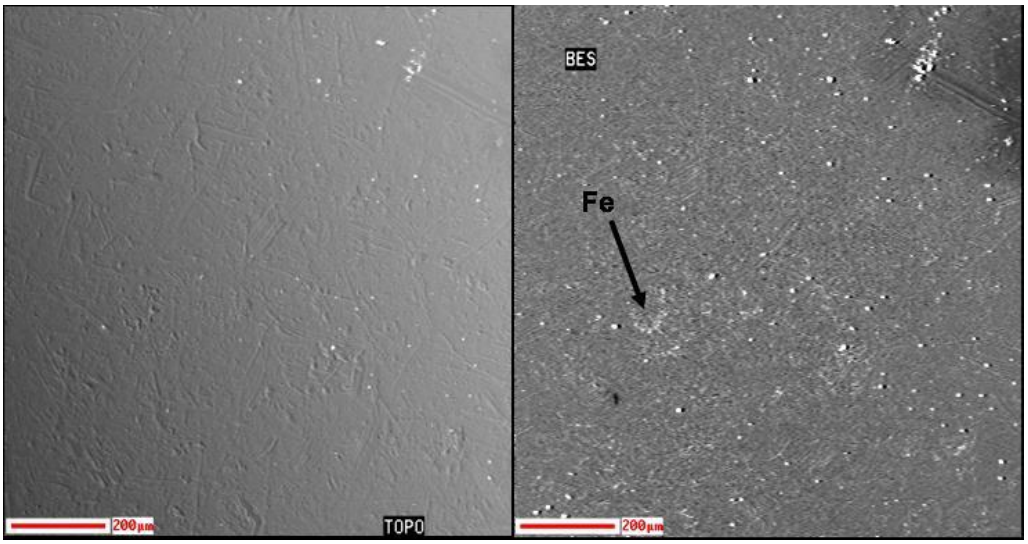

Figure 4.2.4.2-1: Topographical (left) and backscattered images obtained near the center of the wear track on DLC coating 24 after pin on disk testing.

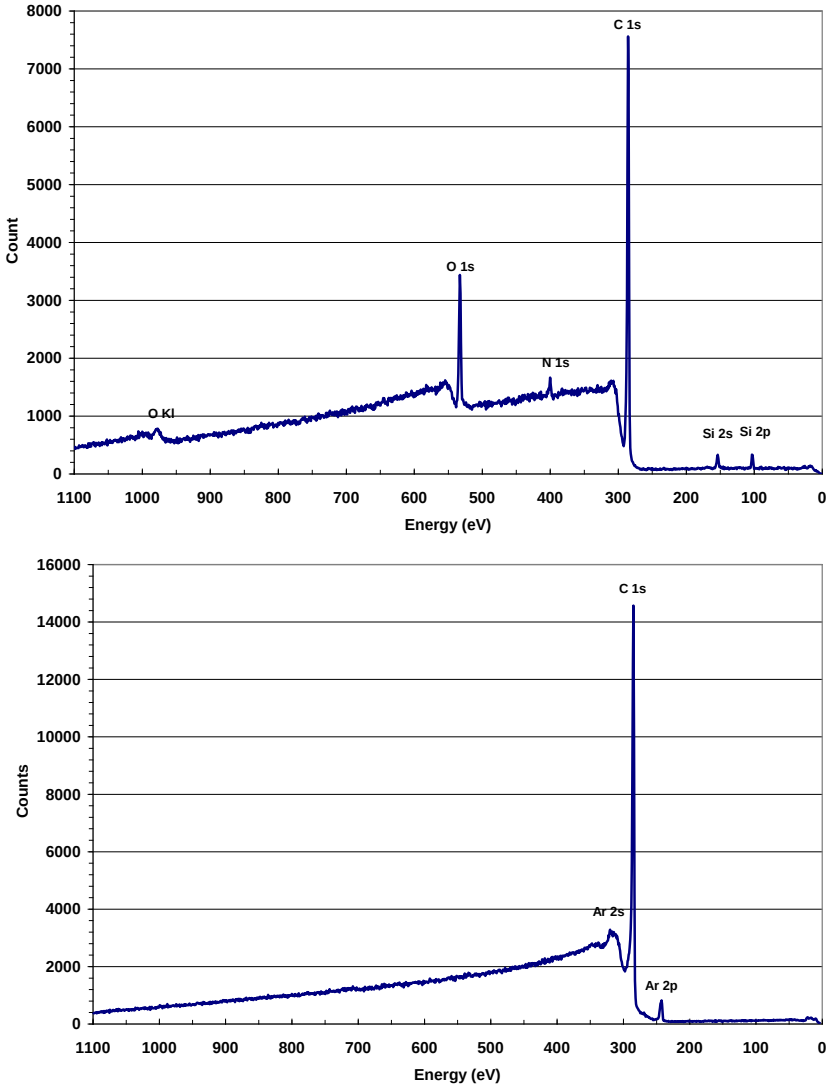

Figure 4.2.4.2-2: XPS signal from DLC coating centered on the wear track after 0 (top) and 15 minutes (bottom) of etching.

The tribological behavior of DLC is dependent on the testing environment. A low-friction condition requires passivation of dangling surface bonds, as the presence of hydrogen has been shown to reduce COF [11]. Atomic hydrogen desorbs relatively easily in air or vacuum ($\varepsilon = 1$) and in other low dielectric constant (ε) environments, lubricating the surfaces in contact. Desorption of hydrogen is inhibited by water vapor and other high- ε environments leading to higher COF values. The dielectric constant of water-glycol is within the range 35 to 80, which is considerably higher than that of typical petroleum-based oils ($\varepsilon_{oil} \sim 2 - 3$), therefore a lower COF is expected in DTE-24 than in water-glycol.

4.2.4.3 $AlMgB_{14}$ -TiB_2 in DTE-24

The wear track was difficult to discern in this specimen. **Figure 4.2.4.3-1** shows topographical (left) and compositional (right) images of a section of the wear track. The only visible indication of the wear track is a slight darkening in the topographical image as a result of reduced surface roughness during the POD test, and a bright contrast band in the compositional image that corresponds to iron transfer from the pin. The higher hardness of the mixed phase boride coating is more abrasive than the DLC coating and thus resulted in an increase in wear on the pin.

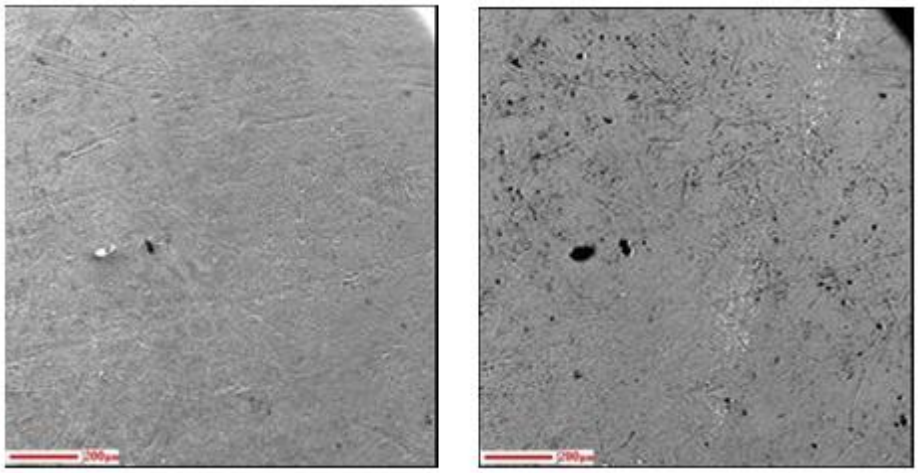

Figure 4.2.4.3-1: Topographical (left) and compositional (right) images of a section of the wear track of $AlMgB_{14}$- TiB_2 tested in DTE-24.

An XPS compositional profile centered on the wear track is shown in **Figure 4.2.4.3-2**, in which enrichment in oxygen can be seen just below the surface. A sputtering time of 10 minutes roughly corresponds to a depth of 30 to 50 nm. By scanning the range of emitted electron energies at a fixed depth, it was possible to associate peaks in the XPS signal with the unique binding energies and bonding environments of specific molecular compounds, thus providing a means of chemical identification. **Figure 4.2.4.3-3** shows an example of one such energy profile within the wear track of this coating, in which distinct peaks are observed at 188 eV, 193 eV, and 193.5 eV, corresponding to B, B_2O_3, and $B(OH)_3$, respectively. It is the presence of boric acid, $B(OH)_3$, that is believed to be responsible for the low COF observed in these tests. Crystalline boric acid consists of layers of $B(OH)_3$ molecules held together by van der Waals bonds, similar to MoS_2 and WS_2. The weak van der Waals bonding causes boric acid molecules to form parallel layers in the solid state, which can slide over one another providing a highly lubricious surface, much like a deck of cards. The strong bonding within each layer of boric acid prevents direct contact between the coating and the pin, minimizing wear.

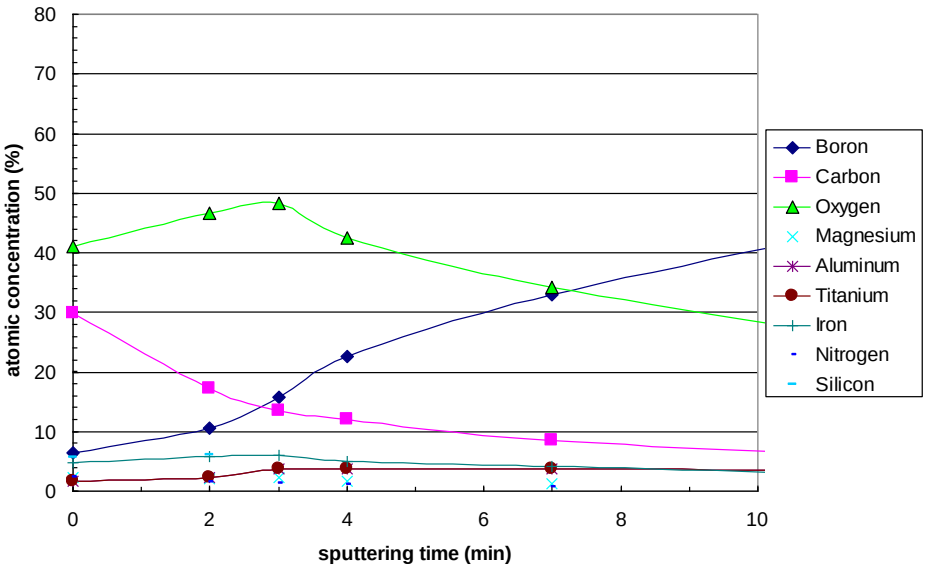

Figure 4.2.4.3-2: XPS depth profile within the wear track of $AlMgB_{14}$-TiB_2 after POD testing in DTE-24. Note the enrichment in oxygen just below the surface.

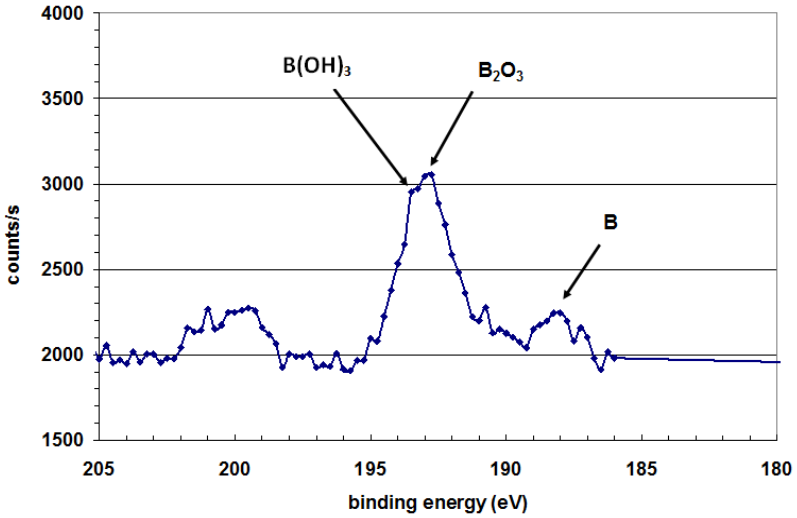

Figure 4.2.4.3-3: Electron binding energy profile at a constant depth within the wear track of $AlMgB_{14}$-TiB_2 after POD testing in DTE-24.

4.2.4.4 $AlMgB_{14}$-TiB_2 in Water Glycol

The most noticeable feature within the wear track of this coating is a polishing effect that the pin appears to have had on the surface morphology. **Figure 4.2.4.4-1** shows topographical and compositional images of a typical region within the wear track, in which it can be seen that the surface roughness is significantly reduced compared with the undisturbed surface of the coating. More Fe transfer from the 52100 pin was found in this coating than in the DLC coating. **Figure 4.2.4.4-2** shows a low magnification compositional image of a portion of the wear track, in which iron is seen to be concentrated near the edge of the track (the bright contrast regions as indicated in the micrograph). **Figure 4.2.4.4-3** shows an XPS depth profile centered on wear track. Note the pronounced enrichment in oxygen just below the surface.

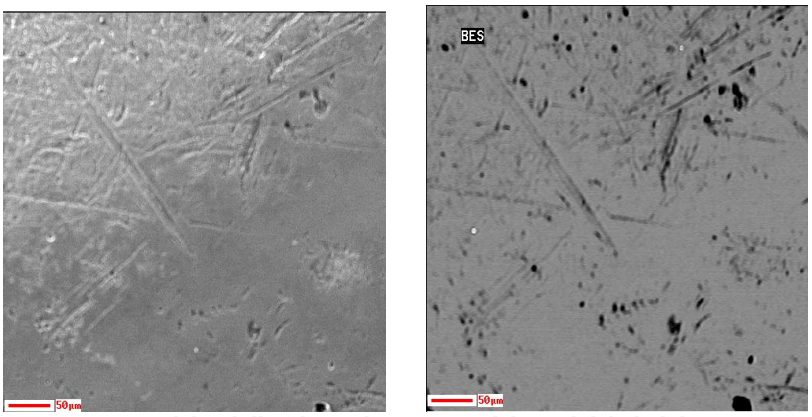

Figure 4.2.4.4-1: Topographical (left) and compositional (right) images of $AlMgB_{14}$-TiB_2 (EB1071A) after POD testing in DTE-24.

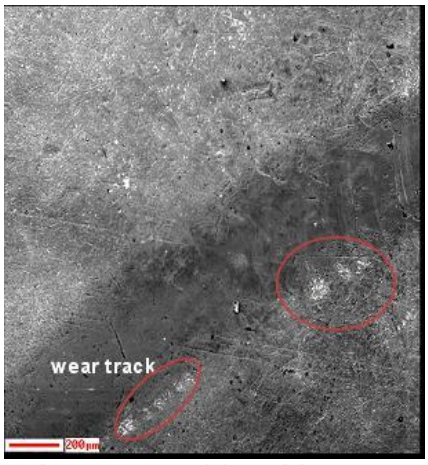

Figure 4.2.4.4-2: Low magnification compositional image of $AlMgB_{14}$-TiB_2 (EB1071A) after POD testing in DTE-24 showing segregation of iron near the edge of the track (denoted by the elliptical markers).

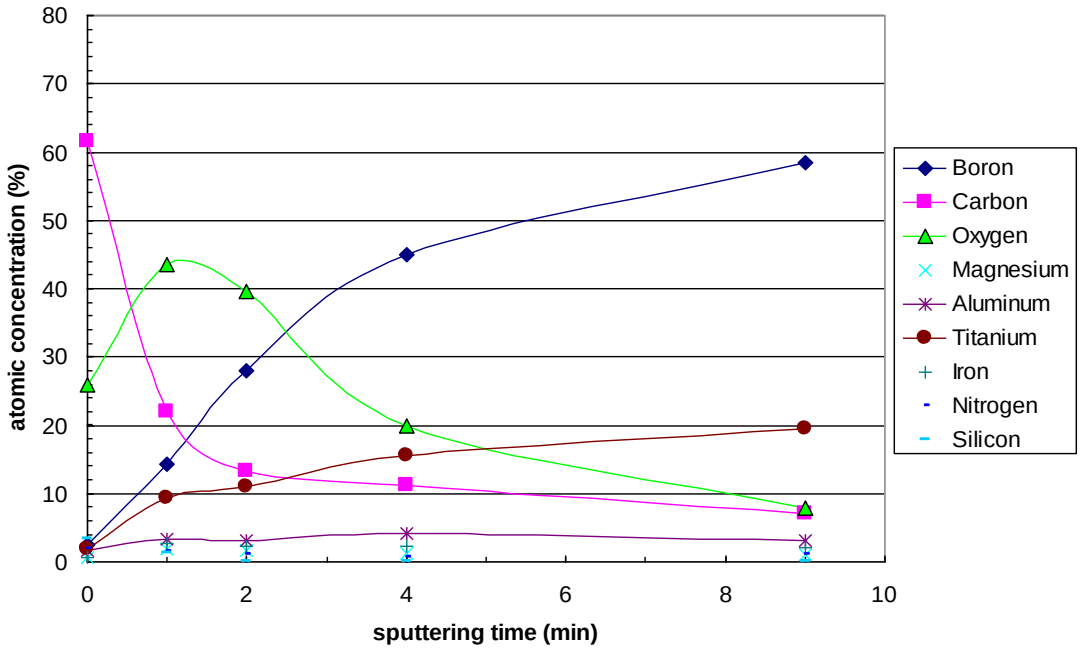

Figure 4.2.4.4-3: XPS depth profile centered on wear track of $AlMgB_{14}$-TiB_2 after POD testing in water glycol. Note the pronounced enrichment in oxygen just below the surface.

A binding energy spectrum from this coating was obtained in a similar manner as with the boride coating tested in DTE-24 oil, and the results are shown in **Figure 4.2.4.4-4**. Again, one can see the peaks corresponding to B, B_2O_3, and $B(OH)_3$; however, there is a noticeable decrease in intensity of the elemental B peak in the coating tested in DTE-24 compared with the water-glycol environment. What was particularly significant about this result is the ratio of peak heights of the boric acid signal to that of boron oxide. In the water-glycol test, the peak intensity of the boric acid signal was higher than that of the boron oxide signal, whereas the situation was reversed in the case of the DTE-24 environment. This was suggestive of a higher concentration of the lubricious boric acid in the water-glycol environment, leading to a lower COF observed.

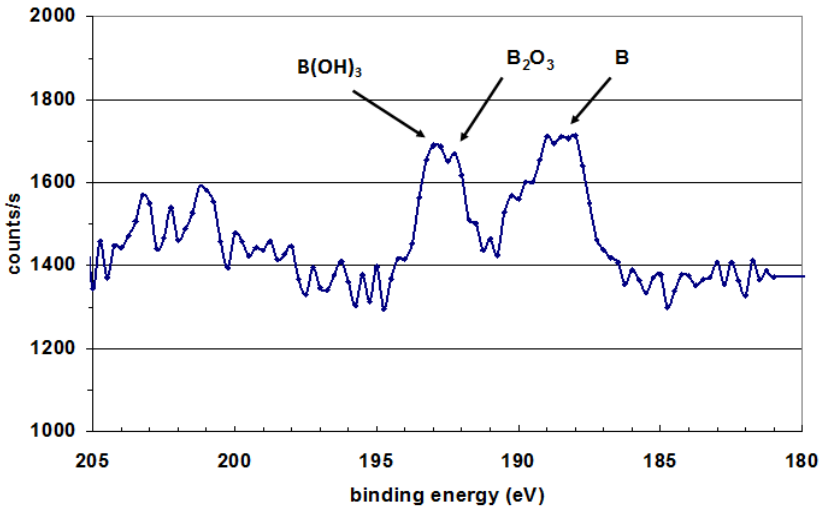

Figure 4.2.4.4-4: Typical XPS binding energy spectrum near the surface of $AlMgB_{14}$-TiB_2 after POD testing in water-glycol. Peaks corresponding to boric acid and boron oxide are noted.

4.2.4.5 TiB_2 in Water Glycol

Also tested for comparison was a TiB_2 coating with a Ti interlayer in a water-glycol environment. In this case, the wear track was readily discernable as seen in the topographical (left) and compositional (right) images of **Figure 4.2.4.5-1**. A higher magnification compositional image within the wear track is shown in **Figure 4.2.4.5-2**, in which discrete nodules and bright streaks can be seen. These nodules and bands give an EDS signature highly enriched in iron, which suggests that they are wear debris from the 52100 pin. An XPS depth profile obtained from the wear track, shown in **Figure 4.2.4.5-3**, again contains evidence of enrichment in oxygen below the surface, similar to the case of the mixed boride coatings, as well as a higher iron concentration, approximately 8 to 10 atomic percent.

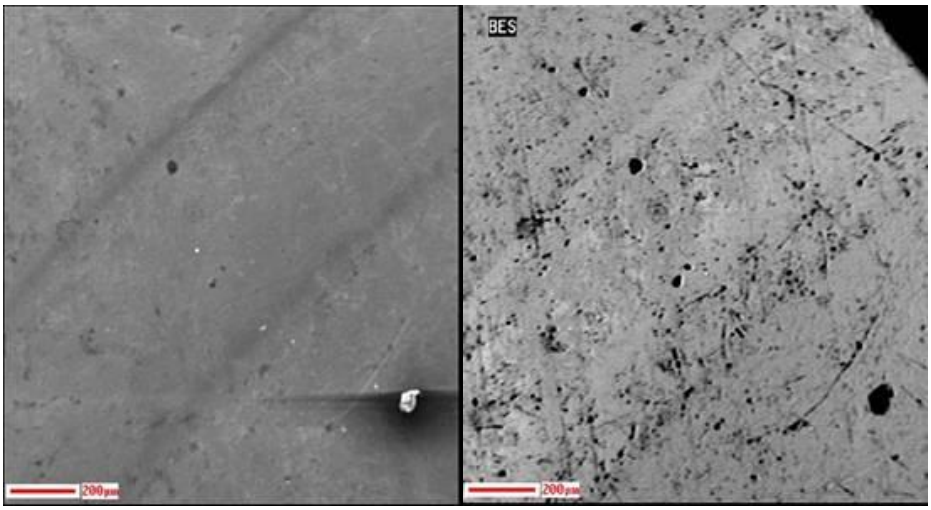

Figure 4.2.4.5-1: Topographical (left) and compositional (right) images of the wear track on TiB_2 after POD testing in water-glycol.

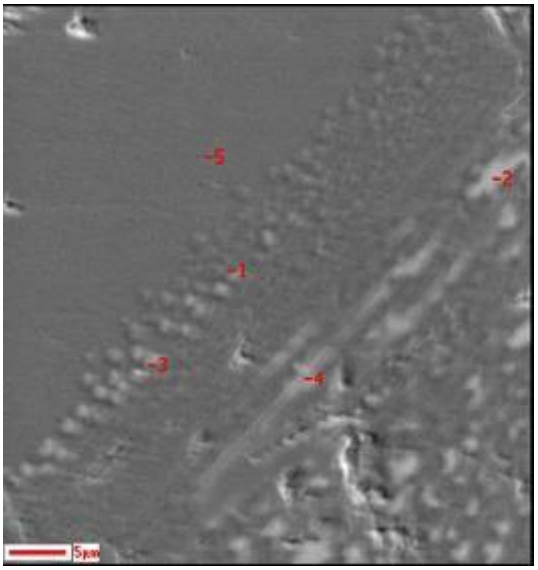

Figure 4.2.4.5-2: Backscattered image within the wear track of TiB_2 after POD testing in water-glycol, showing Fe-rich wear debris from the 52100 steel pin (seen as nodules and bright streaks).

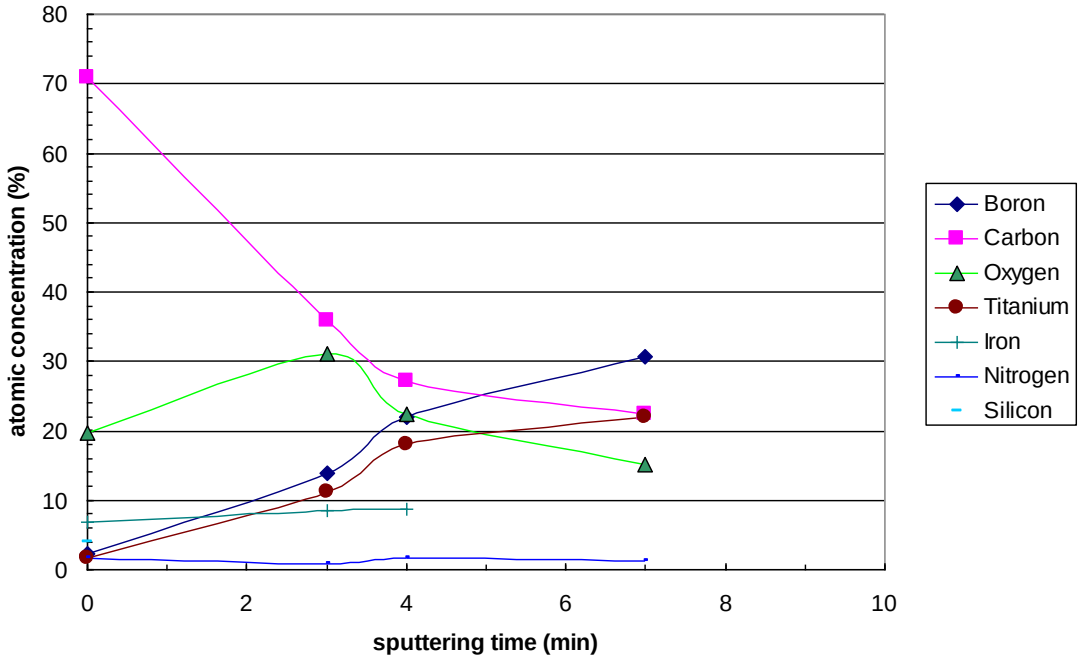

Figure 4.2.4.5-3: XPS depth profile of the wear track on TiB_2 after POD testing in water-glycol.

After reviewing these results, the 52100 steel balls used as counterfaces in the POD tests were obtained from Oak Ridge for similar characterization of compositional depth profiling. A special fixture was machined to hold the spherical pins in a fixed orientation during loading and analysis in the ultra-high vacuum chamber. Secondary electron images of the wear flats on the pins are shown in **Figure 4.2.4.5-4.**

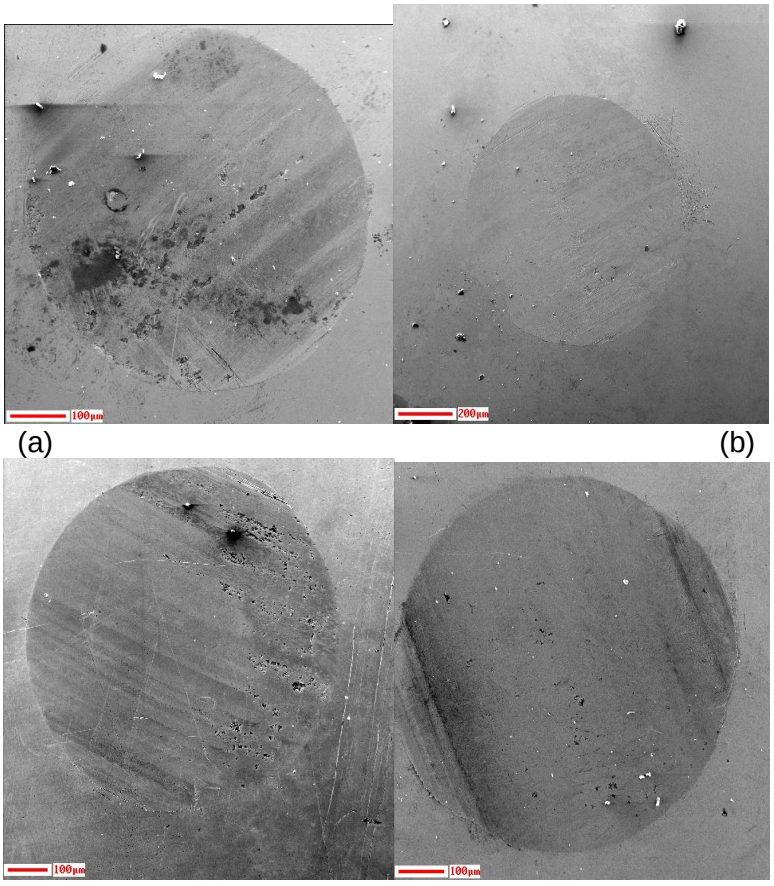

Figure 4.2.4.5-4: Secondary electron images of wear flats on the 52100 steel pins after pin-on-disk tests. DLC with TiN interlayer in DTE-24 (a); $AlMgB_{14}$-TiB_2 in water-glycol (b); $AlMgB_{14}$-TiB_2 in DTE-24 (c); TiB_2 + Ti in water-glycol (d).

The dark regions on the wear flat corresponding to the DLC coating are enriched in carbon, presumably resulting from material transfer from the coating. Most regions of the wear flats show a high surface oxygen content, as expected, that steadily decreases with increasing depth as the iron concentration increases. A few spots on the DLC wear flat are also slightly enriched in Zn, which is an additive in the DTE-24 oil. This was not observed on any other pin. XPS spectra from the boride sample tested in DTE-24 shows only decreasing oxygen and increasing iron, to varying degrees, regardless of the location. In the case of the boride sample tested in water- glycol, there are numerous locations on the wear flat in which the titanium signal is quite pronounced, nearly as large as the surface oxygen signal. The presence of Ti falls off rapidly with depth into the pin, reaching background levels within a depth of a few tens of nanometers. We also observe significant surface Ti enrichment in the case of the TiB_2 coating tested in water- glycol. Typical XPS profiles from these pins are shown in **Figure 4.2.4.5-5**.

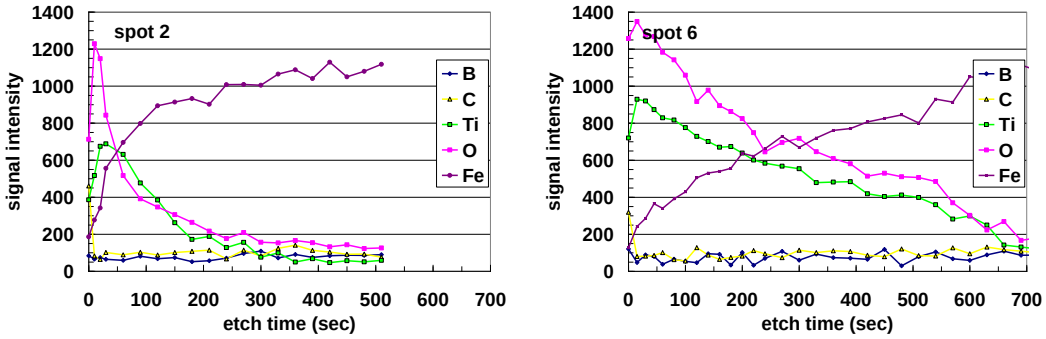

Figure 4.2.4.5-5: Typical XPS depth profiles obtained on wear flat of 52100 steel pins used for pin on disk tests with $AlMgB_{14}$-TiB_2 (left) and TiB_2 (right) coatings in water-glycol. Note the enhancement in Ti near the surface.

An increase in boron activity in the water-glycol-based environment to form $B(OH)_3$ may liberate Ti, which then accumulates on the pin. We observed no such indication of Ti transfer in the case of the mixed-phase $AlMgB_{14}$-TiB_2 coating tested in DTE-24. Our studies of binding energy of surface constituents for the mixed-phase boride coatings showed that the concentration of boric acid in the water-glycol environment is higher than that in a DTE-24 environment. This could account for the observed reduction in friction of the former. The higher wear observed in the water-glycol test may be due to the increased transfer of titanium, a consequence of the preferential formation of boric acid (ΔG_F = -1094kJ/mol [12]) over TiB_2 (ΔG_F = -320 kJ/mol [13]).

4.2.4.6 Development of Quality Assurance Metrics for PVD Nanocoatings

As the Nanocoatings project entered Phase III, some wear-related anomalies appeared which provided the framework for a more comprehensive study of the role of coating morphology in determining wear. The large number of process variables involved in PVD synthesis of Nanocoatings requires an understanding of how each affects coating quality and durability, and how these variables are interrelated. For example, the presence of impurity phases and consolidation temperature can both markedly affect the wear resistance of the bulk targets employed for PVD applications. The deposition process itself contains at least 10 variables including substrate temperature, Ar partial pressure, sputtering power, and acetylene flow. Development of a comprehensive list of process parameter values and acceptable ranges for reproducible performance became a primary objective of this activity. As a starting point, M2 vane samples from three batches of PVD coatings were examined by x-ray photoelectron spectroscopy (XPS) and Auger electron spectroscopy (AES) to determine coating quality. Vanes from batch 1067 exhibited good wear characteristics while batches 1137 and 1167 showed accelerated wear rates. The coating parameters utilized are summarized in the following table:

Table 4.2.4.6-1: Processing variables used for selected vane batches coated at Eaton IC.

Eaton batch ID	1067	1137	1167
New Tech target batch	NTC #1	Greenleaf	NTC #2
Sputtering power	300W	1500W	1500W
EP test stand	old	new	new
Acetylene ramp rate	0.4 ml/40 s	0.4 ml/40 s	0.5 ml/20 s
Total acetylene flow	321 ml	222 ml	488 ml
Coating thickness	~4 μm	2 – 3 μm	~ 4 μm
Process temperature	350°C	300°C	300°C

SEM micrographs of these coated vanes are shown in **Figures 4.2.4.6-1a** and **4.2.4.6-1b**. It can be seen that the microstructure of the coatings appears quite different, depending on particular deposition parameters. Batch 1067 appears to have a more nodular microstructure whereas batch 1137 and 1167 appear smoother. Batch 1137 has numerous Fe inclusions within the coating, all of which possess a central hole that appears to be enriched in C. As discussed below, the targets utilized were processed with WC tools, indicating that the Fe had to originate within the PVD chamber and is possibly an arcing artifact. Batch 1167 appears to have inhomogeneities that are more widespread. Auger elemental maps of the vanes shown in **Figure 4.2.4.6-2** indicate that elemental distribution is uniform in the 1067 vane but is segregated in the 1167 vane. The 1167 vane has large regions deficient in C, which expose the underlying boride coating and could lead to more rapid degradation of the coating during testing.

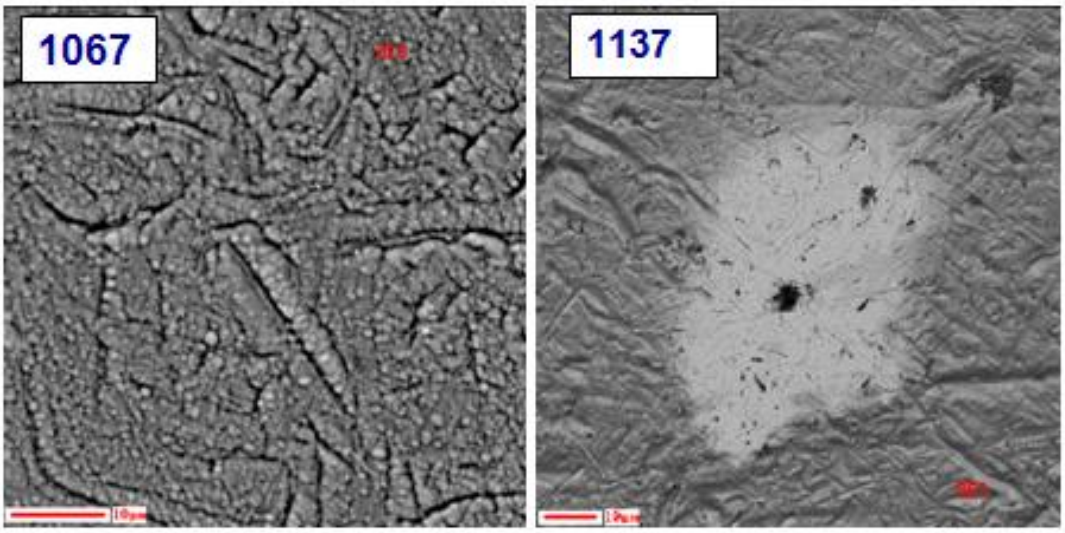

Figures 4.2.4.6-1a: SEM images of batch 1067 (left) and 1137 (right) vanes. The 1137 vane exhibited numerous spots as shown in figure. Light area is Fe and dark center is C. Scale bar is 10 microns.

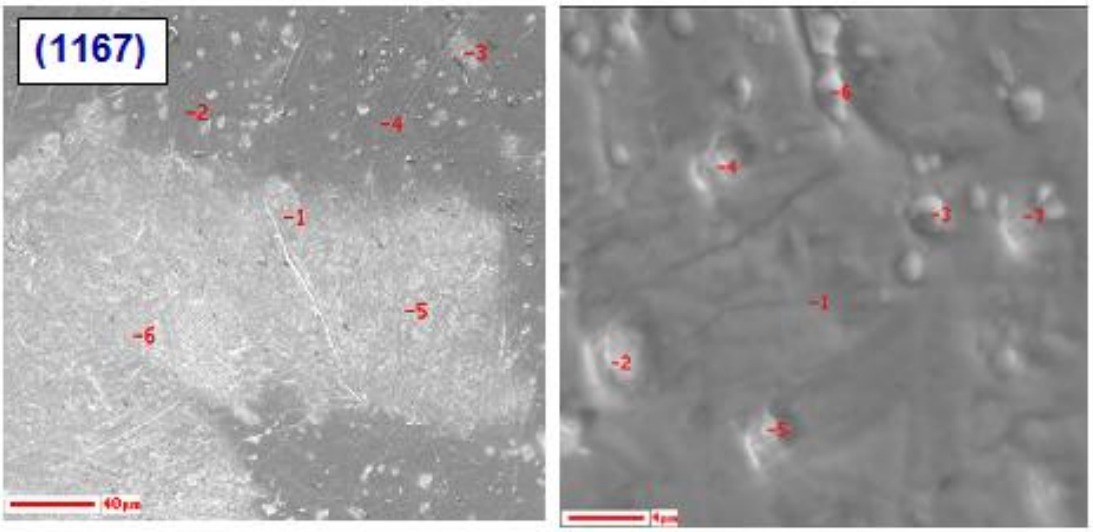

Figures 4.2.4.6-1b: SEM image of M2 vane from batch 1167. Bright area in lower left figure is uncoated region of vane. Scale bar is 40 microns (left) and 4 microns (right).

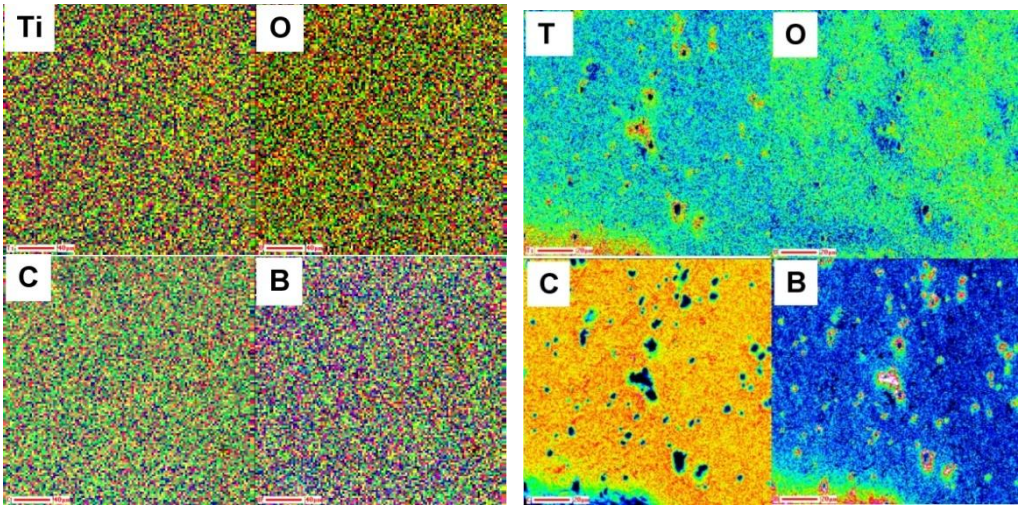

Figure 4.2.4.6-2: Elemental dot maps of vanes 1067 (left) and 1167 (right). Blue represents low concentration, yellow represents high concentration. Scale bars are 40 microns at left, 20 microns at right.

XPS analysis indicated the presence of Al, Mg, B, Ti, O, and C in the good-quality batch 1067 coatings; whereas batch 1167 predominantly showed the presence of C, even after a prolonged etch time. As seen in **Figure 4.2.4.6-3**, the XPS signal from 1167 shows essentially no B or Ti, even after 35 minutes of etching, whereas clear B and Ti signals are seen in 1067. It was highly unusual to see an absence of signal for B, Ti, and Al after such a prolonged etching. As expected, EDS analysis on the vast majority of coatings revealed a carbon peak that obscures all other constituents. However, both B and C were seen in the EDS pattern of batch 1067, indicating a reduced C concentration. This provided unambiguous evidence that excessive carbon was the reason for the anomalous behavior of the coatings.

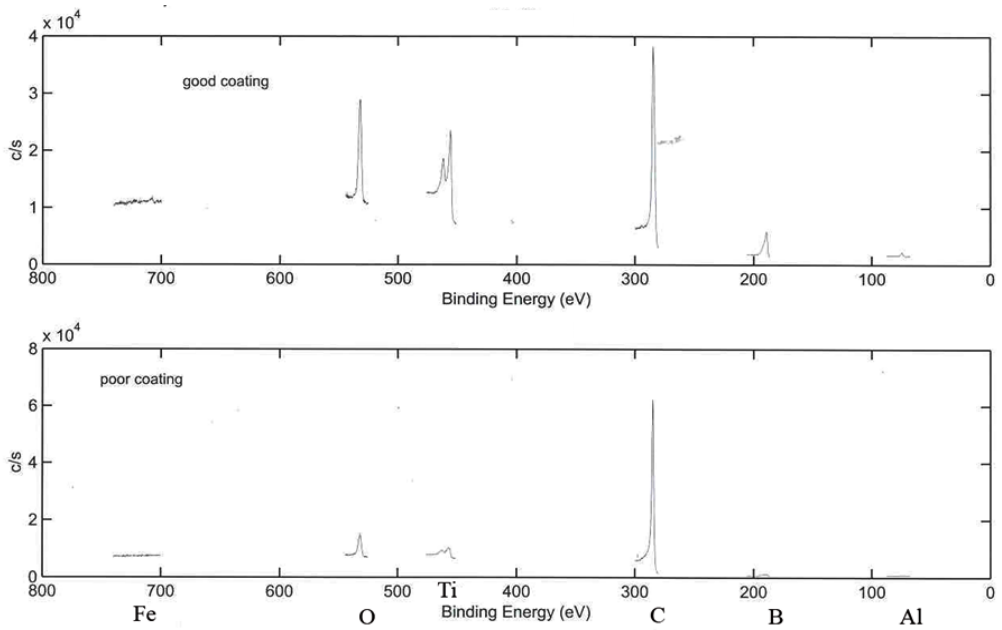

Figure 4.2.4.6-3: XPS binding energy spectra of coating 1067 (top) and 1167 (bottom). Note the low intensity of B and Ti peaks relative to C in 1167, a coating exhibiting high wear rates.

Excessive carbon in the coatings generally corresponds to elevated oxygen concentrations as well. Of the C-containing samples, 1179 exhibited the lowest O concentration. Batch 1181, prepared without C, showed the lowest surface concentration of O. (Due to the low Z of most constituents, quantitative analysis could not be performed with the use of standards.) Ti, Al, Mg, and W were detected as expected, except that in most cases the Mg peak intensity was approximately half that of the Al peak. Ar is also detectable in all the coatings as a result of the sputtering atmosphere.

The excessive carbon was eventually attributed to residue in the chamber originating from the vacuum pump fluids. The presence of the $AlMgB_{14}$-TiB_2 layer was not detected, further evidence that the C layer was abnormally thick and that the $AlMgB_{14}$-TiB_2 had not been deposited to the desired thickness.

Other factors can also affect the quality and performance of the deposited coatings. **Figure 4.2.4.6-4** is an SEM micrograph of four targets used for deposition of the boride Nanocoatings. It can be seen that all four targets contain W contaminants from the ball milling tools. However, no significant differences can be seen between the four targets. While the presence of tungsten in bulk materials, particularly intergranular tungsten, can be highly detrimental to wear behavior by blocking the strong bonding between boride phases, its presence in coatings is not believed to be nearly as pernicious.

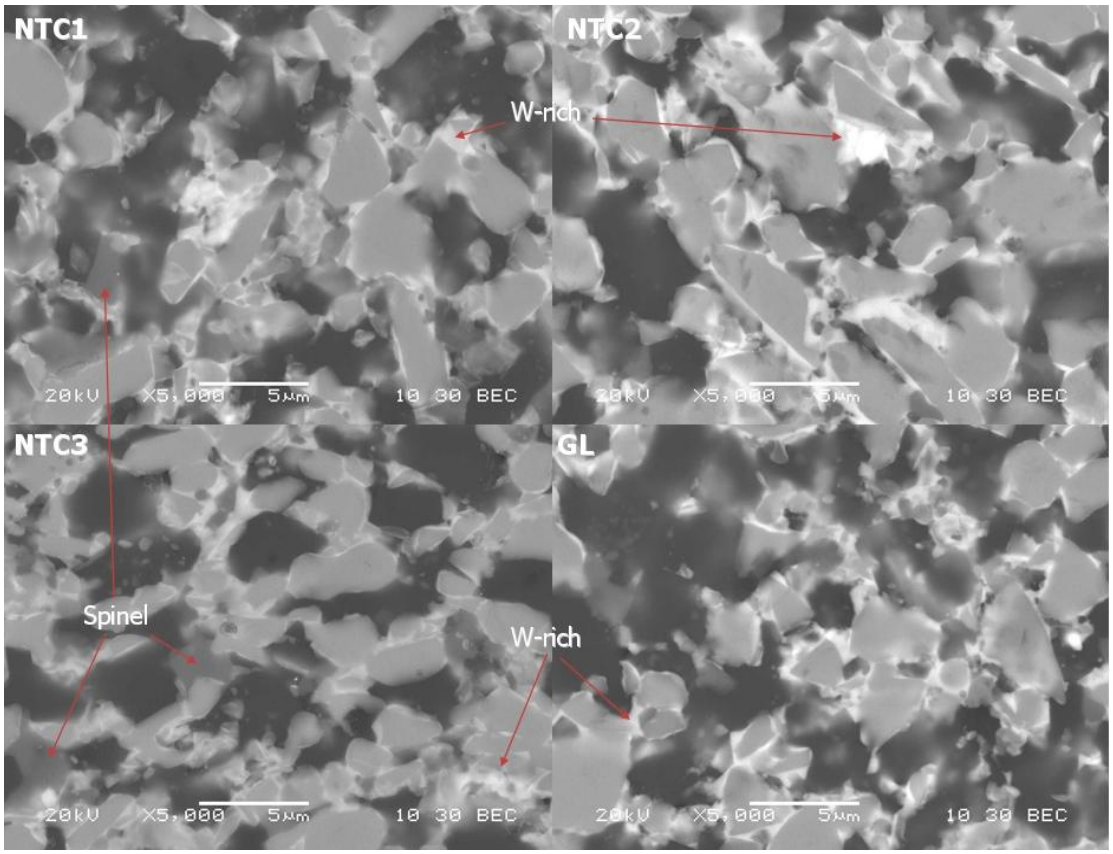

Figure 4.2.4.6-4: Backscattered electron image of $AlMgB_{14}$-TiB_2 targets used for deposition (NTC1, NTC2, NTC3, and GL). Bright phase is W rich from milling wear debris.

With unambiguous identification by XPS and AES of the root cause of the anomalous wear issues, the problem was quickly resolved with a thorough cleaning of the internal surfaces of the PVD chamber, and by implementation of a modification to the gas management procedures during extended downtimes. The anomalous behavior provided an opportunity to examine not only the surface chemistry, but the morphology of Nanocoatings as well. The relationship between morphology and tribological behavior is complex, involving numerous interrelated variables. During the course of this project, a considerable number of PVD coatings were examined in detail by SEM in order to determine which morphological characteristics are most closely associated with low friction and wear rates. A few of the various morphologies are shown and discussed below.

Figure 4.2.4.6-5 contains a summary of selected SEM micrographs of PVD coatings, all taken under identical accelerating voltages and magnification (10kx). It can be seen that the morphology varied considerably, from 1108, which was from a low-temperature deposition, resulting in planar growth, to the more common columnar growth seen in the recent coating batches such as 1181 and 1182. The morphology of batch 1167 exhibits a more flake-like structure

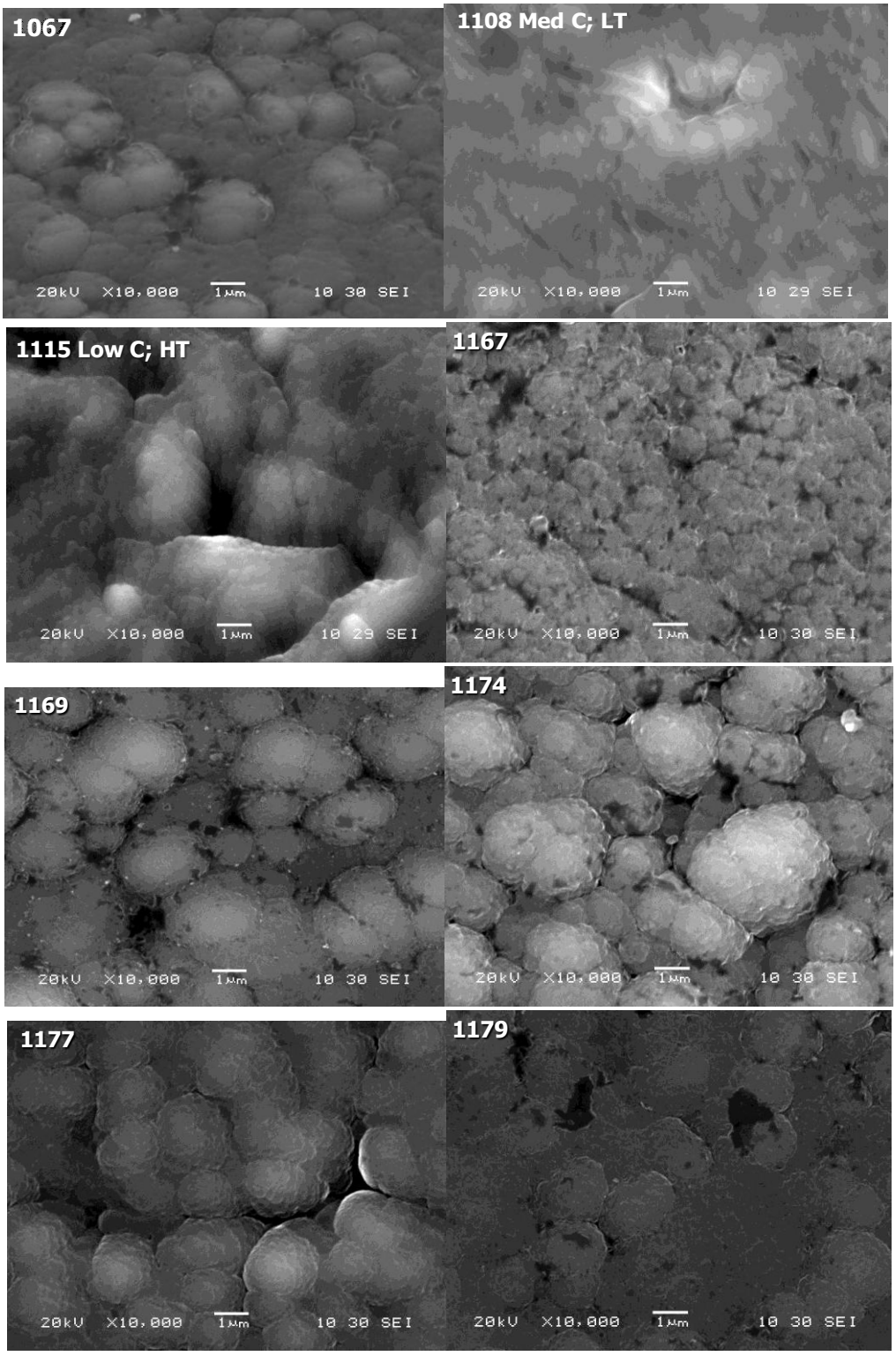
1067
20kV X10,000 1µm 10 30 SEI
1108 Med C; LT
20kV X10,000 1µm 10 29 SEI
1115 Low C; HT
20kV X10,000 1µm 10 29 SEI
1167
20kV X10,000 1µm 10 30 SEI
1169
20kV X10,000 1µm 10 30 SEI
1174
20kV X10,000 1µm 10 30 SEI
1177
20kV X10,000 1µm 10 30 SEI
1179
20kV X10,000 1µm 10 30 SEI

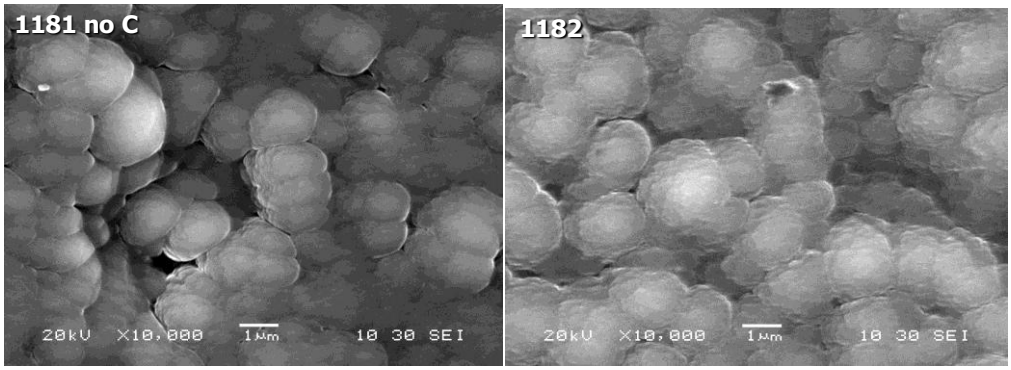

Figure 4.2.4.6-5: SEM micrograph summary of selected PVD coatings, arranged in chronological order.

Since a majority of the growth `columns have a diameter ranging from 1 to 3 microns, a significant amount of coarsening was found to have occurred during deposition. There were also indications of layer-by-layer growth within many of the individual columns.
In general, coating growth occurs through a 4-stage process. Initially, single atoms impinge and nucleate on the surface of the substrate. If the atom's energy is sufficiently high, through either high sputtering power or a high substrate temperature, the atom can migrate to bond with another to form an island. However, if the temperature is too high, the atom can evaporate away from the substrate entirely. Since the energy required for evaporation of multiple atoms is higher than that required for evaporation of a single atom, adatom coalescence leads to formation of stable islands. These islands in turn eventually coalesce to form stable columns. Sputtering power and substrate temperature are the primary variables determining how far adatoms can migrate along the surface before either nucleating or evaporating. Most of the Nanocoatings were deposited at a temperature of 350°C (623K), which is approximately 27% of the absolute melting temperature of $AlMgB_{14}$. Consequently, one would expect limited adatom surface diffusion, depending on local surface roughness. A structure-zone model for PVD film growth is shown in **Figure 4.2.4.6-6**, in which it can be seen that the porous structure of columnar grains seen in many of the $AlMgB_{14}$-TiB_2 coatings roughly corresponds to a transition between zone 1 and zone T behavior.

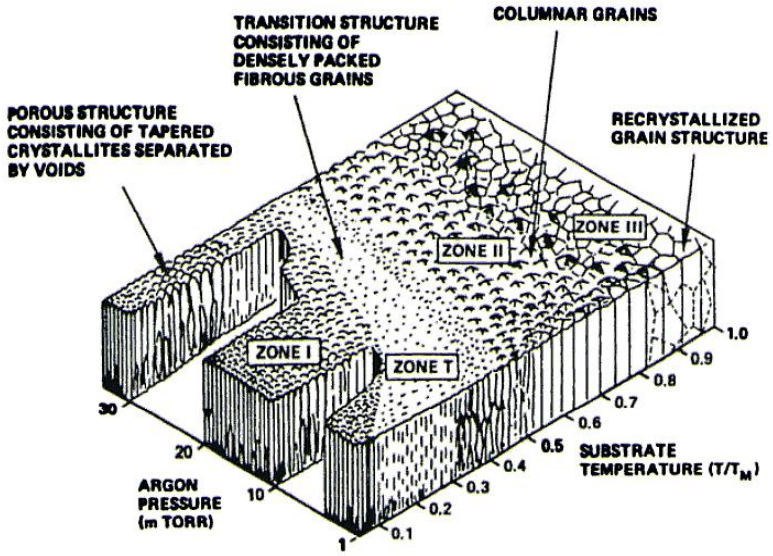

Figure 4.2.4.6-6: Thornton structure-zone map describing PVD coating morphology. A closer examination of the effect of argon pressure during deposition would constitute a useful future activity and help to clarify the relationship between variables.

4.2.4.7 Effect of Substrate Chemistry and Finishing

The nucleation and growth of PVD coatings is a complex dynamical process involving a large number of variables. The effect of substrate chemistry and surface finish (roughness) had not been well documented in the literature. Consequently, a secondary study was launched with the objective of determining the extent to which these variables affected coating morphology. Deposition of the mixed-phase boride on Ti-6Al-4V, superfinished WC/Co, and a superfinished M2 tool steel provided indications that pre-deposition surface treatment was highly influential in determining coating morphology.

While the average coating growth column diameter on standard M2 substrates was around 2-3 microns, the column diameter of a mixed-phase coating on the Ti-6-4 substrate was much smaller - as low as 500nm. In the case of the polished tungsten carbide (0.05 micron polished surface finish), the column diameters were found to be smaller still-approximately 100nm or less. Examples of the coating morphology on Ti-6Al-4V and on the polished WC are shown in **Figure 4.2.4.7-1**(secondary electron mode).

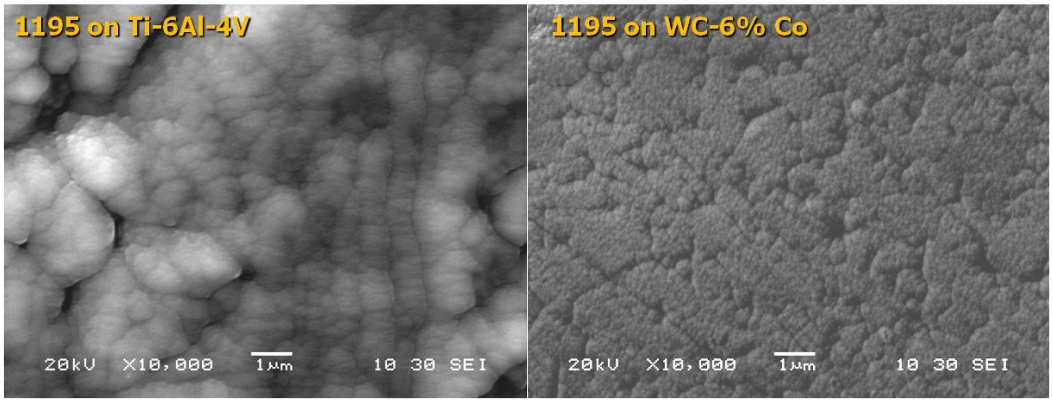

Figure 4.2.4.7-1: Morphology of mixed-phase $AlMgB_{14}$-TiB_2 on Ti-6Al-4V (left) and polished WC-6%Co (right) substrates. Note the fine scale of the growth columns on the WC substrate and the valleys corresponding to grain boundaries between the WC grains.

The growth columns on the polished WC were remarkably small, hardly visible at 10,000x. The coating on the WC substrate also appeared to be nearly planar in nature, which would affect the wear behavior of the coating. That the wear behavior of these coatings is dependent on column morphology and orientation is supported by the fact that cleavage fracture is a dominant failure mechanism, and that surface energy is generally anisotropic. Consequently, some column orientations may be more susceptible to fracture, depending on their orientation with respect to the applied shear. The size of the columns also affects wear behavior, as larger columns translate to increased surface roughness, which in turn decreases the lambda value and shifts the friction mechanism toward boundary lubrication. As a follow up to these results, a standard M2 vane was metallographically polished to 100 nm with colloidal silica, and used as a substrate for a separate mixed-phase deposition (batch 1198 – no carbon gradient). This enabled a direct comparison between two surface finishes on the same substrate chemistry. Results are shown in **Figure 4.2.4.7-2**. The SEM images illustrate the differences between a 20kV accelerating voltage (on the right) and a lower (5kV) accelerating voltage (on the left). One item of note in this comparison is that the lower voltage tends to yield slightly more near-surface detail. It can be seen that the morphology of the coating on the polished M2 vane is different than that on a standard M2 vane. The structure is much finer, and the columns are decorated by occasional larger growth structures. In terms of measurement, the smaller columns were 100-300nm in diameter, whereas the surrounding growth structures were an order of magnitude larger. Another difference between the conventional structures and those observed on the superfinished samples was the absence of valleys and holes in-between the growth columns. This raised the question of whether the valleys serve to reduce friction by retaining some of the lubricating fluid.

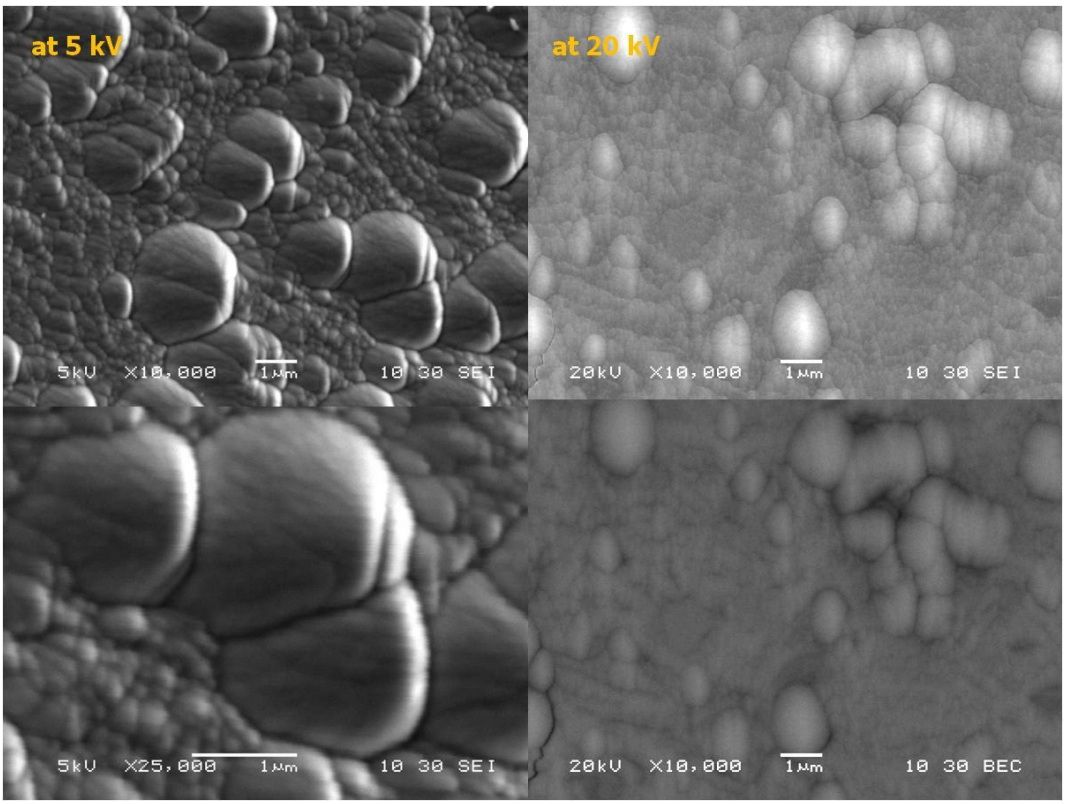

Figure 4.2.4.7-2: SEM images of mixed-phase $AlMgB_{14}$-TiB_2 coating on M2 that was polished to 100 nm prior to deposition. Two accelerating voltages are shown, 5 kV on the left and 20 kV on the right. The lower accelerating voltage produces a smaller interaction volume with the coating and hence shows more surface detail.

A detailed study of the effect of substrate chemistry was performed in which several M2 and A2 substrates were coated with $AlMgB_{14}$-TiB_2 by PVD for short durations. The objective was to obtain sufficiently thin coatings (e.g., < 1 micron) so that early stage growth morphology could be observed and to enable an electron beam from an SEM to penetrate the coating easily to reveal the chemistry of the underlying substrate. In this way, a correlation could be made between features in the coating and the substrate. In support of this effort, Eaton processed 6 evaluation samples by PVD, coated for 15, 30, and 45 minutes. The coating times reflected operation of the CemeCon PVD system at full cathode wattage. In each case, there was a ramp-up to the full 2500W setting. The standard processing recipe for coatings involved operating the system at 500W for 5 minutes, 1000W for 5 minutes, 1500W for 5 minutes, 2000W for 5 minutes, and finally, full cathode power for the remaining duration of the cycle. The 45-minute batch was estimated to produce a coating thickness of approximately 1 micron, while the 15-minute deposition was expected to produce a 0.2-micron thick coating. These coatings, corresponding to batch numbers 1202 through 1205, were all examined using a JEOL 5910 SEM. The M2 carbides were easily identified, as expected. A2 carbides, in contrast, are not significantly different from the base metal in their composition, and so in backscattered electron mode (BSE), they do not stand out as clearly. The following table compares the composition of M2 and A2 steels.

Table 4.2.4.7-1: Chemical composition of M2 and A2 steels

	C	Mn	Si	Cr	Ni	Mo	W	V	Fe
at. weight	12	55	28	52	59	96	184	51	56
M2	0.78-1.05	0.15-0.40	0.2-0.45	3.75-4.50	0.3	4.5-5.5	5.5-6.75	1.75-2.2	bal
A2	0.95-1.05	1.0	0.5	4.75-5.5	0.3	0.9-1.40	--	0.15-0.5	bal

Figure 4.2.4.7-3 contains representative BSE images of 3 deposition times on M2, along with a 15-minute deposition on A2. It is nearly impossible to identify the presence of the carbides in the A2 steel, although a careful examination reveals these inclusions as slightly darker regions, several of which are identified by arrows. Carbides in A2 are mostly Cr-based.

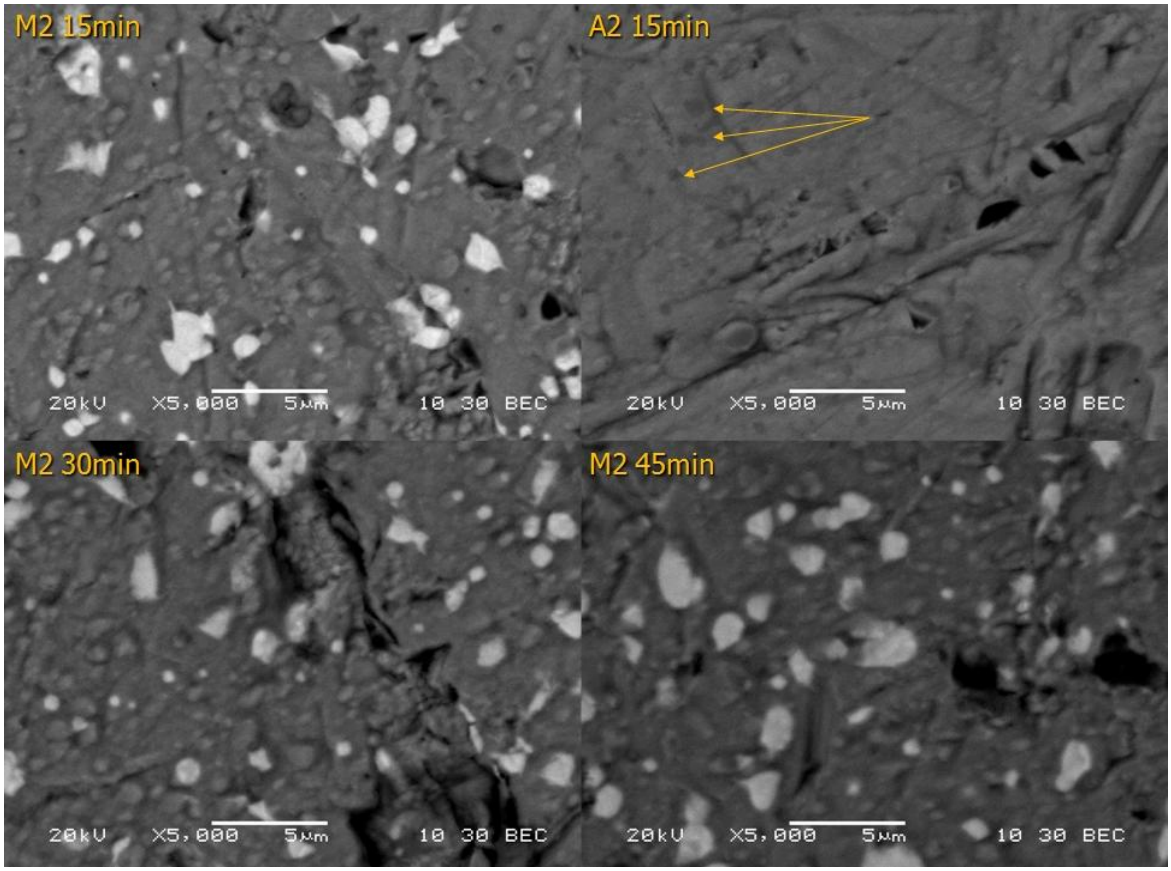

Figure 4.2.4.7-3: BSE images of 15, 30, and 45-minute deposition on M2 steel, along with a 15-minute deposition on A2. (Arrows indicate location of carbides in the A2)

It can be seen that the carbides do not change the general morphology of the growth columns. There were indications that their presence may cause a discontinuity along the carbide-parent metal interface, although this tends to vary from carbide to carbide. **Figure 4.2.4.7-4** shows indications of early-stage growth columns, especially in the 15 and 30-minute coatings.

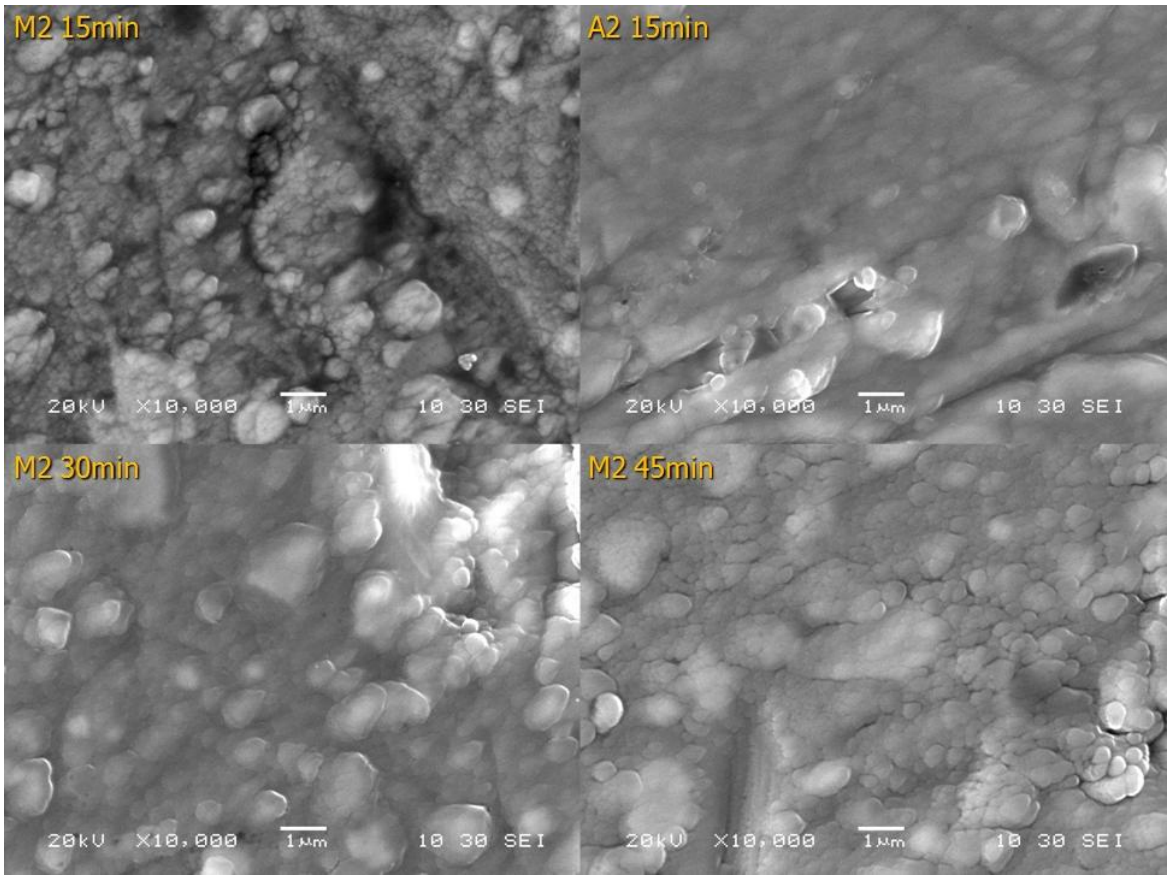

Figure 4.2.4.7-4: Secondary electron images of the coatings at 10,000x. At this magnification, early-stage growth of individual columns can be seen.

Figure 4.2.4.7-5 (top) shows a backscattered image at 25kx, along with the corresponding secondary electron image (bottom), in which the coating morphology can be directly compared with the underlying substrate chemistry. Both images were obtained at an accelerating voltage of 20kV. In the SEI images, it can be seen that a slight discontinuity exists in the columns at the boundary between carbide and iron matrix. However, the size of the columns within the carbides does not appear significantly different from that of the matrix.

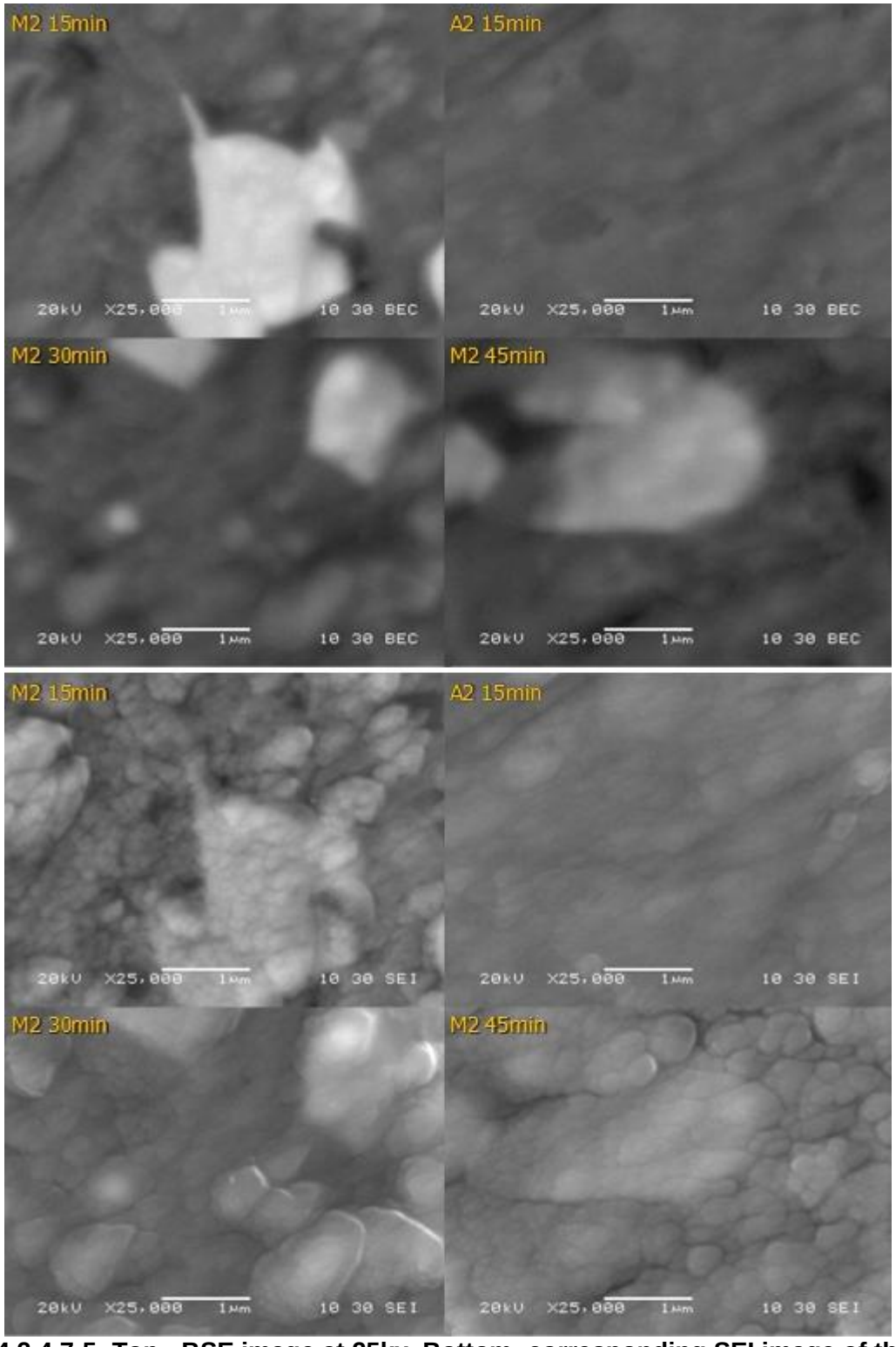

Figure 4.2.4.7-5: Top: BSE image at 25kx. Bottom: corresponding SEI image of the same locations on the coatings. (Note the discontinuity, or boundary, between columns corresponding to the interface between carbide and the steel matrix.

In order to obtain more information about surface details of the coatings, a set of SEI micrographs were obtained at a reduced accelerating voltage of 5 kV. Because of the shallower and dome-shaped interaction volume at lower accelerating voltages, more of the signal originates from the upper-most region of the sample and thereby provides improved imaging of the morphology. **Figure 4.2.4.7-6** shows SEI images obtained at 5kV on the 15 and 45-minute M2 specimen, along with the corresponding BSE images of the same region taken at 20kV.

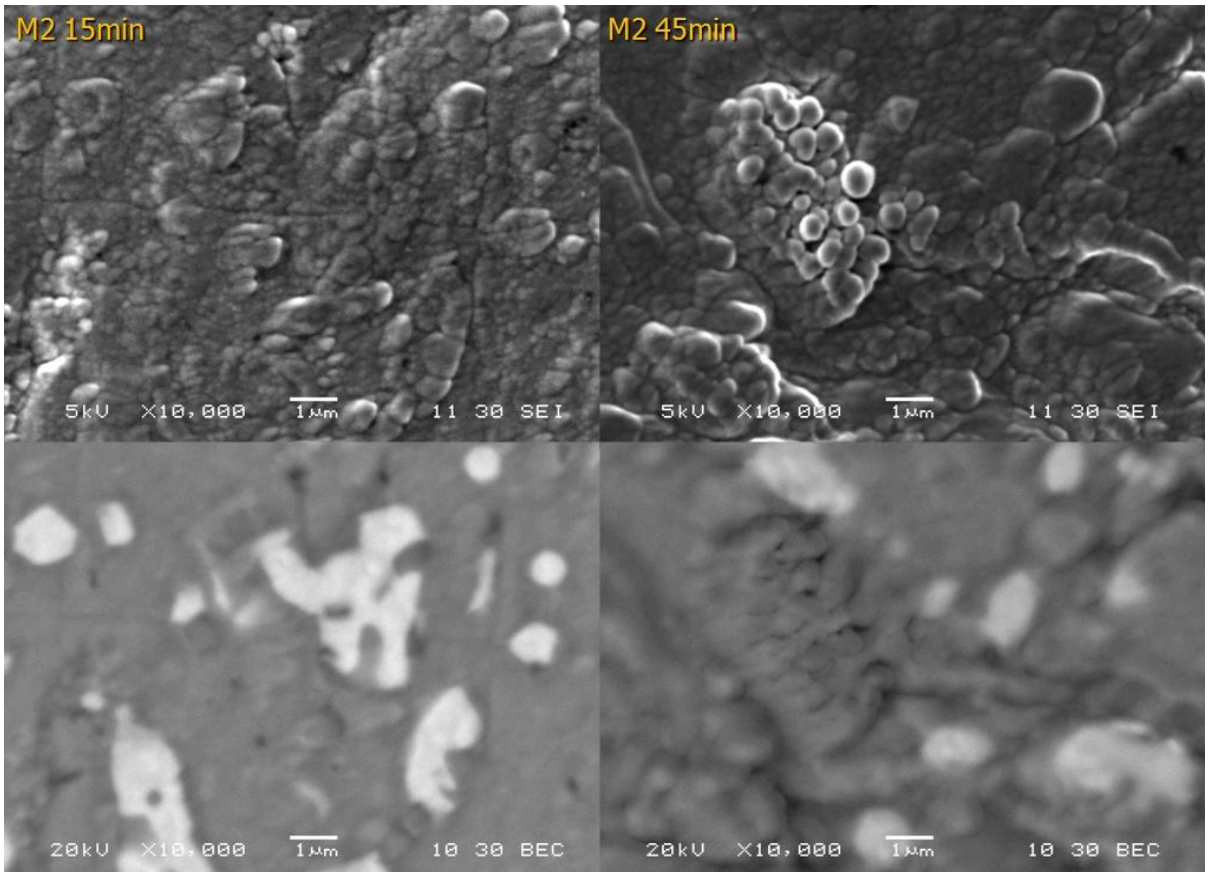

Figure 4.2.4.7-6: Low-voltage SEI images (top) and corresponding BSE images (bottom) of the 15 and 45 minute coatings on M2.

One can see a discontinuity, or boundary, between growth columns corresponding to the interface between carbide and matrix. Otherwise, there is no indication that the carbides affect the shape or size of the growth columns.

4.2.4.8 Characterization of PVD Nanocoatings by Raman Spectroscopy

Another issue affecting coating performance is the nature of the carbon bonding in the carbon gradient layer. The carbon was clearly revealed as a XPS peak around 284 eV. It was of interest to determine if the C is primarily sp^2- or sp^3-bonded. In theory, one could use XPS to obtain this information; however, the XPS lacks sufficient energy resolution to distinguish between the 283.75 eV signature of sp3-bonded C and that of the 284.25 eV signature of sp^2 C. Recognizing that Raman spectroscopy has been applied to other studies of DLC to understand the nature of the carbon bonding in these coatings, we performed a proof-of-concept study with the two aforementioned Nanocoatings (1181 and 1182) using Raman equipment at ISU.

Raman scattering in the various carbon polymorphs depends on number and size of graphitic bonded clusters (sp^2, threefold-coordinated) and the amount of fourfold-coordinated (sp^3) carbon atoms whereas amorphous carbon reveals broad bands caused by the structural disorder with an asymmetrical Raman band in the wavenumber region between 900 cm^{-1} and 1800 cm^{-1}. A graphitic "G"-peak occurs at about 1580 cm^{-1}, which is associated with the E_{2g} optical transition in crystalline graphite and a "D"-peak that occurs near 1350 cm^{-1}. (Note, the designation “D” does not refer to diamond, but rather to disordered graphite, as in activated charcoal or carbon black. Diamond sp^3 bonding is easily identified by a sharp Raman peak at 1332 cm^{-1}). Analyzing the intensity relation I_D/I_G, the peak position, and their FWHM can provide information about the degree of long-range order of within the films and the ratio of sp^3 to sp^2 bonding. **Figure 4.2.4.8-1** depicts the vibrational modes in graphite responsible for the two primary Raman peaks [14].

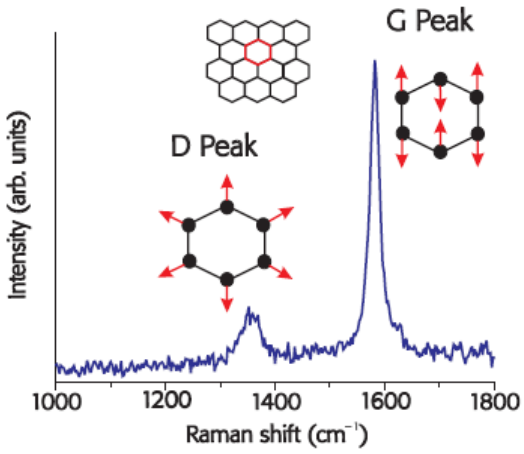

Figure 4.2.4.8-1: Diagrammatic relationship between Raman shift peaks and vibrational modes in graphite (after J. Filik, Spectroscopy Europe, 17 (2005) 10.)

The results of our Raman study on two PVD coatings, batch 1182 that was a mixed-phase $AlMgB_{14}$-TiB_2 with carbon, and batch 1181, which was a straight $AlMgB_{14}$-TiB_2 coating without carbon, are shown in **Figure 4.2.4.8-2.**

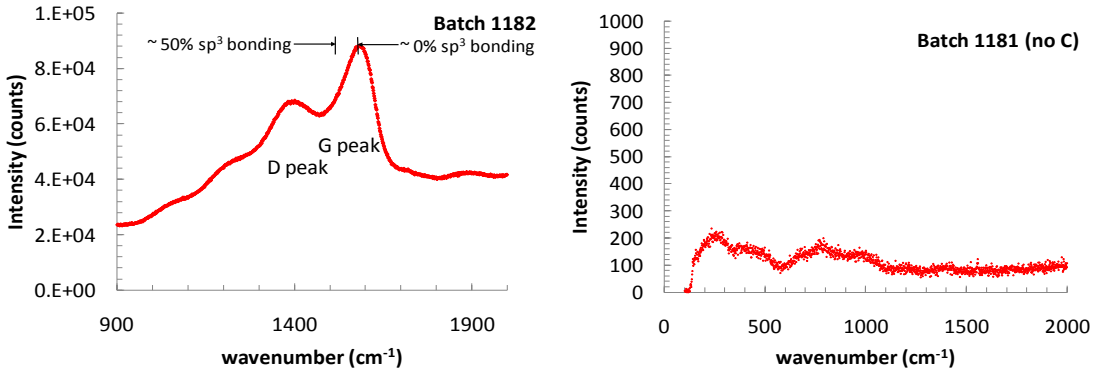

Figure 4.2.4.8-2: Left: Raman spectra of $AlMgB_{14}$-TiB_2+C coating (1182); Right: Raman spectra of $AlMgB_{14}$-TiB_2 coating without C (1181).

In order to understand the significance of the measured spectra, we referred to previous work on DLC films by Marchon et alia [15]. In these studies, the researchers established a correlation between the position of the "G" peak in the Raman spectrum and the substrate temperature, as shown in **Figure 4.2.4.8-3a.** They then examined each sample using electron energy loss spectroscopy (EELS) to measure the ratio of sp^3 to sp^2 bonding directly. The results of this study are shown in **Figure 4.2.4.8-3b.**

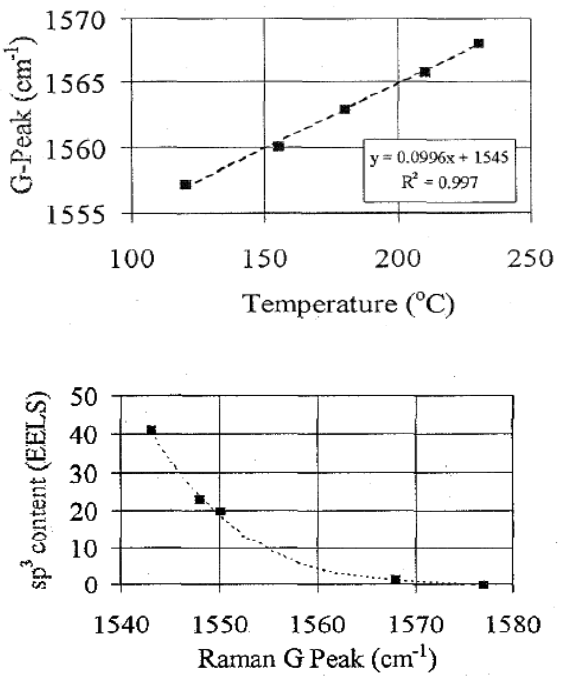

Figure 4.2.4.8-3: (a) Relationship between Raman "G" peak position and deposition temperature for DLC (top). (b) Relationship between Raman "G" peak position and sp^3 bonding content as determined by EELS (bottom).

It was seen that higher deposition temperatures lead to decreased sp^3 bonding (i.e., more graphitic). The graphite peaks are clearly visible in batch 1182 whereas no such peaks are seen in 1181, the control sample without carbon. The G-peak position at > 1580 cm^{-1} shows that the carbon in the PVD coatings is primarily sp^2 (i.e., not diamond-like). An interesting future study would involve examination of low-temp carbon gradient coatings to see if the G-peak position is shifted to lower wavenumbers.

4.2.4.9 Fracture response of PVD Nanocoatings

Introduction of a vibrating probe provided a relative toughness and fracture mode ranking, and showed how the coating tends to fracture in the presence of repeated point-stress contact. The following section describes observations on a number of PVD coatings batches after introducing various fracture modes with the vibrating probe.

The vibrating probe causes deformation of the steel substrate, inducing various modes of cracking in the overlying coating. In addition to fracture and adhesion analysis, this provided an opportunity to perform EDS on some of the lower layers of the coatings. Where the bottom layer of the coating was exposed, the B peak was clear and no C was detected. In addition, O was not detected in these areas. Fe, Mo, and Cr were also detected in various amounts because of the underlying M2 substrate.

Four features appeared to be common in the fracture testing of most of the coatings:

- Delamination between the C-free basal film and the gradient coating
- Good adhesion between the basal film and the substrate
- Inter-cellular fracture (between the columns) in the gradient layer
- Intra-cellular fracture (through the columns) in the basal layer

For example, coating batch 1067 was seen to exhibit all of these features, as shown in **Figure 4.2.4.9-1**. Cracks from the indent to the left of the image are seen to pass through the upper gradient layer (II) following fracture paths between the columns. These cracks then transition to stronger intra-cellular fracture when entering the basal film (III). Fracture in this basal layer is visible due to the spallation of large areas of the gradient film (I) which is much wider than shown in the figure. The basal layer appears to be well adhered to the M2 substrate, exposed steel was only visible where ploughing of the substrate caused buckling of the coating to occur (**Figure 4.2.4.9-2**).

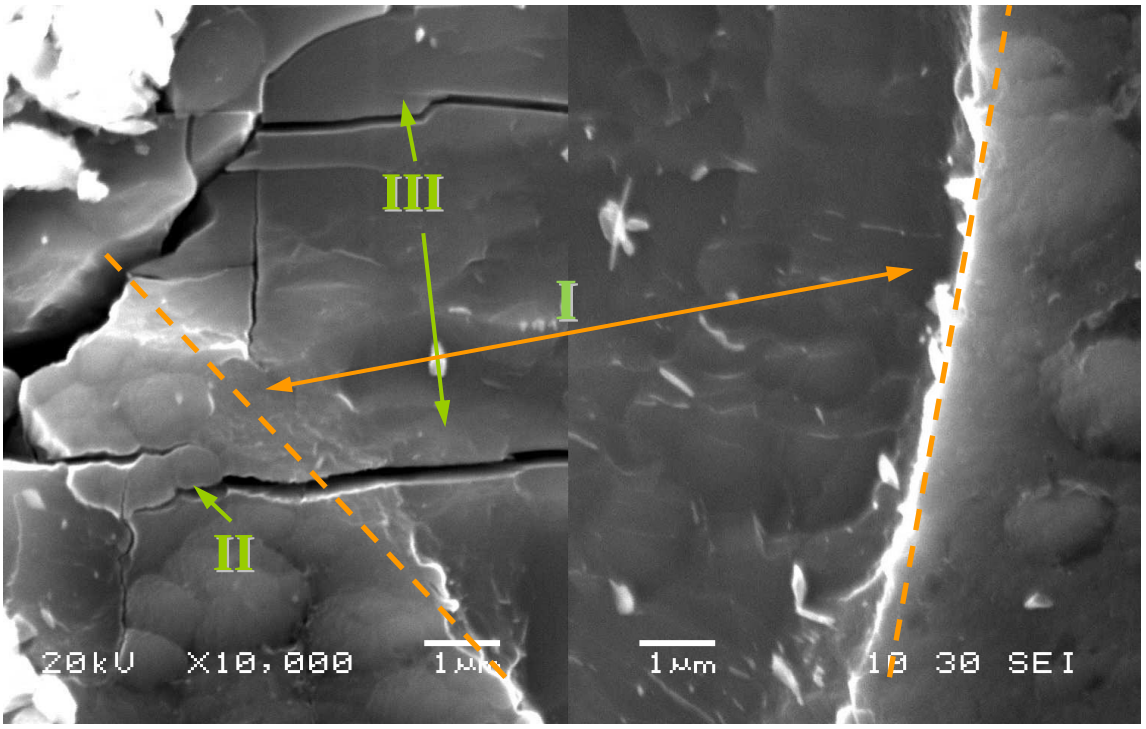

Figure 4.2.4.9-1: 1067 showing delamination of C gradient layer (I, center) and fracture in both gradient (II) and basal (III) layers, caused by indentation originating at the far left.

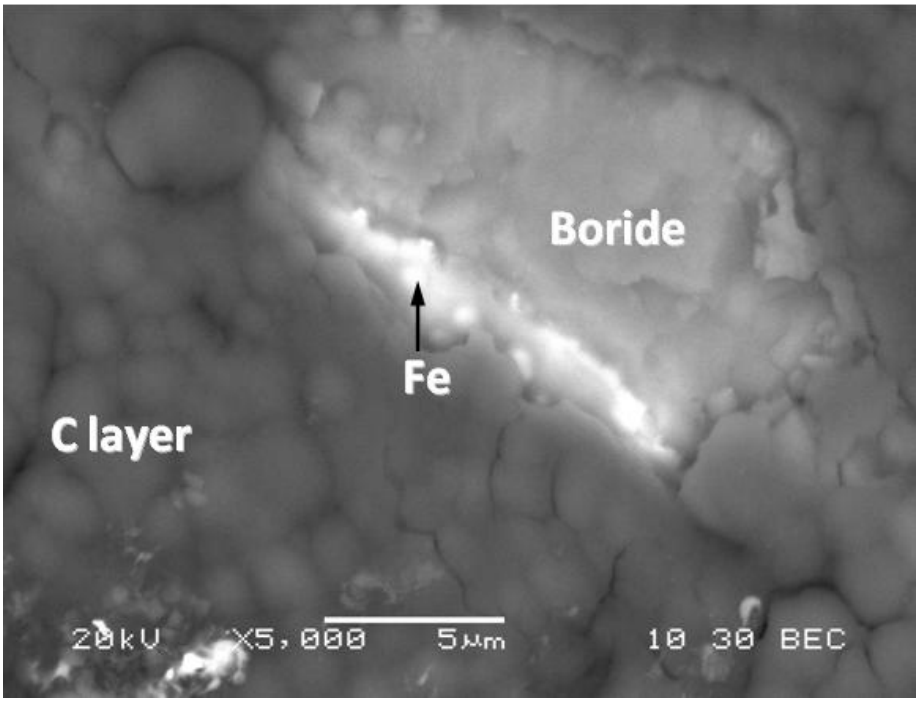

Figure 4.2.4.9-2: Fracture of batch 1177 surface. Note inter-cellular cracking in C gradient layer and exposed Fe where buckling has occurred.

Some additional interesting features were observed in the fracture of other coatings, as shown in **Figure 4.2.4.9-3** and **4.2.4.9-4**. In batch 1169, a progression from smooth to rough fracture can be seen as the delaminating crack passes higher into the C gradient layer. Batch 1176 exhibits spalling in two separate layers, yet the basal film remained strongly bonded to the substrate.

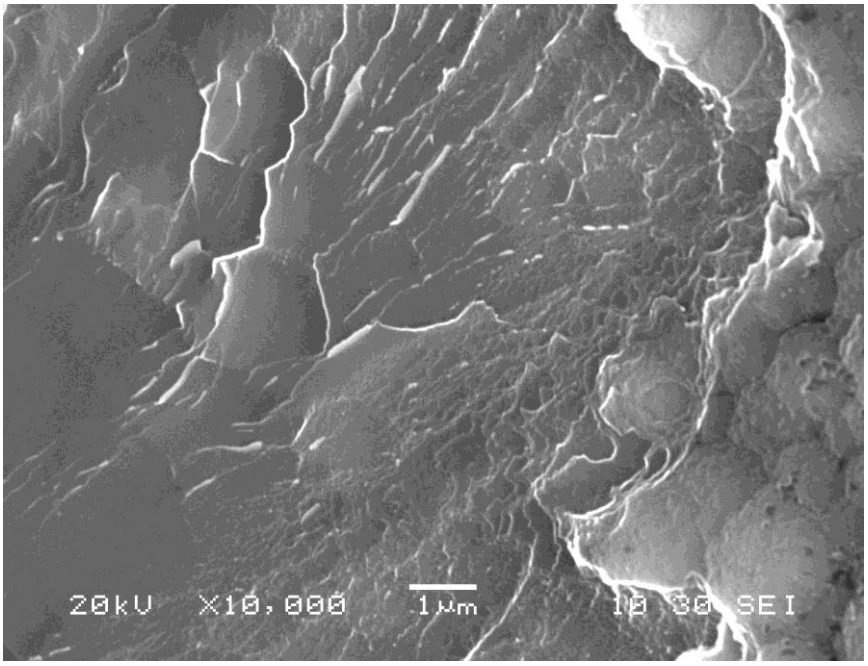

Figure 4.2.4.9-3: Failure in 1169 showing changes in fracture surface as crack progresses through gradient layer. Far left is boride basal layer, at far right is the surface of the C gradient layer.

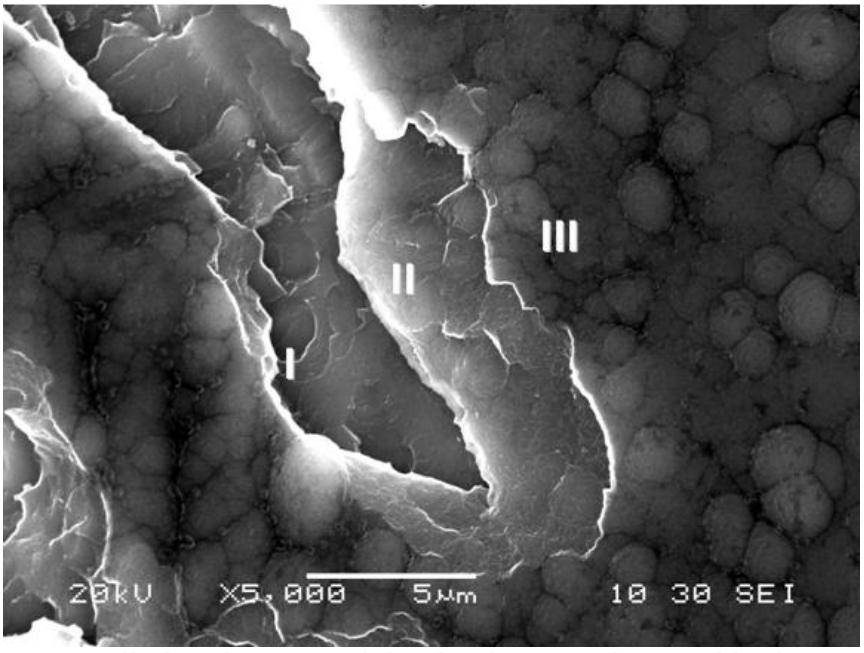

Figure 4.2.4.9-4: Two distinct layers of delamination are observed in the fracture of batch 1179. EDS shows that layer I is the boride coating, not the substrate. Layer III is the top of the carbon layer.

In addition to failure caused by indentation, scratch resistance of several Nanocoatings was tested qualitatively with a diamond stylus. **Figure 4.2.4.9-5** shows one such example in batch 1067 where ploughing and smearing are visible in the top of the image, yet compositional imaging revealed that boride columns below the surface remained intact, protected and/or lubricated by the C-rich film. With moderate-to-heavy applied pressure, the diamond stylus was only able to expose small areas of the steel substrate. While the C layer appeared to weaken the coatings in fracture, it clearly benefits sliding wear, with lubrication from graphitic C (as determined by Raman).

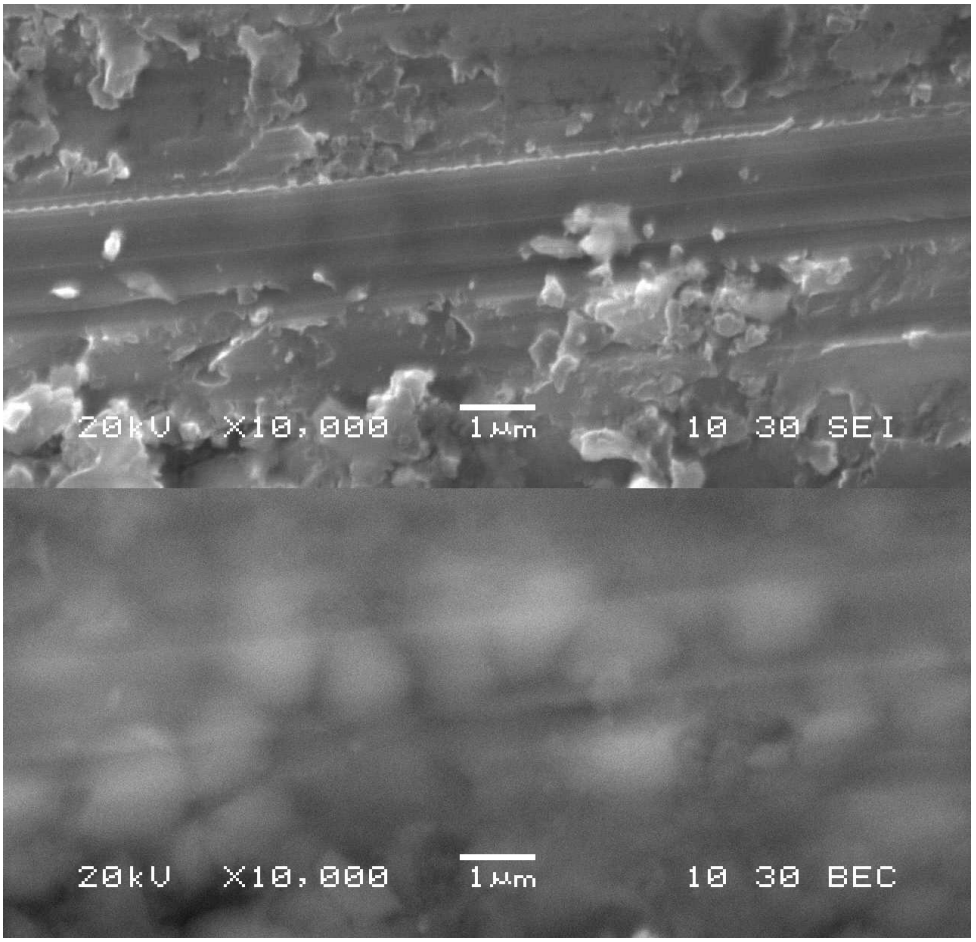

Figure 4.2.4.9-5: Topographic (top) and compositional (bottom) imaging of a scratch path on coating batch 1067.

As discussed in the earlier section on *Effects of Substrate Chemistry and Surface Finish*, superfinishing was found to have a pronounced effect on the morphology of PVD coatings. This coating was also examined in terms of its response to a vibrating probe. The objective was to assess the coating's tendency to form cracks or fracture surfaces and then to characterize these fractures/cracks. Examples of the fracture surfaces are shown in **Figure 4.2.4.9-6**. The fracture surfaces showed typical striation patterns corresponding to the columnar growth structure of the coating. Interestingly, the fracture patterns were not substantially different from those observed in coatings characterized by larger growth columns (see above). The Fe from the M2 substrate is visible as bright regions around the bottom of the craters. The few cracks that are seen appear to be transgranular, indicating the presence of strong bonding between the columns.

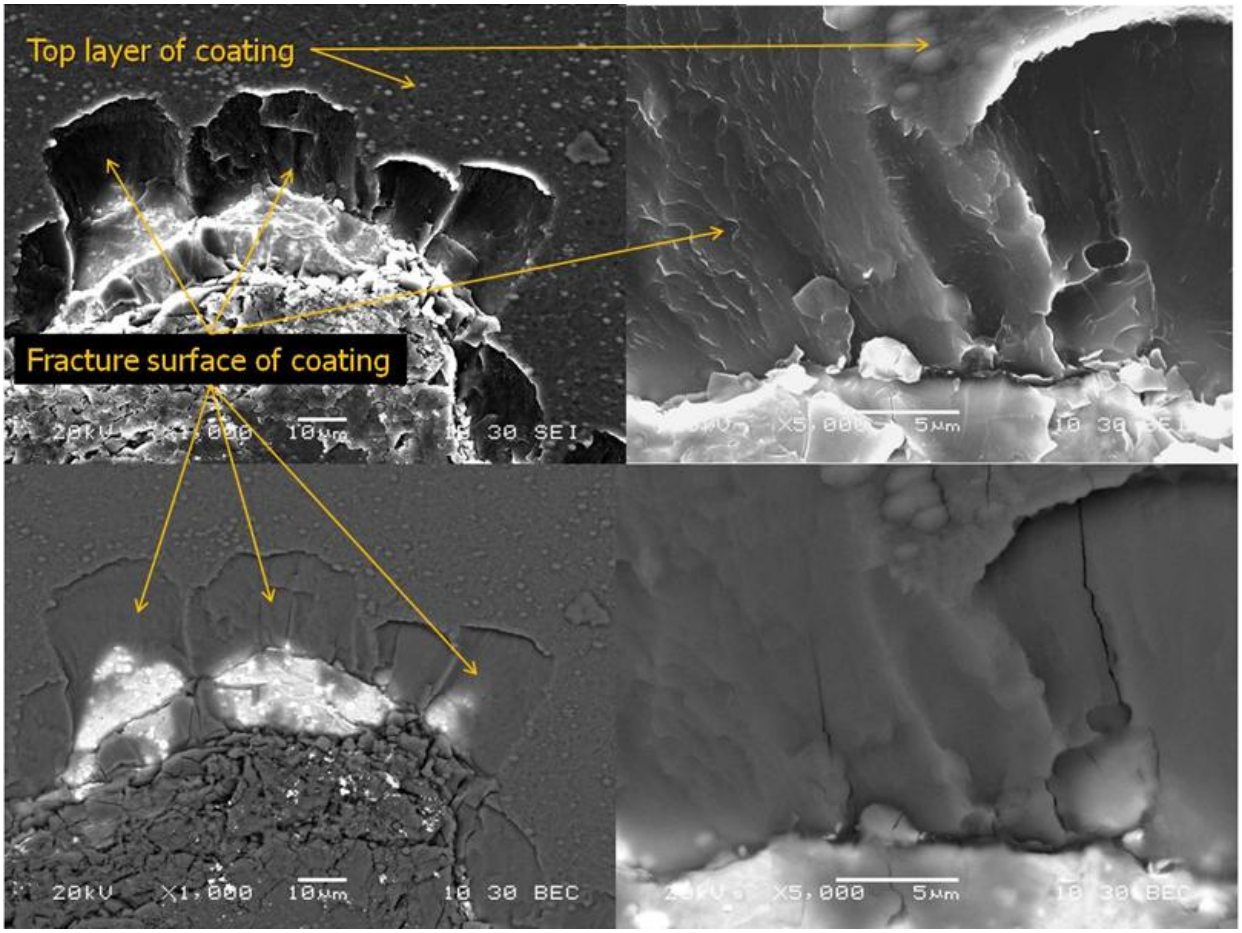

Figure 4.2.4.9-6: Effect of the introduction of a vibrating probe on the mixed-phase coating applied to a superfinished M2 substrate.

A few anomalous growth features were observed in this coating that had not been seen in other batches. These features, an example of which is shown in **Figure 4.2.4.9-7**, tend to be large clusters of columns, extending to 10 microns and larger in certain orientations. The micrograph clearly shows the presence of individual columns on the side of the structure. These features may have formed because of local variations in conditions leading to different points on the Thornton structure-zone map, leading to denser growth of the columns and a more planar morphology. The presence of these features could also be the results of a local cluster of columns sharing the same crystal habit, thereby enhancing their mutual growth through a coarsening effect.

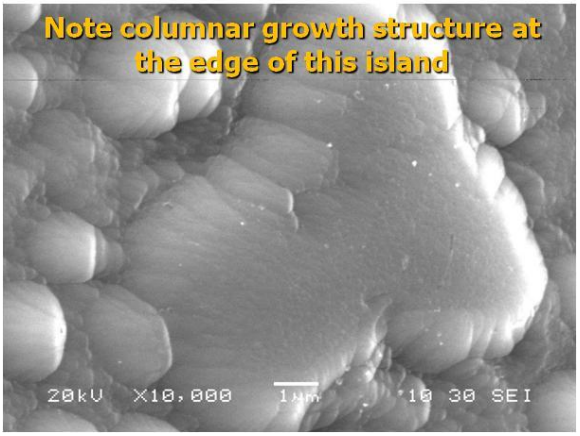

Figure 4.2.4.9-7: Example of an anomalously-large growth cluster in the mixed-phase coating applied to superfinished M2.

Cross-section analysis of PVD Nanocoatings

In order to examine coating adhesion with the substrate directly, the nature of the growth columns, and possible effects of underlying carbides, an M2 vane from a typical PVD processing batch (1182) was sectioned with a low-speed diamond wafering blade to expose a cross section of the coating for examination in an SEM. A number of different locations on the vane were examined, including the planar sides and curved contact zone. Because of the presence of high z-contrast Mo and W carbides in M2 steel, these precipitates were clearly imaged as bright regions by backscattered electrons in the SEM. **Figure 4.2.4.9-8** shows the cross section of the coated vane at 2 locations. Cracking observed near the top of the micrograph is due to differential shrinkage of the metallographic mounting compound used to prepare the specimen. The distribution of carbides in the vane is clearly seen in both the secondary and backscattered images.

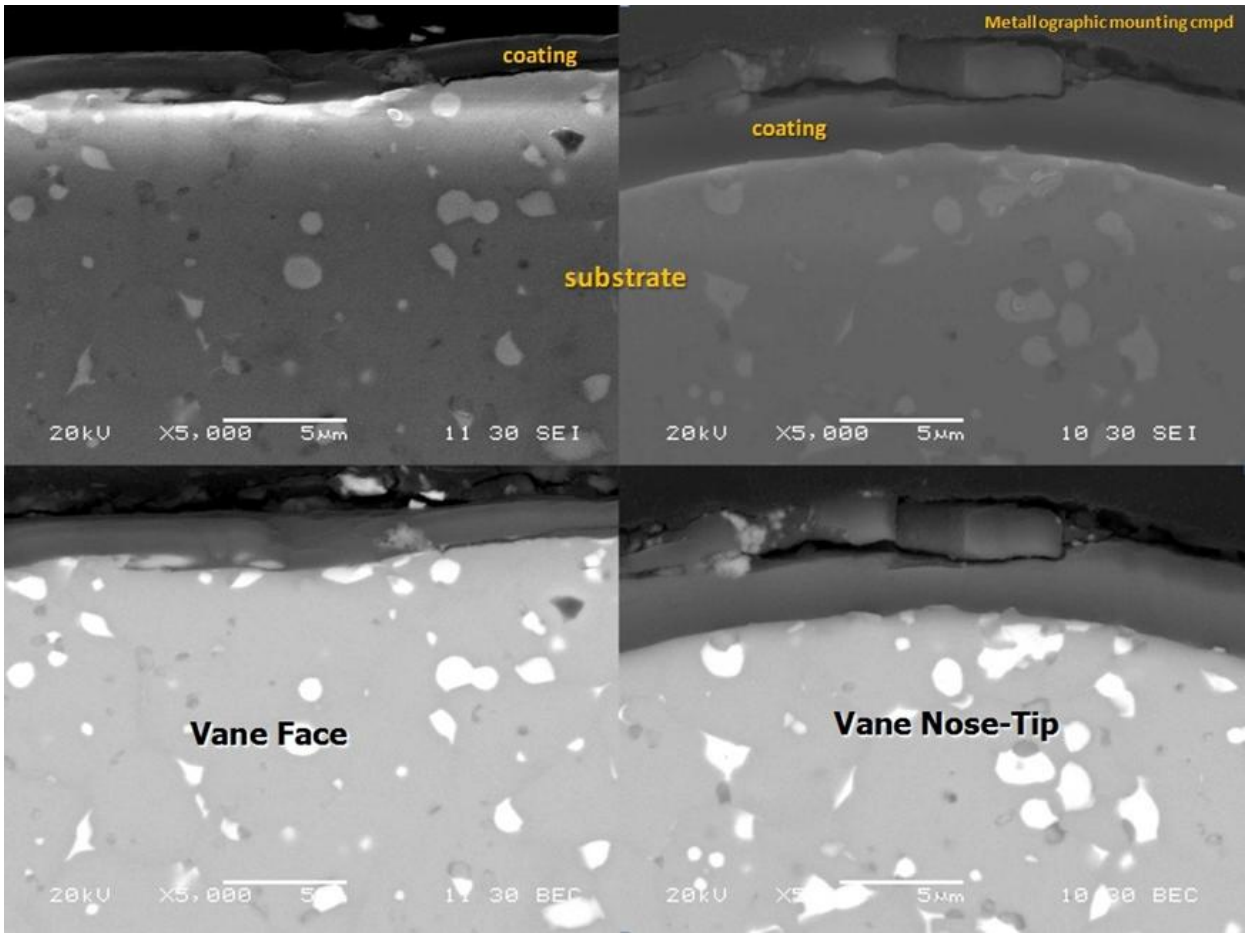

Figure 4.2.4.9-8: SEM images of two locations of a sectioned M2 vane coated with $AlMgB_{14}$-TiB_2+C.

Figure 4.2.4.9-9 shows two images of the coating in which the excellent adherence to the substrate can be seen.

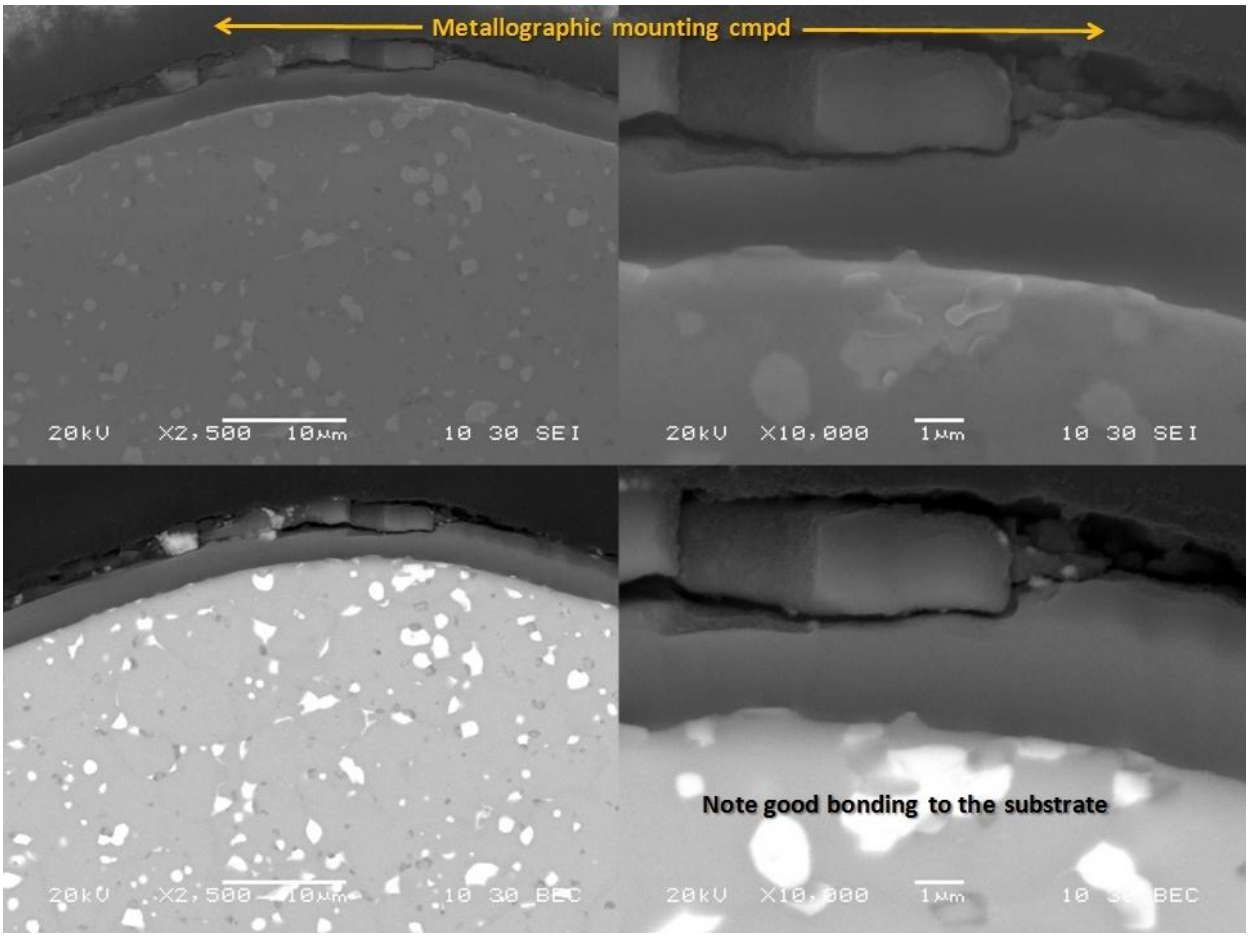

Figure 4.2.4.9-9: Cross-sectional image of coated M2 vane near the point of maximum curvature on the blade tip.

Figure 4.2.4.9-10 shows a relatively large gouge or scratch in the substrate and the way in which the coating filled the volume. This provided evidence of separate nucleation sites within the scratch. For comparison, the average coating growth column is on the order of 1 – 3 microns in diameter.

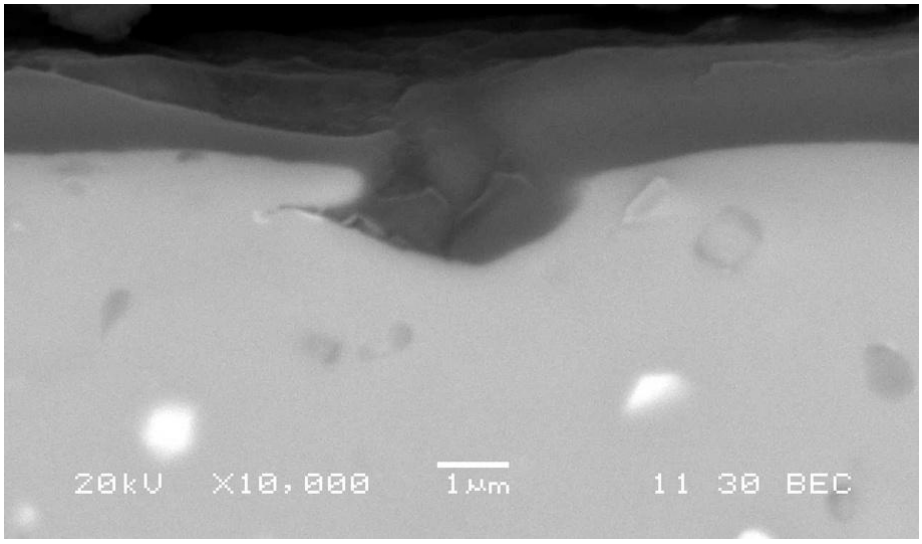

Figure 4.2.4.9-10: High-magnification cross-sectional image of a coated vane showing multiple nucleation sites within a gouge at the surface of the vane.

Figure 4.2.4.9-11 shows the boundaries between coating columns. The columns appear 1 – 2 microns in width and tend to grow normal to the local surface of the substrate.

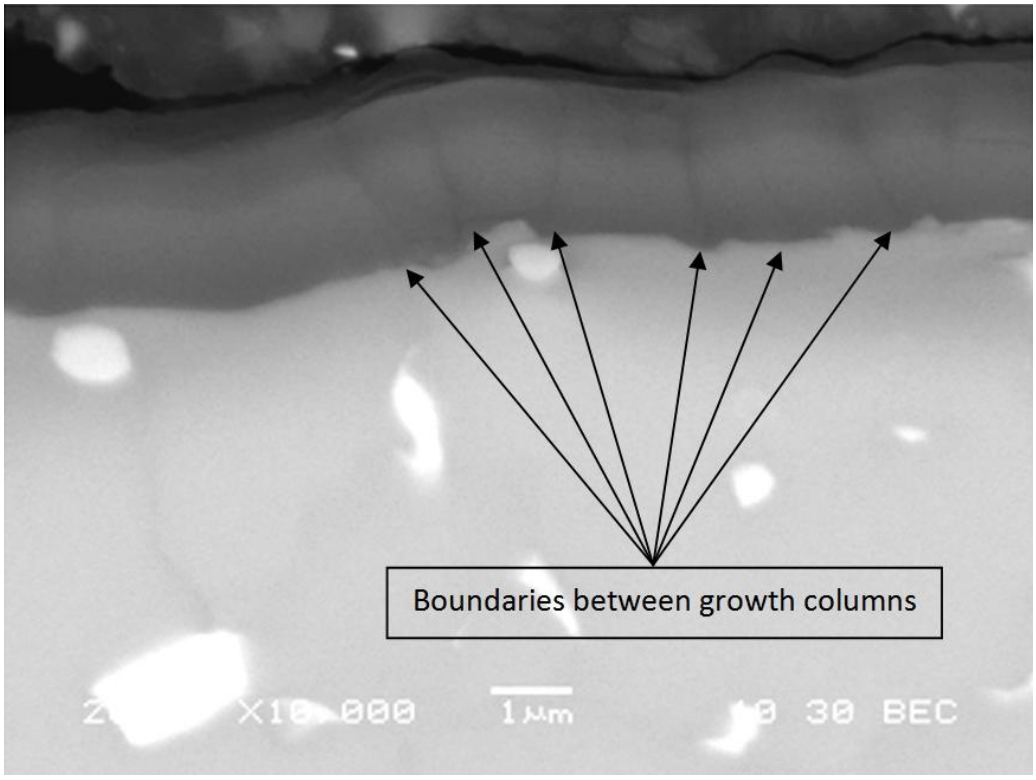

Figure 4.2.4.9-11: High-magnification image of coated M2 vane showing individual growth coating growth columns (indicated by arrows) and carbon-enrichment near the top of the coating (darker layer).

The presence of the carbon-rich top layer is seen as the darker contrast region near the upper portion of the coating. **Figure 4.2.4.9-12** shows a BSE image in which one of the carbide inclusions was located near the surface of the vane. It had been suspected that carbide inclusions might affect the nucleation and growth of the coating. However, as the figure clearly shows, there appears to be no change in coating morphology directly above or adjacent to the inclusion.

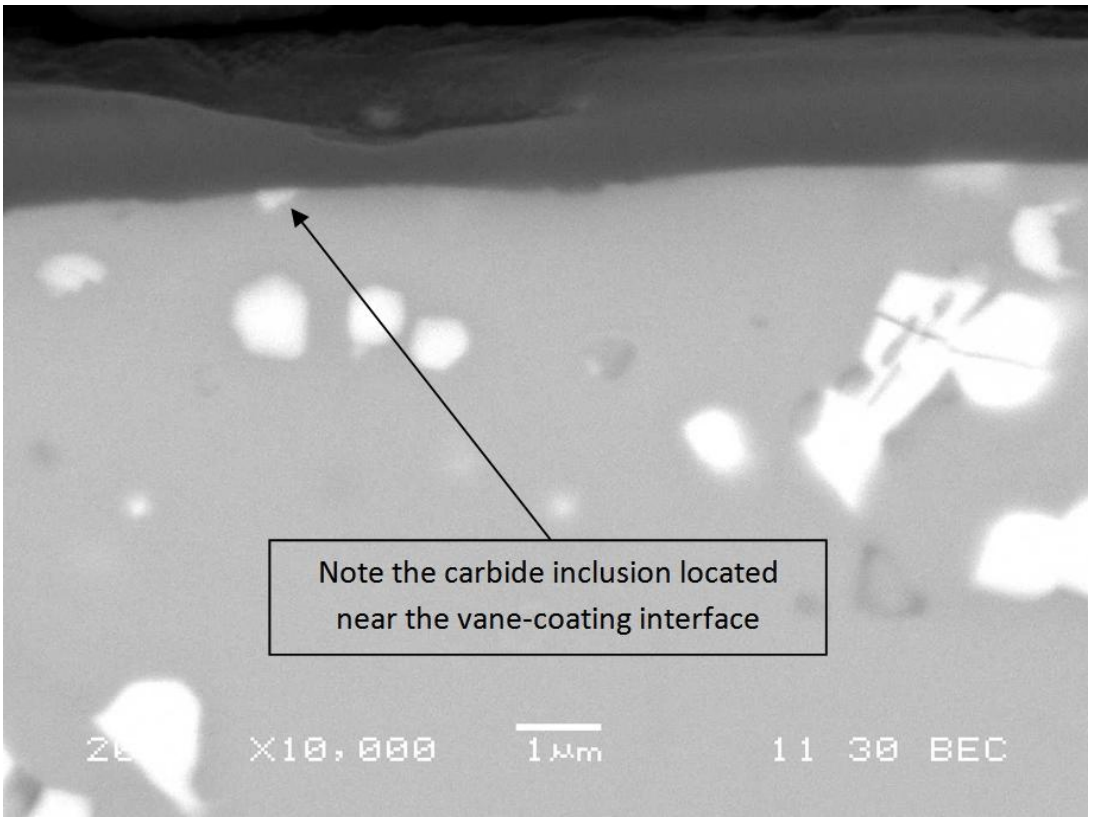

Figure 4.2.4.9-12: BSE micrograph showing the presence of a carbide inclusion near the surface of the vane.

4.2.5 Durability and Performance Testing of Hydraulic Components and Systems

Performance and durability testing of the proposed nanocoating compositions became a significant portion of the project's scope after laboratory proof of concept evaluations and bench-scale friction and wear modeling were complete. As noted in the discussions on the performance needs of each application, the key criteria for a successful product introduction are a coating that: improves upon the individual system's mechanical efficiency, reduces/minimizes any wear that lowers volumetric efficiency with time, maintains any efficiency gains over the life of the product, does not compromise product performance, in spite of the system being operated in a multitude of varying environments, is transparent in its impact to production scheduling and logistics, and can be implemented for a low cost within the overall manufacturing structure such that end customer(s) pay little for the end fuel savings.
On the last item, one of the focuses of the group was identifying suitable alternative materials that would offset some or all of any cost adders associated with the added vapor deposition processing associated with application of the nanocoating.

Bearing all of the aforementioned details in mind, then, the challenges of market acceptance become readily apparent. To address these challenges and reduce as much risk to the business division that would ultimately be responsible for product rollout, Eaton's Innovation Center personnel utilized an internal staged development process that focuses on developing sound business cases, verifying that any hypotheses associated with new technology deployment, and identifying potential business partners and cultivating those supplier-customer relations. The hypothesis testing noted focused on selection of key criteria (regardless of the application or testing performed) that could be translated upwards to tangible results that match the end customer wants and needs. An example of this thought process could be characterized by the following relevant scenario:

'A fleet owner rents skid loaders out for residential housing developments. The fleet owner offers a fuel purchase option in the rental agreement and has a total productivity maintenance system that tracks the fuel economy of each machine. Once fuel economy of a particular machine drops below the established threshold, the owner sells the loader on the open market. Prior to this sale, the owner has to establish the current fuel burn rate, as the used loader market is competitive and any gains that be advertised in diesel consumption of a particular product are desirable. Simply stated, this fleet owner is concerned about fuel efficiency and, when they purchase new equipment, shops the various equipment vendor offerings for higher efficiency. Eaton does not sell pump or motor products directly to the fleet owner, but rather sells to the equipment manufacturers that tout their products as being fuel-efficient. Any efficiency gains that Eaton can demonstrate to the equipment manufacturers that are beyond its competitive base are considered an advantage. New technologies for industrial hydraulics that yield efficiency gains will have to be large enough such that a fuel savings will be realized in the end application. Mechanical tests that the new technology is subject to will focus on measurement of the efficiency gains, verification that the gains are larger than testing error (are not lost within any noise variables), and that any gains can be realized over the life of the product through accelerated life test conditions.'

Note that aforementioned scenario used to tie customer wants and needs to actual product performance requirements does not specifically cover business related items such as costing or delivery, although a similar process will be used in these aspects as well. With the relationship

between test criteria and end-product performance established, the Eaton Innovation Center personnel then pursued dynamometer testing at the Eden Prairie Hydraulics facility to validate all performance metrics associated with the $AlMgB_{14}$-TiB_2-based nanocoatings.

4.2.5.1 Eaton Hydraulics Vane Pump

For the vane pump product line, three key test specifications were used to evaluate the performance of the proposed coatings. Components would first have to pass a brief mechanical efficiency performance test. This testing would be followed up by a step-load testing that simulates the various operating conditions that the end-application experiences in service. The final testing is a 250-hour long endurance schedule used to test long-term performance of the system. Failure of the coating during any of these tests would result in process parameter adjustments, followed up by a new run of vane components for verification.

Key performance metrics for the vane pump application are included below, for reference, in **Table 4.2.5.1-1.**

Table 4.2.5.1-1: Key performance metrics for the vane pump application

Improved Performance in Hydraulic Fluid	
Drop in flow across vane-ring interface	No drop in flow as measured during testing
Mechanical efficiency at peak pressure and speed	Yield a 2% increase in mechanical efficiency
Volumetric efficiency at peak pressure and speed	Must have same or better volumetric efficiency as current design
Maintain product life	
Match current product life	Vane tips and cam ring surfaces to be intact after endurance tests
Durability of coating	
Coating intact after endurance testing	Coating wear shall not exceed 50% of its original thickness
No delamination of coating	No coating delamination shall occur
No degradation of performance in green hydraulic fluids	
Mechanical efficiency at currently held de-rated speeds and pressures	The coating shall enable performance above the current de-rated pressure and speed while maintaining or improving upon existing mechanical efficiencies in water-based lubricants.
Volumetric efficiency at currently held de-rated speeds and pressures	The coating shall enable performance above the current de-rated pressure and speed while maintaining or improving upon existing volumetric efficiencies in water-based lubricants.
Drop in flow across vane-ring interface	No drop in flow as measured during testing

Testing results that illustrate the performance of the proposed nanocoating composition with respect to both the baseline product and a product coated with a commercially viable DLC coating are included for reference in **Figures 4.2.5.1-1.**

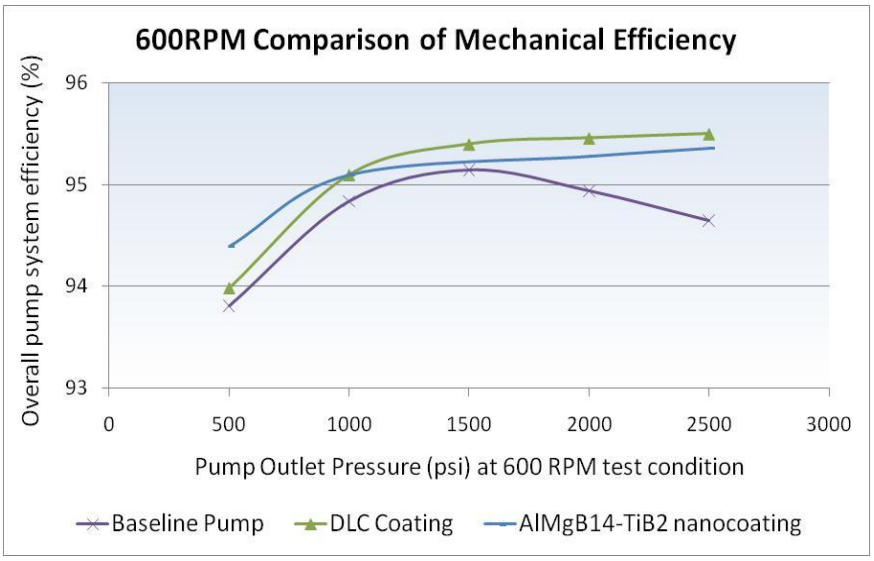

Figures 4.2.5.1-1: Mechanical efficiency characterization of hydraulic vane pump system operating at speeds of 600 RPM and outlet pressures ranging from 500-2500 psi.

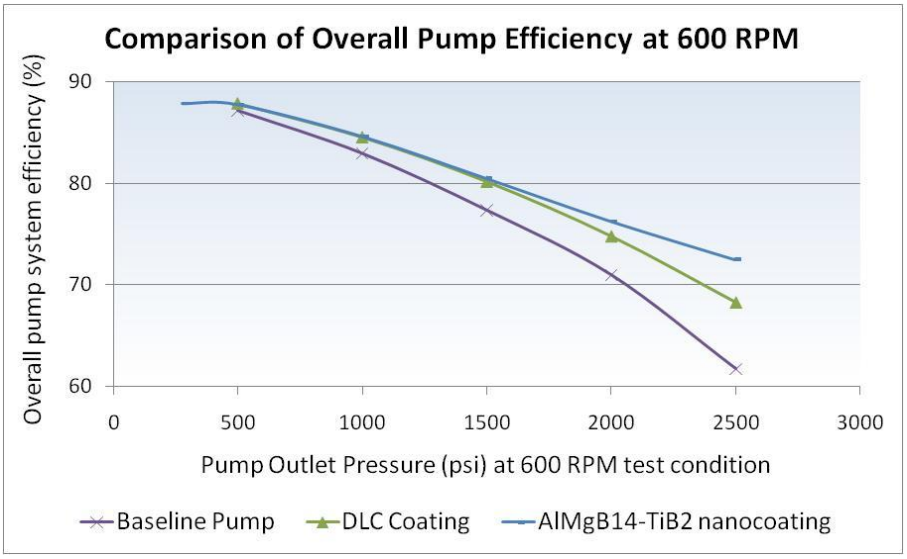

Figures 4.2.5.1-2: Overall efficiency characterization of hydraulic vane pump system operating at speeds of 600 RPM and outlet pressures ranging from 500-2500 psi.

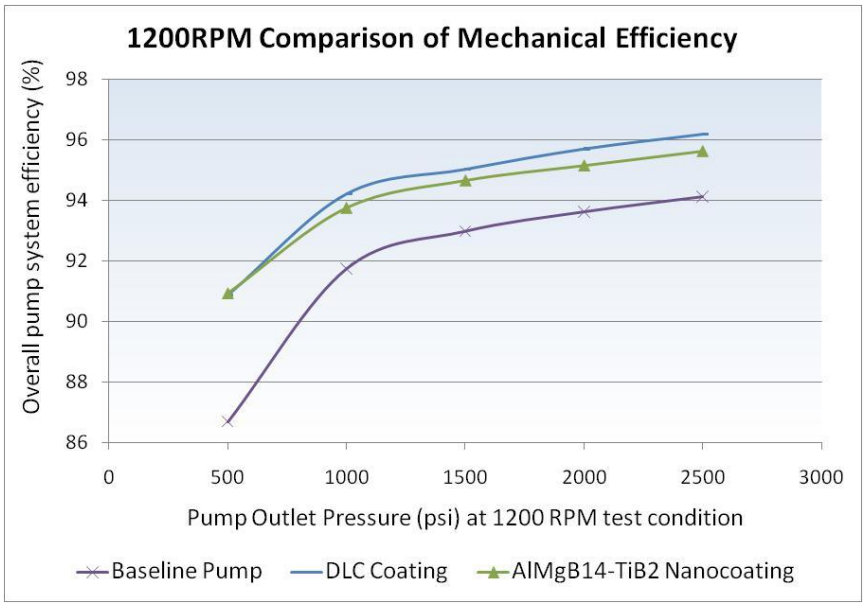

Figures 4.2.5.1-3: Mechanical efficiency characterization of hydraulic vane pump system operating at speeds of 1200 RPM and outlet pressures ranging from 500-2500 psi.

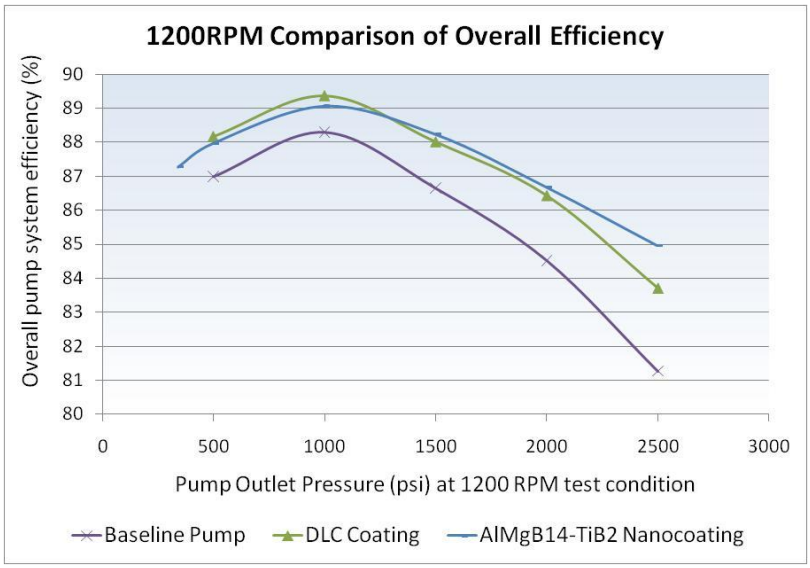

Figures 4.2.5.1-4: Overall efficiency characterization of hydraulic vane pump system operating at speeds of 1200 RPM and outlet pressures ranging from 500-2500 psi.

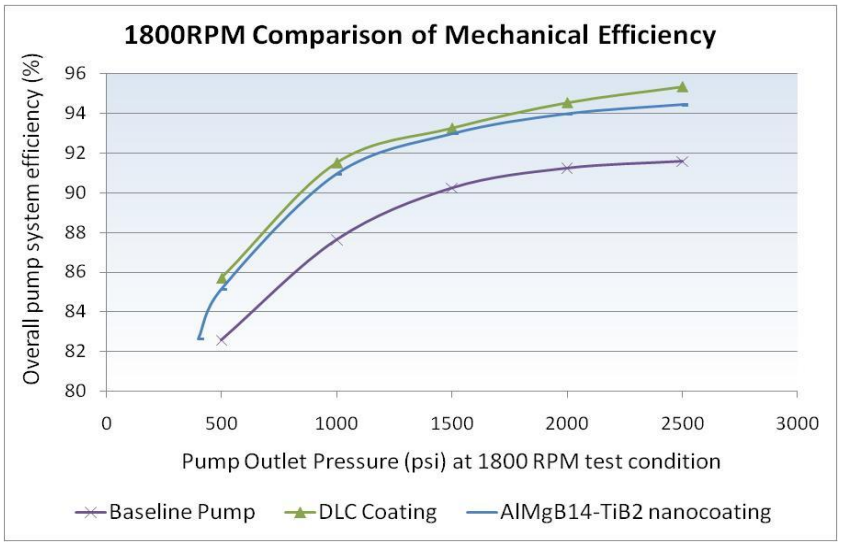

Figures 4.2.5.1-5: Mechanical efficiency characterization of hydraulic vane pump system operating at speeds of 1800 RPM and outlet pressures ranging from 500-2500 psi.

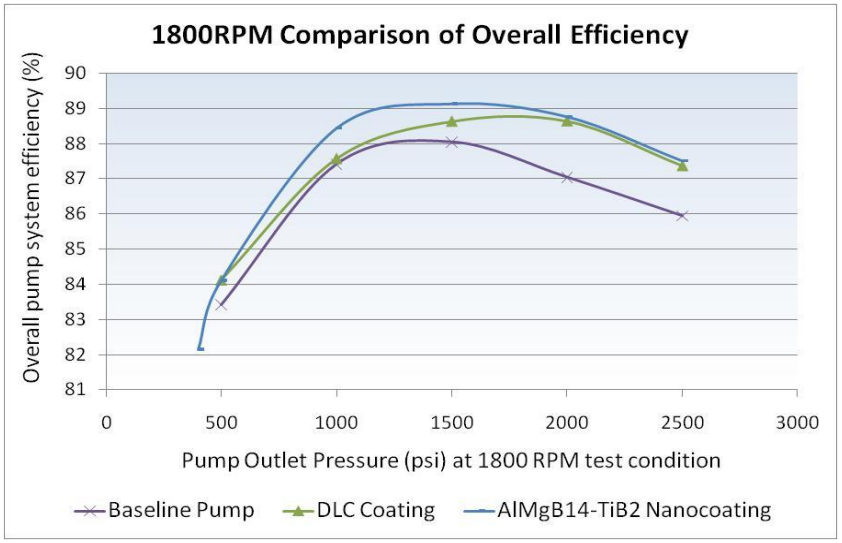

Figures 4.2.5.1-6: Overall efficiency characterization of hydraulic vane pump system operating at speeds of 1800 RPM and outlet pressures ranging from 500-2500 psi.

Evaluations performed after each of these performance tests (please note that these tests are typically short, less than 28 hours in length) indicate that there is at least a 2% efficiency gain associated with implementation of the $AlMgB_{14}$-TiB_2 nanocoating. In some cases, most notably at lowered speeds, the efficiency gains are even larger.

When the focus was shifted to use of the coatings in green hydraulic lubricants, a similar effect was noted; whereby the efficiency of the system was found to be as good or better than existing product, even when the system's speed and pressure were increased by over 10%. Note that in water-glycol-based hydraulic fluids, vane pumps are 'de-rated' to reduce the damage imparted to the components through operating in high viscosity fluids.

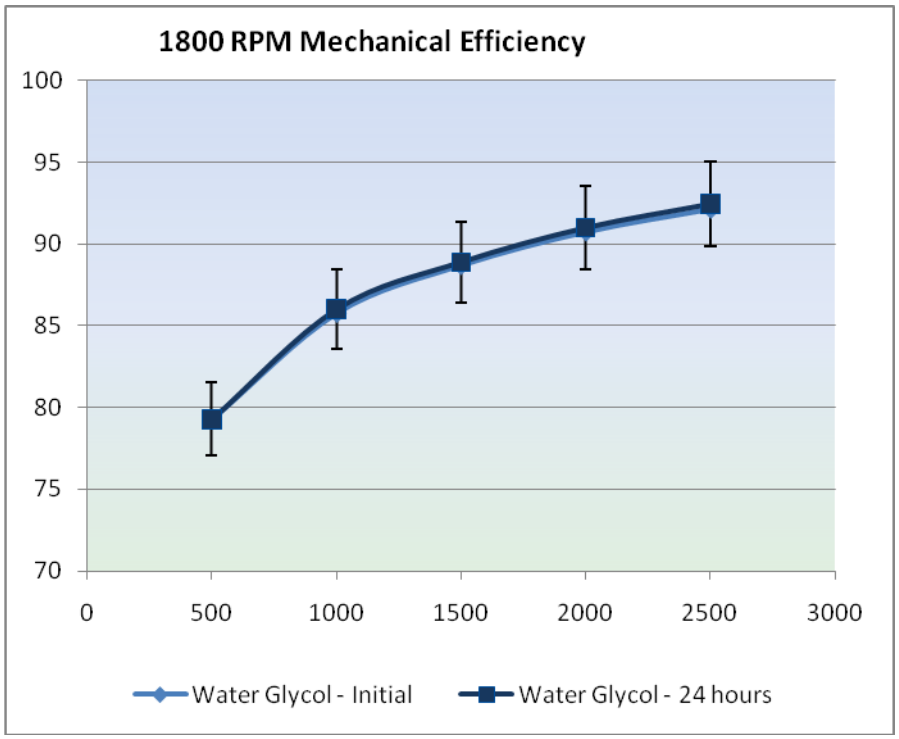

Figures 4.2.5.1-7: Mechanical efficiency characterization of hydraulic vane pump system operating at speeds of 1800 RPM and outlet pressures ranging from 500-2500 psi. Note that this particular system was operating with water-glycol.

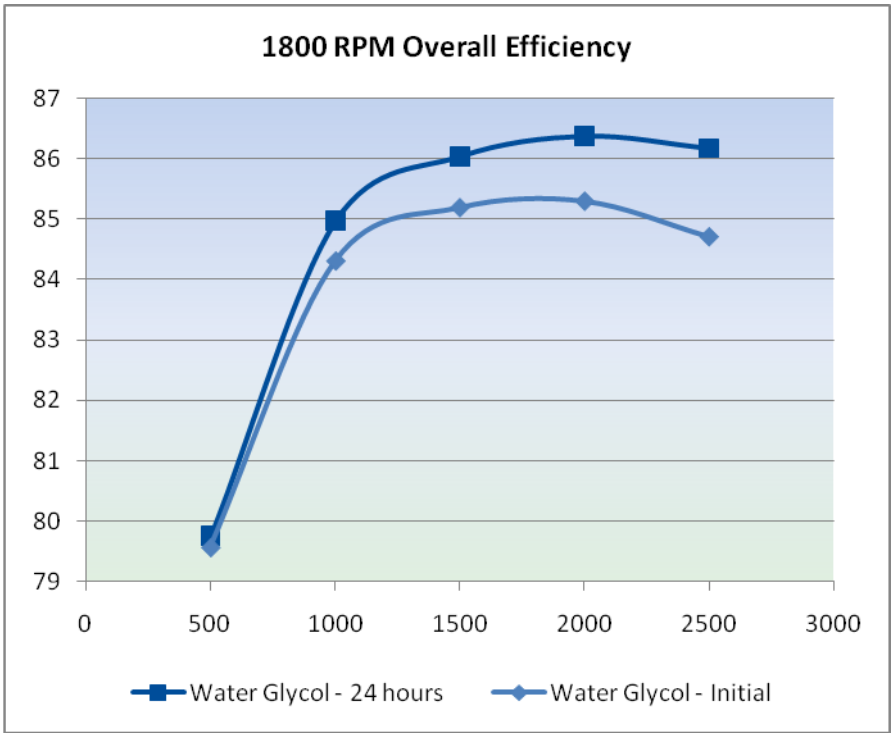

Figures 4.2.5.1-8: Overall efficiency characterization of hydraulic vane pump system operating at speeds of 1800 RPM and outlet pressures ranging from 500-2500 psi. Note that this particular system was operating with water-glycol. Also note that the system's efficiency improves with time.

The plots illustrating the performance of the coated vane pump blades show that, over time, the overall efficiency of the system actually improves in spite of little to no changes in the mechanical efficiency (remember, again, that overall efficiency is the product of volumetric efficiency and mechanical efficiency). In the testing data shown, the volumetric efficiency gains associated with an even wearing coating are a significant influence on the system's performance. It was found, through this testing, that the even wearing nature of the boride films enhances the volumetric efficiency of vane pump products by elimination of asperity contacts and in the restoration of a linear contact area. Any small volumetric losses across the interface are eliminated as the coatings (and the counterface) begin to wear. A correlative plot was developed to show the relationship between end of performance surface finish and volumetric efficiency. While not a direct relationship, there is an inherent tendency for evenly wearing films to exhibit a higher volumetric efficiency than films that spall or wear unevenly.

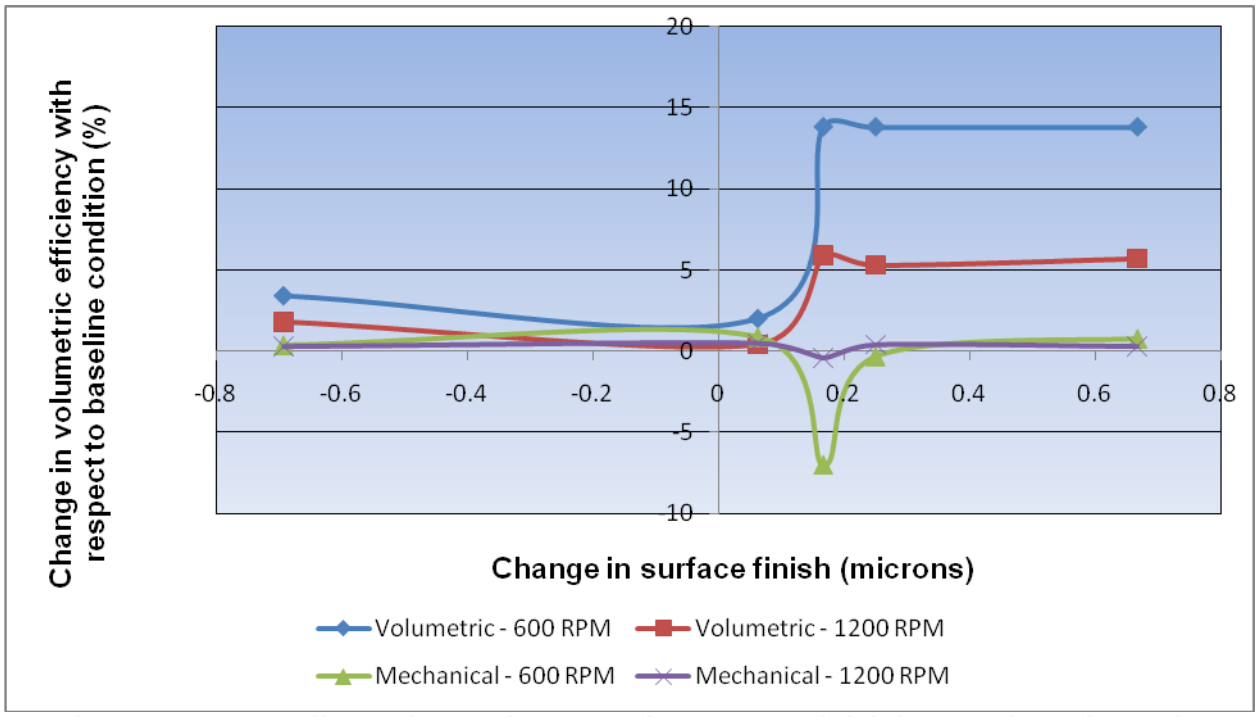

Figures 4.2.5.1-9: Illustration of the effect that surface finish has on the volumetric efficiency performance of hydraulic vane pumps operating in Mobil DTE-24™ fluid.

To ensure that after all performance tests the various applied coatings were not removed, scanning electron microscopy and energy dispersive spectroscopy were performed at Eaton's Innovation Center. On many of the $AlMgB_{14}$-TiB_2 films deposited, no exposed base material was identified after the short (less than 30 hours) performance test. Evaluation of the vanes that yielded mechanical efficiency gains both before and after the 250-hour long endurance test showed insignificant changes to the coating structure and morphology; the coated surfaces of the vane were found to be in very good condition and the coating was well adhered to the surface. After thorough examination, some very small areas exhibited exposed substrate, though even these areas still exhibited the presence of a thin film of TiB_2. While several films also showed complete removal of the coating, this is directly related to the applied processing parameters and not the nature of the boride films themselves.

Post durability analysis was performed on the vane blades that were run in water- glycol (Houghton 419R). A key finding in regards to these vane blades over tested parts run in DTE-24 is that the surfaces were very finely polished (below 0.03 micron surface finish along the contact interface). Further analysis of these vanes revealed that the coating itself was removed completely, confirming that the reaction between the water- glycol and the developing boric acid/boron oxide occurred. The final item to note on the development of very finely polished surfaces is that the water-glycol testing helps establish the theory that gradual wear to coatings, even those that are completely removed, results in greater volumetric efficiencies than coatings that wear rapidly or unevenly with respect to time.

4.2.5.2 Eaton Hydraulics valve-in-star motor

For the hydraulic motor (VIS) product line, two key test specifications were used to evaluate the performance of the proposed coatings. Coated components would first have to demonstrate efficiency gains at lowered operating speeds (below 4 RPM) to simulate the startup conditions of hydraulic motors in field use. This would be followed by performance testing at rated motor speeds. This second round of tests would be used to assess any mechanical efficiency gains associated with the general operation of the system. When translated upwards into market use-case terms, low speed motor efficiency means that the system is more fuel efficient in start-stop-start cases. Similarly, the torque response associated with this particular motor's design would be improved at low equipment speeds. As an example, a strong emphasis is placed on lifting power while the equipment is stationary. More work can be done over a fixed period if the motors torque is more readily available. For the tests at rated motor speeds, increased performance at the application level translates to greater fuel economy.

Key performance metrics for the valve-in-star (VIS) motor application are included below, for reference, in **Table 4.2.5.2-1**

Table 4.2.5.2-1: Key performance metrics

Performance Related Functionality	
Starting torque efficiency	Yield at least a 10% gain in mechanical efficiency over the baseline system
Mechanical efficiency at rated motor speeds	Yield at least a 3% increase in mechanical efficiency
Volumetric efficiency at rated motor speeds	Yield at least a 3% increase in volumetric efficiency
Maintain product life	
Match current product life	All critical components to be intact after endurance tests
Improve open system life at 100rpm and intermittent pressure changes near rated system pressure	Demonstrate a 20% improvement in system life above the baseline
Durability of coating	
Coating intact after endurance testing	Coating wear shall not exceed 50% of its original thickness
No delamination of coating	No coating delamination shall occur

As reviewed in the section discussing the various performance needs, efficiency gains were realized when the critical components were coated. The improvements in mechanical efficiency were not as significant as originally hoped, though, and so a new array of testing was planned to assess the impact of single, main effects as well as interaction effects. Refer to **Table 4.2.5.2-2** for the planned design of experiments testing used to assess the impact of the nanocoatings. Main effects and interaction plots are included for reference in **Figures 4.2.5.2-1** through **4.2.5.2-4.**

Table 4.2.5.2-2: Mechanical efficiency performance using nanocoatings on single, dual, and triple components of the VIS Motor.

Coating DOE Test Results					
Test Run	Ring	Roll	Star	Coated Parts	Min. Mech. Eff.
1	0	0	0	Baseline (None)	46.3%
2	0	0	1	Star	50.4%
3	0	1	0	Roll	51.7%
4	1	0	0	Ring	49.7%
5	0	1	1	Roll & Star	52.3%*
6	1	0	1	Ring & Star	46.4%*
7	1	1	0	Ring & Roll	54.4%
8	1	1	1	Ring, Roll & Star	58.0%

Note: "0" = No Coating, "1" = Coating

* Observed coating delamination on rolls when running against coated star
** Observed some delamination on star potentially due to assembly

Part	Coating
Ring	$AlMgB_{14}$-TiB_2+C
Roll	DLC
Star	$AlMgB_{14}$-TiB_2+C

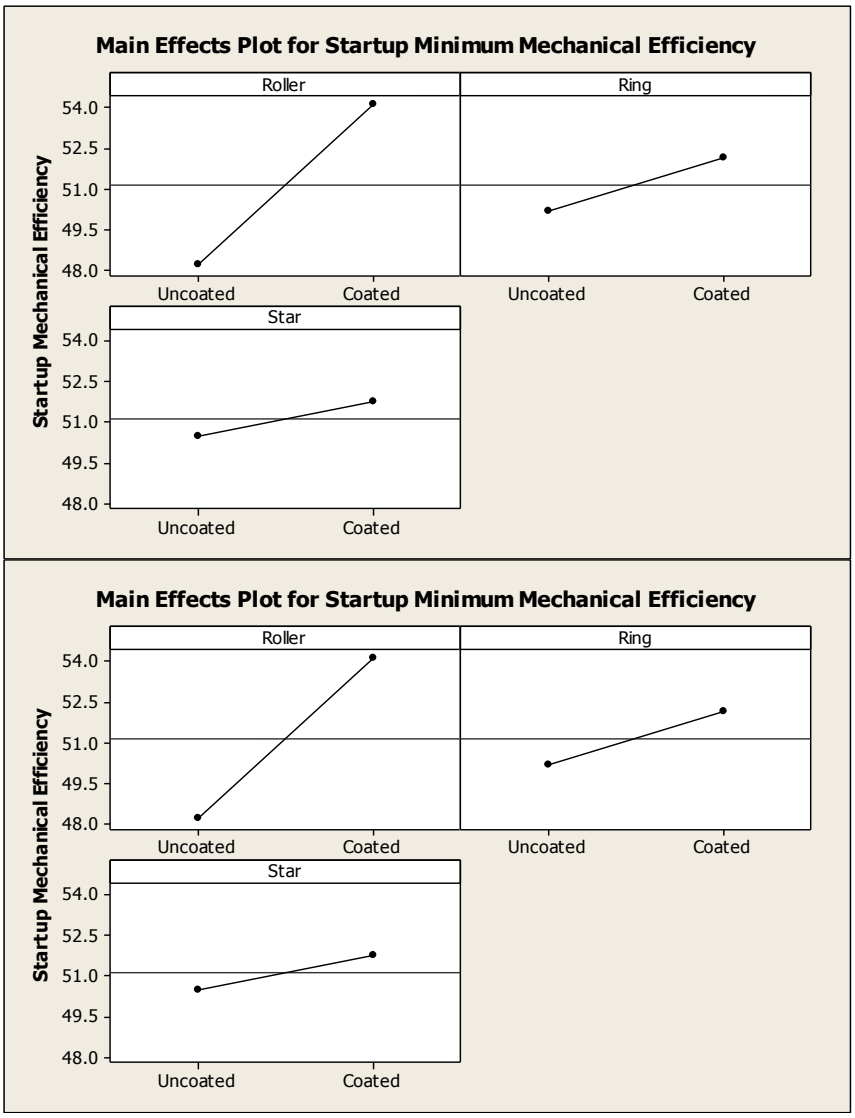

Figure 4.2.5.2-1: Design of experiments main effects plots used to identify the single largest contributor to efficiency improvements in the tested hydraulic VIS motors.

Note that main effects plots simply demonstrate which factor, amongst all those evaluated, has the greatest degree of influence over the tested outcome. Following this line of reason, were only a single component coated, application of the $AlMgB_{14}$-TiB_2+C coating to motor rollers would produce the greatest efficiency gain.

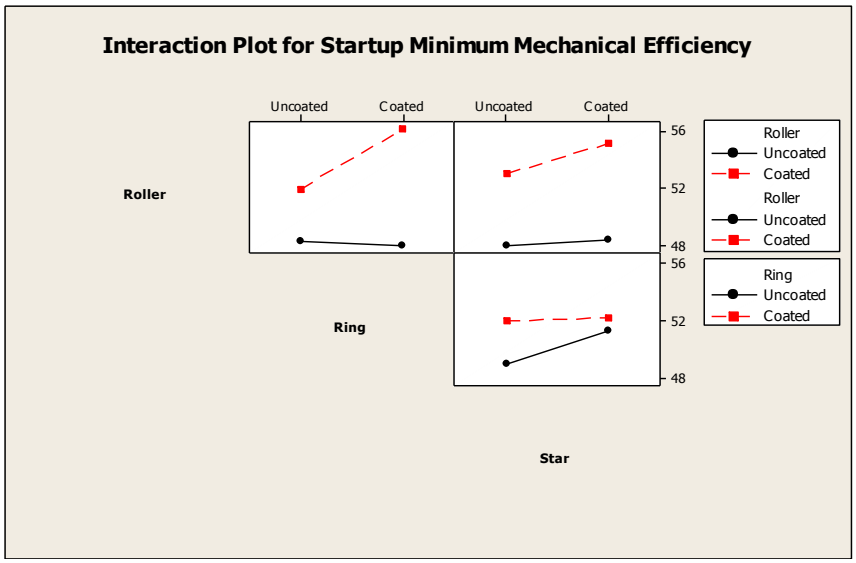

Figure 4.2.5.2-2: Design of experiments interaction effects plots used to identify any positive (or negative interactions) that contribute to efficiency improvements in the tested hydraulic VIS motors. In this particular system, it is apparent that there are no strong interactions and that addition of the coating, regardless of the component, yields a gain in mechanical efficiency.

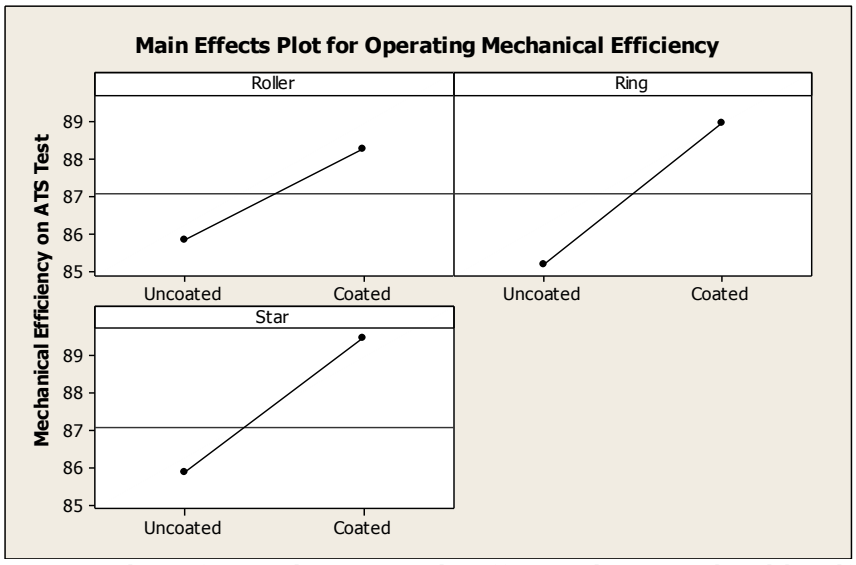

Figure 4.2.5.2-3: Design of experiments main effects plots used to identify the single largest contributor to efficiency improvements in the tested hydraulic VIS motors. For the tests at rated motor speed, all of the factors appear to exhibit similar significance in the improvement of mechanical efficiency.

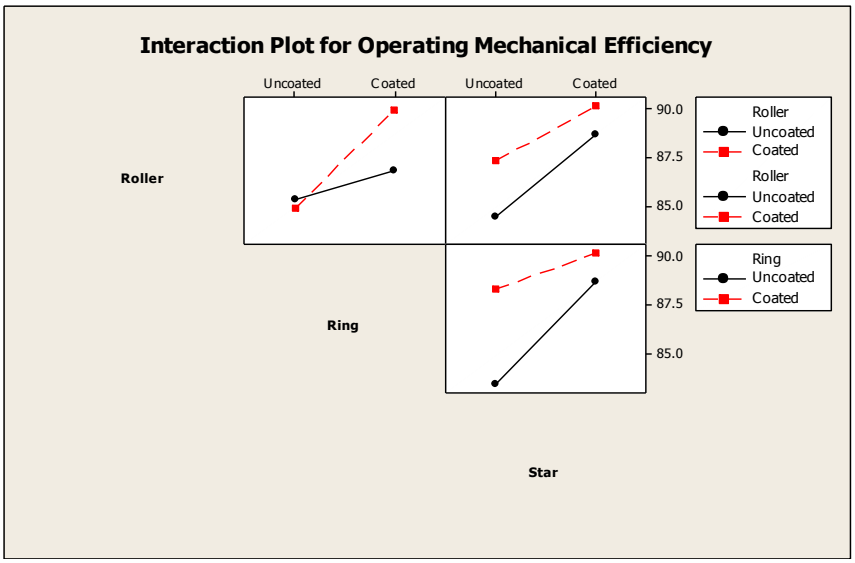

Figure 4.2.5.2-4: Design of experiments interaction effects plots used to identify any positive (or negative interactions) that contribute to efficiency improvements in the tested hydraulic VIS motors (at rated motor speed). From this particular plot it could inferred that there may be a slight interaction between coating the rollers (application of DLC) and the ring (application of Eaton's $AlMgB_{14}$-TiB_2+C coating). This interaction, however, appears to be cooperative in nature; coating either the ring or the rollers also yields an efficiency gain.

The primary reason for choosing these particular combinations of components lies in the fact that testing performed on DLC-coated rollers resulted in significant coating removal. Testing of $AlMgB_{14}$-TiB_2 + C coated rollers would confirm if this phenomenon was unique to DLC-coated rollers against an $AlMgB_{14}$/TiB_2 + C coated star valve, or if this is due to excessive contact stresses that develop between the star valve and roller that tends to shear the coating. A key finding in the second round of testing is that manufacturing tolerances of both the roller and the star valve play a significant role in the overall performance of the coating (and, accordingly, in a coated motor system as well). In tests performed on motor systems with little to no machining tolerances to accommodate the coating thickness, the performance of tested motors actually dropped because of excessive contact stresses that sheared the coating from the roller substrate material. Given that the tolerances associated with both star and roller components are specified in the 0.001" realm (25.4 μm) and the associated coatings range from 3-4 microns, the coating thickness was considered a negligible addition to the overall dimensions of these components. Internal discussions and reviews revealed that, in some cases, the motor components have to be machine-pressed together for final assembly. In perspective, while the original tests had negated the impact of geometric tolerancing, further studies incorporated machine stock removal into the manufacture of test components. Refer to Table VI for performance data illustrating the effect of this efficiency drop on coated motor systems identified as having interference fits and Figures 6 and 7 for representative photomacrographs documenting the coating removal that occurred during their assembly and operation. Note that both motor systems 09A and 09B consisted of $AlMgB_{14}$-TiB_2+C coated rollers. In the case of kit 09A, the star valve was coated with $AlMgB_{14}$-TiB_2+C and the ring was not coated. In kit 09B, ring was coated with $AlMgB_{14}$-TiB_2+C and the star valve was not coated.

Table 4.2.5.2-3: Performance data for VIS motor systems coated with $AlMgB_{14}$-TiB_2+C as compared to baseline system.

Motor	Day	Speed	Pressure	Min. Mech. Eff.	Max. Mech. Eff.	Avg. Mech. Eff.
1	Baseline	0.1	5000	49.37	65.66	57.77
1	09A	0.1	5000	41.64	60.25	51.51
1	09B	0.1	5000	45.83	62.52	54.70

Figure 4.2.5.2-5: Evidence of coating removal, suspected to be due to assembly and operation, noted on VIS motor roller.

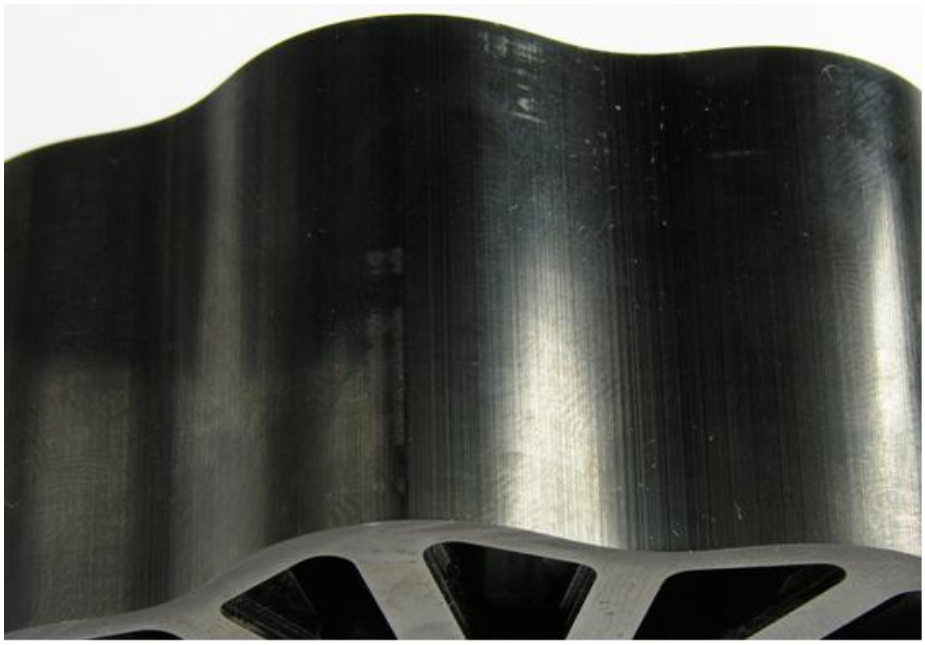

Figure 4.2.5.2-6: Evidence of coating removal (scuffing) associated with assembly and operation on VIS motor star valve.

A final review of the various test conditions and coating parameters revealed that coating the motor rollers does lead to short term efficiency gains, although the exceedingly high contact pressures associated with long term performance (greater than 150ksi) does tend to produce coating delamination. Operation of the motor system with coated star valves and coated rings will still yield performance improvements in excess of the 10% target set.

Long term (200-hour) testing of the coated motor system was performed and the results indicate that the initial performance gains noted during the proof-of-concept evaluation were indeed sustainable. Refer to these results in **Table 4.2.5.2-4.**

Table 4.2.5.2-4: Dynamometer test data for coated VIS motor components tested on the product endurance schedule.

	ATS Testing			Startup Efficiency Testing	
	Volumetric Efficiency (%)	Mechanical Efficiency (%)	Overall Efficiency (%)	clockwise (%)	counter clockwise (%)
Prelife	NA	NA	NA	59	54
22 hrs	88	93	82	58	53
44.5 hrs	88	93	82	57	49
68.5 hrs	87	93	81	56	49
92.5 hrs	92	90	83	56	49

Data from a baseline VIS motor is included below to illustrate the gains noted when using nanocoatings.

Table 4.2.5.2-5: Dynamometer test data for baseline (not coated) VIS motor components tested on the product endurance schedule.

	ATS Testing			Startup Efficiency Testing	
	Volumetric Efficiency (%)	Mechanical Efficiency (%)	Overall Efficiency (%)	clockwise (%)	counter clockwise (%)
Baseline	82	93	76	44	49

Efficiency plots for the coated components are included in **Figure 4.2.5.2-7.**

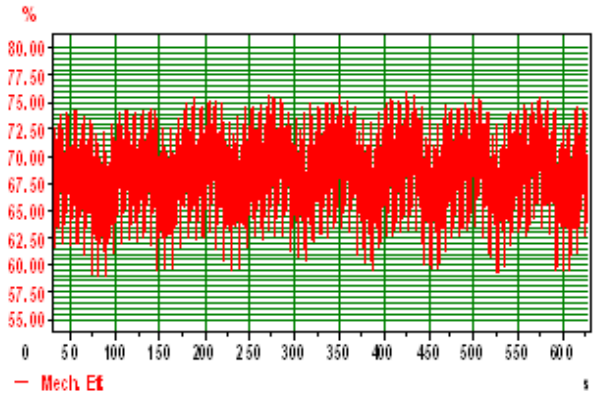

14a. Efficiency trace at "Pre-Life" stage of testing.

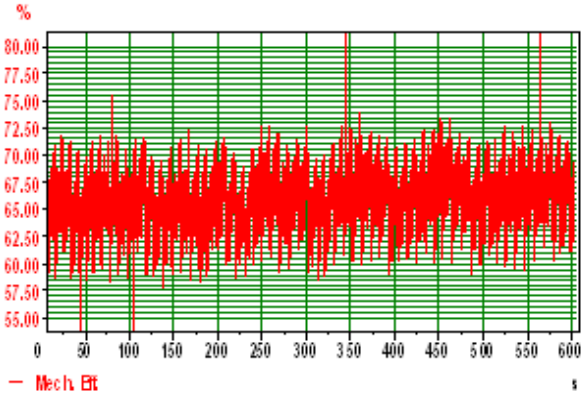

14b. Efficiency trace at 22 hours into testing.

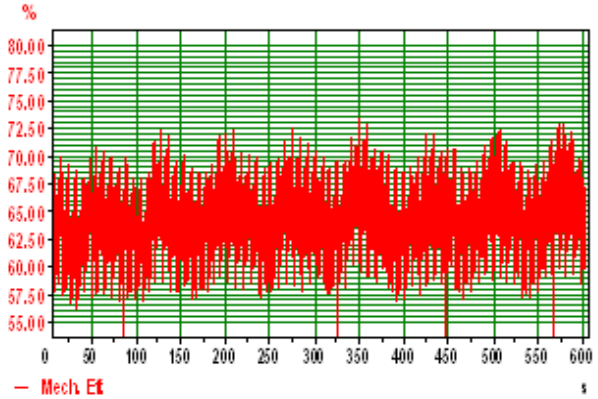

14c. Efficiency trace at 45 hours into testing.

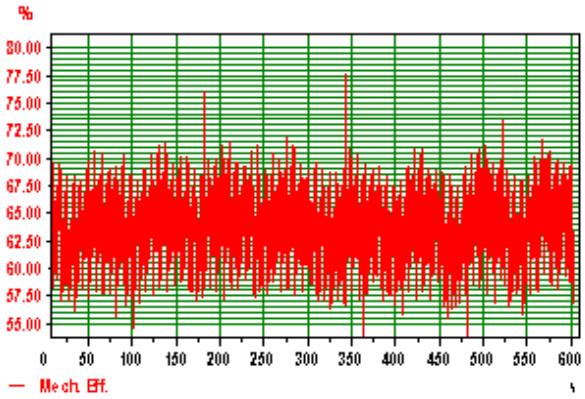

14d. Efficiency trace at 69 hours into testing.

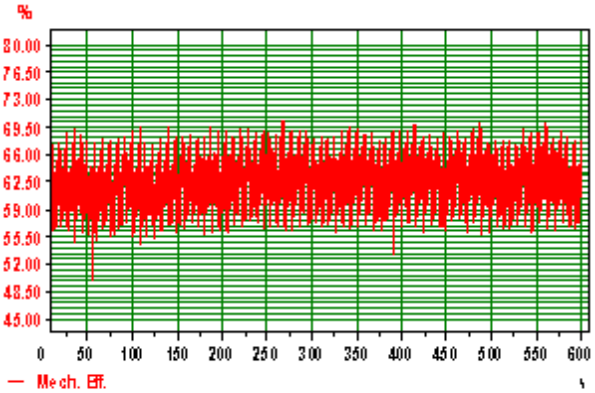

14e. Efficiency trace at 92 hours into testing

Figure 4.2.5.2-7: Mechanical efficiency plots for startup torque dynamometer testing.

4.2.5.3 Eaton Hydraulics Piston Pump

Testing from vane pumps and VIS motors showed that the $AlMgB_{14}$-TiB_2-based nanocoating provides both efficiency and durability improvements above the current baselines. The milestone amongst team members was that similar product enhancements would be realized in hydraulic piston pumps as well. For reference, current annual volumes of these systems are, on average, 4-5 times those of either vane pumps or VIS motors. With this noted, any realized efficiency gains would be translated to much larger energy savings assuming market acceptance. As a multitude of components were selected for the first round of evaluations, any performance tests would be repeated on an individual component basis, followed on by system testing where all of the selected components were coating using the Eaton $AlMgB_{14}$-TiB_2 derivative. The final testing selected was 250+-hour endurance schedule followed by a post-durability mechanical efficiency evaluation. The first round of mechanical testing performed confirmed that there was indeed a mechanical efficiency gain associated with application of the nanocoating. In some components, these gains were as large as 4% over the baseline system. Similarly, efficiency gains were realized when all coated components were tested simultaneously. Results are summarized in **Table 4.2.5.3-1.**

Table 4.2.5.3-1: The impact of coating singular components to Eaton's aerospace piston pump system efficiencies. For reference, the final row represents the combined impact of all components coated.

Component coated	Efficiency improvement over baseline system
Nutating plate	1%
Wear plate	2%
Pistons	3%
Wafer Plate	4%
All components	4%

Noting in **Table 4.2.5.3-1.**, it would appear that, if only one component was preferred because of cost or simplicity of production, then the wafer plate would be chosen. What this table does not take into consideration is the interactive effect of two components (e.g. the piston and the wafer plate). Although an "all components coated" test was pursued, further evaluation using a design of experiments (DOE) approach would be warranted.

Full performance profiles of the system, including each operating condition and the before/after durability schedule (280+ hours) are included in **Figure 4.2.5.3-1 through 4.2.5.3-6.**

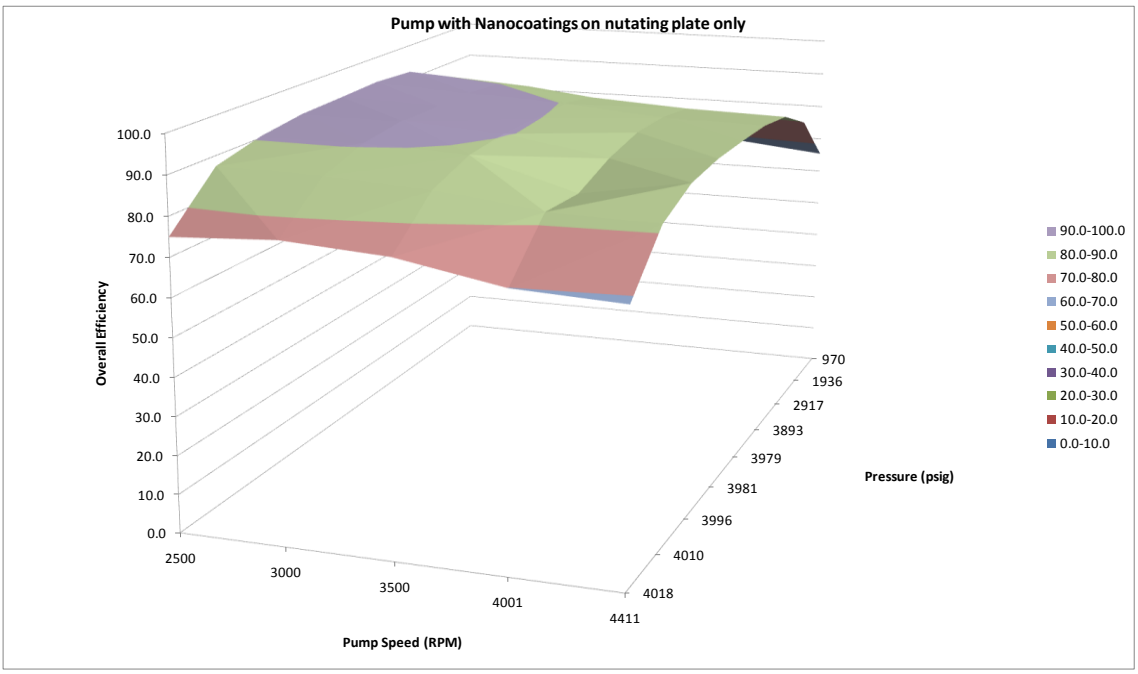

Figure 4.2.5.3-1: Impact of pump efficiency associated with the application of the $AlMgB_{14}$-TiB_2+C coating on the nutating plate. It was not expected that coating this component would yield a significant improvement in system efficiency, as the contact points are relatively small.

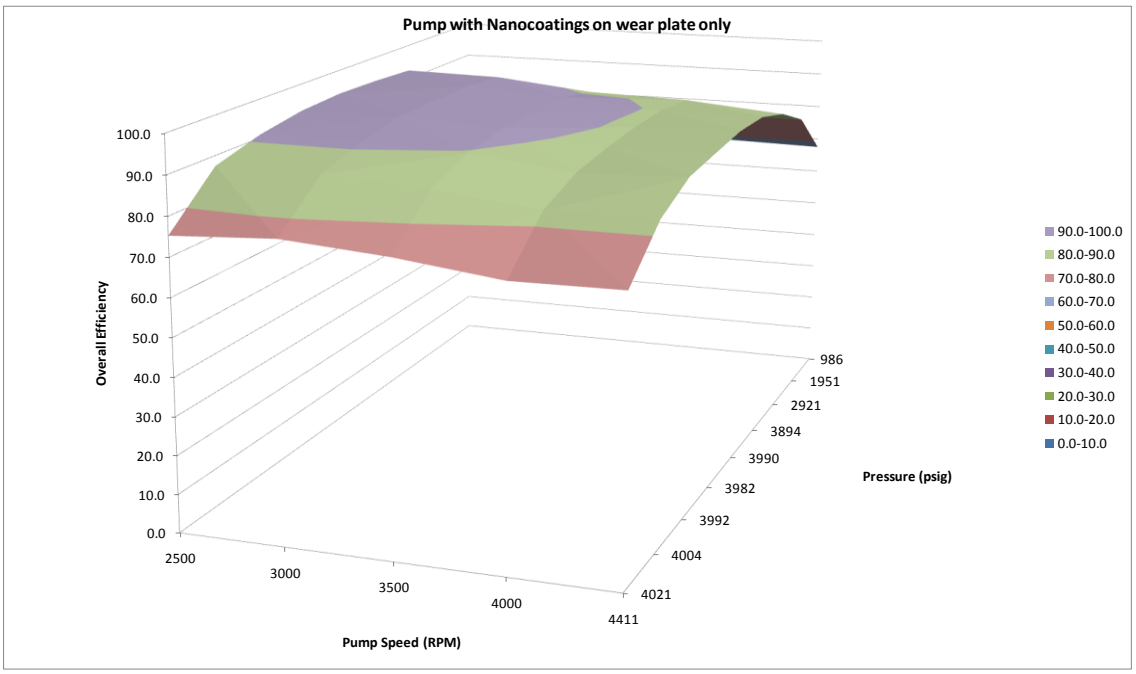

Figure 4.2.5.3-2: Impact of pump efficiency associated with the application of the $AlMgB_{14}$-TiB_2+C coating on the wear plate. It was not expected that coating this component would yield a significant improvement in system efficiency, as the piston shoes are pressure balanced as the rotating kit increases in relative velocity.

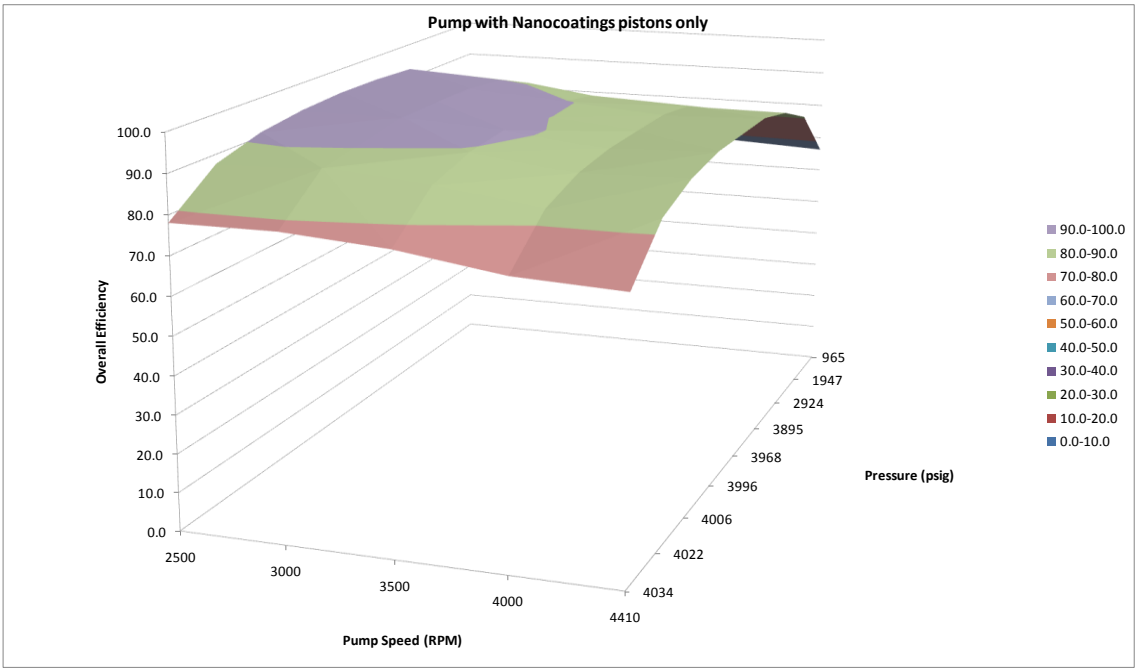

Figure 4.2.5.3-3: Impact of pump efficiency associated with the application of the $AlMgB_{14}$-TiB_2+C coating on the pumping pistons. The gains associated with the pistons exceed the margin of error (MOE) associated with the test setup and instrumentation. Note that the primary improvements in efficiency were in the low-speed, mid-pressure operating condition.

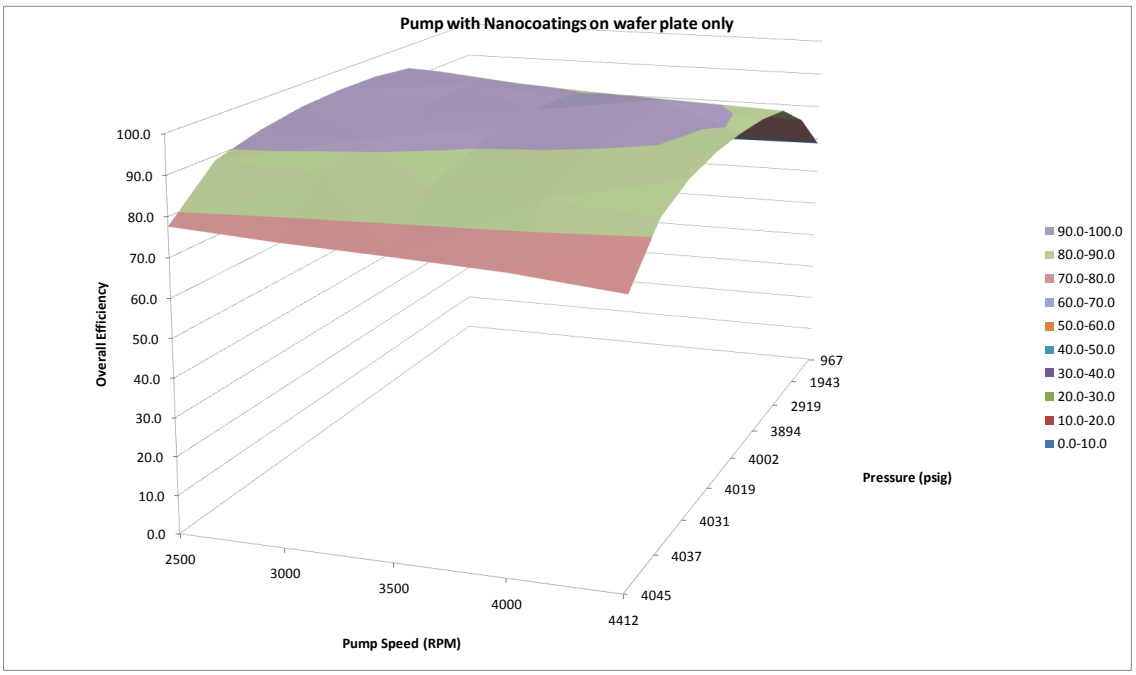

Figure 4.2.5.3-4: Impact of pump efficiency associated with the application of the $AlMgB_{14}$-TiB_2+C coating on the wafer/valve plate. As with the pumping pistons, the efficiency gains associated with the wafer plate exceed the margin of error (MOE) associated with the test setup and instrumentation. Note that the primary improvements in efficiency spanned the entire speed range and a wide pressure range.

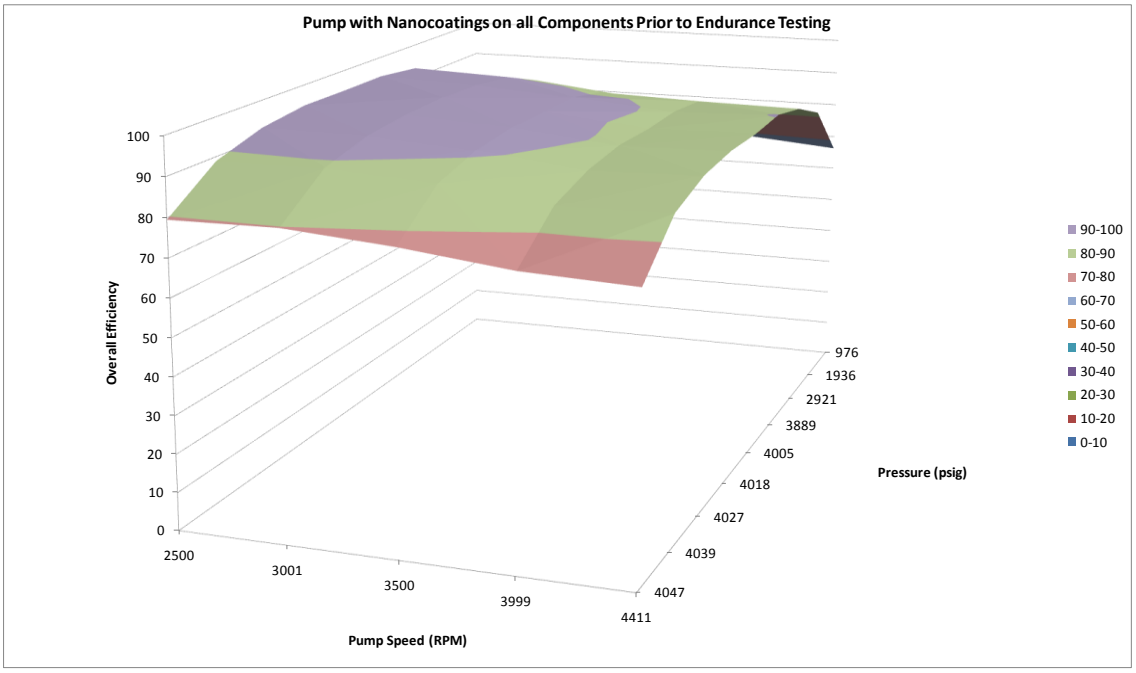

Figure 4.2.5.3-5: Impact of pump efficiency associated with the application of the $AlMgB_{14}$-TiB_2+C to all pump components (prior to durability testing). While the gains realized do exceed the MOE for the test setup and instrumentation, further study is warranted on why the improvements do not cover a wider degree of operating speeds and pressures (as in the case of the coating applied to the wafer plate).

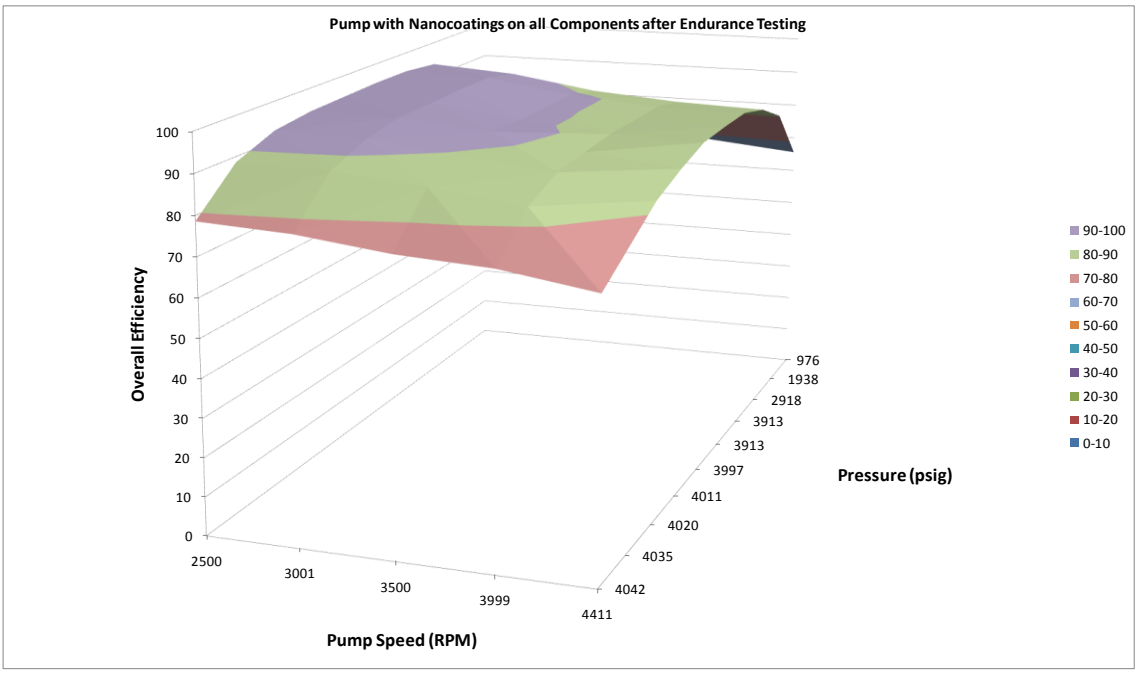

Figure 4.2.5.3-6: Performance of the pump with $AlMgB_{14}$-TiB_2 coating applied to the working components after full-scale (280+-hour) durability schedule. Note that peak efficiency of the pump has dropped somewhat with respect to the pre-endurance system, though when the results are compared to the baseline system (e.g. in Figures 4.2.2-19 and 4.2.2-20), the improvement is noticeable.

From a durability standpoint, the efficiency gains associated with application of the $AlMgB_{14}$-TiB_2+C coating would only be beneficial if the coating survived the rigors of broad operating conditions – hence the endurance schedule. **Figures 4.2.5.3-7 through 4.2.5.3-9** illustrate that the coating remained intact on the working components and should provide a continued benefit to the system's performance well into service.

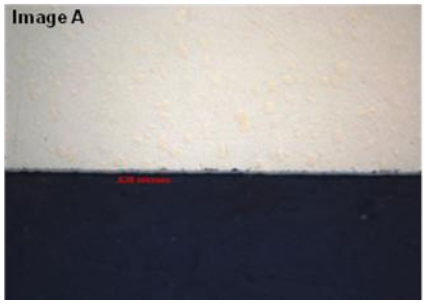

Figure 4.2.5.3-7: Working surface of the 11-hole nutating plate illustrating the presence of the $AlMgB_{14}$-TiB_2 base layer coating (approximately 20-30% of original thickness).

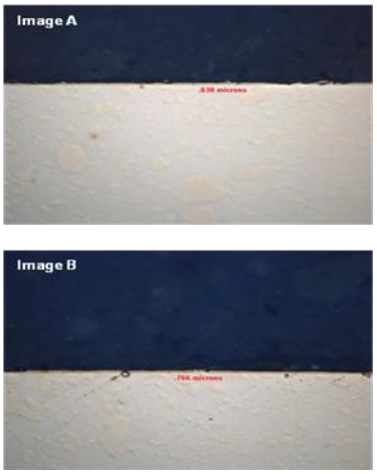

Figure 4.2.5.3-8: Working surfaces of one of the pumping pistons illustrating the presence of the $AlMgB_{14}$-TiB_2 base layer coating (approximately 20-30% of original thickness). Note that region 'A' represents an area of the piston that extends outside of the housing during operation. This would explain the slight discoloration.

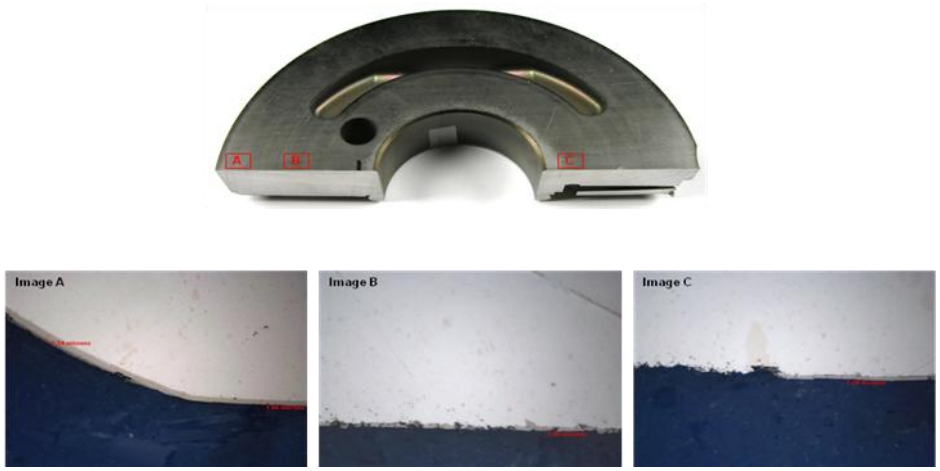

Figure 4.2.5.3-9: Working surfaces of the piston pump wafer plate illustrating the presence of the $AlMgB_{14}$-TiB_2 base layer coating (approximately 40-50% of original thickness).

With performance and durability testing complete, end application calculations were performed to establish the relationship between system power loss and system efficiency. Note that the hydraulics system in an aerospace application is typically used to control actuation surfaces, landing gear, pressurize the passenger cabin, and so forth. Hence, efficiency savings would translate in lowered parasitic losses while in operation. The engines will still consume fuel, though less energy would be wasted by a more efficient hydraulics system. Horsepower savings plots illustrating the savings are included in **Figures 4.2.5.3-10 through 4.2.5.3-11.**

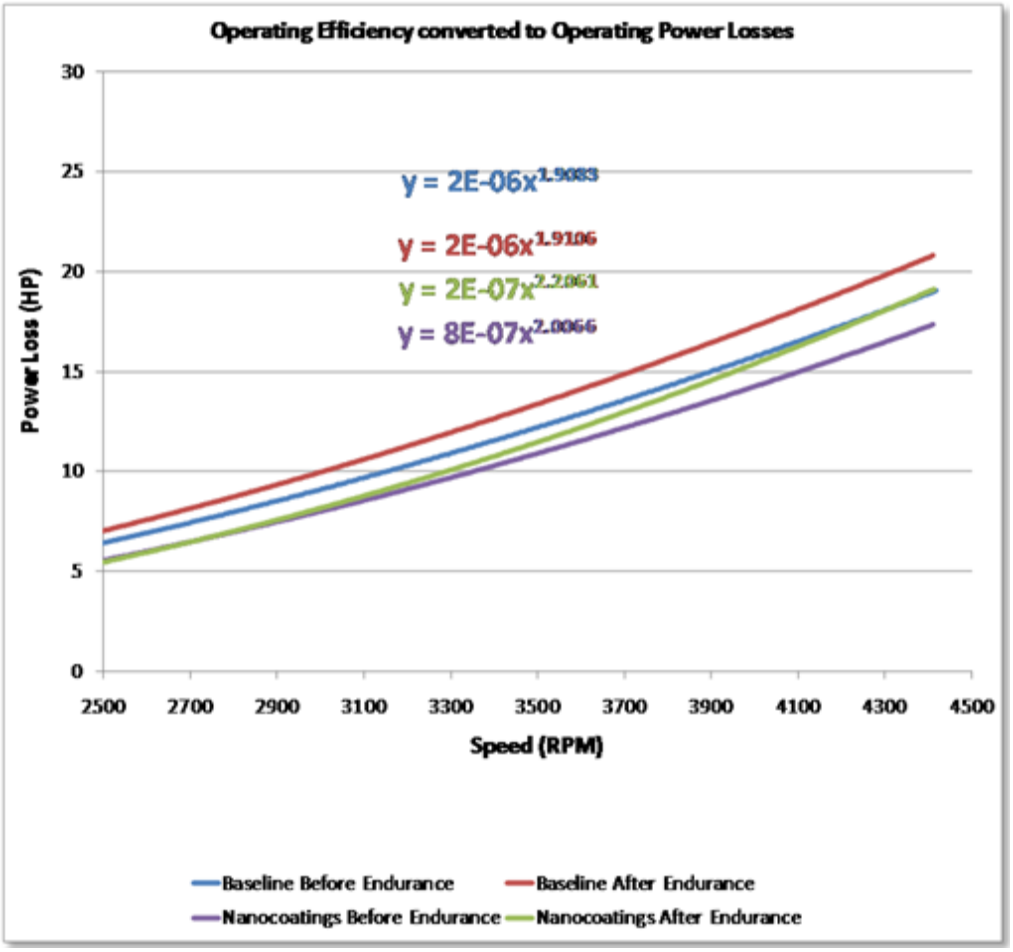

Figures 4.2.5.3-10: Hydraulic pump power loss plot for dynamometer performance testing with $AlMgB_{14}$-TiB_2+C coated components (represented by the purple and green colored data). The red and blue lines represents the baseline pump prior to and after the endurance testing.

The data from **Figures 4.2.5.3-10** was transposed to yield a final power savings associated with use of the nanocoatings at various pump speeds. This data is shown for reference in Figure 7. As predicted, the efficiency gains associated with use of $AlMgB_{14}$-TiB_2+C coated components also yield power loss "savings." In the case of the systems run prior to endurance testing, this was approximately 1.5 HP over a pump speed range of 2500-4400rpm. A savings of approximately 1.5HP (ranging from 1.2HP - 1.9HP) was determined after the endurance test was completed.

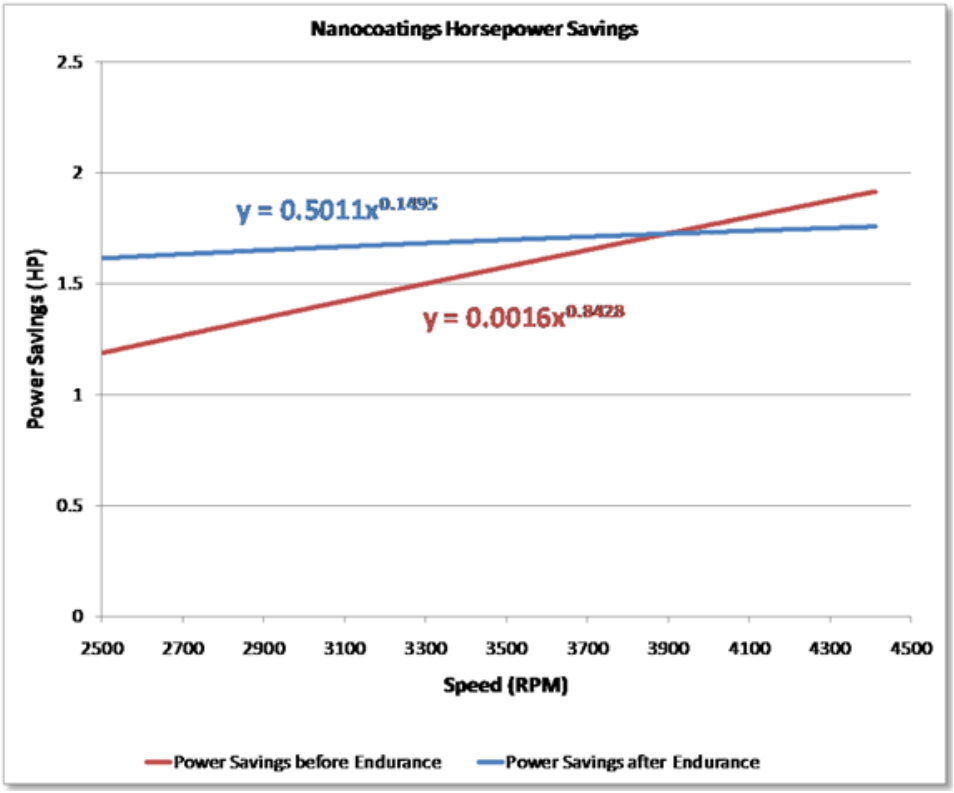

Figures 4.2.5.3-11: Hydraulic pump power loss savings plots for dynamometer trials run before (blue line) and after (red line) 280+ hours of endurance tests. Note that the average lost power savings is approximately 1-1.5 HP per pump and that several of these pumps may be used in the end commercial (or military) application.

In an effort to evaluate the wear performance of $AlMgB_{14}$-based nanocoatings (beyond the current focus on improving fuel economy through reduced friction and higher overall system efficiencies) in hydraulic piston pump applications, Eaton's Innovation Center performed simulative tribology testing on coupons manufactured out of the same materials as the end use aerospace piston pump selected. The specific components that were the focus of the testing are the cylinder block (barrel) and valve plate, and it has been noted that, in baseline testing of the system, the sintered bronze applied to the cylinder block smeared onto the hardened tool steel valve plate at a high pressure*velocity (P*V) product.

Due to the material grades used in the study, low temperature PVD processing was selected. Two of the six coupons provided were processed using the $AlMgB_{14}$-TiB_2+C coating and another two samples were coated with a new composition being evaluated, (Ti, Zr)B_2. Refer to **Figure 4.2.5.3-12** for representative images of the laboratory coupons.

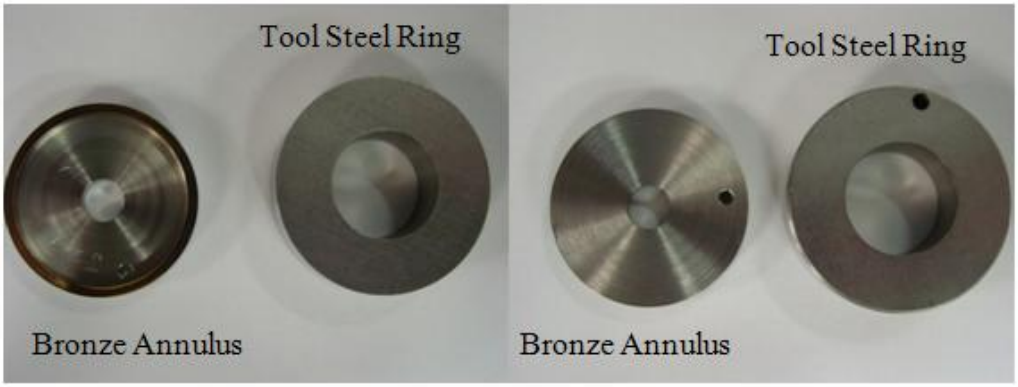

Figures 4.2.5.3-12: Falex tribology coupons provided to the Eaton Innovation Center for coating and wear trials. The aim of this study is to eliminate the "smearing" that occurs and to minimize the wear to the tool steel ring. The leftmost image represents the "working faces" of the samples. The back-face of each coupon is shown on the right image to illustrate the thermocouple wire placement.

The pressure*velocity (P*V) information provided with the coupons indicated that the current point of failure, meaning bronze from the annulus smearing onto the ring through adhesive wear, is approximately 1.5 million psi*sfm. Simple calculations showed that an applied load of 500 lbs and a rotational speed of 2300 RPM would equate to a similar P*V. The lubricant for the selected Falex testing was Skydrol V, a newly developed fluid that is being targeted at replacing older formulations such as 500B4 and LD-4. Skydrol 5 offers higher temperature capability than Type IV fluids, the lowest density, and better paint compatibility. The failure point on this graph (identified as the point where measured torque dramatically increases) corresponds to a P*V of approximately 1.35 million psi*sfm. While slightly less than the value provided from the end-use piston pump application, this P*V product indicates that the test setup is very close to simulating the system.

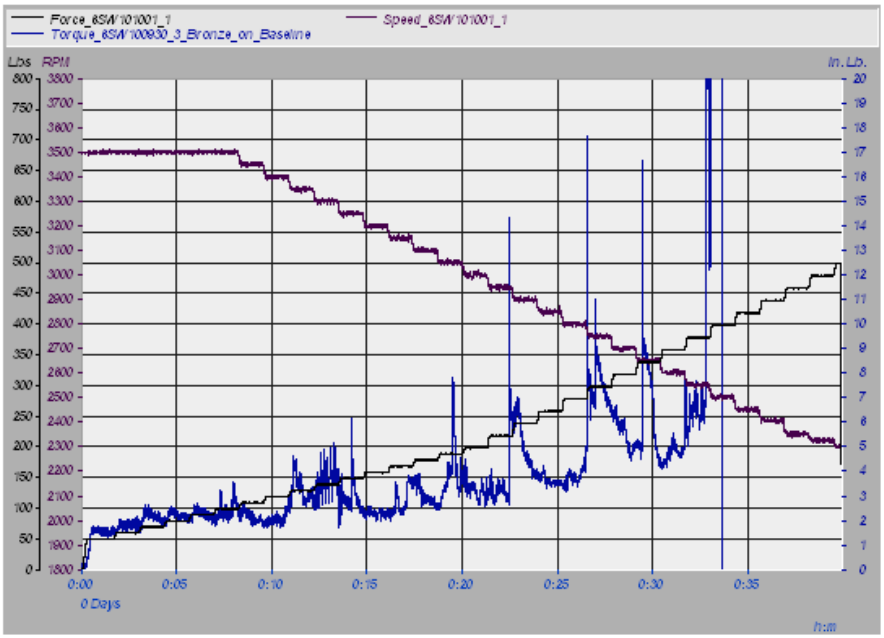

Figures 4.2.5.3-13: Falex wear plot illustrating the point of failure identified for the baseline bronze-on-uncoated tool steel sample. The point at which the test was interrupted corresponds to 380 lbs load and 2550 RPM (P*V product of 1.35 million psi*sfm).

The test was repeated for the coated specimens and the results are included for reference in **Figures 4.2.5.3-14 and 4.2.5.30-15.** Note that, in each of the coated trials, the testing was interrupted prior to full completion of the test. It is believed that this has more to do with exceeding the shear strength of the bronze on the annulus than any adhesive wear occurring between the two interfaces.

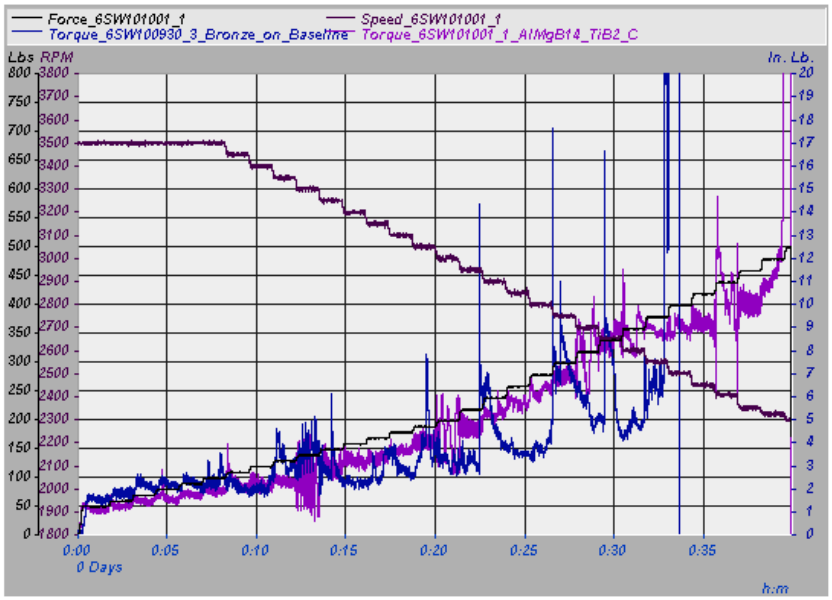

Figures 4.2.5.3-14: Comparison of $AlMgB_{14}$-TiB_2+C coated sample set to baseline. Note that the test was interrupted at a load of 480 lbs and a rotational speed of 2325 RPM. This corresponds to a full-contact P*V product of 1.48 million psi*sfm

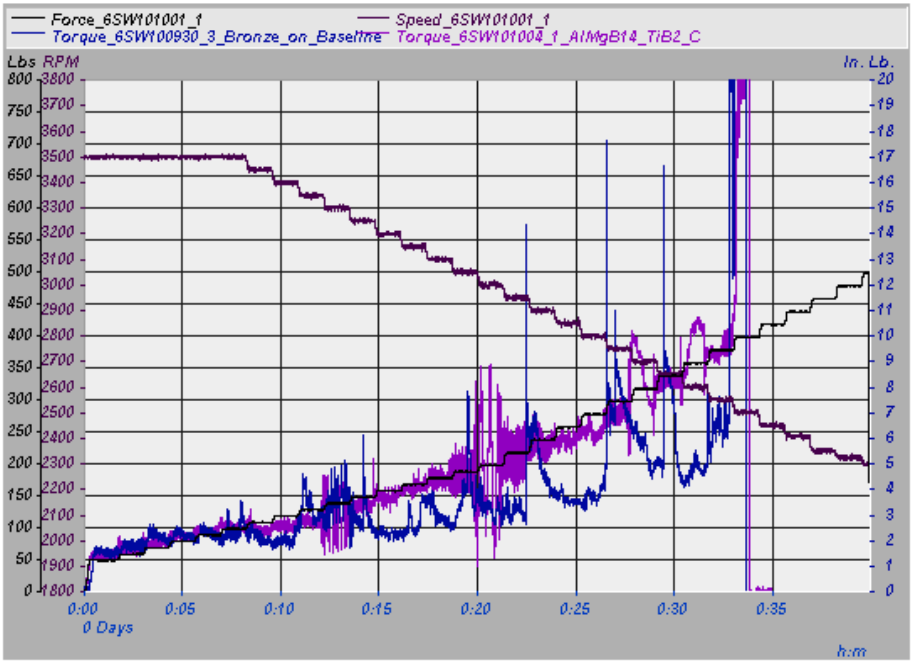

Figures 4.2.5.3-15: Comparison of second $AlMgB_{14}$-TiB_2+C coated sample set to baseline.

Note that the test was interrupted at a load of 400 lbs and a rotational speed of 2500 RPM. This corresponds to a full-contact P*V product of 1.32 million psi*sfm.

Optical profilometry was performed on each of the tested samples as a means to quantify the impact of the material transfer on the baseline sample. Measurements were also performed on the coated samples to assess the ring and annulus wear. Refer to **Figures 4.2.5.3-16 and 4.2.5.3-17** for profilometry data.

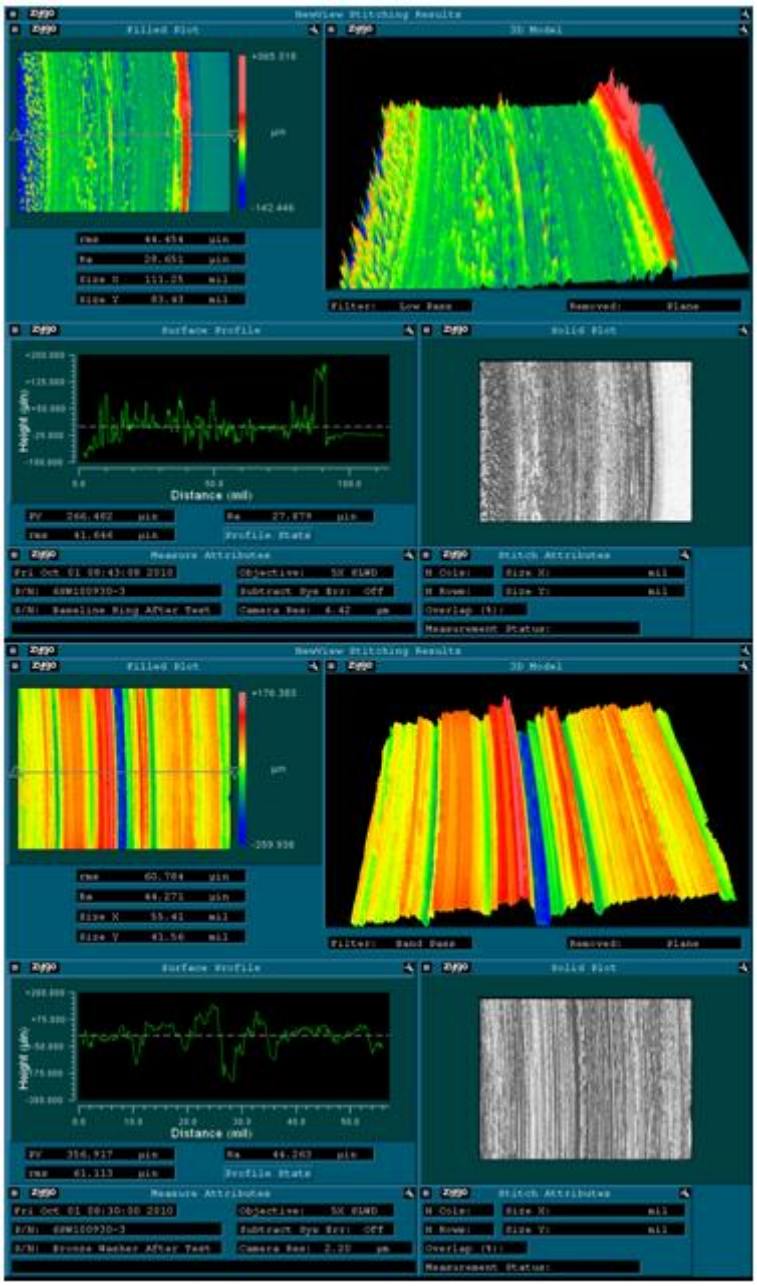

Figures 4.2.5.3-16: Post-test optical profilometry data for the baseline ring sample (top) and the bronze annulus (bottom). For reference, the PV value of the ring prior to the Falex wear study was 2 micro-inches. The PV value for the annulus prior to the Falex wear study was 32 micro-inches. As shown, the post-test for PV for the ring is 26 micro-inches and the post-test PV for the annulus is 357 micro-inches.

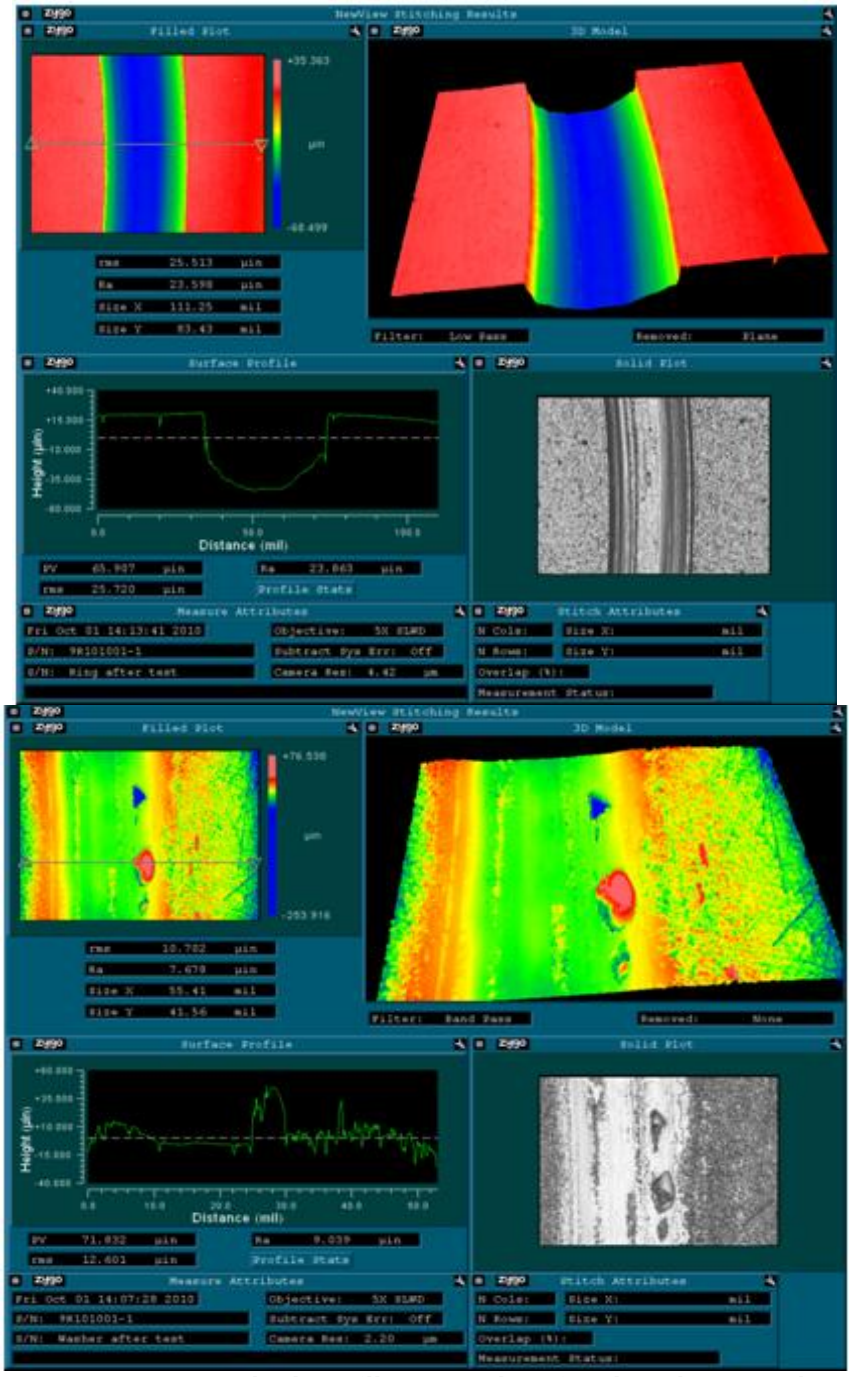

Figures 4.2.5.3-17: Post-test optical profilometry data for the $AlMgB_{14}$-TiB_2+C coated ring sample (top) and the bronze annulus (bottom). For reference, the PV value of the ring prior to the Falex wear study was 2 micro-inches. The PV value for the annulus prior to the Falex wear study was 34 micro-inches. As shown, the post-test for PV for the ring is 66 micro-inches and the post-test PV for the annulus is 72 micro-inches.

A summary of all of the results is included in **Table 4.2.5.3-2**. For reference, the P*V pressure*velocity calculation for the coated samples was broken down into two terms: The first term represents full contact of the bronze annulus on the coated ring. The second term represents partial contact of the bronze annulus on the coated ring. Through profilometry measurement, it was determined that the wear track widths on the coated rings represent approximately ½ of the full annulus thickness.

Table 4.2.5.3-2: Falex test data and post-test observations for Eaton aerospace coupons.

Sample	Speed (RPM)	Force (lbs)	P*V product (psi*sfm)	Sample Condition
Baseline	2550	380	1.28 million	Heavy galling, material transfer
$AlMgB_{14}$-TiB_2-C	2325	480	4.53 million (1.48 million)	Slight wear to bronze, small wear channel on coated ring
$AlMgB_{14}$-TiB_2-C	2500	400	3.96 million (1.32 million)	Slight wear to bronze, small wear channel on coated ring
$(Ti,Zr)B_2$	3100	180	1.31 million (741,000)	Minimal wear to bronze, very small wear channel on coated ring
$(Ti,Zr)B_2$	2500	400	5.21 million (1.32 million)	Minimal wear to bronze, little to no wear on coated ring

4.2.6 Scale up of PVD Films from Laboratory Coupons to Field Machining Trials

This section focuses on tooling end applications of $AlMgB_{14}$ coated components. An outline of results is presented below. Benchmark testing was used to evaluate PLD and PVD coatings for end metal machining applications. Performance of transition from laboratory PLD to industrial scale-up PVD coatings were optimized and evaluated. Benchmark testing then was transitioned to field trials for extended testing.

Outline of machining trials

1) Bench testing
   a. Machining inefficiencies and optimization considerations
   b. Estimation of power consumption of industrial machines
   c. PLD (laboratory scale coating reactor) compared with PVD (large scale commercial coating reactor)
   d. Carbon gradient coating evaluation and coating process optimization
   e. Competitive evaluation - TiB_2, TiAlSiCN, AlTi-CrN, TiAlN
   f. Machining cast iron, low alloy steel, stainless steel, and nickel- based superalloys

2) Field trials, 9 applications in roughing and finishing of titanium alloys
   a. Turning
   b. Boring
   c. High pressure coolant

1) *Bench testing*

Currently Greenleaf uses WC-6%Co along with TiAlN coated WC-6%Co for low-speed machining Ti alloys such as Ti-6Al-4V. These coatings will be the baselines against which the newly developed coatings are measured. The first goal is to improve on these by 10-50% in both increased speed and tool life. A secondary goal is to find applications for the new coating technology in high-speed machining of other high-strength and metal alloys. The study will include coating/substrate architecture as well as coating on tooling substrate materials.

Figure 4.2.6-1: Agathon grinder for making precision custom cutting inserts.

Bench testing is a controlled test using an industrial lathe. Tungsten carbide (WC) and TiAlN coated WC cutting tool inserts with chipforms are used to machine 8 inch diameter rods as shown below, **Figure 4.2.6-2**.

Fail criteria for finish machining on flank (side) and crater (top) wear is typically 0.015” or 300 microns.

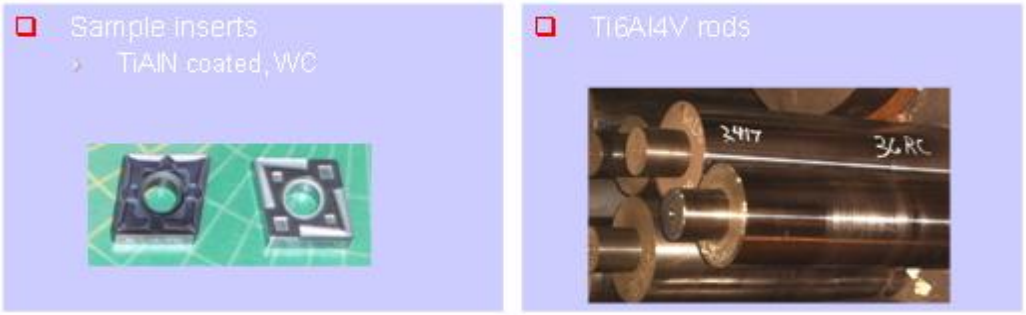

Figure 4.2.6-2: Testing inserts on left with chipforms, right are metal rods 8-inch diameter for testing.

Machining parameters for lathe turning are spindle speeds, feedrate, and depth-of-cut, which dictate how fast the material is being removed over time. Definition of cutting surface speed in square feet per minute (SFM) is described by the equation:

$$Vc = \frac{\pi * D * n}{12}$$

Where *Vc* is cutting speed (ft/min), *D* is machining diameter of the workpiece (inch), and *n* is the spindle speed (rev/min).

4.2.6.1 Machining Inefficiencies and Optimization Considerations

In all machining applications, careful optimization need to be considered at the higher speeds as the tool life dramatically decreases with increasing cutting speeds. A standard tool optimization is considered for machining titanium in **Figure 4.2.6.1-1**. The tool tip lasts 30 minutes at 194 SFM, while only 1 minute of machine time is obtained at 350 SFM. Considering the tool costs and time to change the tool, it is not efficient to run at the higher speeds using standard tools.

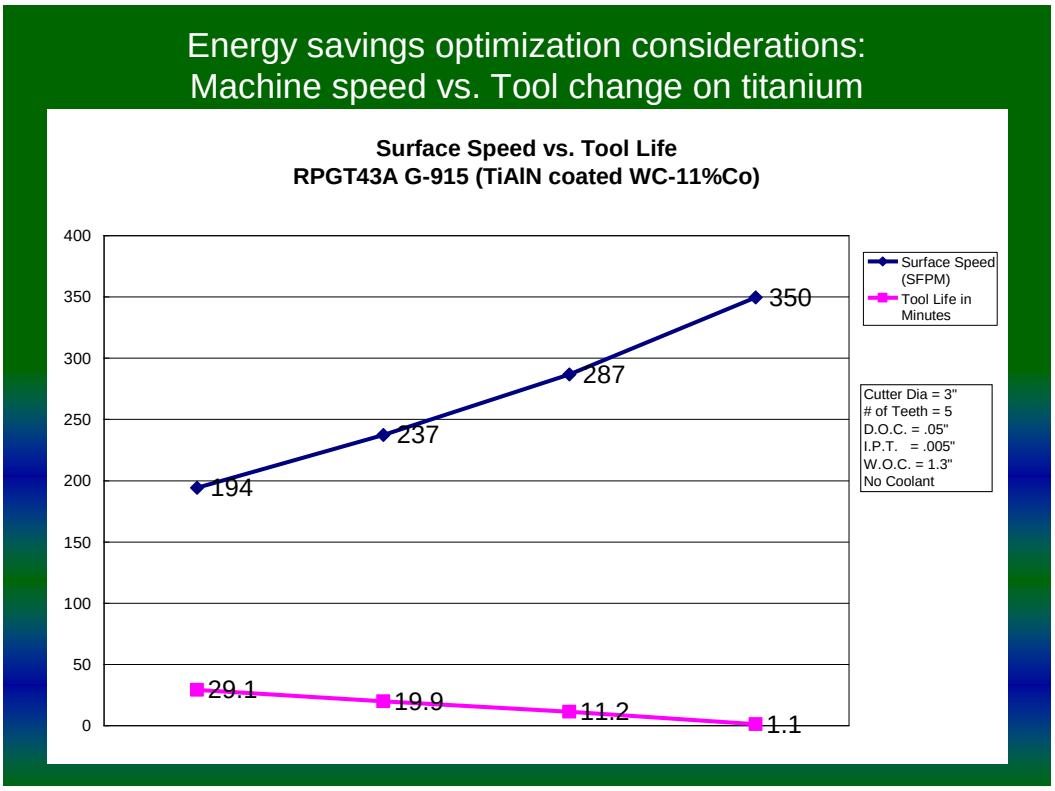

Figure 4.2.6.1-1: Tool life as a function of increasing machine speeds for titanium alloys using traditional machine tooling without coating.

4.2.6.2 Estimation of Direct Power Consumption of Industrial Machines

There are two parts to conserve energy during machining operations. First is direct energy consumption to run the machines. This is directly observable by the amount of electricity spent while running a lathe or milling machine. The second category for energy savings is time saved by increasing the speed of the machine, therefore producing parts faster by utilizing new technologies. Second category is discussed in detail in the energy savings section. This section explains the electricity saved using the $AlMgB_{14}$ coated cutting tools.

Additional power is being consumed during machining with increasing tool pressure from frictional contact. The power was measured by directly connecting an amp meter to the spindle load while machining titanium (Ti6Al4V) as a function of increasing surface speed. Alternative cutting forces can be measured with a dynamometer and power consumption can be calculated. Surprisingly, operators often times can hear the machine 'whine' and can indirectly correlate this to an increase in cutting force with tool wear.

The spindle load accounts for majority of the power consumed for a standard lathing operation. Other variables remain fixed during this test. Machining variables are presented in **Table 4.2.6.2-1. Figure 4.2.6.2-1** compares the measured power at idle spindle load and during finish machining.

Table 4.2.6.2-1: Machine variables for baseline power measurements.

Material	Ti6Al4V
Insert geometry	CNGG432TF
Edge prep	A hone
IPR	0.005
DOC	0.02
Lead angle	-5°
LOC	3"
Cutting fluid	yes

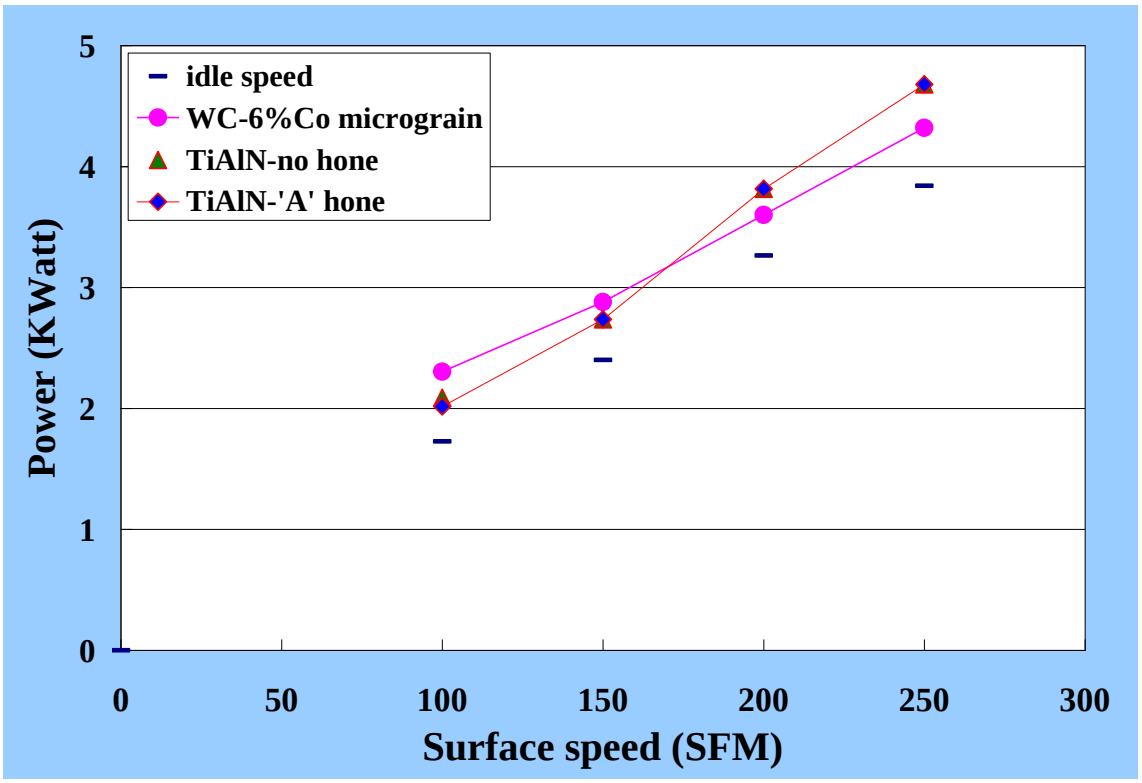

Figure 4.2.6.2-1: Baseline power consumption during machining of titanium using standard uncoated WC-6%Co and TiAlN coated inserts.

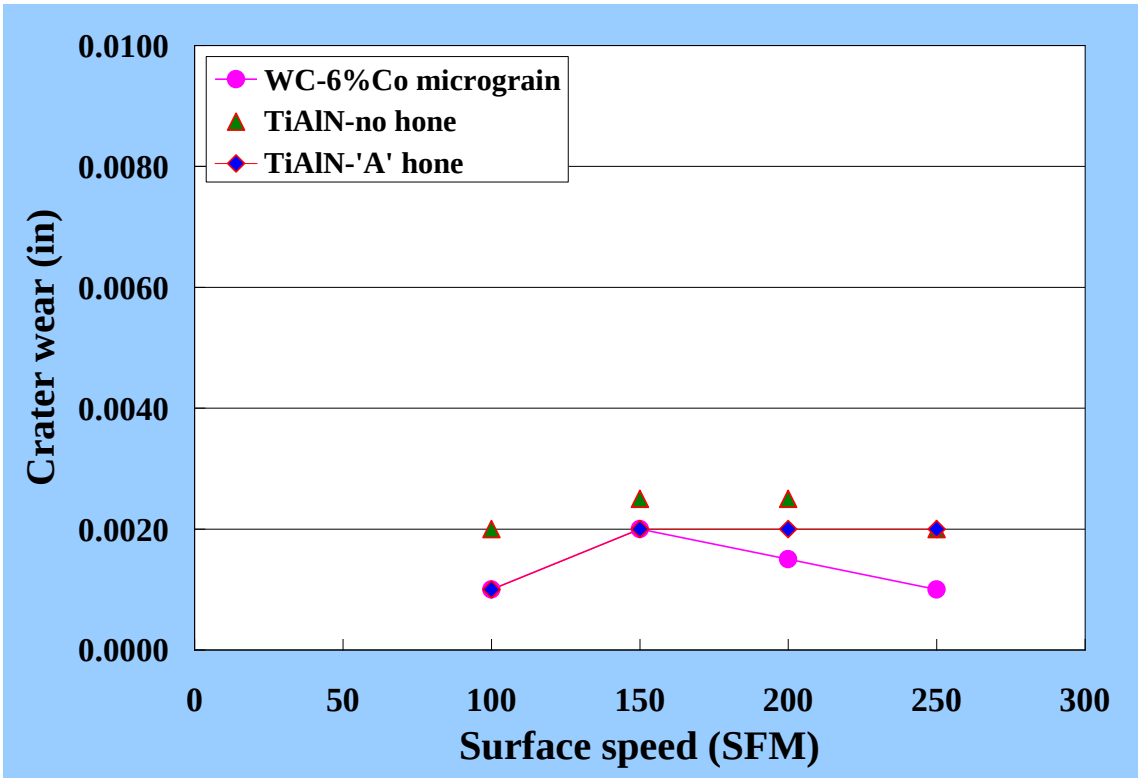

Figure 4.2.6.2-2: Tool wear corresponding to the baseline power consumption measurements.

The spindle power increased linearly with increasing speed. The tool wear of WC and TiAlN coated tools correlated with power consumption **Figure 4.2.6.2-2**. At lower speeds, the TiAlN showed slightly lower power consumption; while at the higher speed, the WC had slightly lower power consumption. This trend is evident with the tool wear as higher speeds showed WC had better tool life. The power consumed at 100 SFM is 1.7 K-Watt idle and 2.3 K-Watt using WC uncoated tool, a difference of 0.6 K-Watt (35% increase from idle). At 250 SFM the idle power is 3.8 and up to 4.7 K-Watt, a difference of 1.1 K-Watt (29% increase from idle). Spindle power from 0.6-1.1 K-Watt would represent the maximum savings from frictional reduction under these conditions. Generally, with increased speeds and depths-of-cut, the cutting force increased and more energy is consumed.

$AlMgB_{14}$ coated tools were compared with the baseline WC uncoated and TiAlN coated tools at 400 SFM in **Figure 4.2.6.2-3**. The idle spindle power was 8.4 K-Watt. Generally, the $AlMgB_{14}$ had 0.4 K-Watt less power consumed during titanium metal removal. WC and TiAlN coated tools failed at 1.5 cm^3 of metal removal while the $AlMgB_{14}$ tools failed at 3.5 cm^3. After the tool wore, the energy consumed for all the tools were 8.8 K-Watt and above.

This results in a 5-6% energy savings by using the low friction $AlMgB_{14}$ coated tools compared with standard tools.

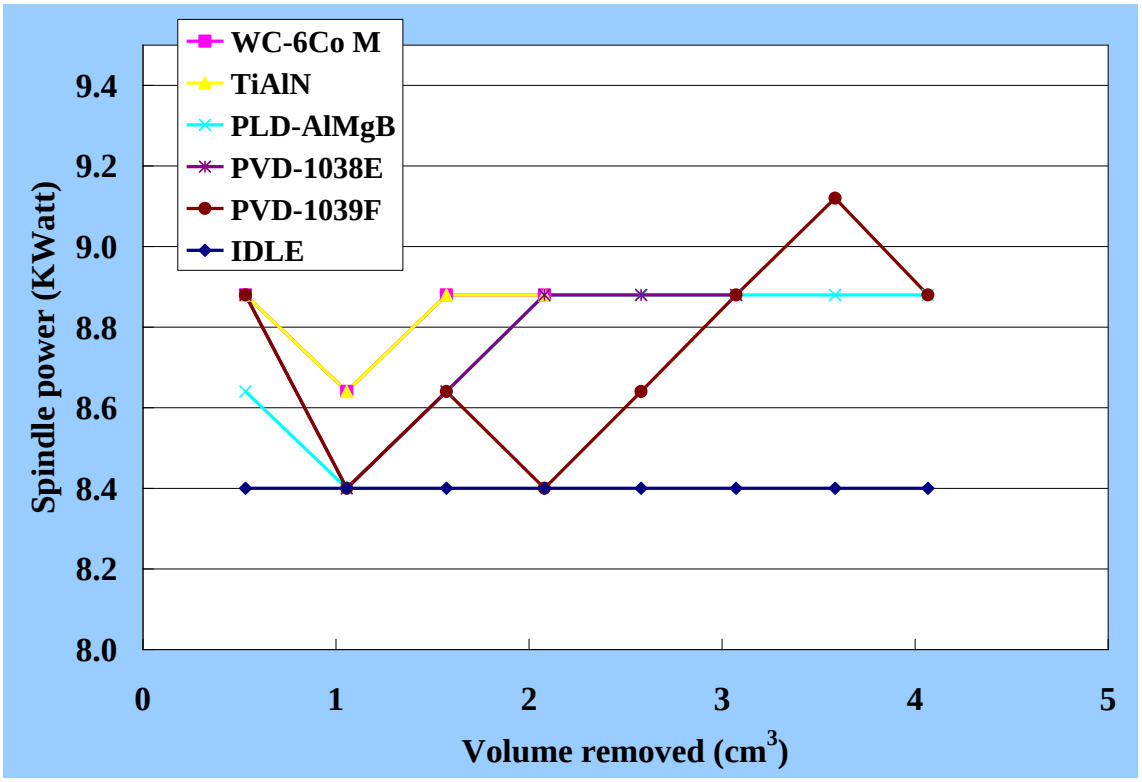

Figure 4.2.6.2-3: Spindle power while machining titanium at 400SFM under finishing conditions. $AlMgB_{14}$ coated tools are compared with standard WC and TiAlN tools.

4.2.6.3 Bench Machine Testing, PLD Compared with PVD

Overall production feasibility of $AlMgB_{14}$-based coatings on WC substrates for machining Ti6Al4V thus far appears very promising. Titanium alloys are generally hard to machine primarily due to its low thermal conductivity and reactivity. This reduces the overall machining efficiency, with current production speed to less than 400 surface feet per minute (SFM) along with reduced tool life.

The two standard cutting tool materials for Ti-alloy machining are WC-6%Co micrograin (G-20M, substrate) and TiAlN (G-925) coated grades, these will be used as industrial standards for comparison. Ames' pulsed laser deposited (PLD) $AlMgB_{14}$ (S082307), Eaton physical vapor deposited (PVD) $AlMgB_{14}$ (EB1038E), and Eaton PVD co-sputtered $AlMgB_{14}$-TiB_2 (EB1039F) were the coating test grades. In summary, all of the $AlMgB_{14}$-coated inserts significantly outperformed the industry standards in finish machining applications.

Finish machining (relatively light cuts) bench lathe cutting tool tests were conducted at 400SFM (**Figure 4.2.6.3-1, 4.2.6.3-2**). The crater (top) and flank (side) wear was measured as a function of volume of Ti-alloy removed. One cutting edge was measured continuously to failure as the Ti-material was being removed. A recommended fail line in red represents the end of tool life for finishing that indicate relative performance difference between the cutting tools tested. This data clearly shows a significant improvement for the $AlMgB_{14}$ coated tools. All tests showed that the Ames (S082307) and Eaton (EB1039F) coatings more than doubled the life of standard

industrial grades at 400SFM, and enabled more than 25% improvement in speed with same tool wear.

Higher speeds exposed the tool to higher temperatures accelerating wear at 500SFM (**Figures 4.2.6.3-3, 4.2.6.3-4**) with water-based coolant. At 500SFM rapid degradation occurred due to the thermal limitations of the WC substrate. In particular the cobalt binder (6wt %) in WC approaches its melting point (<1500°C) and rapidly degrades the tool. WC without binder is thermally stable (melting point <2300°C). Although the machining operation is 20% faster at 500SFM compared with 400SFM, the volume of titanium removed is reduced by 50%. Any coatings on the WC tool had limited impact at 500SFM as the substrate limited the performance. There is a slight improvement however with the $AlMgB_{14}$ coatings even at these higher speeds.

One of the precautions when machining titanium is careful removal of heat with the titanium chip. Dry machining titanium is not recommended because hot titanium chips can combust and cause metal fires. As a fundamental test however, titanium was machined without any coolant at the lower speeds at 300SFM (**Figures 4.2.6.3-5, 4.2.6.3-6**). The $AlMgB_{14}$ coatings outperformed the standards and showed very small incremental tool wear.

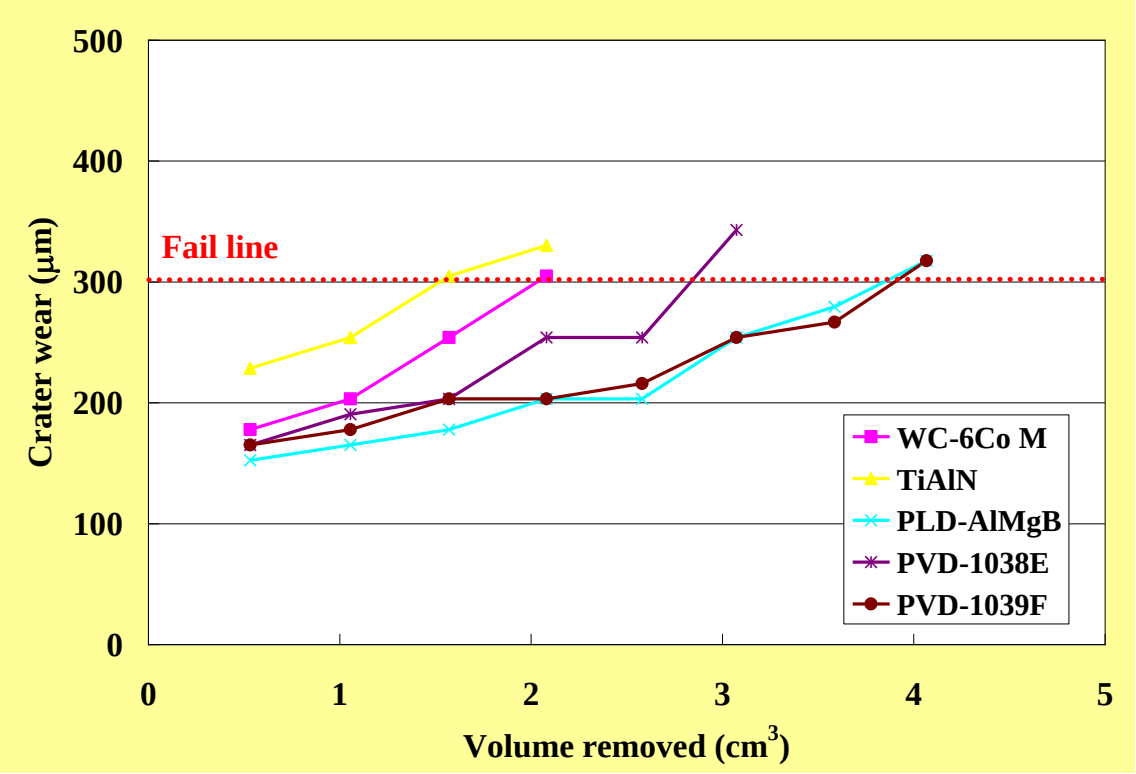

Figure 4.2.6.3-1: Measured crater wear as a function of volume of Ti machined at 400SFM.

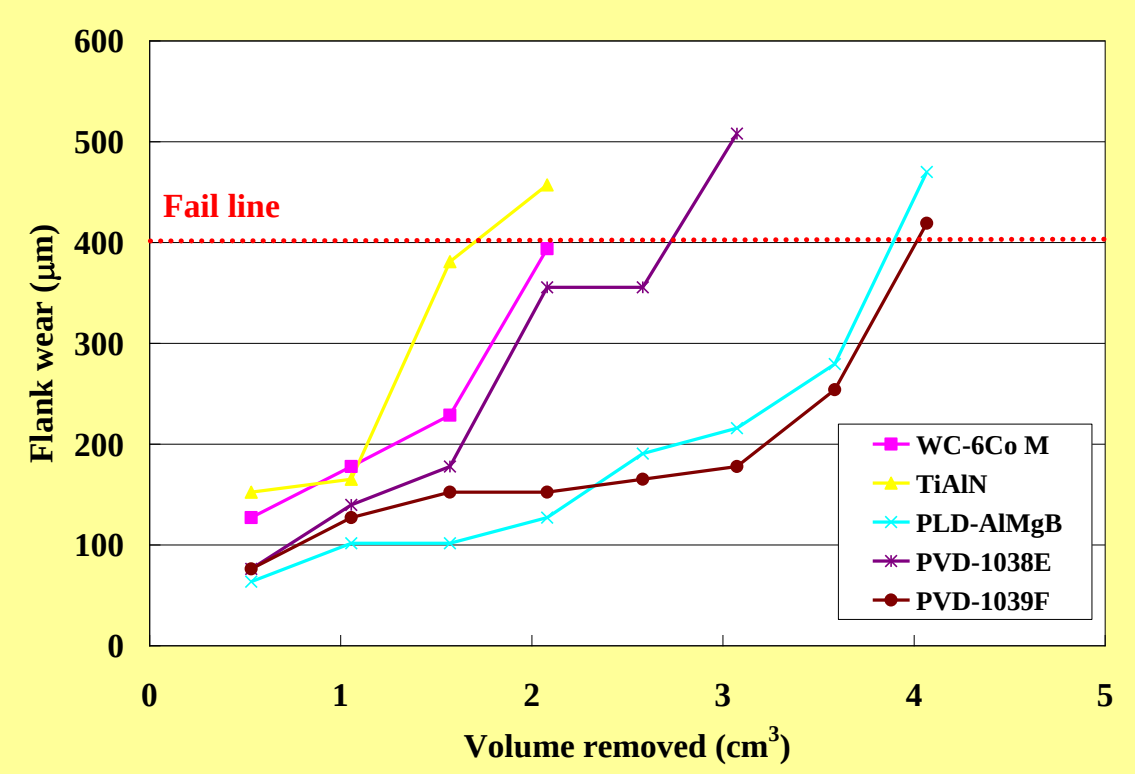

Figure 4.2.6.3-2: Measured flank wear as a function of volume of Ti machined at 400SFM.

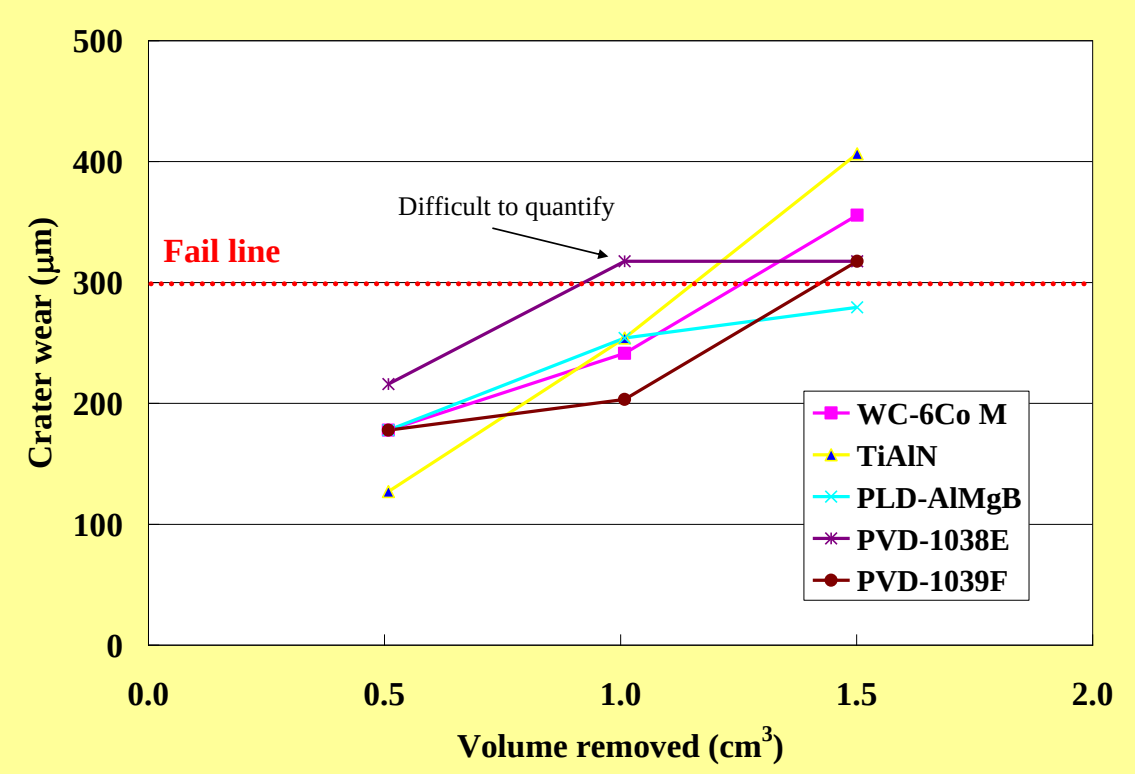

Figure 4.2.6.3-3: Measured Crater wear as a function of volume of Ti machined at 500SFM.

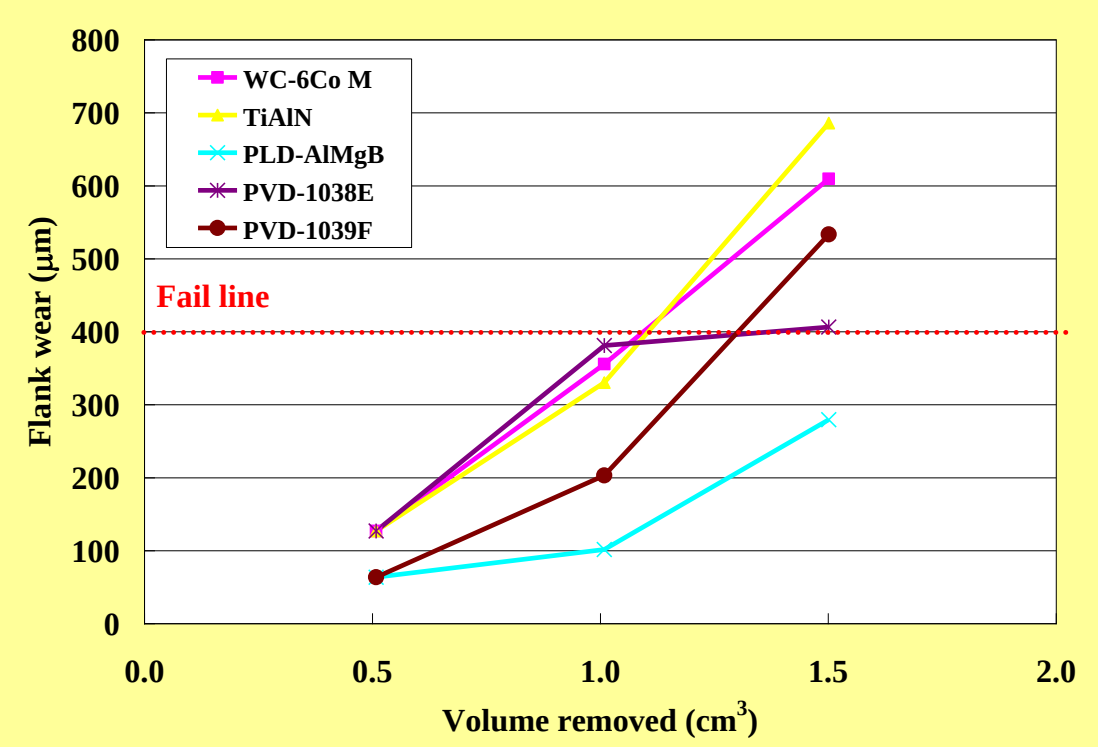

Figure 4.2.6.3-4: Measured flank wear as a function of volume of Ti machined at 500SFM.

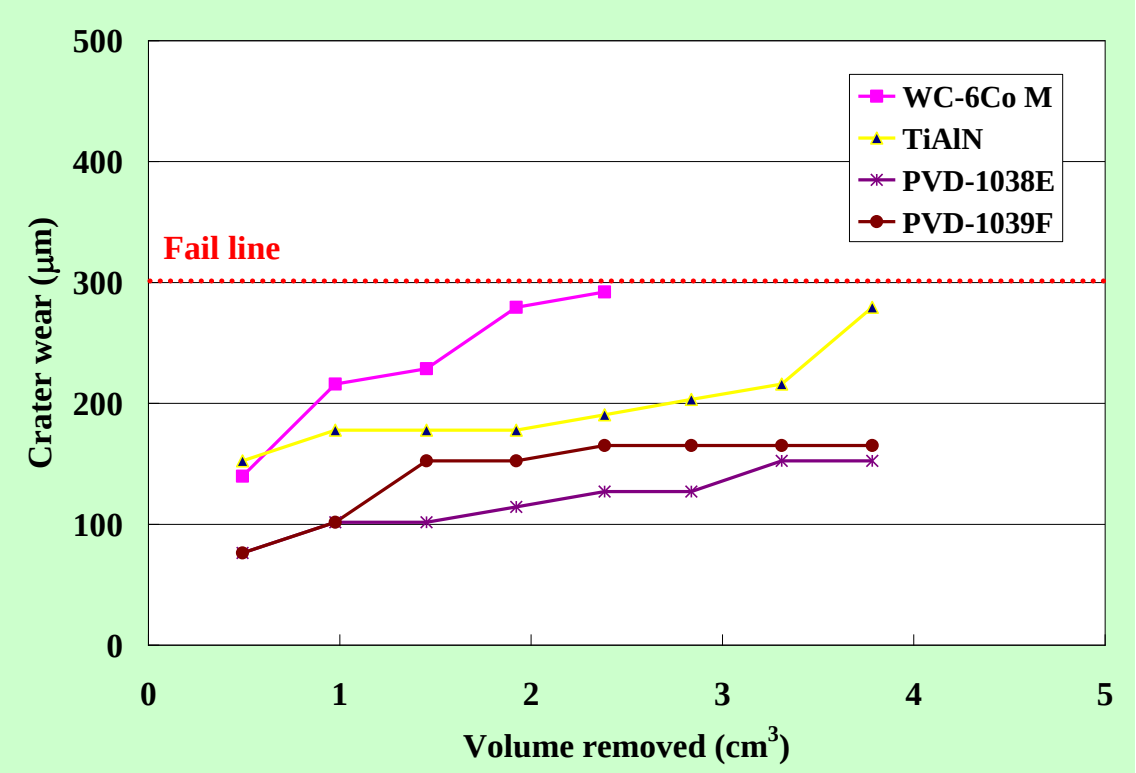

Figure 4.2.6.3-5: Measured crater wear as a function of volume of Ti dry machined at 300SFM.

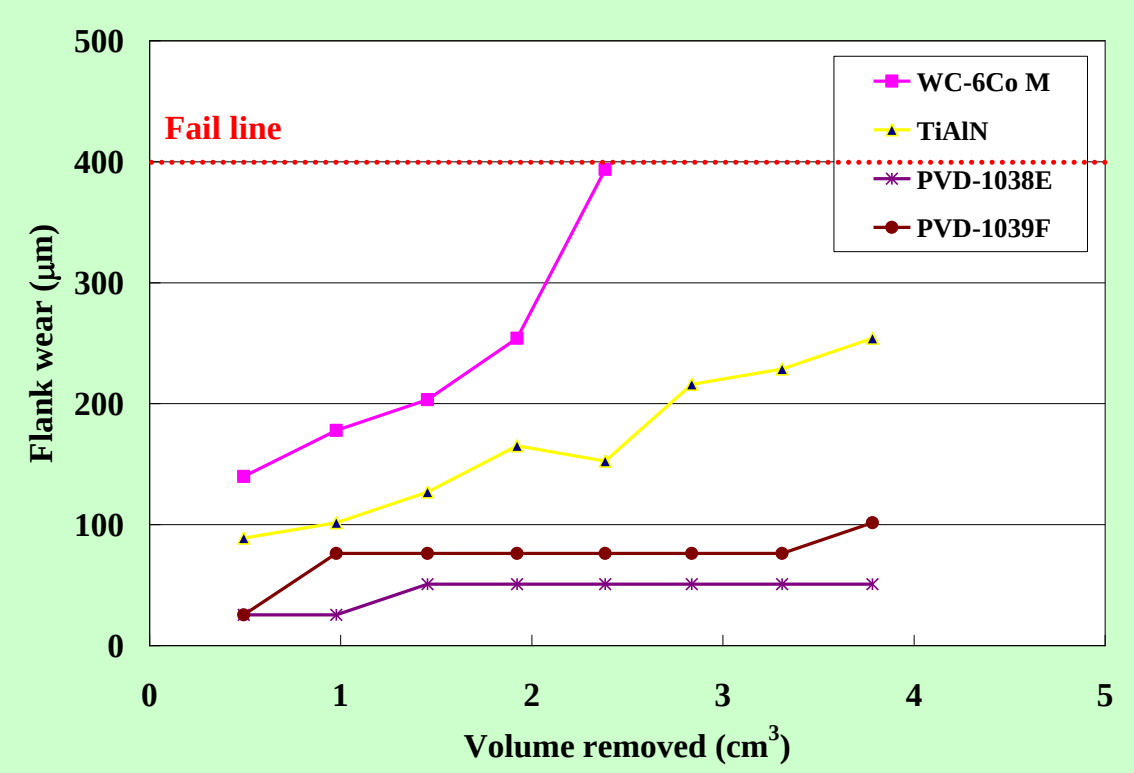

Figure 4.2.6.3-6: Measured flank wear as a function of volume of Ti dry machined at 300SFM.

In order to get these coatings to production, we must successfully transition from lab scale PLD to production sized PVD system. PLD systems are typically smaller and limited due to low deposition rates, and high capital costs of the lasers at least for most cutting tool applications.

Surprisingly, the non-uniformly covered and thin (<0.5 microns) PLD coating exhibited performance as good as the uniformly covered and thicker PVD (2-3 microns) coatings by Eaton. These results clearly indicate the possibility of scale-up, and opportunity for further improvement.

4.2.6.4 Carbon Gradient Coating Evaluation and Coating Process Optimization

Cutting tool geometry will affect the tool life along with selected materials grade. A combination of geometry and material is vital to the performance of the tool in specific applications. In the case of titanium, the cutting tool must remain sharp as the increased contact area at the interface generates excess heat along with chemical and frictional interaction. **Figure 4.2.6.4-1** compares the WC substrates (G-20M) with and without an A-hone. A-hone is a radius at the cutting tip ranging from 0.0005-0.001inches (13-25 microns). Baseline performance of the A-honed insert is half that of the sharp tipped tool without an engineered radius.

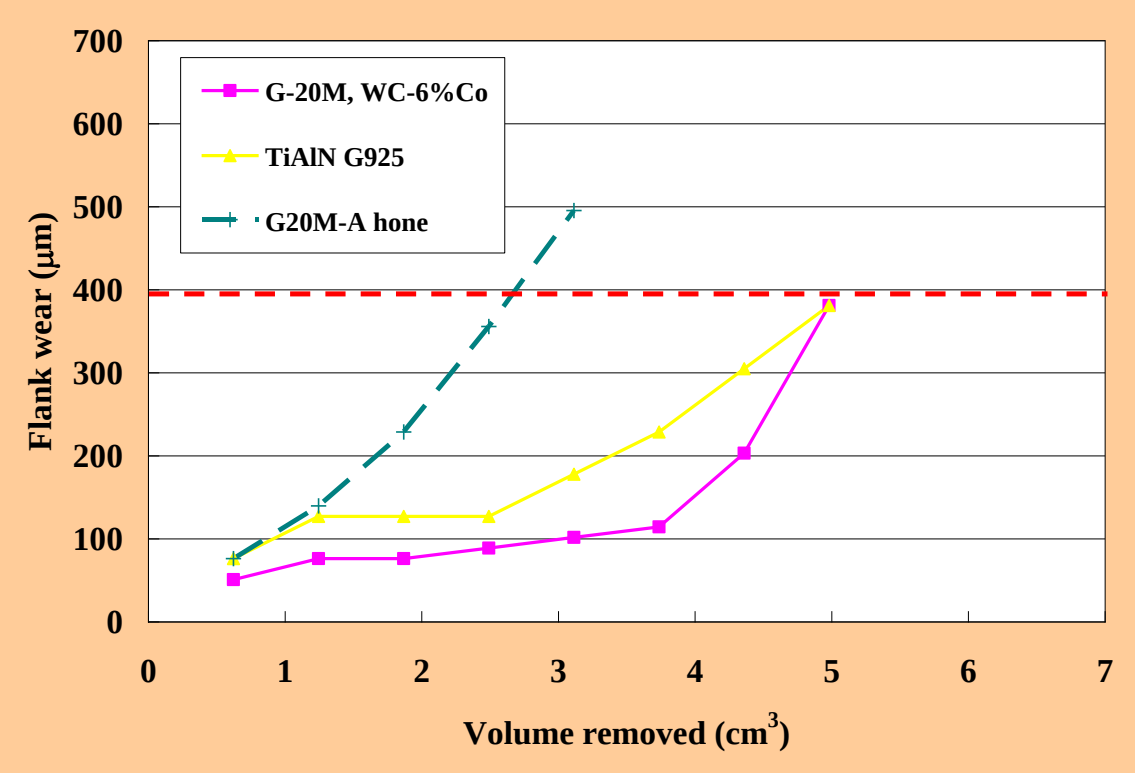

Figure 4.2.6.4-1: Cutting tool performance of titanium machining using an A-hone radius (13-25 micron radius) versus a sharp cutting tip.

Two major advancements were made to improve the performance of cutting tools. First, substrate heating provided a reduced stress with good adhesion of PVD films. It was clear that the substrate-heated sample outperformed the low temperature depositions. Secondly, the cutting tool performances of $AlMgB_{14}$/TiB_2/carbon gradient multilayer films were also beneficial at the standard machining conditions. However, the carbon gradient film's temperature stability may be compromised at the higher speed, higher temperature cutting conditions. The thermal stability of carbon layers are <400°C, although there are benefits to the starting lubrication. The advantage of improved target material and Eaton's innovative multilayer designs in the scaled-up PVD system is proving very valuable thus far in Greenleaf's bench cutting tests. Several combinations of high temperature and low temperature heating (carbon gradients from solid graphite target versus deposition from acetylene gas) were compared. Generally, the higher temperatures are favored for WC substrates. It should be noted that acetylene gas deposition of the gradient carbon is typically more efficient for PVD coatings. This test compares the performance of these parameters, and the machining test conditions are in **Table 4.2.6.4-1**. The $AlMgB_{14}$ coatings outperformed the industry standards at 400 surface feet per minute speeds as shown in **Figure 4.2.6.4-2**. Analogous secondary SEM images are in **Figure 4.2.6.4-3** and backscattered compositional contrast SEM images are in **Figure 4.2.6.4-4**. Uncoated WC, TiAlN coated, $AlMgB_{14}$ coated at low temperature deposition failed at 5 cm^3 metal removal. The higher temperature deposited $AlMgB_{14}$ had higher tool life exceeding 6 cm^3 of metal removal. The $AlMgB_{14}$ deposited at the higher temperature with carbon gradient using the acetylene gas outperformed the other coatings.

Table 4.2.6.4-1: Machine testing conditions for carbon gradient coating evaluation and coating process optimization.

Fixed SFM, fixed loc, vary length of cut	
Material	Ti6Al4V
Insert	CNGG432TF
Grade	G20M as substrate
Edge	not honed
Feed rate (IPR)	0.005 in/rev.
Cutting detpth (DOC)	0.02 in
Cutting length (LOC)	4"
Lead angle	-5°
Cutting fluid	Yes

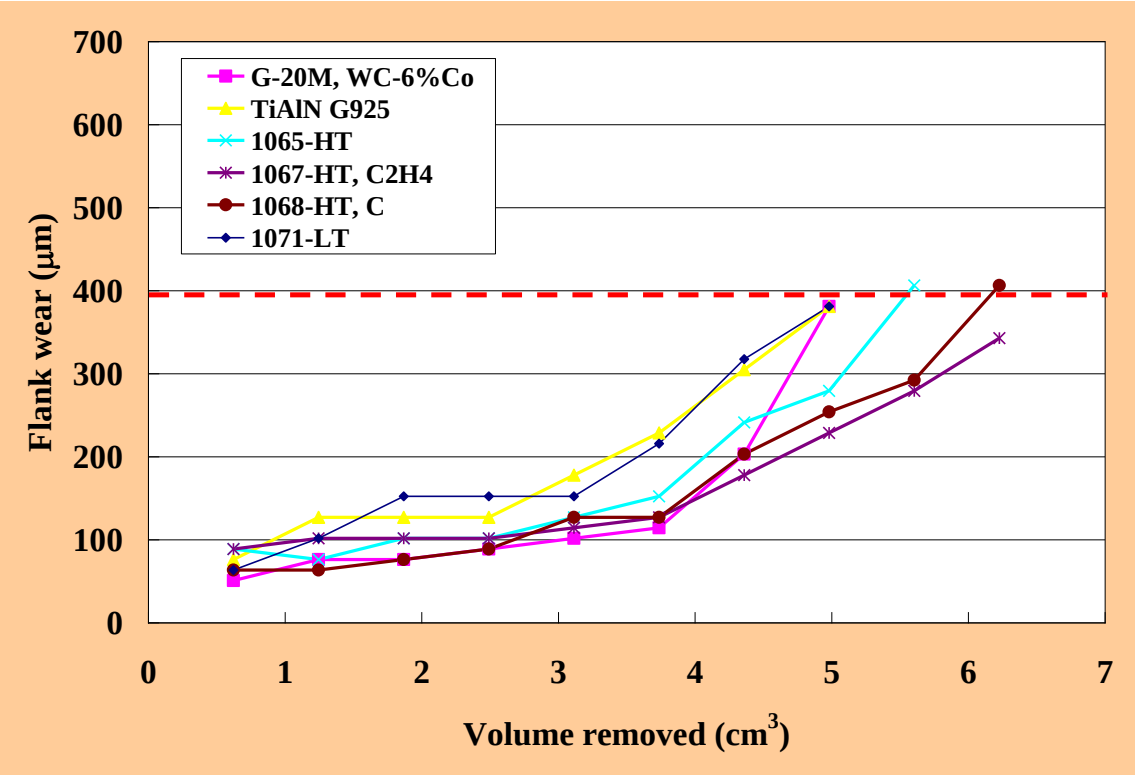

Figure 4.2.6.4-2: Cutting tool performance of $AlMgB_{14}$-TiB_2 coated tool on Ti6Al4V alloy. G-20M (WC substrate) and G-925 (TiAlN coated) are industrial standard coatings at 400 SFM.

The compositional contrast SEM images show titanium bonded to the tool. A close up image of WC in **Figure 4.2.6.4-5** explains the case of Ti interaction. The edge buildup of bonded titanium metal to the WC tool illustrates the problems associated with chemical interaction that reduces tool life. Chemical wear and edge buildup is less with the $AlMgB_{14}$ coated tools.

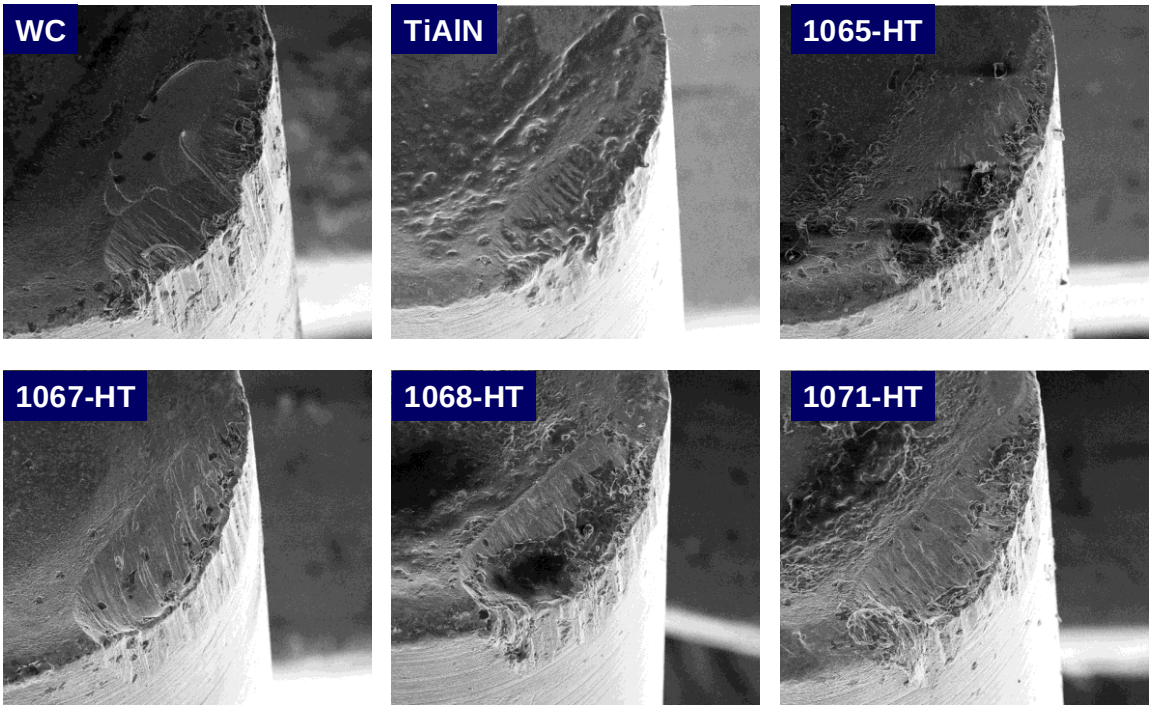

Figure 4.2.6.4-3: SEM images of worn cutting tips at 400 SFM. Although comparable in wear, the 1067-HT with C2H4 and 1068-HT with C had better wear then others.

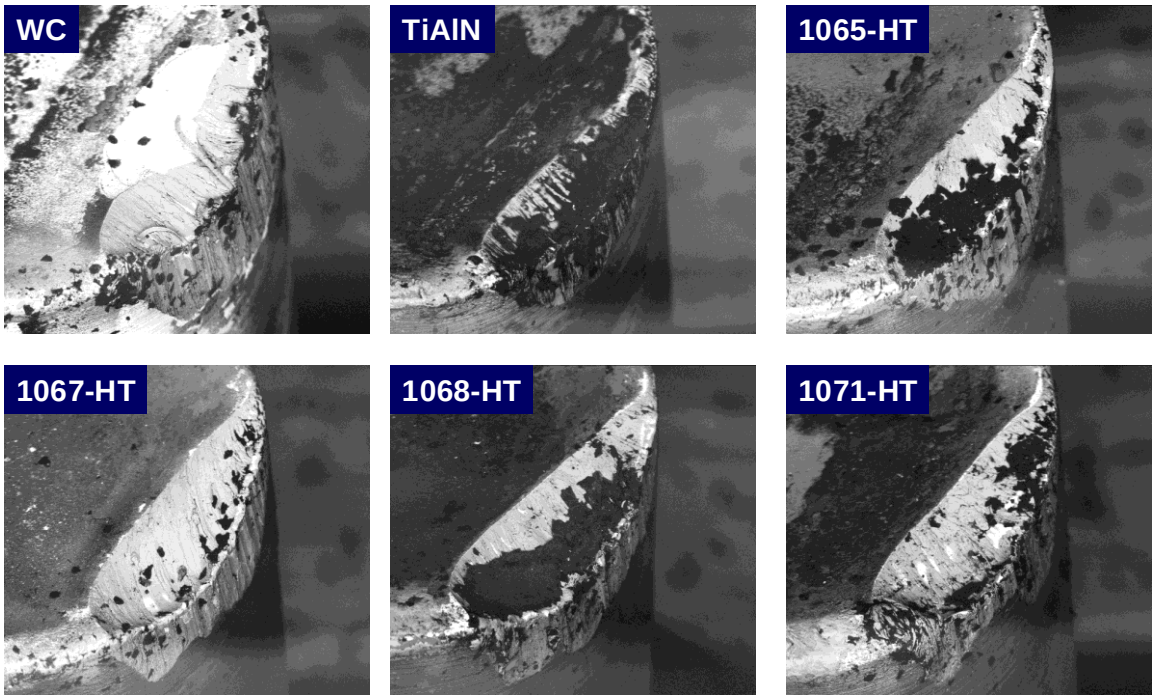

Figure 4.2.6.4-4: SEM backscattered compositional contrast images of worn cutting tip after 400 SFM test. The black is leftover oil residue and bright white areas are titanium metal that is attached to the gray WC tip.

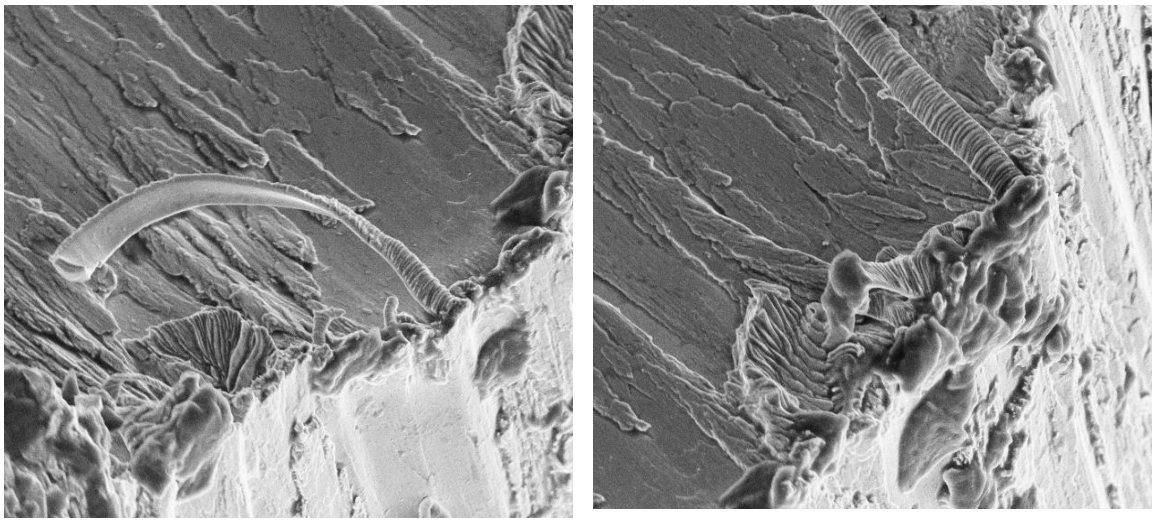

Figure 4.2.6.4-5: SEM images of WC cutting tip showing the bonded titanium metal strips after machining.

Higher speeds at 500SFM shows even faster wear rate in **Figure 4.2.6.4-6.** The uncoated WC, TiAlN, and $AlMgB_{14}$ deposited at low temperature performed the least, while $AlMgB_{14}$ deposited at the higher temperatures showed the best performance. In this test, the carbon gradient did not have additional benefits as thermal limitations of carbon gradient may be realized at the higher cutting speeds.

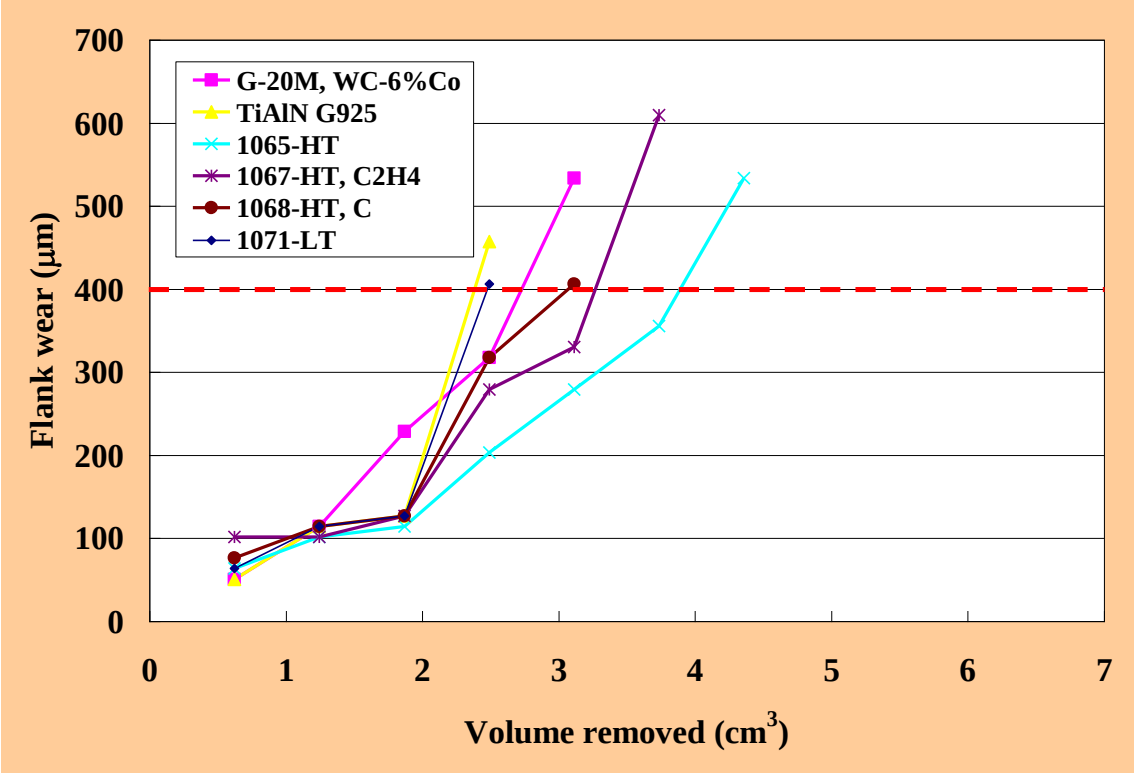

Figure 4.2.6.4-6: Cutting tool performance of $AlMgB_{14}$-TiB_2 coated tool on Ti6Al4V alloy. G-20M (WC substrate) and G-925 (TiAlN coated) are industrial standard coatings at 480 SFM.

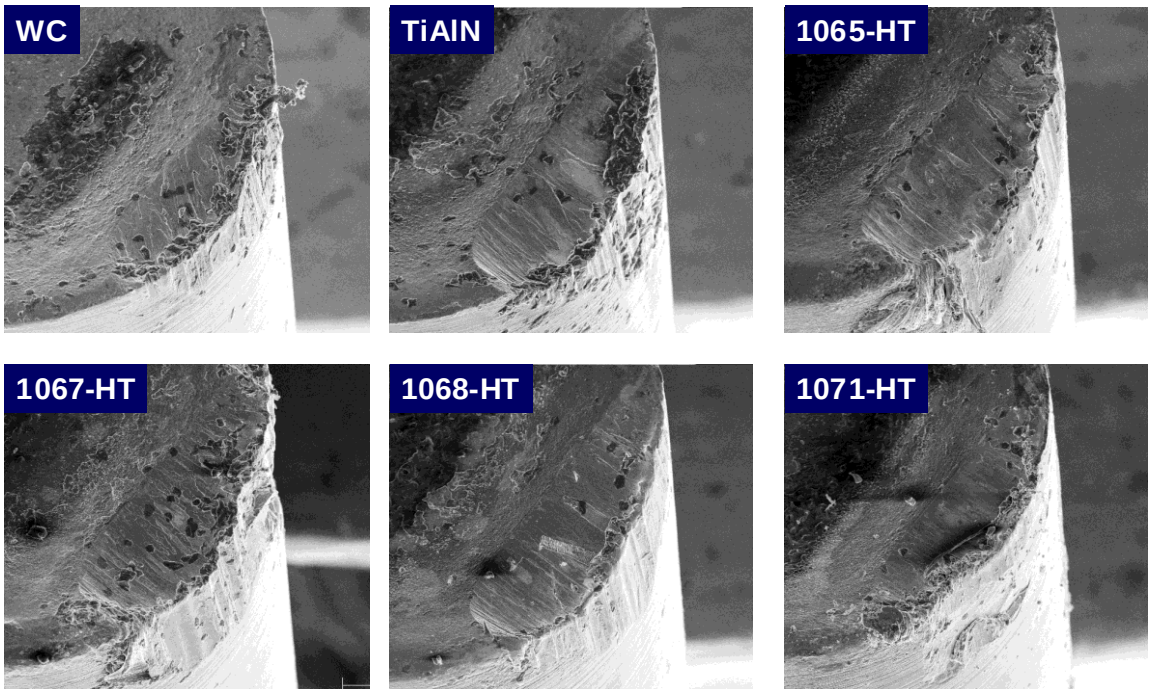

Figure 4.2.6.4-7: SEM images of worn cutting tips after 480 SFM test on titanium.

Summary of tool life improvement is shown in **Table 4.2.6.4-2**. Up to 38% improvement with bench test was observed using the scale-up PVD system on real geometry WC cutting tools. This should easily commercialize if the performance can be duplicated in the field.

Table 4.2.6.4-2: Summary of coating optimization at 400 and 480 SFM. High temperature depositions performed the best along with the carbon gradient, particularly deposited using acetylene gas source.

	Volume removed		%improvement	
	400SFM (cm^3)	480SFM (cm^3)	400SFM	480SFM
G20M	5.0	2.7	0	0
TiAlN	5.0	2.4	0	-12
1065-HT	5.6	3.7	11	38
1067-HT, C2H4	6.2	3.7	23	36
1068-HT, C	6.7	3.1	33	14
1071-LT	5.0	2.5	0	-7

4.2.6.5 Competitive Evaluation – TiB_2, TiAlSiCN, AlTi-CrN, TiAlN

Bench testing of 3 new commercial coatings on G-20M (WC-6%Co) was compared. Commercial coatings consisted of TiB_2, TiAlSiCN, AlTiC-CrN PVD coatings. **Figure 4.2.6.5-1** show new commercial coatings for Ti-based cutting tests with TiAlN (G-925) as a standard.

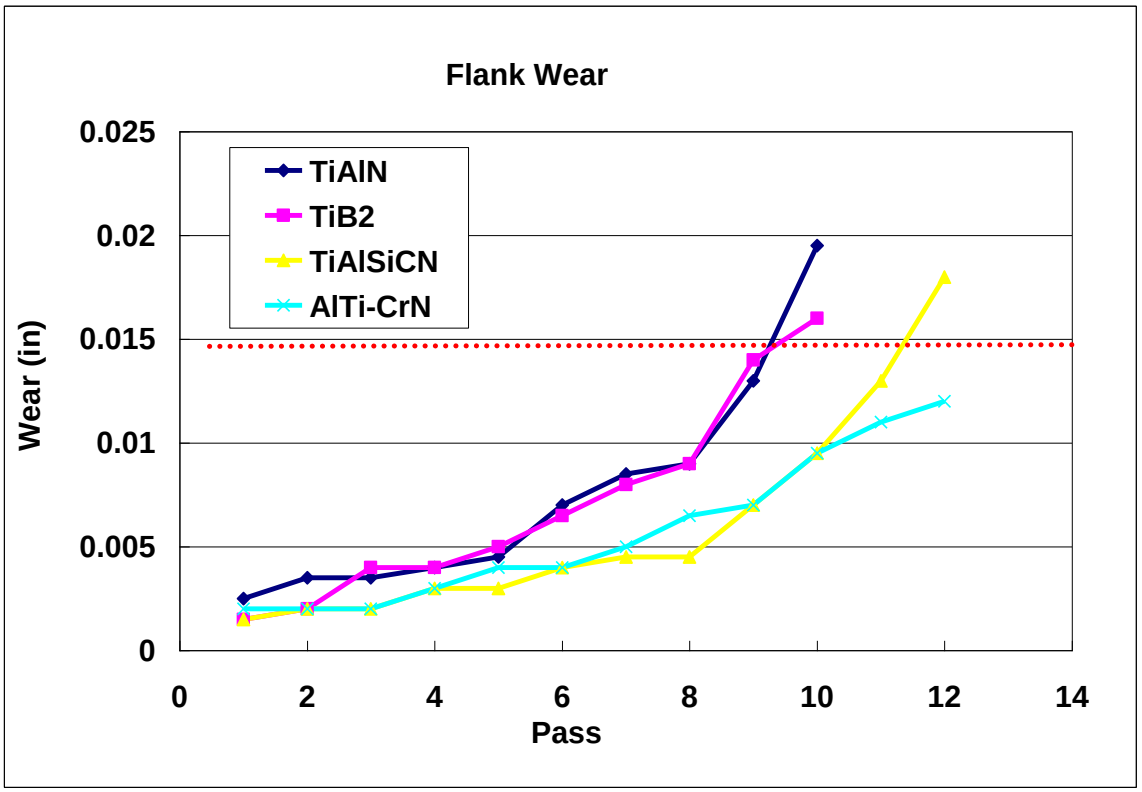

Figure 4.2.6.5-1: Bench Ti6Al4V machine testing of new commercial coatings compared with standard TiAlN coated G-20M (WC-6%Co).

The test show that TiAlSiCN and AlTiC-CrN both had significant improvements (more then 20%) over the standard TiAlN. The commercial TiB_2 coatings showed similar wear to the standard. This is slightly below the performance of the $AlMgB_{14}$ coatings. AlTi-CrN based coatings may have good potential for Ti-machining application.

1f) Machining cast iron, low alloy steel, stainless steel, and nickel based superalloys

The commercialization potential for $AlMgB_{14}$-TiB_2-based coatings in machining applications appears, at least at this time, to be limited to titanium alloys. It appears that the $AlMgB_{14}$-TiB_2 coating is not a good candidate for Ni-alloy machining, grey cast iron, stainless steels, and low alloy steels. It is anticipated, however, that there is potential in the aluminum markets for this particular material as a coating. Aluminum test was deleted out of the test matrix due to long test durations (weeks of machine time) and limited marketability of advanced coatings. We are exploring the potential of this material in other niche markets for cutting tool applications. **Table 4.2.6.5-1** summarizes the aforementioned market potential for each metal alloy base and standard comparative materials. It is noteworthy to mention that the coatings were tested on ceramic-based cutting tools such as Al_2O_3-TiC composite and Al_2O_3-SiCw whiskered composite tools for stainless steels and nickel alloys.

Table 4.2.6.5-1: Summary of machining compatibility of $AlMgB_{14}$-TiB_2 coatings with various metals relative to commercially competitive coatings

Summary of material compatibity

	Coated carbide tool material		**Ceramic based substrates**	
Metal alloys	$AlMgB_{14}$-TiB_2	TiAlN	Al_2O_3-TiC	Al_2O_3-SiCw
Titanium	Excellent	Good		
Nickel-inconel	Poor	Good		
Grey cast iron	Poor	Good		
Low alloy steel	Poor	Good		
Stainless steel	Poor	Poor	Excellent	Good
Hardened steel	Poor	Poor	Excellent	Good
~~Aluminum~~	~~TBD~~	~~Good~~		

Greenleaf is testing other potential machining applications. $AlMgB_{14}$-TiB_2 coated carbide was tested on 1018 low alloy steel work pieces. The substrates are all WC-6%Co. Commercially available TiAlN-PVD coated carbide still clearly outperformed other grades in machining low alloy steel materials. WC-6%Co is the base substrate without coating, AlTi-CrN is a competitive commercial coating; $AlMgB_{14}$-TiB_2 based coatings (runs 1138 and 1137) with and without a gradient carbon. **Figure 4.2.6.5-2** illustrates the flank wear (in this case the limiting factor in tool life, as compared to crater and notch wear). The testing conditions were light finish conditions at 600SFM speed, 0.025" depth of cut. **Figure 4.2.6.5-3** includes SEM pictures of the cutting tip after wear testing. The $AlMgB_{14}$-TiB_2 coatings did not perform well with low alloy steels.

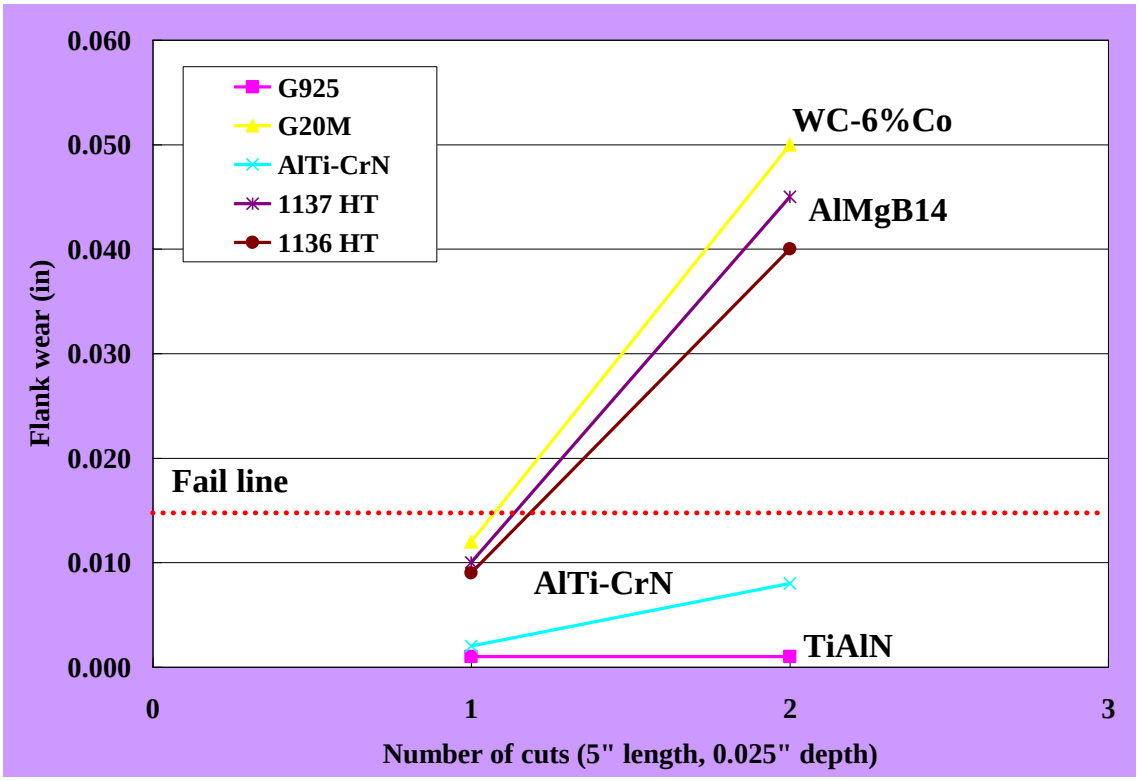

Figure 4.2.6.5-2: Finish turn testing of low alloy steel showing no improvement of $AlMgB_{14}$ coatings over commercial coatings.

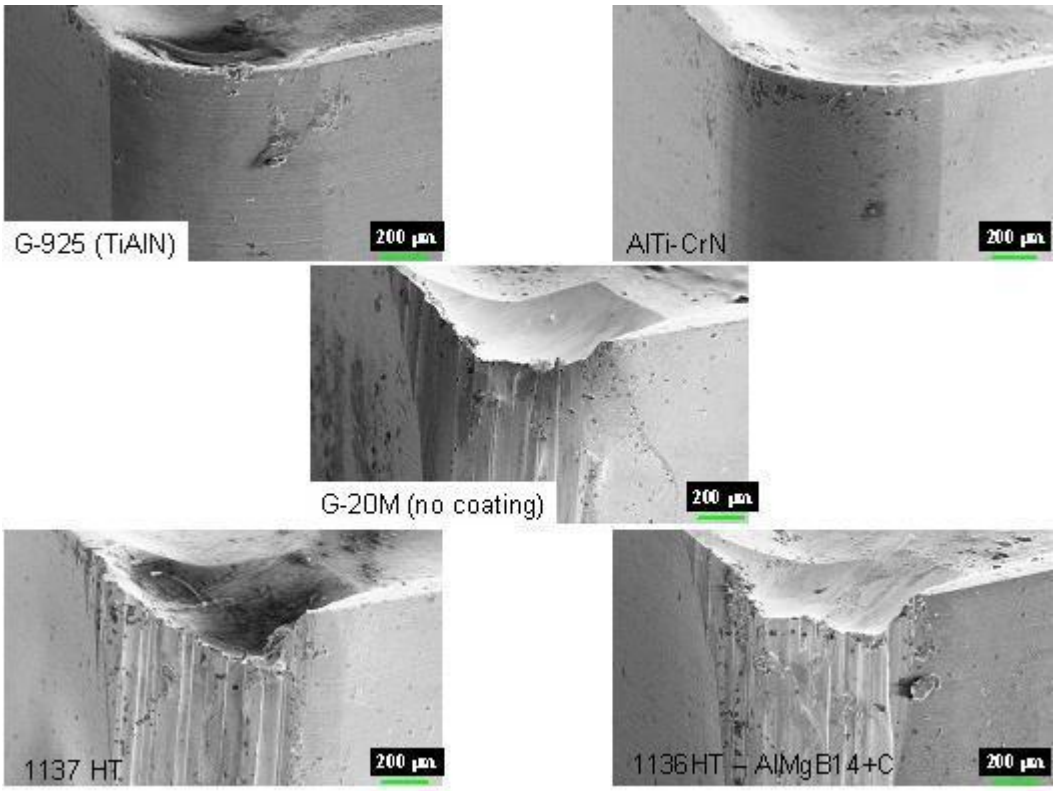

Figure 4.2.6.5-3: SEM images of the cutting edges after finish turning test on low alloy steel. The flank wear on WC, $AlMgB_{14}$ (with and without carbon gradient) is obvious.

$AlMgB_{14}$-TiB_2 coated carbide was tested on grey cast iron work pieces. Our G-925, TiAlN-PVD coated carbide was used as a industry standard for machining grey cast iron materials, G20-M is WC-6%Co without a coating, AlTi-CrN is already a commercial coating that tested well with titanium alloys, 1137 and 1138 are the two $AlMgB_{14}$-TiB_2 based coatings with and without a gradient carbon surface layer for improved lubricity. **Figure 4.2.6.5-4** illustrates the flank wear (in this case the limiting factor in tool life, as compared to crater and notch wear). The testing conditions were light finish conditions at 600SFM speed, 0.025" depth of cut. Typical cutting speeds for grey cast iron can exceed 1000SFM. The test results are not surprising since previous tests showed that $AlMgB_{14}$-TiB_2 may not be a good candidate for Fe-based materials.

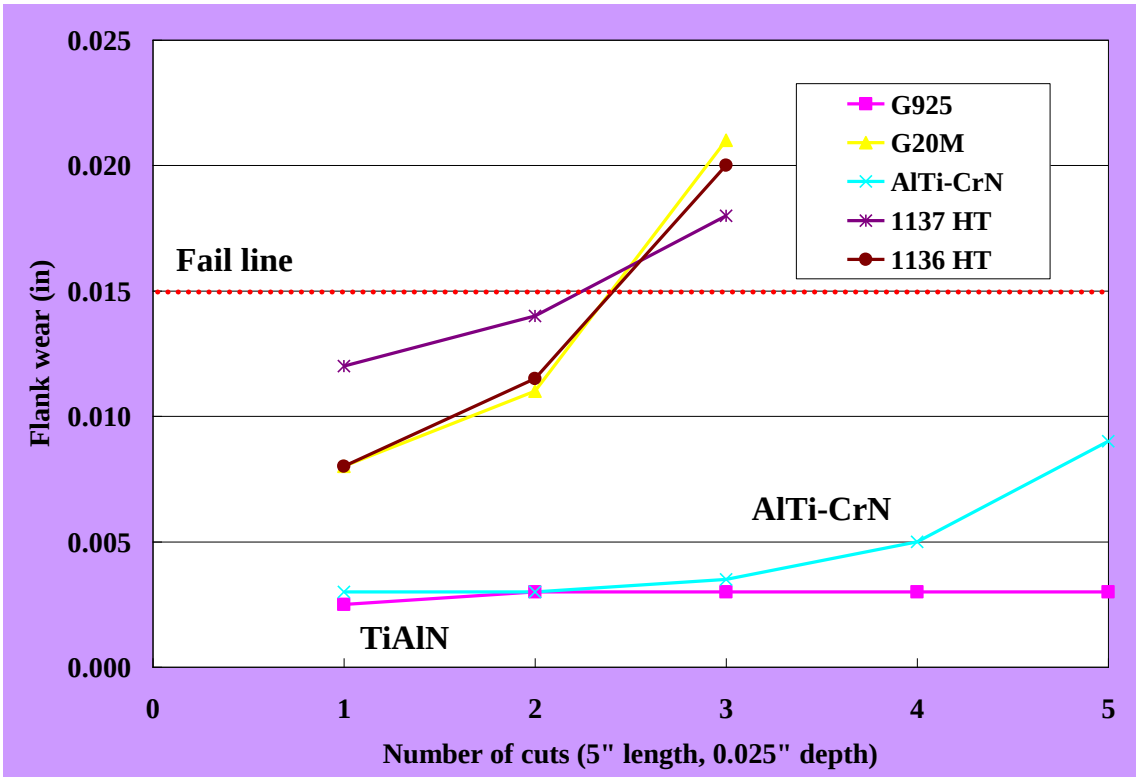

Figure 4.2.6.5-4: Bench machine testing of grey cast iron

Our standard G-925, TiAlN-PVD, still outperformed all other coated carbide grades in grey cast iron. The wear pattern suggests that there is little difference between bare substrate in comparison to the $AlMgB_{14}$-TiB_2 coated grades as shown in the SEM images in **Figure 4.2.6.5-5.**

Initial testing of $AlMgB_{14}$-TiB_2 coatings suggests that there may be a reaction with Fe-based alloys. The oxidation resistance of the $AlMgB_{14}$ coating was a large advantage in titanium machining; however, in high thermal conductivity work pieces such as grey cast iron it may not be as beneficial until higher temperatures are reached at the cutting tip.

We are continuing with our testing of other Fe-based materials. Testing on low thermally conductive materials such as stainless steel may reveal whether this coating is being limited by a chemical reaction with iron.

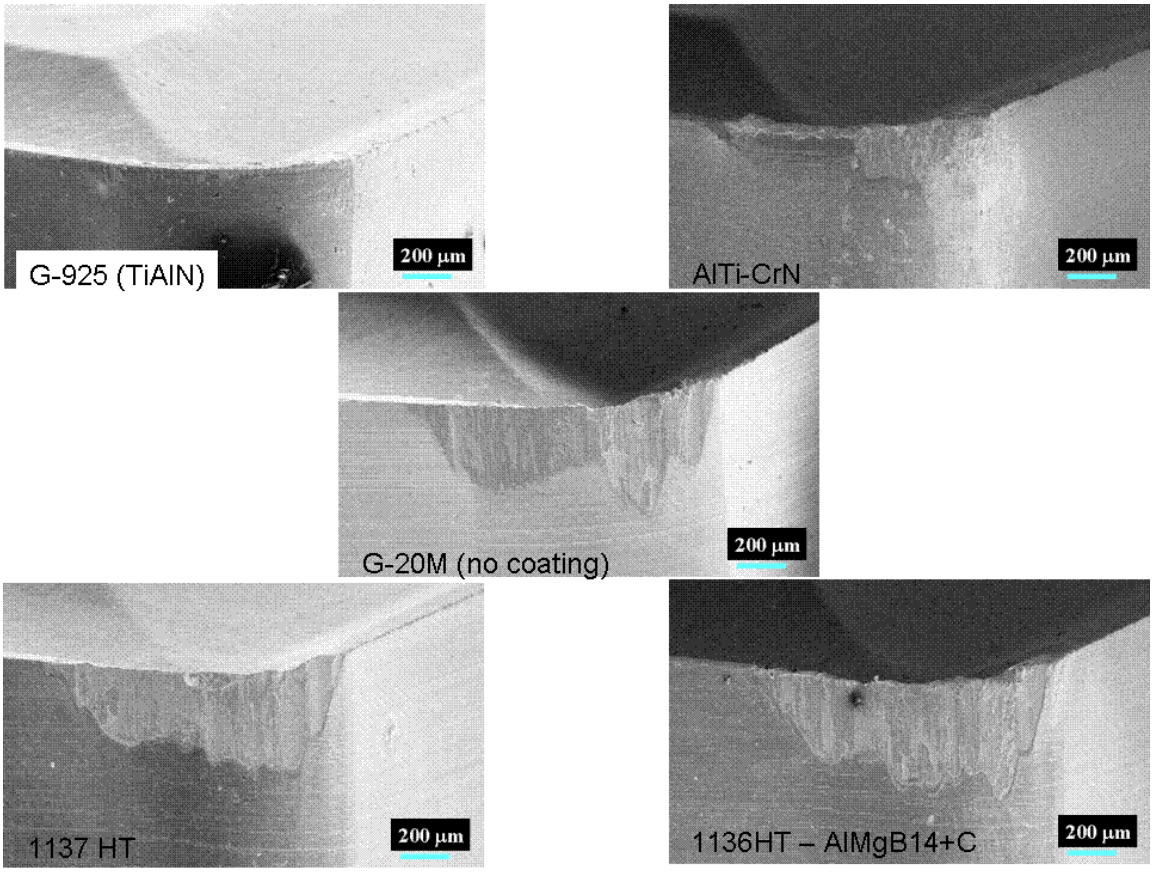

Figure 4.2.6.5-5: SEM images documenting flank wear on various tool inserts after grey cast iron machining.

We demonstrated the feasibility to coat $AlMgB_{14}$-TiB_2+C coatings on three different ceramic substrates. The ceramic materials offer wider machining applications over WC-based tools. Part of the tool limitations in machining titanium is the thermal and oxidation degradation of WC-Co substrates. The other limitation is dependent on the flammability and cooling of the titanium chips during machining. While ceramic substrates may be able to offer better thermal corrosion resistance, it can be limited by poor thermal shock resistance, increased cost, and ability to make complex chipformed geometries (limited to flat surfaces). First test was simple triangle test geometries to check overall feasibility to coat on ceramics and to evaluate machining on stainless steel.

Three alumina based ceramic composite substrates Al_2O_3-SiCw, Al_2O_3-TiC-SiCw, and Al_2O_3-TiC were coated with $AlMgB_{14}$-TiB_2 with and without a carbon gradient. The coatings were well adhered with no signs of flaking on all three substrates. This was the first time ceramic substrates were coated.

Figure 4.2.6.5-6 was a setup test to determine which substrate would give us best results for 1018 stainless steel. Clearly, the Al_2O_3-TiC had the least amount of wear, and the focus of the 1018 stainless steel tests was coatings on Al_2O_3-TiC ceramic.

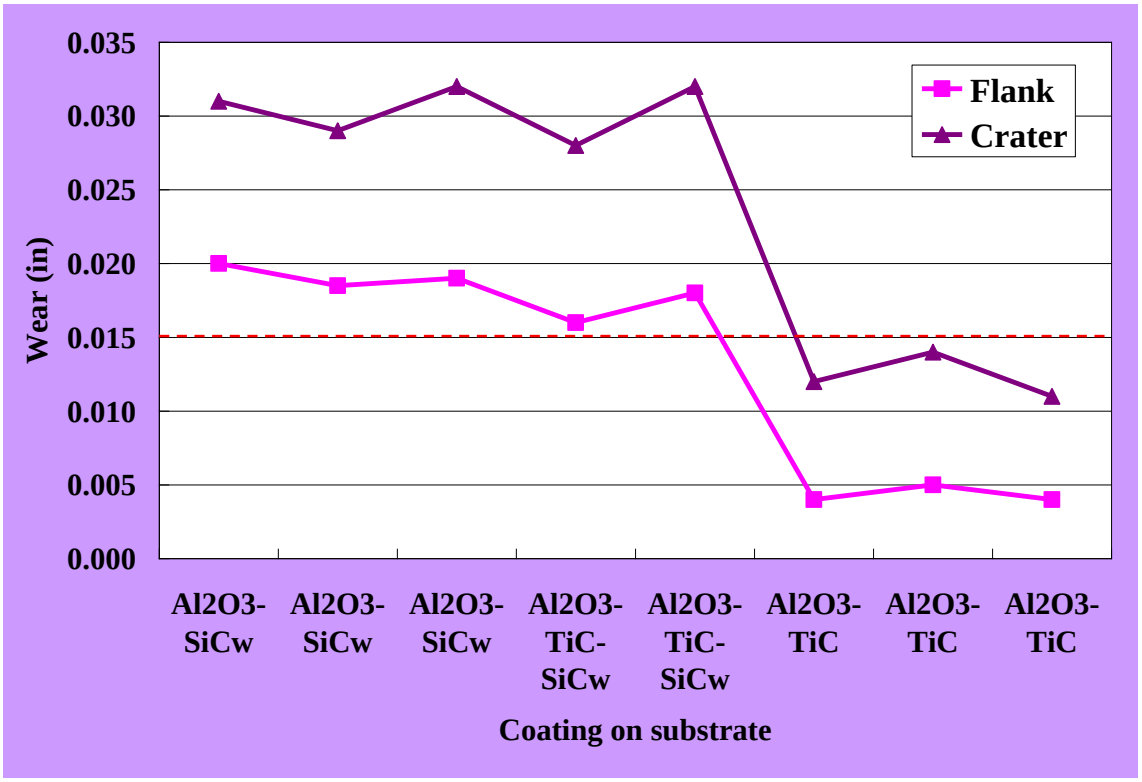

Figure 4.2.6.5-6: Crater and flank wear after machining 1018 stainless steel with uncoated ceramic substrates.

Previous testing of iron-based materials using $AlMgB_{14}$-based coatings showed poor performance. What we did not know was whether the tool life was thermally or chemically limited. Thermal limitation is dependent on heat removal, and chemical limitation is dependent on reactivity between the tool and the work piece. Titanium is a poor conductor of heat, and cast iron appears to react with $AlMgB_{14}$ coatings. The success of the coating in titanium machining applications is due largely to the higher thermal resistance of the coating. Stainless steel has low thermal conductivity in comparison to cast iron (20 versus 60 W/m-K, respectively), thus there is a higher probability for $AlMgB_{14}$ coatings to enhance the tool life than previously tested iron-based materials.

Accelerated wear testing on 1018 stainless steel at surface speed of 800 SFM is presented in **Figure 4.2.6.5-7** Comparison of non-coated Al_2O_3-TiC versus the $AlMgB_{14}$-TiB_2 (with and without carbon gradient) tools were crater wear limited. The two coated tools had higher wear than non-coated, indicating that the wear mechanism was still chemically limited. Further testing at 1250 (**Figure 4.2.6.5-8**) and 1700 SFM (**Figure 4.2.6.5-9**) showed no improvement with coatings. Interestingly, the speed did not have a direct influence on tool life. This would indicate that higher speed and more heat generation did not have much influence in tool life with a ceramic base.

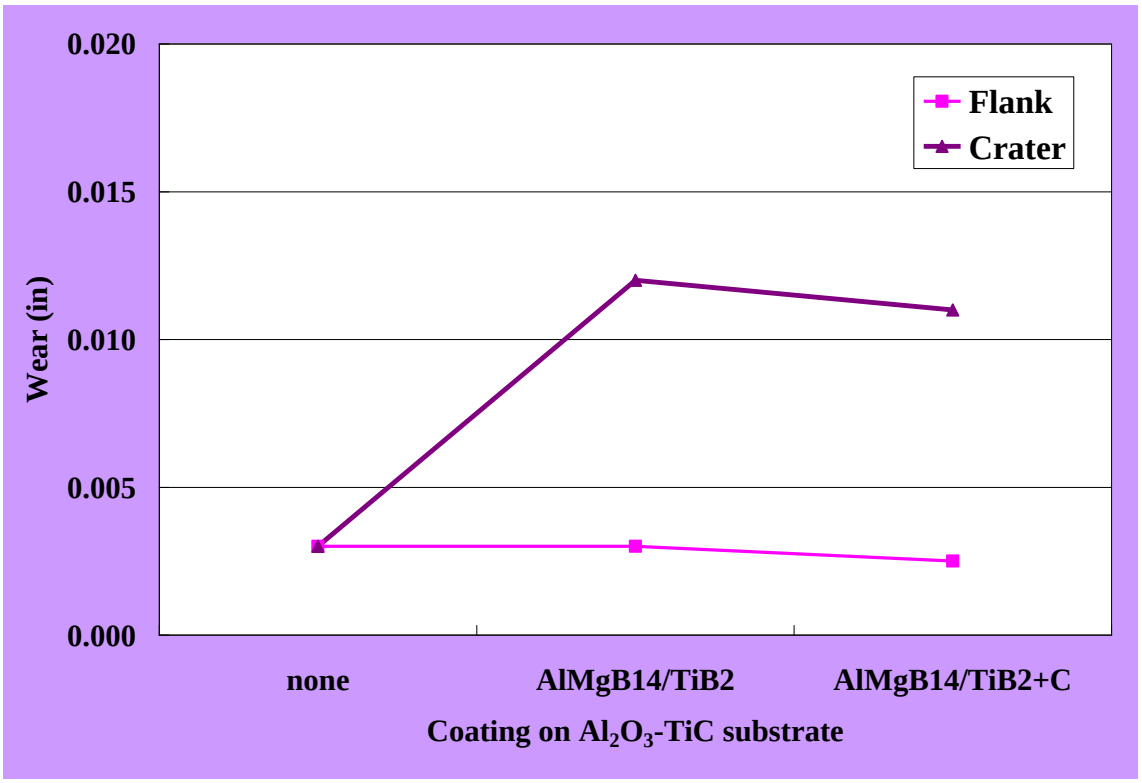

Figure 4.2.6.5-7: Stainless steel machine test at 800 SFM.

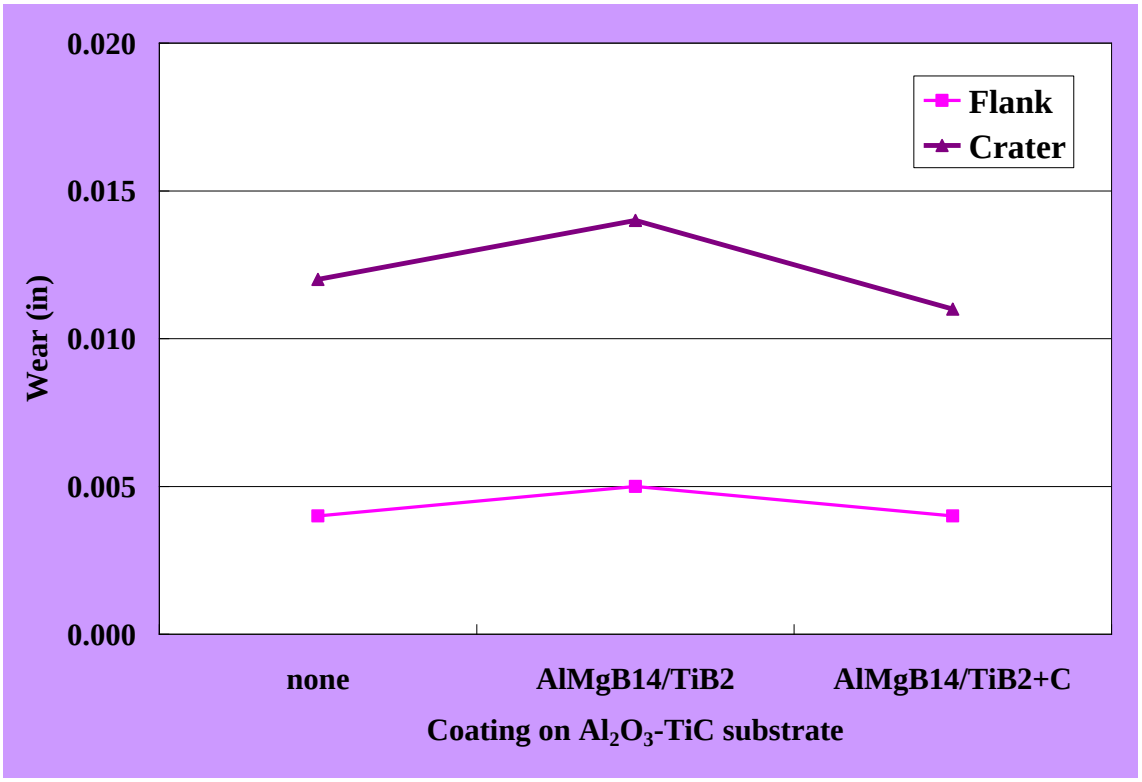

Figure 4.2.6.5-8: Stainless steel machine test at 1250 SFM.

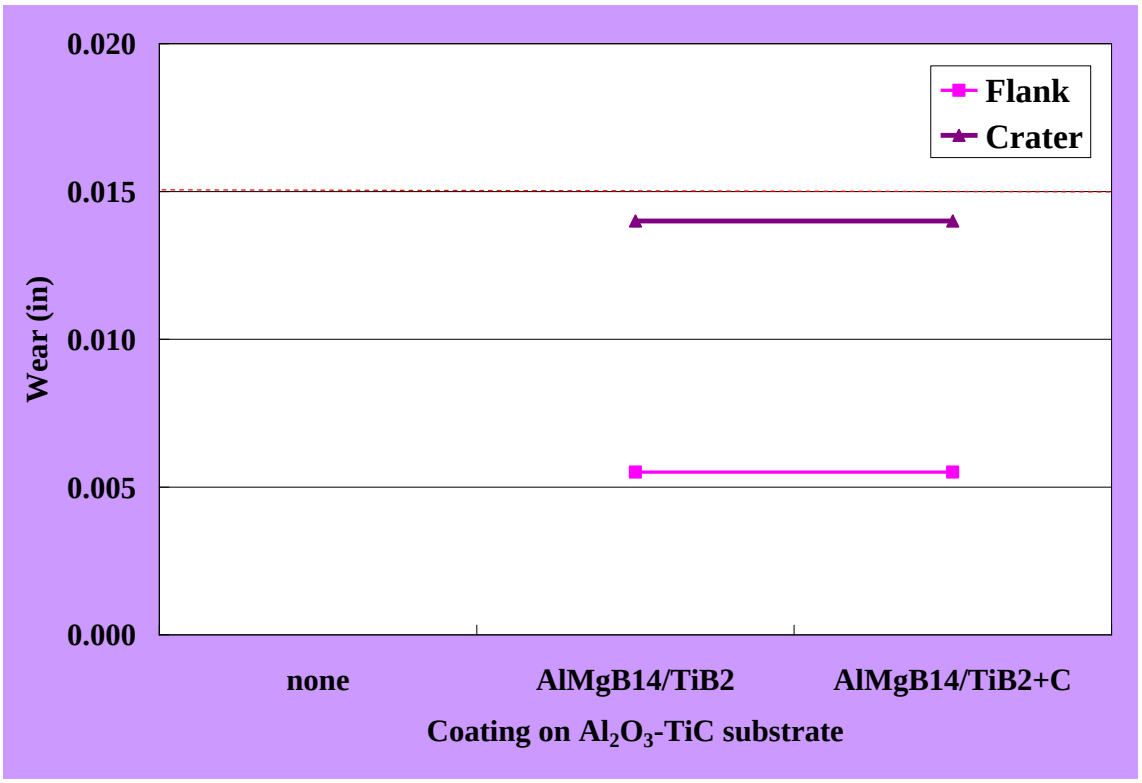

Figure 4.2.6.5-9: Stainless steel machine test at 1700 SFM.

Detailed plots of progressive wear on stainless steel machining are shown in **Figure 4.2.6.5-10 and Figure 4.2.6.5-11.** While the curves still show that this was crater-limited and the coatings did not provide additional wear protection, the carbon gradient coating influence had a detrimental effect. Although the coating offered no performance gains in stainless steel machining, it is interesting to note that it performed better with stainless steels then with other iron-based metals tested. This provides some evidence that perhaps the increase in tool life of the $AlMgB_{14}$ coated inserts for titanium machining is based largely on chemical resistance with the metal at elevated temperatures.

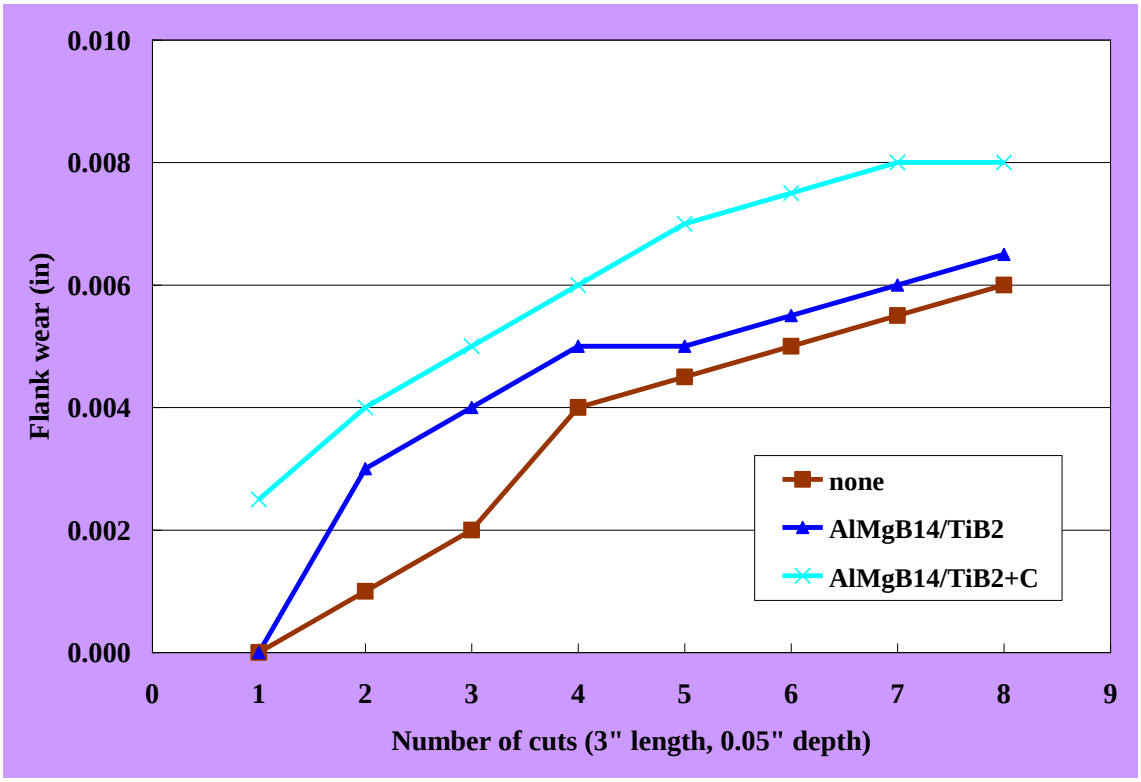

Figure 4.2.6.5-10: Flank wear of stainless steel machine test at 800 SFM.

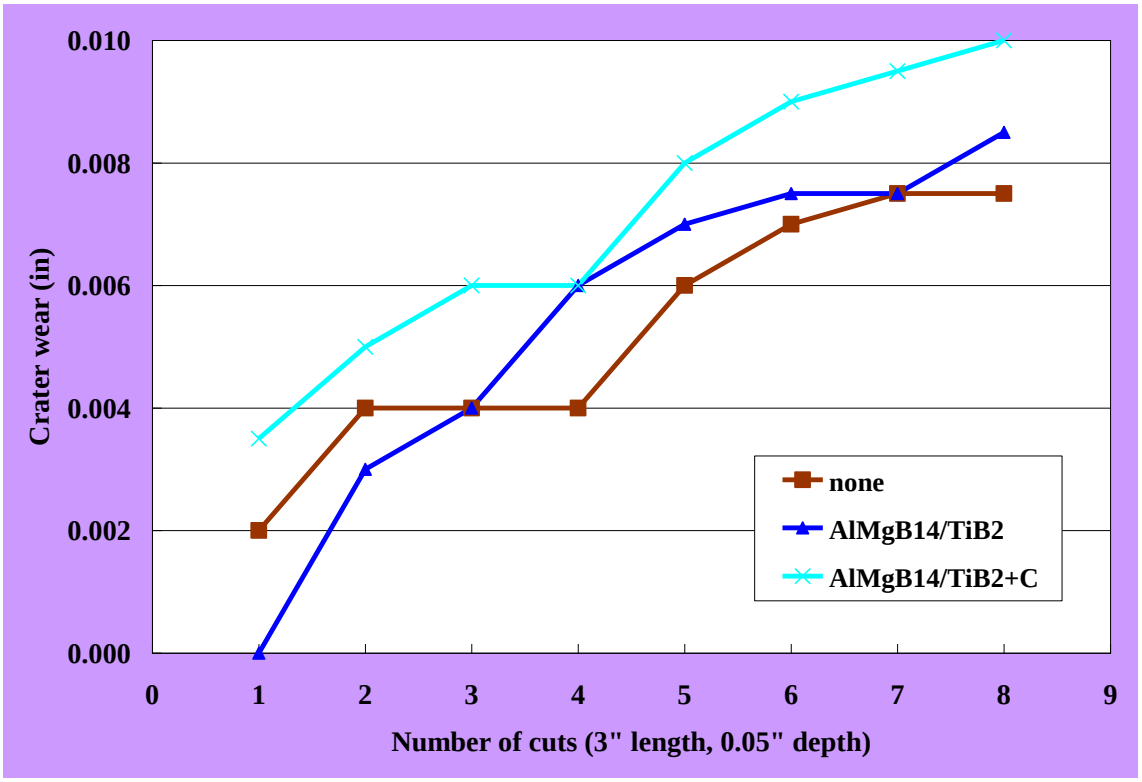

Figure 4.2.6.5-11: Crater wear of stainless steel machine test at 800 SFM.

Overall, the stainless steels and other iron alloys appear to be limited by the reactivity of iron with the coating. Because machining on stainless steel had significantly better performance than other iron alloys with higher thermal conductivity, this coating may be reformulated for better performance.

The potential for $AlMgB_{14}$ coating for titanium machining seems evident, and the coatings may provide its usefulness in other material applications. Other difficult to machine alloys used in the aerospace applications include nickel-based superalloys; one such example being hardened Inconel 718. The first test was a finishing application; relatively low speed in comparison at 275 SFM. **Table 4.2.6.5-2** outlines the test conditions and the results of the bench performance evaluation.

Table 4.2.6.5-2: Inconel 718 (hardened) machine testing of $AlMgB_{14}$ coated tools.

Finishing bar - coating comparison test
Material: Inconel 718 heat treated to 47RC
CNGG432TF, 1136, 1137, G-925, GA5026

Depth of cut 0.030 in
Feedrate 0.006 in/rev

	GA5026	G-925	1137	1136
Description	**TiCN/Al2O3/TiN-CVD**	**TiAlN-PVD**	**BAM+C**	**BAM**
Cutting speed (SFM)	275	275	275	275
Length of cut (in)	5	5	4.5	4.5
Crater wear (inch)				
Flank wear (inch)	light	less then BAM	excessive	excessive

$AlMgB_{14}$ coating all showed heavy signs of wear compared to TiAlN and $TiCN/Al_2O_3/TiN$ multilayered coatings. These results are consistent with previous observations that nickel and $AlMgB_{14}$ materials have a tendency to react with one another. **Figure 4.2.6.5-12** provides a comparison of the obvious differences after this test. Repeated tests showed similar results.

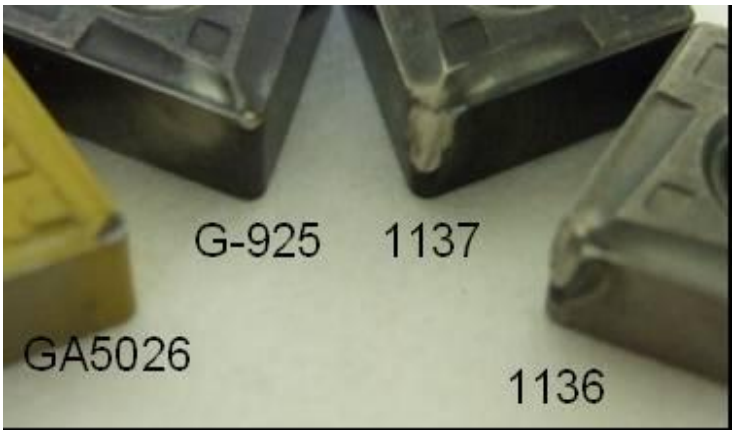

Figure 4.2.6.5-12: Wear comparison of $AlMgB_{14}$-based coatings (1136, 1137) vs. commercial coatings on WC-6% Co based substrates.

4.2.6.6 Field trials

Field trials are an extension of bench testing. These tests more accurately represent field conditions in insert styles and parts that are machined and are a verification of the benefits realized in bench tests. The focus of the field trials was on titanium metal alloys. One major difference in field evaluation from bench testing is that the parts are machined to completion and we are not always able to evaluate the tools incrementally with clear trends in tool life. Some of the data collected are low-resolution optical images limited by field evaluations although the tool wear measurements are accurate. The major benefits of field trials are that they more accurately represent real component machining and often require complex machining paths. The $AlMgB_{14}$-coated tool was compared with the most common tool used for that application. They are not necessarily Greenleaf tools for comparison. These would be labeled competitive inserts.

Fail criteria for field trials is applications dependent and relative to the popular tools that are being used for the application.

Summary of titanium alloys tested and applications are listed in **Table 4.2.6.6-1.** All the testing showed successful comparable results with bench testing. The successful tests showed significant improvements in both speed and tool life of the cutting tools.

Table 4.2.6.6-1: Summary of field evaluations on titanium alloys.

Summary of field evaluation on titanium alloys				
Alloys tested		Ti6Al4V Ti-6-2-4-2 Ti-6-2-4-6		
Applications	Roughing	boring	→	Successful
		bar	→	Successful
		plunge and turn	→	Test limited
	Finishing	all applications	→	Successful
High pressure coolant				
	Roughing	turning	→	Successful
	Finishing	turning	→	Successful

4.2.6.6.1 Field trials, Application 1

Three coating grades were selected based on initial lathe performance testing for field evaluation. Application 1 was for rough boring of Ti6Al4V, with a 0.110-inch depth of cut and a 0.006-inch/rev feedrate (30HP TNZ horizontal CNC lathe). The results are shown in **Table 4.2.6.6.1-1**. The field tests showed a speed increase from 135 SFM to 160 SFM, a 20% improvement in roughing. **Figure 4.2.6.6.1-1** shows the tool tip after testing. The rough boring speed was capped for safety reasons and we will realize the full potential with the next set of tests. The summary of the rough machining field test was “Faster cutting time, minimal wear on the insert. Competitor insert would need to be indexed (new tip) after each part, but Greenleaf insert #1067 could continue roughing.”

Table 4.2.6.6.1-1: Rough boring of Ti6Al4V for Application 1

	Standard	1067
Cutting speed (SFM)	135	161
Cutting time (min)	15	12

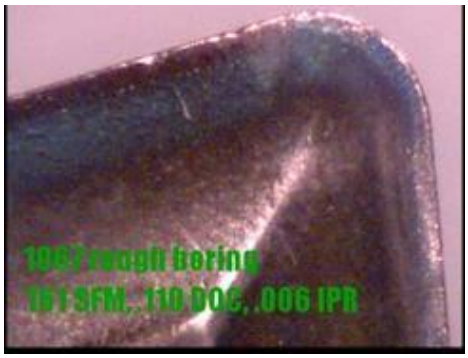

Figure 4.2.6.6.1-1: Optical microscope image of used cutting tip after rough boring of Ti6Al4V showing no wear at the cutting tip

4.2.6.6.2 Field trials, Application 2

Application 2 is a finish machining operation (Monarch Ultra Center 50HP) of Ti 6-2-4-2 material using three different $AlMgB_{14}$ coatings, #1065, #1067, #1068, against standard KC730, a standard TiAlN coated on WC substrate. The depth of cut was 0.010 inch and feed rate was 0.006 inch/rev. Ti-6-2-4-2 material is a tougher titanium grade that we have not previously used to establish performance of our coatings. The initial field performance summary is shown in **Table 4.2.6.6.2-1.**

Table 4.2.6.6.2-1: Finish machining of Ti-6-2-4-2 for Application 2

Finish turning
Material: Ti 6-2-4-2 (tougher then Ti6Al4V)
CNGG432 no hone Batch #1065, 1067, 1068

Depth of cut	0.010 in			
Feedrate	0.006 in/rev			
	Competitor	1065	1067	1068
Cutting speed (SFM)	240	400	400	400
Cutting time (min)	8.3	5	5	5
Crater wear	0.002"	none	0.002"	none
Surface finish	excellent	excellent	excellent	excellent

Minimum 67% improvement

The $AlMgB_{14}$-TiB_2-based coatings all performed better than the standard inserts with 67% improvement in speed. This resulted in completion of this segment of the machining operation in 5 minutes compared to 8.3 minutes using a standard insert. The surface finish of the machined component was excellent. Insert run 1067 showed initial signs of wear as compared to the 1065 and 1068 inserts with no observable wear as shown in **Figure 4.2.6.6.2-1**. The summary of the field report was, “Faster cutting time, minimal wear on the insert. Competitor insert showed similar wear after 1 part, but at 240 SFM – longer cycle time, compared to 400 SFM and less cycle time.”

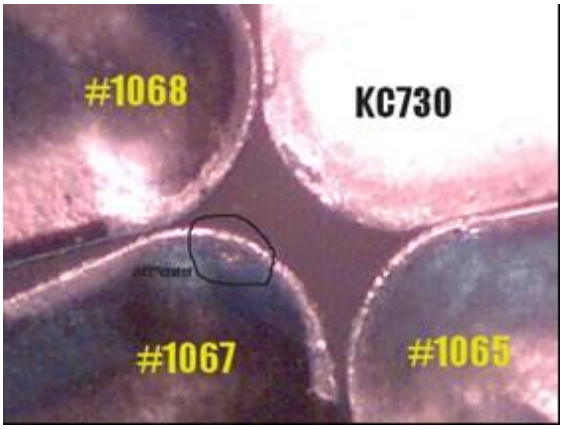

Figure 4.2.6.6.2-1: Crater wear pattern after Ti-6-2-4-2 for Application 2 machining. Standard KC730 and 1067 showed slight wear, the 1065 and 1068 showed no wear.

The initial field tests were very exciting and the initial data seem to support our findings from bench performance tests. Thus far, these results were very positive and this initial test generated much interest and excitement.

4.2.6.6.3 Field trials, Application 3

Field tests were performed for rough bar and finish turning tests for Applications 3 and 4 for titanium (Ti6Al4V) machining. The test involved duplicate coating and substrate combinations as previous testing; however, a new geometry and two new applications were tested.

Application 3 is a rough bar test that compared one competitor grade with Greenleaf's standard G-925 (TiAlN coated WC-6%Co), and 4 different $AlMgB_{14}$-TiB_2 coatings (1106, 1107, 1109, CT-1) summarized in **Table 4.2.6.6.3-1**. Three tests were conducted varying feed rates and machine speeds. Test 2 shows the overall speed improvement was from 180 SFM to 320 SFM. While the standard G-925 grade failed at these conditions, the $AlMgB_{14}$-based coating performed well, with a speed improvement over the competitive grade and 78% less wear. The unhoned 1109 had better surface finish and wear then honed inserts, consistent with previous bench testing.

Roughing at higher speeds of 350 and 400 SFM all resulted in failed inserts as shown in **Table 4.2.6.6.3-2.**

Table 4.2.6.6.3-1: Application 3, Test 1, Rough machining

Roughing bar - coating comparison test
Material: Ti6Al4V
Monarch Ultra Center 50HP
DNGG432 1107, 1106, 1109, no hone

Depth of cut	0.080	in
Feedrate	0.005	in/rev

	Competitive	G-925	1106	1107	1109	CT-1
Cutting speed (SFM)	180	320	320	320	320	320
Cutting time (min)	5	5	5	5	5	5
Crater wear (inch)	0.015	0.010	0.009	0.0085	0.0075	0.008
Flank wear (inch)	0.015	0.004	0.003	0.004	0.004	0.005

78% improvement, small improvement over competitive G-925 (TiAlN)

Table 4.2.6.6.3-2: Application 3, Test 2 of DNGG432 inserts for rough bar machining of Ti6Al4V.

Roughing bar - coating comparison test
Material: Ti6Al4V
Monarch Ultra Center 50HP
DNGG432 1107, 1106, 1109, no hone

Depth of cut	0.080 in
Feedrate	0.010 in/rev
	350 - 400 SFM, all inserts failed

Substrate limitations at higher speeds

4.2.6.6.4 Field trials, Application 4

Application 4 is a finish turning test on highly repeatable geometry component. In this test a competitive insert was tested against 1107-A and 1109-A (A-honed edge preparation, A-honed typically had 1/2 the tool life as no honed inserts in finish machining). **Table 4.2.6.6.4-1** shows the summarized experiment, test 2 results are in Table **4.2.6.6.4-2**. The 1107 and 1109 samples both successfully improved the speed by 50% with less wear. There is opportunity for improvement since the standard 15 min of cutting time resulted in only 1/3 of the wear even at the 50% higher speeds.

Table 4.2.6.6.4-1: Application 4, Test 1 of DNGG432 inserts for finish lathing of Ti6Al4V.

Finish turning - coating comparison test
Material: Ti6Al4V
Monarch Ultra Center 50HP
DNGG432 1107, 1106, 1109, A-hone

Depth of cut	0.010	in
Feedrate	0.005	in/rev

	Standard	**1107-A**	**1109-A**
Cutting speed (SFM)	270	400	400
Cutting time (min)	15-20	15	15
Crater wear (inch)	0.015	0.005	0.006
Flank wear (inch)	0.015	0.0025	0.0025

50% improvement, 1/3 tool life

Table 4.2.6.6.4-2: Application 4, Test 2 of finish machining Ti6Al4V.

Finish turning - coating comparison test
Material: Ti6Al4V
Monarch Ultra Center 50HP
DNGG432 1107, 1106, 1109, A-hone

Depth of cut	0.080	in
Feedrate	0.010	in/rev

	Competitive	G-925	1109	1109-A
Cutting speed (SFM)	180	320	320	320
Cutting time (min)		5	5	5
Crater wear (inch)	0.015	FAIL	0.01	0.01
Flank wear (inch)	0.015	FAIL	0.0035	0.005

78% improvement

Additional testing at 480 SFM (Application 4, Test 2) showed that both inserts failed for flank wear.

4.2.6.6.5 Field trials, Application 5

This field evaluation was machining 28-inch diameter Ti6Al4V metal in rough plunge and turn application. Tests were repeated at each condition with a standard TiAlN coating on a special chip form geometry, PVD $AlMgB_{14}$-TiB_2 + gradient C batch 1136, PVD $AlMgB_{14}$-TiB_2 batch 1137, TiAlSiCN, and AlTi-CrN. This is the first time the G-01M (WC-9-11%Co) substrate grade and round style inserts were used in a field evaluation. The roughing trials and test geometries are outlined below (**Table 4.2.6.6.5-1**).

Table 4.2.6.6.5-1: Application 5, plunge and rough turning of 28" diameter Ti6Al4V.

Plunge and turn rough turning - 28" diameter
Material: Ti6Al4V, 28" diameter
Lathe 40HP, 48" chuck
RPGN3V, RPGN-4V, batch 1136, 1137, G-01M substrate

Depth of cut	0.040 in				
Feedrate	0.012 in/rev				
	Standard	**1136**	**1137**	**TiAlSiCN**	**AlTi-CrN**
Cutting speed (SFM)	310	310	310	310	310
Cutting time (min)	20	20	20	20	20
Crater wear (inch)	NM	NM	NM	NM	NM
Flank wear (inch)	NM	NM	NM	NM	NM

Chipform on the geometry a factor for standard geometry
No difference, equal wear
Operator did not want to change any parameters

The results at 310 SFM surface speeds showed no significant visual wear differences after 20 min. of machining. The tests were repeated three times, however without much difference. Because of the risk with a 28-inch diameter part, the machine parameters were not explored for further optimization. The geometry of the standard had a chipform preparation while the test grades did not. The chipform should improve the cutting performance by more efficiency removing the hot metal chips away from the hot interface. The good news was that the nanocoated tool (batch 1136 and 1137) performed about the same at these normal conditions without a chipformed round inserts.

4.2.6.6.6 Field trials, Application 6

A lathe machine test was performed using Bullard 50HP for finish facing of a test ring of titanium 17 with an outer diameter of 30 inches and an inner diameter of 20 inches. The test rig had high-pressure coolant system attached to the tool holder assembly delivering 1,000 psi of coolant directly at the cutting interface. Numerous tests were conducted with varying speeds up to 600 SFM. This section is a summary of the highlights. The feed rate was 0.008 inches/revolution and depths of 0.010 inches, i.e., typical finishing operation. Four types of coatings on the same WC-6%Co were compared, commercial TiAlN, commercial AlTiC-CrN, $AlMgB_{14}$-TiB_2 (by Eaton) batch 1181, and $AlMgB_{14}$-TiB_2+C gradient (by Eaton) batch 1182. The first test was at surface speed of 500SFM. Results are presented in **Table 4.2.6.6.6-1.**

Table 4.2.6.6.6-1: Titanium machine testing at surface speed of 500 SFM with high-pressure coolant

Grade	G-925	RD4869	1181	1182
Description	TiAlN	AlTiC-CrN	BAM	BAM+C
Cutting speed (SFM)	500	500	500	500
Time in cut (min)	8.2	8.2	8.2	8.2
Crater wear (inch)	0.008	0.006	0.007	0.008
Flank wear (inch)	0.010	0.005	0.004	0.006

The objective of this experiment was to find the maximum allowable speed with acceptable wear. Evaluation criterion was based primarily on flank wear (wear just below the nose of the insert). The standard TiAlN coated inserts had 0.010 inches of flank wear compared that with 1181 $AlMgB_{14}$-TiB_2-coated inserts with 0.004 inches of flank wear. This was a 60% reduction in wear compared to that of the common TiAlN grade. This translates into more than double the tool life of a standard TiAlN grade. The other commercial competitor grade AlTiC-CrN also had good wear with 50% reduction in wear. **Figure 4.2.6.6.6-1** shows flank wear optical microscopy images taken in the field of the tool wear after machining.

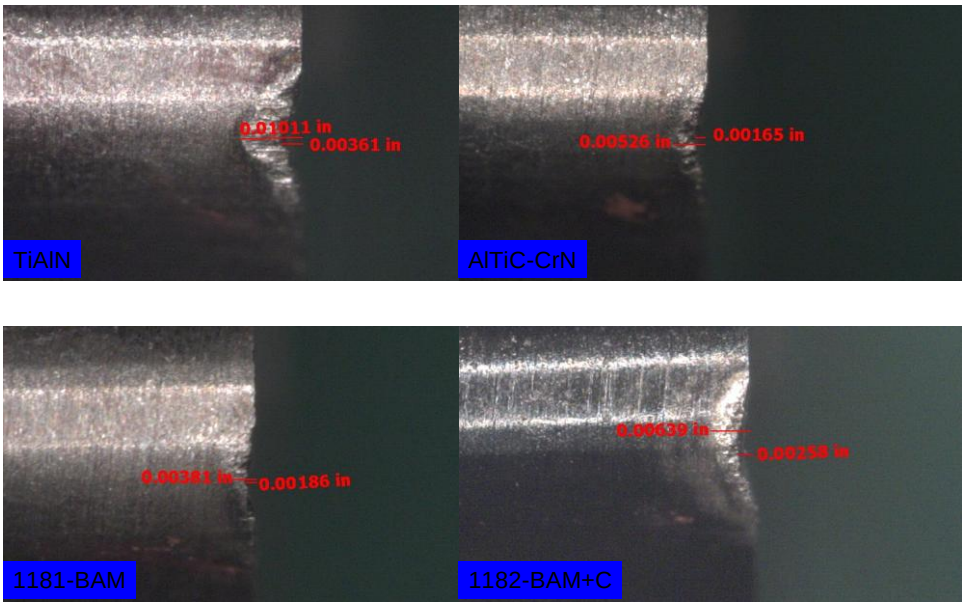

Figure 4.2.6.6.6-1: Comparative flank wear after 500 SFM lathe machine test.

Clearly, the $AlMgB_{14}$-TiB_2 lot 1181 had the best flank wear. This test demonstrated that $AlMgB_{14}$-TiB_2 was superior to other coatings. The $AlMgB_{14}$-TiB_2+C gradient did not perform as well as expected. In previous titanium testing, the carbon gradient showed somewhat improved wear without the high-pressure coolant. The carbon layer for cutting tool applications theoretically should enhance lubrication and aid in removing hot machine chips. Carbon layer in general is a low temperature lubrication film generally below 500°C in air. The role of carbon film in a high-pressure coolant system may be different than without it. The additional thickness was perhaps slightly rounded the cutting edge or cooling effect of the high-pressure water coolant water was diminished by changing the wetting properties. The carbon gradient coating wear mechanism with high pressure cooling is still uncertain.

4.2.6.6.7 Field trials, Applications 7 and 8

Greenleaf was engaged with machine testing with high-pressure coolant system. The high-pressure coolant reduces the interface temperature between titanium and tool by efficiently delivering the coolant fluid at the hot interface using high pressure. With improved cooling, higher machine speeds were tolerated. Previous experience in the field with high-pressure coolant systems and coated tools was that the coatings did not help with tool life. This was our second evaluation of $AlMgB_{14}$-TiB_2-coated tools for the high-pressure coolant application. In the first study, Greenleaf successfully demonstrated more than double the tool life against commercially competitive TiAlN coatings. This second test was a continuation of the testing using finish machine conditions.

Lathe machine test was performed using Bullard 50HP for finish facing of a test ring of Ti6Al4V with an outer diameter of 30 inches and an inner diameter of 20 inches. The test rig had a high-pressure coolant system attached to the tool holder assembly delivering 1,000 psi of coolant directly at the cutting interface. Numerous tests were conducted with varying speeds up to 600 SFM. This section is a summary of the highlights. Four types of coatings on the same WC-6% Co were compared, commercial TiAlN, commercial AlTiC-CrN, $AlMgB_{14}$-TiB_2 (by Eaton) batch 1181, and $AlMgB_{14}$-TiB_2 + Carbon gradient (by Eaton) batch 1182. The feed rate was 0.008 inches/revolution and depths of 0.010 inches, typical finishing operation reported in **Figure 4.2.6.6.7-1**

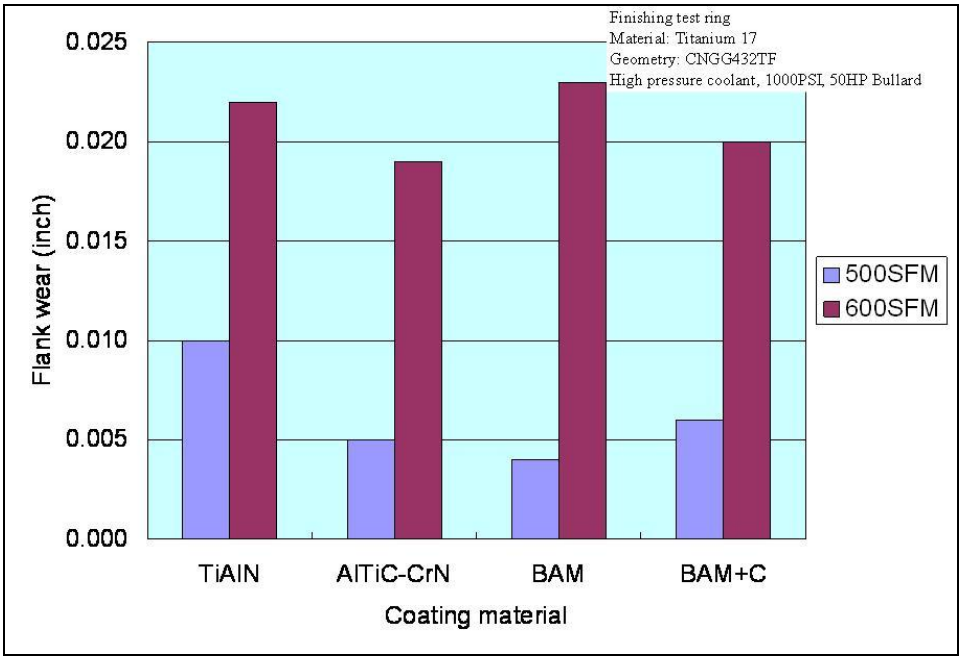

Figure 4.2.6.6.7-1: Coated tools in high pressure machining of titanium.

$AlMgB_{14}$-TiB_2 had the lowest flank wear, with best tool life of 60% greater than TiAlN standard coatings. AlTiC-CrN for competitive evaluation showed 50% improved tool life. At 600 SFM, all tools failed, limited by thermal limitations of the WC substrate.

Extended tests using the high-pressure coolant in **Figure 4.2.6.6.7-2** shows increase in cutting speed up to 500SFM compared with conventional flood coolant. For reference, this test was performed using a Bullard 50HP lathe for finish facing of a titanium test ring with an outer diameter of 30 inches and an inner diameter of 20 inches. The test rig had a high-pressure coolant system attached to the tool holder assembly, and was capable of delivering 1,000 psi of coolant directly at the cutting interface. Numerous tests were conducted with varying speeds up to 600 SFM. The feed rate selected was 0.008 inches/revolution and the depths of cut were set to 0.010 inches, typical of a finishing operation. Four types of coatings on the same WC-6%Co substrate were compared: commercial TiAlN, commercial AlTiC-CrN, $AlMgB_{14}$-TiB_2 (by Eaton)-batch 1181, and $AlMgB_{14}$-TiB_2 + Carbon gradient (by Eaton)-batch 1182. The first test was at a surface speed of 500SFM. Results are presented in **Table 4.2.6.6.7-1**

Note that the $AlMgB_{14}$-TiB_2 coated tools are highlighted as blue diamonds on the plot, with a trend line that predicts the tool life of the insert. The tool life of TiAlN coatings lasted 9 minutes, versus the $AlMgB_{14}$-TiB_2 tool lasting nearly 20 min at 500SFM.

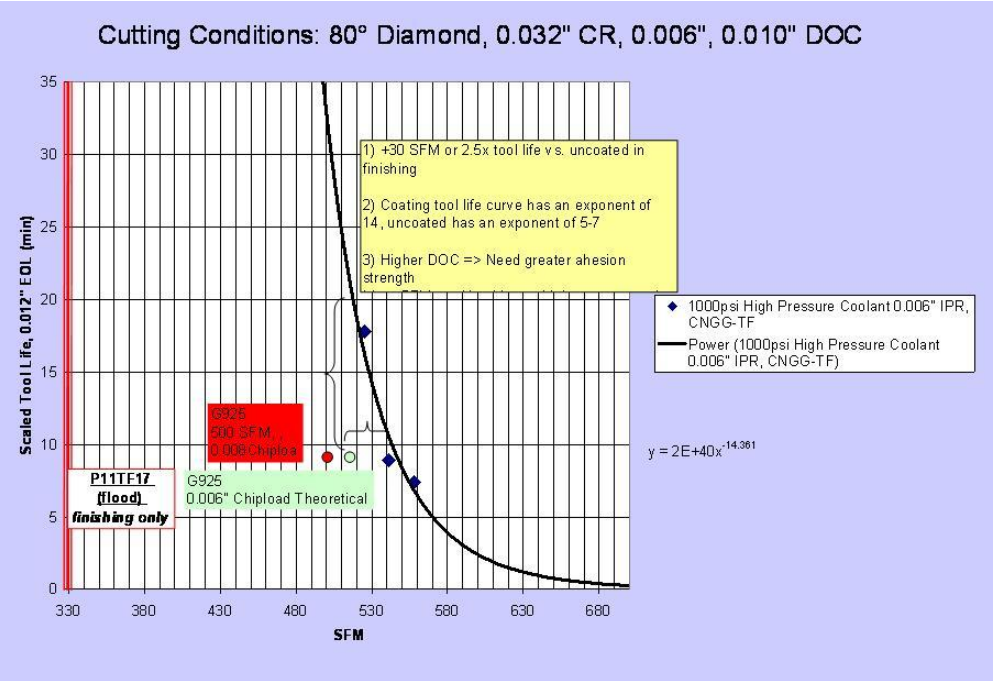

Figure 4.2.6.6.7-2: Improved tool life using $AlMgB_{14}$-TiB_2 -coated tools in high-pressure machining. The blue trend line is an estimate of tool life with given speeds.

Table 4.2.6.6.7-1: Titanium machine testing at surface speed of 500 SFM with high pressure coolant

Grade	G-925	RD4869	1181	1182
Description	TiAlN	AlTiC-CrN	BAM	BAM+C
Cutting speed (SFM)	500	500	500	500
Time in cut (min)	8.2	8.2	8.2	8.2
Crater wear (inch)	0.008	0.006	0.007	0.008
Flank wear (inch)	0.010	0.005	0.004	0.006

.

4.2.6.6.8 Field trials, Application 9

In this application, Greenleaf suggested RPGR-3V with a TF chip form. Insert geometry is outlined below along with some benefits of the insert geometry selected:

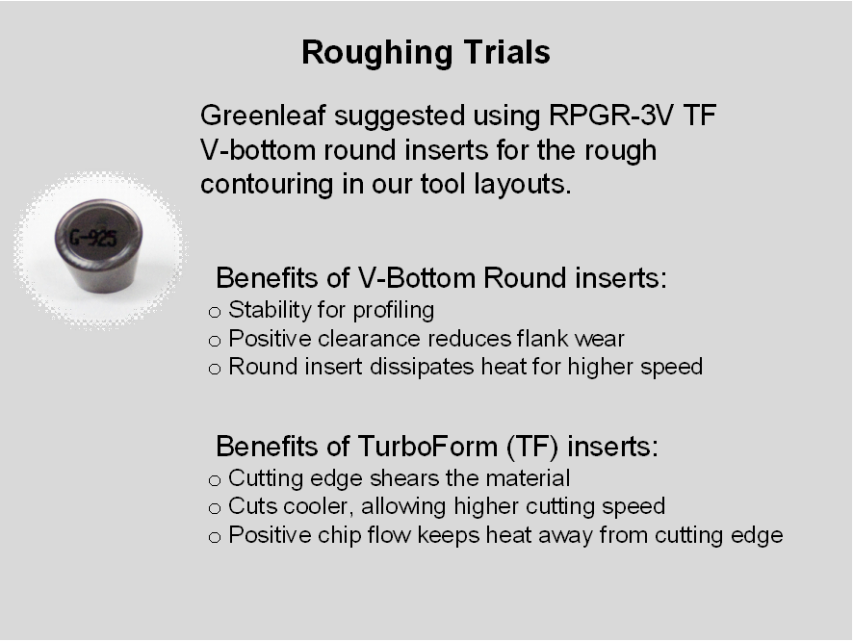

Figure 4.2.6.6.8-1: Roughing Trials

Desired depth-of-cut for this application was 0.25inches, however due to the limited titanium stock; it was scaled back to 0.125 inches. The depth-of-cut is very demanding and expensive to prototype test because of the expensive titanium stock. Detailed test conditions and results are in **Table 4.2.6.6.8-1.**

Table 4.2.6.6.8-1: Greenleaf rough machine testing conditions.

Greenleaf In-house testing conditions

- Material Ti 6-2-4-6
  - 36 HRc
  - 8” diameter x 8” long
  - OD turn with center
- Machine
  - Mori-Seiki NL2500 Slant bed Lathe – 25 HP
- Roughing, RPGN3V-TF
  - Depth of cut .125”
  - Standard speed is 120 SFM

Figure 4.2.6.6.8-2 plots tool wear of coated tool inserts as a function of increasing surface speed. TiAlN is a standard insert and the AlTiC-CrN is a competitive grade. This shows that as we increase surface speed, the tool life degrades more rapidly with the standard TiAlN coating. It also shows that it may be possible to increase the speed to 180 SFM without degrading the tool life. Above 180 SFM, the crater wear increased sharply.

Detailed testing was performed at 180 SFM as shown in **Figure 4.2.6.6.8-3.** All three grades proved very capable of roughing at 180 SFM. There was still no measurable flank wear at this point, only crater wear. $AlMgB_{14}$-TiB_2 had the least amount of wear over the longest cut time of the three grades. **Figure 4.2.6.6.8-4** is an SEM composition image showing the cutting edges after 180 SFM testing. The images show that titanium was transferred onto the material. The TiAlN coated grade had exposed WC substrate. $AlMgB_{14}$-TiB_2 was not worn through and the WC substrate was not detected.

The functional prototype testing suggests that with the $AlMgB_{14}$-TiB_2 coated tool the operations were improved 50%. No further machine damage was found with the increase in machine speeds.

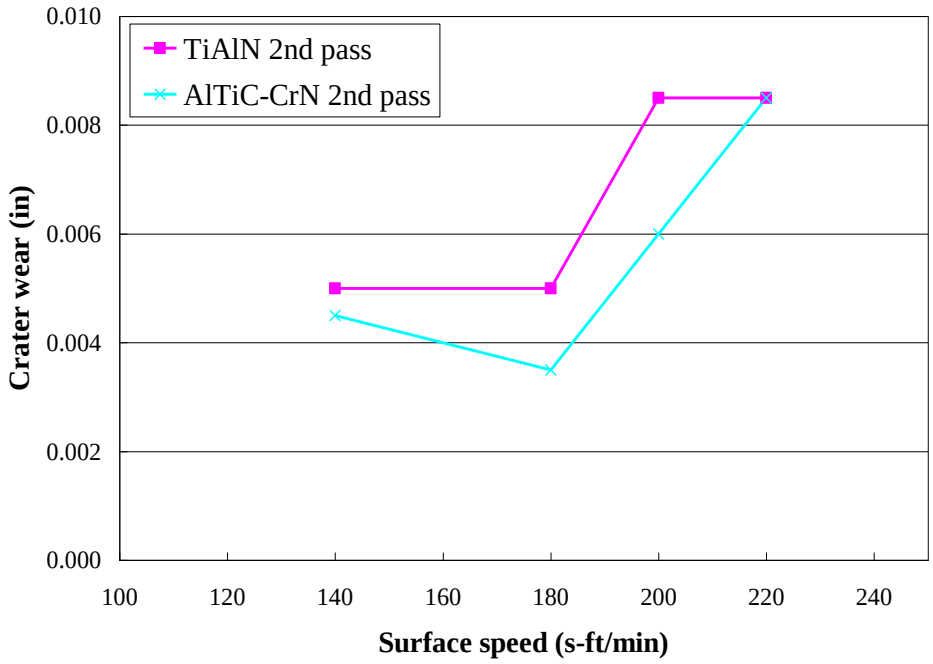

Figure 4.2.6.6.8-2: Speed effects on rough machining showing that the tool life is good until the surface speed is above 180 SFM.

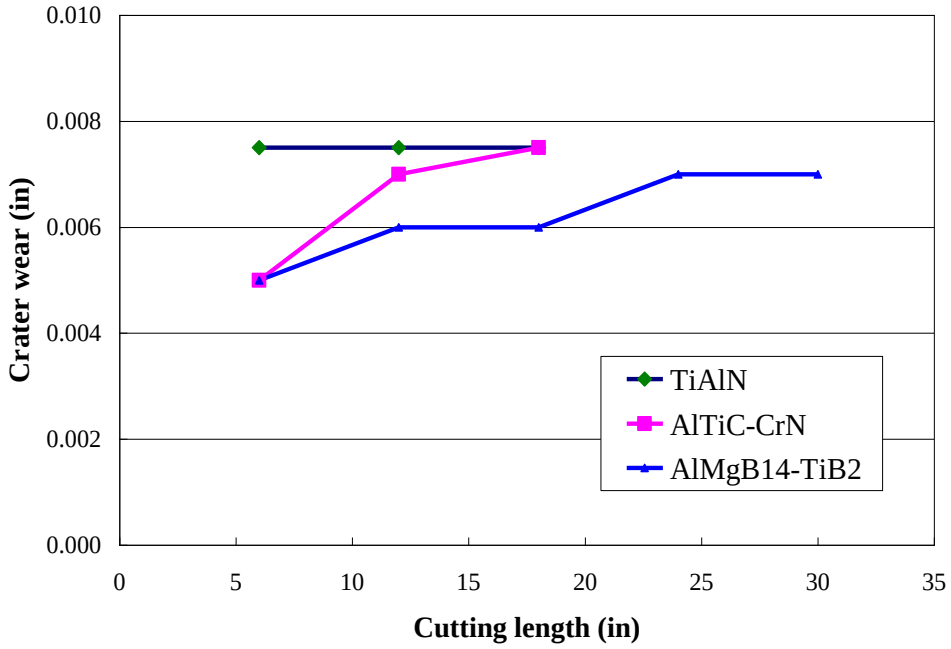

Figure 4.2.6.6.8-3: Extended tool life test at 180 SFM. The $AlMgB_{14}$-TiB_2 had best tool life.

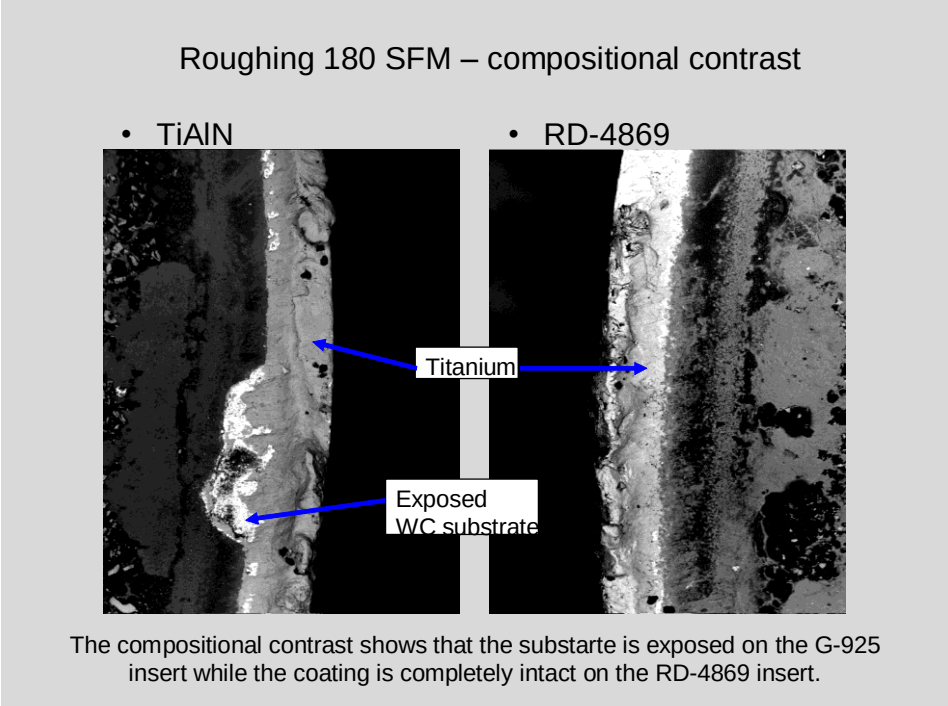

Figure 4.2.6.6.8-4: SEM composition contrast image showing transferred titanium and exposed substrate at the cutting edges.

Field evaluations of $AlMgB_{14}$-TiB_2+C for titanium applications still appear very promising. The overall impact and improvement in efficiency is up to 180%, or nearly three times current commercial grade. As a result, the time required to machine a component is cut to one third. Current titanium cutting grades typically machine below 320 SFM and the $AlMgB_{14}$ coated tools are reaching upwards of 400SFM, limited by the WC-Co substrate. Cast iron typically runs up to 3000 SFM and stainless steels run 1200 SFM, approximately 4-10 times faster than titanium today. With increasing quantity of titanium used in industry, this coating would have a large impact in the aerospace and emerging markets.

5.0 Benefits Assessment

Final energy savings calculations for each of the respective applications (and markets) have been determined, based on divisional engineering and marketing input. The energy savings reported in **Tables 5.0-1** through **Table 5.0-4** illustrate that even a small product introduction will result in a large energy savings and greenhouse gas (GHG) emission reduction.

Table 5.0-1: Vane pump energy savings calculations for two specific use cases

Vane Product	Pressure, Speed, and HP	Baler Application Energy savings per year		Injection Molding Energy savings per year	
		Light Duty	Heavy Duty	Light Duty	Heavy Duty
V-series 35V38	2500 psi, 1800 rpm, 90 HP	$0.7x10^6$ BTU	$1.9x10^6$ BTU	$4.1x10^6$ BTU	$6.9x10^6$ BTU
VMQ series 35VMQ	3680 psi, 1832 rpm, 150 HP	$1.3x10^6$ BTU	$3.3x10^6$ BTU	$6.9x10^6$ BTU	$11.1x10^6$ BTU

Assumptions:
Baler Application: Light Duty is at 30 hrs per week at 20% use. Heavy Duty is at 120hrs per week at 60% use
Injection Molding Application: Light Duty is at 30hrs per week at 50% use. Heavy Duty is at 120hrs per week at 60% use
Operation of pump is 75% at 1800 RPM, 15% at 1200 RPM, 10% at 600 RPM
Overall efficiency gains: ~2% at 1800RPM, 4% at 1200RPM, 11% at 600 RPM
Typical balers and injection molding machines use two vane pumps

For the vane pump use cases identified in **Table 5.0-1**, the assumptions represent typical operating conditions for each application. As an example, an injection molding machine operating at 50% of capacity for 30 hours per week would consume approximately $120x10^6$ BTU of electrical energy in a year's time. Based on Eaton's current market share and the volume of vane pumps sold annually, the energy savings associated with Eaton's implementation (alone, as a single entity) of the nanocoatings technology in this application will be in excess of 86 billion BTU annually. Carbon and/or greenhouse gas emissions would be reduced by 5,600 tonnes through this energy savings. Assuming *only* the use cases presented above, implementation of this technology across the total available market worldwide for vane pumps, the energy savings would reach to 1.4 TBTU/year. As vane pumps are used in many more applications beyond the two identified in **Table 5.0-1**, this energy savings is expected to be larger through full market adoption.

Table 5.0-2: VIS Motor energy savings calculations for mobile hydraulics use case

Application	Light Duty	Heavy Duty
Hours of vehicle operation per year	450	900
Energy usage per vehicle operation (BTU/yr)	$9.6x10^7$ BTU/yr	$1.9x10^8$ BTU/yr
Energy to power Hydraulics system (BTU/yr)	$1.6x10^7$ BTU/yr	$3.2x10^7$ BTU/yr
Projected energy savings based on 10% improvement in motor Efficiency (BTU/yr)	$2.0x10^6$ BTU/yr	$4.0x10^6$ BTU/yr

Assumptions:

200+ skid steer loaders built in 2003 and 2005 with hours listed were used for duty cycle
Of the 84HP average that the engine is rated to deliver for this particular application, 1/6 of this is used to drive the hydraulics motors powering the wheels.
Diesel fuel GHG emissions are calculated to be approximately 161 lbs per 1 million BTU's

For the VIS motor use case identified in **Table 5.0-2**, the assumptions represent standard operating conditions for the application identified. As an example, this particular equipment operating at 450 hours per year would be in operation approximately 1-2 hours per day for a 5-day workweek. Based on Eaton's current market share and the volume of hydraulic valve-in-star motors sold annually, the energy savings associated with Eaton's implementation (alone, as a single entity) of the nanocoatings technology will be in excess of 140 billion BTU annually. Carbon and/or greenhouse gas emissions associated with the diesel fuel savings would be reduced by 12,000 tonnes. Assuming implementation of this technology across the total available market worldwide for low-speed, high torque hydraulic motors (referred to as G/G motors), the energy savings would reach to 2.6 TBTU/year. Taking similar gains into the total available worldwide market for *all* hydraulic motors (in excess of $2.8B in sales per year) results in an annual energy savings of 14.6 TBTU.

Table 5.0-3: Piston pump energy savings calculation for aerospace system use case

Airline Engine	Cruise Thrust (Gross)	Cruise Thrust (Net)	Throttle Specific Fuel Consumption	Fuel Flow	Engine Efficiency
GE CF6-80	16,700 lbs	6,600 lbs	0.362	2400 lb/hr	0.682

Assumptions
GE CF6-80 engine equipped on a mid-size passenger jet at 460kts, 35,000 feet altitude, and a throttle of 70% total engine power at cruising speeds
Current jet fuel usage stands at 55 billion gallons per year
Energy density of Jet A fuel is 18,000 BTU/lb and fuel density is 6.76 lbs/gallon
There are an estimated 87,000 flights per day (based on 2009 total number of global takeoffs)
The estimated annual energy burn of jet fuel alone is 2004 x10^{15} BTU
Current estimates for GHG emissions associated with Jet A fuel burned are 70.88 kg CO2 per million BTU

For the aerospace piston pump application identified in **Table 5.0-3**, the assumptions represent the best available estimates of typical operating conditions. Current calculations show a per-engine savings of 1-2 HP, based on the application of coatings to each pump's pistons, valve plate, nutating plate, and wear plate. Current power estimates for the GE CF6-80 engine are 50,000 shaft horsepower. Application of the coating to the hydraulic pumps onboard would result in a drop in fuel consumption of 0.3lb/hour, equivalent to 86 billion BTU in annual energy savings when Eaton's market share and annual volume are considered. Carbon and/or greenhouse gas emissions associated with the Jet A fuel savings would be reduced by 11,987,000 kg, nearly 12,000 tonnes. Assuming implementation of this technology across the total available market worldwide for axial-orientation, variable displacement, aerospace piston pumps, the energy savings would reach 209 billion BTU/year.

Table 5.0-4: Piston pump energy savings calculation for mobile hydraulics application.

Agricultural Tractor	Mid-Size, Agricultural
Energy usage per vehicle operation (BTU/yr)	7.8×10^{8} BTU/yr
Energy to power Hydraulics system (BTU/yr)	1.9×10^{7} BTU/yr
Projected energy savings based on 5% improvement in Pump Efficiency (BTU/yr)	9.8×10^{6} BTU/yr

Assumptions:
The hydraulic system referenced consisted of one variable piston pump
Diesel fuel carbon emissions are 161 lbs per 1 million BTU's

For the piston pump agricultural use case identified in **Table 5.0-4**, the assumptions represent standard operating conditions of the tractor. As an example, the hydraulics circuit will utilize approximately 1/3 of the available engine power, assuming that operation of the auxiliary circuit is necessary (e.g., any attachment/implement connected to the power-take-off (PTU) shaft). Given Eaton's market presence and the annual volume of pumps produced, the equivalent energy savings associated with implementation of the nanocoatings technology will be in excess of 3 billion BTU annually. Carbon and/or greenhouse gas emissions associated with the diesel fuel savings would be reduced by 23,000 tonnes. While relatively small in contrast to the annual pump energy usage cited in the Introduction of this paper, this savings does not account for the total available market or the impact that the technology will have on similar products used in other applications. Assuming implementation of this technology across the total available market worldwide for *only* mobile, open-circuit piston pump products, the energy savings reaches 76 billion BTU/year. Full adoption of the technology into the total available worldwide market for *all* hydraulic piston pumps (well in excess of $4.2B in sales per year), regardless of the application, results in an annual energy savings of 3.7 TBTU.

When the aforementioned applications are combined into one complete product portfolio, the associated annual energy savings becomes quite substantial; application to Eaton hydraulic products alone by 2030 would total 6.4 TBTU (at a rate of 0.32 TBTU annually). **Moreover, total implementation into hydraulic products worldwide would exceed 19.9 TBTU annually for today's market. Assuming an annual worldwide industrial growth rate of 4%[16] and *no* cumulative effect associated with legacy products, the energy savings would be equivalent to 46 TBTU/year by 2030.** As a note, initial energy savings estimates associated with worldwide implementation of the technology were calculated to be 30 TBTU/year by FY 2030.

Domestic cutting tool market estimates are estimated for 2010 in Table XII. We estimate nearly 400 million inserts being used in the marketplace with approximately 8.5% being used for special applications and difficult to machine alloys where majority of the ceramics are being used.

Table 5.0-5: Cutting tool market estimates for 2010 with approximately 34 million inserts used for specialty materials such as titanium and nickel super alloys.

Domestic cutting tool market estimates 2010 (similar to 2002 NAICS data code 33351503)	
# inserts (in millions)	*$ (in millions)*
	$3,000 tools in US (WC and HSS, saw blades, all tools)
400	$2,000 indexable WC tools in US
	$5 /insert, average selling price
	85% coated
340	$1,700in coated grades
34	10% of coated in high special materials applications, like Ti, Ni-superalloys
World wide is 3x US	
1200	$9,000 inserts in 2010 (approx)

The total machine time estimated from economic census data suggest 2.63×10^8 hours per year with an approximately 7.5 TBtu energy being spent [17] [18]

There are three ways to save energy in machining applications. First, if the tool runs two times faster, it takes half the number of machines to perform the same task. This is a 50% energy savings with building overhead. Secondly, approximately 20% or ~5hrs/day is being spent on tool change and setup. The extended tool life can reduce the setup time. Thirdly, previous data on energy savings using the low friction coatings showed a maximum of 6% reduction in machine power.

In titanium applications, it is estimated that 7% of total machining hours are used. With a 50% machine time savings, the total energy consumed is represented by:

$$7.5\text{TBtu/year} * 3.5\% = 0.263\text{TBtu/year} \; or \; 7.9\text{TBtu total in 30 years.}$$

6.0 Commercialization

A significant portion of Phase III of the project focused on developing commercialization plans for the two applications, industrial hydraulics and cutting tools. Given the end-application fuel and energy savings associated with market acceptance of the technology, significant effort has been spent in making the technology viable for wide-release, determining the costs associated with added vapor deposition processing, and planning which products will (and will not) be introduced bearing the technology.

6.1 Industrial Hydraulics

Testing performed on the various systems illustrates that there is an associated benefit to using the $AlMgB_{14}$-TiB_2 nanocoating and its derivatives. In an effort to maximize the number of potential applications, though, any added costs associated with the coating itself or ancillary added processing needs to be offset. This is imperative to ensuring that Eaton and/or any other adopters of the technology will be competitive - especially in markets where even significant advancements in product performance may not justify a cost increase.

The first of two key aspects to establishing a [relatively] low cost approach is in leveraging other application spaces (most notably those that are not as price sensitive as industrial hydraulics) to defray the costs. As would be expected, processed component volumes, labor, materials, and capital all influence the actual costs to coat each component. While counterintuitive, systems such as the vane pump evaluated actually can be a hindrance to achieving low coating costs. As thousands of these components (or parts of similar size) can be processed using a large-scale, industrial PVD furnace, respective volumes need to be substantially large enough to amortize the processing equipment, the labor required to fixture a batch, and the materials needed for coating. With a relatively low annual volume, however, other applications need to be pursued.

As an alternative to outside processing, Eaton Corporation investigated in-house processing as an alternative to subcontracting the production to an outside facility. $AlMgB_{14}$-TiB_2 targets are available for purchase through NewTech Ceramics, the current licensee of the technology. While the costs associated with this path to commercialization are more controllable (e.g. labor rates, material, delivery, scheduling, and so forth), this path does require significant expenditure in form of initial capital and manufacturing floor space required to perform the vapor deposition. The same limitations associated with low component volumes can be applied to this particular scenario.

An alternative approach to leveraging an organization’s product portfolio is through the pairing a of less costly substrate material with the ultra-hard film. This particular path proved effective for Eaton throughout the project in that suitable materials were identified that could be paired with the $AlMgB_{14}$-TiB_2 nanocoatings. In the hydraulic vane pump, as an example, AISI 52100 was tested as a replacement to the M2 tooling material. Given the former material’s lower alloy content, an overall savings would be realized. The limitations to this approach are that material changes may (and often do) require tooling changes, switches to the supply base, re-validation, and customer approval.

Eaton's efforts to commercialize the coating throughout the project coupled each of the two aspects discussed. Discussions with NewTech Ceramics focused on leveraging the other potential applications as a means to minimize associated coating costs. Conversely, discussions with Eaton's steel suppliers focused on the availability of alternative materials, the use of existing tooling, and changes to scheduling.

With the industrial and mobile hydraulic markets declining by as much as 40% over the 2008-early 2010 period, Eaton found its customer base shifting their focus away from efficiency gains through technology. Both the original equipment manufacturers and distributor base began to pursue significant price reductions on all power and motion control products. Adoption of the $AlMgB_{14}$-TiB_2 nanocoatings technology is unlikely at this time in these particular markets until diesel fuel prices return to the pre-2008 levels.

6.2 Cutting Tools

Greenleaf primarily markets cutting tool inserts within the machining industry, where initial implementation of new tools is a significant commercialization hurdle. The improved productivity, wear performance, and reduced cost of machine tool operation demonstrated by the new technology facilitate its adoption by customers. Thus far, Greenleaf has demonstrated continuous success with titanium machining using Eaton's PVD system and the internally developed processing parameters for the $AlMgB_{14}$-TiB_2 nanocoating. The laboratory testing, pilot trials, and field evaluations were successful and demonstrate a clear readiness for the technology to move forward as a commercial product. Greenleaf's next step is to test the equivalent commercial grade $AlMgB_{14}$-TiB_2 offerings using a production-intent supplier. Future performance comparisons between the Eaton derivative and the production coating will facilitate creating a robust production-intent process. Greenleaf's current commercialization plan is at the decision point between evaluating a coatings supplier and investing in capital equipment to produce the coated tools internally. The decision tree for bringing coated tools to market is included:

Decisions as to in-house processing and outsourcing needs for coating are determined by available capacity and volume requirements, along with capital and personnel resources available for production. In-house processing offers an advantage in that further modification to the material may result in enhanced performance-beyond that which has been demonstrated in previous pilot trials. Additional challenges associated with external processing are:

- Unknown cost/quality – the cost of cutting tools is relatively inexpensive and the handling of the tools is time-consuming when compared to other applications. Greenleaf's potential coating suppliers are predicting a higher cost, although exact figures are unknown. The quality and consistency of the commercial-intent coating have not been proven through the subcontractor(s).

- Negotiating NDA and supplier agreements – the terms and conditions associated with both the NDA and supplier agreements need to be evaluated carefully to ensure Greenleaf's profitability with the new, $AlMgB_{14}$-TiB_2 coated tools.

- Qualification with customers – as a bulk of the titanium components that have been tested are used for aerospace applications, an extensive qualification period for new processes, including new cutting tools, is required. Successful customer pilot trials may expedite this rather lengthy process, but the timing associated should not to be discounted.

The disadvantage to in-house processing lie in the costs associated with capital and any associated expenditures beyond the PVD processing equipment itself (cleaning lines, incoming power conditioning, and so forth). The challenges associated with in-house processing are discussed further:

- Purchase of a PVD unit – a moderate-sized, commercial grade physical vapor deposition system represents an approximate capital investment of 2 million dollars. Further expenditures include the necessary cleaning tanks and drying ovens required to condition parts before the deposition. These systems often require a separate climate-controlled laboratory space. Deionized water systems and cooling lines are necessary to ensure that the system does not overheat during operating. Custom-fixturing is often required for maximum utilization. Lastly, acquiring an operator skilled in both PVD processing and process development/optimization is not a negligible expense.

- Redeveloping powder processing, target fabrication, and coating – for Greenleaf to optimize the nanocoating's composition beyond that developed during the course of this project requires powder processing, hot-press systems, and other ancillary equipment.

- Intellectual property protection – Develop and optimization of the $AlMgB_{14}$-TiB_2 nanocoatings to yield performance gains beyond those developed during the course of this project may result in intellectual property. The development of new compositions and formulations will need to be part of any licensing or supplier agreements.

- As with externally-processed coatings, a significant effort to production-level $AlMgB_{14}$-TiB_2-based nanocoatings will be in customer qualification of the new cutting tools. This includes further pilot trials, design reviews, audits, and first-article inspection.

7.0 Accomplishments

Included are the main accomplishments of the project.

7.1 Technical

- The ability to use Physical Vapor Deposition (PVD) and Pulsed Laser Deposition (PLD) processes to make nanocoatings of single phase $AlMgB_{14}$ and mixed phase $AlMgB_{14}$-TiB_2, with varying compositions.

- Novel, low friction nanocoatings through the incorporation of gradient carbon layers within single phase and mixed phase $AlMgB_{14}$ based compositions.

- Increasing the PLD coating deposition rate of $AlMgB_{14}$-based films by tenfold using a femtosecond laser with up to a 1000 HZ pulse repetition.

- Simulative friction and wear tribology testing developed for both industrial hydraulics and machining operations. These tests were effectively used to determine the relative frictional characteristics and durability of the nanocoatings being developed.

- Novel processing techniques for the manufacture of $AlMgB_{14}$-TiB_2 composite target tiles were established for the development of PVD targets.

  The gradient carbon $AlMgB_{14}$-TiB nanocoating was deposited onto austenitic stainless steel plates for evaluation as a possible alternative to fluorine-based polymer (Teflon) coatings. ISU's food science group reported very favorable results of this trial.

- Customer field trials confirmed that $AlMgB_{14}$-based coatings can improve the efficiency of high pressure coolant machining.

7.2 Publications

In addition to these technical accomplishments achieved, the various team members published several technical papers in a variety of peer reviewed journals and proceedings.

- Qu, J., Blau, P.J., Zhu, D., Cook, B.A., Elmoursi, A.A., "Tribological Characteristics of AlMgB14 and Nanocomposite AlMgB14-TiB2 Superhard Coatings,' Proceedings of IJTC2008 STLE/ASME International Joint Tribology Conference, Miami, FL, Oct. 20-22, 2008.

- J. Qu, P. J. Blau, A. A. Elmoursi, C. Higdon, and B. A. Cook (2010) $AlMgB_{14}$-TiB_2-C and DLC Coatings to Improve the Startup Efficiency for Hydraulic Motors," presented at the 2010 Annual Meeting of the Society for Tribologists and Lubrication Engineers, Las Vegas, NV, May 16-20, 2010.

- B. A. Cook, J. L. Harringa, J. Anderegg, A. M. Russell, J. Qu, P. J. Blau, C. Higdon, and

A. A. Elmoursi, “Analysis of Wear Mechanisms in Low Friction $AlMgB_{14}$-TiB_2 Coatings,” Surface & Coatings Technology 205 (2010), 2296-2301.

C. Higdon, B. Cook, J. Goldsmith, J. Qu, and P. Blau, et al (2011) “Friction and wear mechanisms in $AlMgB_{14}$-TiB_2 nanocoatings,” accepted for the 2011 International Conference on Wear of Materials, presentation and journal article in Wear.

7.3 Patents

The following patent applications were filed at the USPTO during the project’s period of performance:

- 09-rCLP-352 (NC). Serial Number 12/792324. *Ion Beam Sputter Target and Method of Manufacture*. 6/15/2010. Clifton Higdon, Alaa Elmoursi, Jason Goldsmith, Bruce Cook, Peter Blau, Jun Qu, Robert Milner

- 08-rCLP-099(V). Serial Number 12/493713. *Friction and Wear Reducing Coating*. 2/4/2010. Dong Zhu, Alaa Elmoursi, Robert Milner

- 08-rCLP-007(G). Serial Number 12/493885. *Energy Conversion Device and Method of Reducing Friction Therein.* Dec 31, 2009. Lyudmila Solovyeva, Kyle Jansson, Alaa Elmoursi, Dong Zhu, Robert Milner, Earl Daugherty, Clifton Higdon, Kamel Elagamy, Aaron Hicks.

7.4 Recognition

The team was selected for a regional technology transfer award by the Federal Laboratory Consortium. In being selected, the project is eligible for a national technology transfer award, to be announced in January of 2011.

The Federal Laboratory Consortium for Technology Transfer (FLC) is a nationwide network of federal laboratories that provides a forum to develop strategies and opportunities for linking laboratory mission technologies and expertise with the marketplace. The FLC was organized in 1974 and formally chartered by the Federal Technology Transfer Act of 1986 to promote and strengthen technology transfer nationwide. Today, more than 250 federal laboratories and centers and their parent departments and agencies are FLC members.

8.0 Conclusions

Given the scope of the project and the extent to which the $AlMgB_{14}$-TiB_2 coatings were investigated, there are several key conclusions that can be drawn. The functional performance testing on production-intent prototype components demonstrates that there are significant gains in the energy/fuel/time/processing efficiency results associated with application of the coating. For example:

- A 97% reduction in coefficient of friction when running $AlMgB_{14}$-TiB_2 + C coated tool steel in water glycol hydraulic fluid using a pin-on-disk tribometer.

- Dynamometer testing showed a greater than 10% improvement in start-up mechanical efficiency when $AlMgB_{14}$-based nanocoatings were applied to Eaton's hydraulic motor components. Additional dynamometer testing of other Eaton hydraulic pumps showed a gain of at least 3% in mechanical efficiency when using the $AlMgB_{14}$-based nanocoatings

- Implementation of the $AlMgB_{14}$-based nanocoatings into worldwide industrial pump and motor markets (assuming similar mechanical efficiency gains) would account for 46 YBTU/year in energy savings by 2030, greater than the 30 TBTU/year originally calculated using the GPRA analysis.

- A 38% improvement in WC cutting tool life was shown when using the group's novel gradient carbon $AlMgB_{14}$-TiB_2 nanocoatings.

In terms of basic scientific and technical understanding of the coatings technology, the following additional conclusions were reached:

- A key influence on the low friction of the $AlMgB_{14}$-TiB_2 films is the formation of boric acid between the interfacial contacts. The inherent self-lubricating nature of $B(OH)_3$ films in effect "polishes" the two counterfaces.

- Boric acid formation is largely derived from the reactivity of the crystalline TiB_2 phase and not the amorphous $AlMgB_{14}$ phase. It would appear, based on upon the X-ray photoelectron spectroscopy results, that the TiB_2 phase tends to dissociate into boron oxide through the reaction given in equation 1 [19].

$$2TiB_2+5O_2 \rightarrow 2TiO_2+2B_2O_3 \quad (1)$$

The boron oxide produced by this transformation reacts with water (liquid or vapor) to form boric acid, shown in Equation 2.

$$\frac{1}{2}B_2O_3+\frac{3}{2}H_2O \rightarrow B(OH)_3 \quad (2)$$

Given that one of the key reactions in each of the equations listed above is oxygen, the transformation is more likely to occur in water-based hydraulic fluids than petroleum-based fluids. Longer-term exposure to water-based fluids in a load-bearing application would, based on this finding, lead to the applied coating acting as a sacrificial layer. It has been shown that coated components operating in water-based lubricants exhibit a higher degree of coating removal than similar components operated in mineral oil.

- $AlMgB_{14}$-TiB_2 films are cost-competitive to current commercial coatings, such as DLC, and have been shown to lead to lower coefficients of sliding friction, decreased wear under aggressive load conditions, and result in higher mechanical and volumetric efficiencies of hydraulic pump and motor systems. $AlMgB_{14}$-based coatings yield far greater sustainable feed rates in the industrial machining of aerospace titanium alloys than competitive offerings when processed using high-pressure coolant delivery.

9.0 Recommendations

The following recommendations are made for further development and implementation of this technology:

1. $AlMgB_{14}$-based films that are specified for low interface frictional performance should include a gradient carbon layer. This particular aspect of the processing parameters has been repeatedly shown to lower interfacial friction further beyond the performance of the base nanocomposite coating.
2. Where appropriate, the nanocomposite constituent compositions could be tailored to favor wear or low friction performance. A coating bearing higher percentages of the TIB_2 phase would trend towards better low friction performance due to this phase's favored tendencies to form boron oxide, and, subsequently, boric acid. Conversely, in an application in which increased wear resistance is generally favored, the percentage of TiB_2 phase could be lowered, as the research has shown that the amorphous $AlMgB_{14}$ constituent does not form boric acid.
3. Organizations pursuing the development of $AlMgB_{14}$-TiB_2 films should strongly consider implementation of the various test methods discussed in this report as a means to evaluate the coatings for performance prior to end-application development. Many process parameters have been shown to influence coating performance, and so careful process monitoring and predictive evaluation techniques are critical to success.
4. Further enhancements to the $AlMgB_{14}$-TiB_2 nanocoatings could be made by increasing the current density of states. Initial research has shown that, for example, hardness of the bulk material could be enhanced twofold through stoichometric changes to the overall coating compositions.

10.0 References

Specific Citations

[1] Energy Use, Loss and Opportunities Analysis: U.S. Manufacturing & Mining, Prepared by Energetics, Inc. and E3M, Inc. for the U.S. Department of Energy Office of Energy Efficiency and Renewable Energy Industrial Technologies Program, Dec. 2004.

[2] K. Holmberg and A. Matthews, Coatings Tribology, Elsevier, The Netherlands (2009) 560 pp.

[3] A. V. Sumant, A. R. Krauss, D. M. Gruen, O. Auciello, A. Erdemir, M. Williams, A. F. Artiles, and W. Adams, Tribology Trans., 48 (2005) p. 24-31.

[4] B.A. Cook, J.L. Harringa, T.L. Lewis, and A.M. Russell, Scripta Materialia, 42 (2000) 597–602.

[5] J. Qu, P. J. Blau, D.Zhu, B. A. Cook, and A. A. Elmoursi, Proceedings of IJTC2008 STLE/ASME International Joint Tribology Conference, October 20-22, 2008, Miami, FL, USA.

[6] W. D. Sproul, Surface and Coatings Tech. 81 (1996) 1-7.

[7] Y-W Chung and W. D. Sproul, MRS Bulletin 28 (2003) 164.

[8] O. Auciello, A.R. Krauss, D.M. Green, A. Jayatissa, A. Sumant, J. Tucek, D. Mancini, N. Molodvan, A. Erdemir, D. Ersoy, M.N. Gardos, H.G. Bushman, E.M. Meyer, “Science and Technology of Ultrananocrystalline Diamond (UNCD) Thin Films for Multifunctional Devices,” U.S. Department of Energy, Office of Basic Energy Science, and Office of Transportation Technology under contract W-3-1-109-ENG-38.

[9] B. Cook and A. Russell, "Advanced Wear-resistant Nanocomposites for Increased Energy Efficiency," U.S. Department of Energy Award # DE-FG36-06GO15015, Ames Laboratory.

[10] B.J. Hamrock and D. Dowson (1981) *Ball Bearing Lubrication – The Elastohydrodynamics of Elliptical Contacts,* A Wiley-Interscience Publication, John Wiley & Sons, New York.

[11] T. L. Hu, et al., “Lubricating properties of diamond-like carbon,” Wear 181-183 (1995) 766.

[12] G. Johnson and W. Hubbard, J. Chem. Thermo., 1 (1969) p. 459.

[13] N. P. Bansal, Handbook of Ceramic Composites, Springer Publishing (2005), p. 203.

[14] J. Filik, Spectroscopy Europe, 17 (2005) 10.

[15] B. Marchon, et al., “*Photoluminescence and Raman Spectroscopy in Hydrogenated Carbon Films*,” IEEE Trans. Magn., 33 (1997) 3148 – 3150.

[16] Central Intelligence Agency, *The World Factbook,* Industrial Production Growth Rates, https://www.cia.gov/library/publications/the-world-factbook/fields/2089.html#

[17] Fundamentals of Tool Design, 5th ed., Society of Manufacturing Engineers, Dearborn, MI, 2003, p.43.

[18] Modern metal cutting, Sandvick Coromant, First North American edition published 1996.

[19] S.P. Gordienko, “Role of Nitrogen during Oxidation of Titanium Diboride in Air,” Poroshkovaya Metallurgiya, Nos. 5-6(431), pp. 79-83, May-June, 2003. Original article submitted December 20, 2001.

Additional References

B.A. Cook, J.L. Harringa, A.M. Russell, J.S. Peters, and A. Ahmed, U.S. Patent 7,517,375, “Wear-resistant boride composites with high percentage of reinforcement phase,” April 14, 2009.

B.A. Cook, Y. Tian, A.P. Constant, J.L. Harringa, A.M. Russell, and P. Molian, U.S. Patent 7,238,429, “An Ultra-hard, Low Friction Coating Based on $AlMgB_{14}$ for Reduced Wear of MEMS and Other Tribological Components and Systems," July 3, 2007.

B.A. Cook, A.M. Russell, J.L. Harringa, S.B. Biner, and I. Anderson, U.S. patent 7,172,641, “Ultra-hard boride-based matrix reinforcement,” February 6, 2007.

B.A. Cook, A.M. Russell, and J.L. Harringa, U.S patent 6,921,422, "Ductile binder phase for use with $AlMgB_{14}$ and other hard ceramic materials," July 2005.

B.A. Cook, J.L. Harringa, and A.M. Russell, U.S. Patent 6,099,605, “Superabrasive Boride and a Method of Preparing the Same by Mechanical Alloying and Hot Pressing," August 8, 2000.

B.A. Cook, A.M. Russell, J.S. Peters, and J.L. Harringa, "Estimation of surface energy and bonding between $AlMgB_{14}$ and TiB_2," *J. Physics and Chemistry of Solids*, doi:10.1016/j.jpcs.2010.02.009, 2010.

K. Holmberg and A. Matthews, *Coatings Tribology*, Netherlands, 2009, p. 560.

B.A. Cook, J.L. Harringa, T.L. Lewis, and A.M. Russell, *Scripta Materialia*, 42, 2000, p. 597–602.

Society of Manufacturing Engineers, *Fundamentals of Tool Design*, 5th edition, 2003, p.43.

Sandvick Coromant, *Modern Metal Cutting*, First North American Edition, 1996.

H. Duumlzcuumlkogbrevelu, M. Acarogbrevelu. "Lubrication Properties of Vegetable Oils Combined with Boric Acid and Determination of Their Effects on Wear,” *Energy Sources, Part A: Recovery, Utilization, and Environmental Effects*, Volume 32, Issue 3, 2010, p. 275-285.

L. Pauling, *The Nature of the Chemical Bond and the Structure of Molecules and Crystals*, Cornell University Press, 1960 p. 98.

B.A. Cook, A.M. Russell, J.L. Harringa, A.J. Slager, and M.T. Rohe, “A new ductile binder phase for use with $AlMgB_{14}$ and other ultra-hard ceramics,” *J. Alloys Compd.*, Vol. 366, 2004, p. 145.

U.S. Department of Energy Office of Energy Efficiency and Renewable Energy Industrial Technologies Program , *Energy Use, Loss and Opportunities Analysis: U.S. Manufacturing & Mining, Prepared by Energetics, Inc. and E3M, Inc.*, 2004.

A.M. Russell, B.A. Cook, J. L. Harringa, and T. L. Lewis, “Coefficient of Thermal Expansion of $AlMgB_{14}$,“ Scripta Materialia 46 (2002) 629 – 633.

T. L. Lewis, A.M. Russell, B.A. Cook, and J. L. Harringa, “Al_2MgO_4, Fe_3O_4, and FeB Impurities in $AlMgB_{14}$," Mater. Science & Engineering A, 351 (2003) pp. 117-122.

B. A. Cook, A. M. Russell, J. A. Harringa, A. J. Slager, and M. T. Rohe, “A New Ductile Binder Phase for use with $AlMgB_{14}$ and other Ultra-Hard Ceramics,” J. Alloys & Compounds. 366 (2004), 145-151.

M. Stock and P. Molian, “Femtosecond pulsed laser deposition of amorphous, ultra hard thin films,” J. Vacuum Sci. & Tech. A, 22 (2004) 670 – 675